NIST Special Publication 1018
Sixth Edition

Fire Dynamics Simulator Technical Reference Guide Volume 1: Mathematical Model

Kevin McGrattan
Simo Hostikka
Randall McDermott
Jason Floyd
Craig Weinschenk
Kristopher Overholt

National Institute of Standards and Technology
U.S. Department of Commerce

VTT Technical Research Centre of Finland

NIST Special Publication 1018
Sixth Edition

Fire Dynamics Simulator Technical Reference Guide Volume 1: Mathematical Model

Kevin McGrattan
Randall McDermott
Craig Weinschenk
Kristopher Overholt
Fire Research Division
Engineering Laboratory
Gaithersburg, Maryland, USA

Simo Hostikka
VTT Technical Research Centre of Finland
Espoo, Finland

Jason Floyd
Hughes Associates, Inc.
Baltimore, Maryland, USA

November 26, 2013
FDS Version 6.0.1
SVN Repository Revision : 17529

U.S. Department of Commerce
Penny Pritzker, Secretary

National Institute of Standards and Technology
Patrick D. Gallagher, Under Secretary of Commerce for Standards and Technology and Director

Certain commercial entities, equipment, or materials may be identified in this document in order to describe an experimental procedure or concept adequately. Such identification is not intended to imply recommendation or endorsement by the National Institute of Standards and Technology, nor is it intended to imply that the entities, materials, or equipment are necessarily the best available for the purpose.

National Institute of Standards and Technology Special Publication 1018
Natl. Inst. Stand. Technol. Spec. Publ. 1018, 149 pages (April 2013)
CODEN: NSPUE2

FDS Developers

The Fire Dynamics Simulator and Smokeview are the products of an international collaborative effort led by the National Institute of Standards and Technology (NIST) and VTT Technical Research Centre of Finland. Its developers and contributors are listed below.

Principal Developers of FDS

Kevin McGrattan, NIST
Simo Hostikka, VTT
Randall McDermott, NIST
Jason Floyd, Hughes Associates, Inc., Baltimore, Maryland, USA
Craig Weinschenk, NIST
Kristopher Overholt, NIST

Principal Developer of Smokeview

Glenn Forney, NIST

Principal Developer of FDS+Evac

Timo Korhonen, VTT

Contributors

Susan Kilian, hhpberlin, Germany
Vivien Lecoustre, University of Maryland, USA
Charles Luo, Global Engineering and Materials, Inc., Princeton, New Jersey, USA
Anna Matala, VTT
William Mell, U.S. Forest Service, Seattle, Washington, USA
Topi Sikanen, VTT
Ben Trettel, The University of Texas at Austin, USA

About the Developers

Kevin McGrattan is a mathematician in the Fire Research Division of NIST. He received a bachelor of science degree from the School of Engineering and Applied Science of Columbia University in 1987 and a doctorate at the Courant Institute of New York University in 1991. He joined the NIST staff in 1992 and has since worked on the development of fire models, most notably the Fire Dynamics Simulator.

Simo Hostikka is a Principal Scientist and Team Leader at VTT Technical Research Centre of Finland. He received a master of science (technology) degree in 1997 and a doctorate in 2008 from the Department of Engineering Physics and Mathematics of the Helsinki University of Technology. He is the principal developer of the radiation and solid phase sub-models within FDS.

Randall McDermott joined the Fire Research Division at NIST in 2008. He received a B.S. from the University of Tulsa in Chemical Engineering in 1994 and a Ph.D. from the University of Utah in 2005. His research interests include subgrid-scale models and numerical methods for large-eddy simulation, adaptive mesh refinement, immersed boundary methods, and Lagrangian particle methods.

Jason Floyd is a Senior Engineer at Hughes Associates, Inc., in Baltimore, Maryland. He received a bachelor of science and a doctorate in the Nuclear Engineering Program of the University of Maryland. After graduating, he was awarded a National Research Council Post-Doctoral Fellowship at the Building and Fire Research Laboratory of NIST. He is a principal developer of the combustion, control logic, and HVAC sub-models within FDS.

Craig Weinschenk joined the Fire Research Division as a National Research Council Postdoctoral Research Associate in 2011. He received a B.S. from Rowan University in 2006 in Mechanical Engineering. He received an M.S. in 2007 and a doctorate in 2011 from The University of Texas at Austin in Mechanical Engineering. His research interests include numerical combustion, fire-structure interaction, and human factors research of fire-fighting tactics.

Kristopher Overholt joined the Fire Research Division at NIST in 2013. He received a B.S. in Fire Protection Engineering Technology from the University of Houston-Downtown in 2008, an M.S. in Fire Protection Engineering from Worcester Polytechnic Institute in 2010, and a Ph.D. in Civil Engineering from The University of Texas at Austin in 2013. He works on aspects of FDS related to verification and validation, continuous integration testing, and quality metrics. His research interests include inverse fire modeling problems, soot deposition in fires, and the use of fire models in forensic applications.

Glenn Forney is a computer scientist in the Fire Research Division of NIST. He received a bachelor of science degree in mathematics from Salisbury State College and a master of science and a doctorate in mathematics from Clemson University. He joined NIST in 1986 (then the National Bureau of Standards) and has since worked on developing tools that provide a better understanding of fire phenomena, most notably Smokeview, an advanced scientific software tool for visualizing Fire Dynamics Simulation data.

Timo Korhonen is a Senior Scientist at VTT Technical Research Centre of Finland. He received a master of science (technology) degree in 1992 and a doctorate in 1996 from the Department of Engineering Physics and Mathematics of the Helsinki University of Technology. He is the principal developer of the evacuation sub-model within FDS.

Susan Kilian is a mathematician with numerics and scientific computing expertise. She received her diploma from the University of Heidelberg and received her doctorate from the Technical University of Dortmund in 2002. Since 2007 she has been a research scientist for hhpberlin, a fire safety engineering firm located in Berlin, Germany. Her research interests include high performance computing and the development of efficient parallel solvers for the pressure Poisson equation.

Vivien Lecoustre is a Research Associate at the University of Maryland. He received a master of science in Aerospace Engineering from ENSMA (France) in 2005 and a doctorate in Mechanical Engineering from the University of Maryland in 2009. His research interests include radiation properties of fuels and numerical turbulent combustion.

Charles Luo is a Senior Research Scientist at Global Engineering and Materials, Inc., in Princeton, New Jersey. He received a B.S. in Theoretical and Applied Mechanics from the University of Science and Technology of China in 2002, and a doctorate in Mechanical Engineering from the State University of New York at Buffalo in 2010. His research interests include fire-structure interaction, immersed boundary methods, and fire response of composite and aluminum structures.

Anna Matala is a Research Scientist at VTT Technical Research Centre of Finland and a Ph.D. candidate at Aalto University School of Science. She received her M.Sc. degree in Systems and Operations Research from Helsinki University of Technology in 2008. Her research concentrates on pyrolysis modelling and parameter estimation in fire simulations

William (Ruddy) Mell is an applied mathematician currently at the U.S. Forest Service in Seattle, Washington. He holds a B.S. degree from the University of Minnesota (1981) and doctorate from the University of Washington (1994). His research interests include the development of large-eddy simulation methods and sub-models applicable to the physics of large fires in buildings, vegetation, and the wildland-urban interface.

Topi Sikanen is a Research Scientist at VTT Technical Research Centre of Finland and a graduate student at Aalto University School of Science. He received his M.Sc. degree in Systems and Operations Research from Helsinki University of Technology in 2008. He works on the Lagrangian particle and liquid evaporation models.

Ben Trettel is a graduate student at The University of Texas at Austin. He received a B.S. in Mechanical Engineering in 2011 and an M.S. in Fire Protection Engineering in 2013, both from the University of Maryland. He develops models for the transport of Lagrangian particles for the Fire Dynamics Simulator.

Preface

This document provides the theoretical basis for the Fire Dynamics Simulator (FDS), following the general framework set forth in the "Standard Guide for Evaluating the Predictive Capability of Deterministic Fire Models," ASTM E 1355 [1]. It is the first of a four volume set of companion documents, referred to collectively as the FDS Technical Reference Guide [2]. Volumes 2, 3 and 4 describe the model verification, experimental validation, and configuration management, respectively.

A separate document, *Fire Dynamics Simulator, User's Guide* [3] describes how the FDS software is actually used.

Disclaimer

The US Department of Commerce makes no warranty, expressed or implied, to users of the Fire Dynamics Simulator (FDS), and accepts no responsibility for its use. Users of FDS assume sole responsibility under Federal law for determining the appropriateness of its use in any particular application; for any conclusions drawn from the results of its use; and for any actions taken or not taken as a result of analysis performed using these tools.

Users are warned that FDS is intended for use only by those competent in the fields of fluid dynamics, thermodynamics, heat transfer, combustion, and fire science, and is intended only to supplement the informed judgment of the qualified user. The software package is a computer model that may or may not have predictive capability when applied to a specific set of factual circumstances. Lack of accurate predictions by the model could lead to erroneous conclusions with regard to fire safety. All results should be evaluated by an informed user.

Throughout this document, the mention of computer hardware or commercial software does not constitute endorsement by NIST, nor does it indicate that the products are necessarily those best suited for the intended purpose.

Acknowledgments

The development and maintenance of the Fire Dynamics Simulator has been made possible through a partnership of public and private organizations, both in the United States and abroad. Following is a list of contributors from the various sectors of the fire research, fire protection engineering and fire services communities:

FDS is supported financially via internal funding at both NIST and VTT, Finland. In addition, support has been provided by the following:

- The US Nuclear Regulatory Commission Office of Research has funded key validation experiments, the preparation of the FDS manuals, and the development of various sub-models that are of importance in the area of nuclear power plant safety. Special thanks to Mark Salley, Jason Dreisbach, and David Stroup for their efforts and support.

- The US Forest Service has supported the development of sub-models in FDS designed to simulate the spread of fire in the Wildland Urban Interface (WUI). Special thanks to Mark Finney and Tony Bova for their support.

- The Minerals Management Service of the US Department of the Interior funded research at NIST aimed at characterizing the burning behavior of oil spilled on the open sea or ice. Part of this research led to the development of the ALOFT (A Large Outdoor Fire plume Trajectory) model, a forerunner of FDS. Special thanks to Joe Mullin for his encouragement of the modeling efforts.

At VTT, the FDS development has been supported by

- The Finnish Funding Agency for Technology and Innovation (TEKES) has supported the development of fire and evacuation simulation capabilities.

- The Finnish State Nuclear Waste Management Fund (VYR) under the national research programmes on nuclear safety.

- The European Union through the FP6 and FP7 research projects FIRE PARADOX, TRANSFEU and FIRE-RESIST.

The following individuals and organizations played a role in the development of the underlying mathematical model of FDS.

- Originally, the basic hydrodynamic solver was designed by Ronald Rehm and Howard Baum with programming help from Darcy Barnett, Dan Lozier and Hai Tang of the Computing and Applied Mathematics Laboratory at NIST, and Dan Corley of the Building and Fire Research Laboratory (BFRL). Jim Sims of CAML developed the original visualization software.

- The direct Poisson solver (CRAYFISKPAK) was written by Roland Sweet of the National Center for Atmospheric Research (NCAR), Boulder, Colorado.

- Kuldeep Prasad added the multiple-mesh data structures, paving the way for parallel processing.
- Charles Bouldin devised the basic framework of the parallel version of the code.
- William Grosshandler (retired from NIST) and Tom Cleary (currently at NIST) developed an enhancement to the smoke detector activation algorithm, originally conceived by Gunnar Heskestad of Factory Mutual.
- Steve Olenick of Combustion Science and Engineering (CSE) implemented the smoke detector model into FDS.
- William Grosshandler is also the developer of RadCal, a library of subroutines that have been incorporated in FDS to provide the radiative properties of gases and smoke.
- Professor Fred Mowrer, formerly of the University of Maryland, provided a simple model of gas phase extinction to FDS.
- Ezgi S. Oztekin of the Fire Research Program at William J. Hughes Technical Center together with Kiyoung Moon and Jung-il Choi of Yonsei University in Seoul, South Korea, developed the log law model for convective heat transfer.
- The authors would like thank Sean Smith of the University of Utah for insightful discussions on the turbulent combustion model.

Contents

List of Figures

List of Tables

Chapter 1

Introduction

Howard Baum, NIST Fellow Emeritus

The idea that the dynamics of a fire might be studied numerically dates back to the beginning of the computer age. Indeed, the fundamental conservation equations governing fluid dynamics, heat transfer, and combustion were first written down over a century ago. Despite this, practical mathematical models of fire (as distinct from controlled combustion) are relatively recent due to the inherent complexity of the problem. Indeed, in his brief history of the early days of fire research, Hoyt Hottel noted "A case can be made for fire being, next to the life processes, the most complex of phenomena to understand" [4].

The difficulties revolve about three issues: First, there are an enormous number of possible fire scenarios to consider due to their accidental nature. Second, the physical insight and computing power required to perform all the necessary calculations for most fire scenarios are limited. Any fundamentally based study of fires must consider at least some aspects of bluff body aerodynamics, multi-phase flow, turbulent mixing and combustion, radiative transport, and conjugate heat transfer; all of which are active research areas in their own right. Finally, the "fuel" in most fires was never intended as such. Thus, the mathematical models and the data needed to characterize the degradation of the condensed phase materials that supply the fuel may not be available. Indeed, the mathematical modeling of the physical and chemical transformations of real materials as they burn is still in its infancy.

In order to make progress, the questions that are asked have to be greatly simplified. To begin with, instead of seeking a methodology that can be applied to all fire problems, we begin by looking at a few scenarios that seem to be most amenable to analysis. Hopefully, the methods developed to study these "simple" problems can be generalized over time so that more complex scenarios can be analyzed. Second, we must learn to live with idealized descriptions of fires and approximate solutions to our idealized equations. Finally, the methods should be capable of systematic improvement. As our physical insight and computing power grow more powerful, the methods of analysis can grow with them.

To date, three distinct approaches to the simulation of fires have emerged. Each of these treats the fire as an inherently three dimensional process evolving in time. The first to reach maturity, the "zone" models, describe compartment fires. Each compartment is divided into two spatially homogeneous volumes, a hot upper layer and a cooler lower layer. Mass and energy balances are enforced for each layer, with additional models describing other physical processes appended as differential or algebraic equations as appropriate. Examples of such phenomena include fire plumes, flows through doors, windows and other vents, radiative and convective heat transfer, and solid fuel pyrolysis. Descriptions of the physical and mathematical assumptions behind the zone modeling concept are given in separate papers by Jones [5] and Quintiere [6], who chronicle developments through 1983. Model development since then has progressed to the point where documented and supported software implementing these models are widely available [7].

The relative physical and computational simplicity of the zone models has led to their widespread use in

the analysis of fire scenarios. So long as detailed spatial distributions of physical properties are not required, and the two layer description reasonably approximates reality, these models are quite reliable. However, by their very nature, there is no way to systematically improve them. The rapid growth of computing power and the corresponding maturing of computational fluid dynamics (CFD), has led to the development of CFD based "field" models applied to fire research problems. Virtually all this work is based on the conceptual framework provided by the Reynolds-averaged form of the Navier-Stokes equations (RANS), in particular the $k-\varepsilon$ turbulence model pioneered by Patankar and Spalding [8]. The use of CFD models has allowed the description of fires in complex geometries, and the incorporation of a wide variety of physical phenomena. However, these models have a fundamental limitation for fire applications – the averaging procedure at the root of the model equations.

RANS models were developed as a time-averaged approximation to the conservation equations of fluid dynamics. While the precise nature of the averaging time is not specified, it is clearly long enough to require the introduction of large eddy transport coefficients to describe the unresolved fluxes of mass, momentum and energy. This is the root cause of the smoothed appearance of the results of even the most highly resolved fire simulations. The smallest resolvable length scales are determined by the product of the local velocity and the averaging time rather than the spatial resolution of the underlying computational grid. This property of RANS models is typically exploited in numerical computations by using implicit numerical techniques to take large time steps.

Unfortunately, the evolution of large eddy structures characteristic of most fire plumes is lost with such an approach, as is the prediction of local transient events. It is sometimes argued that the averaging process used to define the equations is an "ensemble average" over many replicates of the same experiment or postulated scenario. However, this is a moot point in fire research since neither experiments nor real scenarios are replicated in the sense required by that interpretation of the equations. The application of "Large Eddy Simulation" (LES) techniques to fire is aimed at extracting greater temporal and spatial fidelity from simulations of fire performed on the more finely meshed grids allowed by ever faster computers.

The phrase LES refers to the description of turbulent mixing of the gaseous fuel and combustion products with the local atmosphere surrounding the fire. This process, which determines the burning rate in most fires and controls the spread of smoke and hot gases, is extremely difficult to predict accurately. This is true not only in fire research but in almost all phenomena involving turbulent fluid motion. The basic idea behind the LES technique is that the eddies that account for most of the mixing are large enough to be calculated with reasonable accuracy from the equations of fluid dynamics. The hope (which must ultimately be justified by comparison to experiments) is that small-scale eddy motion can either be crudely accounted for or ignored.

The equations describing the transport of mass, momentum, and energy by the fire-induced flows must be simplified so that they can be efficiently solved for the fire scenarios of interest. The general equations of fluid dynamics describe a rich variety of physical processes, many of which have nothing to do with fires. Retaining this generality would lead to an enormously complex computational task that would shed very little additional insight on fire dynamics. The simplified equations, developed by Rehm and Baum [9], have been widely adopted by the larger combustion research community, where they are referred to as the "low Mach number" combustion equations. They describe the low speed motion of a gas driven by chemical heat release and buoyancy forces. Oran and Boris provide a useful discussion of the technique as applied to various reactive flow regimes in the chapter entitled "Coupled Continuity Equations for Fast and Slow Flows" in Ref. [10]. They comment that "There is generally a heavy price for being able to use a single algorithm for both fast and slow flows, a price that translates into many computer operations per time step often spent in solving multiple and complicated matrix operations."

The low Mach number equations are solved numerically by dividing the physical space where the fire is to be simulated into a large number of rectangular cells. Within each cell the gas velocity, temperature, etc., are assumed to be uniform; changing only with time. The accuracy with which the fire dynamics can

be simulated depends on the number of cells that can be incorporated into the simulation. This number is ultimately limited by the computing power available. Present day, single processor desktop computers limit the number of such cells to at most a few million. This means that the ratio of largest to smallest eddy length scales that can be resolved by the computation (the "dynamic range" of the simulation) is on the order of 100. Parallel processing can be used to extend this range to some extent, but the range of length scales that need to be accounted for if all relevant fire processes are to be simulated is roughly 10^4 to 10^5 because combustion processes take place at length scales of 1 mm or less, while the length scales associated with building fires are of the order of tens of meters. The form of the numerical equations discussed below depends on which end of the spectrum one wants to capture directly, and which end is to be ignored or approximated.

Chapter 2

Overview of the FDS Model

This chapter presents the governing equations of FDS and an outline of the general solution procedure. Details are included in subsequent chapters. The purpose of this chapter is to highlight aspects of the solution methodology that make it practical for thermally-driven flow simulations, in particular fire. Some of the major features of the model, in its default operation, are:

- Low Mach, large-eddy simulation (LES)
- Explicit, second-order, kinetic-energy-conserving numerics
- Structured, uniform, staggered grid
- Simple immersed boundary method for treatment of flow obstructions
- Generalized "lumped species" method (simplified chemistry using a reaction progress variable)
- Deardorff eddy viscosity subgrid closure
- Constant turbulent Schmidt and Prandtl numbers
- Eddy dissipation concept (fast chemistry) for single-step reaction between fuel and oxidizer
- Gray gas radiation with finite volume solution to the radiation transport equation

The model, however, is not limited to these simple algorithms. For example, the user may specify multiple reactions, finite-rate chemistry, a wide-band radiation model, and a variety of other special features. The more detailed physics incur increased computational cost and it is incumbent on the user to justify the added expense in terms of improved accuracy for a particular application. The default model options have been selected based on results from a wide variety of full-scale validation experiments [11].

The algorithm outlined below has evolved over roughly three decades. Initially, it was designed to study buoyant plumes in the Boussinesq limit; that is, the fluid was assumed incompressible but included a source term for buoyancy. This approach was based on a long tradition in fire research of modeling smoke movement using dyed salt water introduced into a tank filled with fresh water. Eventually, this approach proved too limiting, but some of the major features of the algorithm, like the low Mach number approximation, were retained.

2.1 LES Formalism

The equations for large-eddy simulation (LES) are derived by applying a low-pass filter, parameterized by a width Δ, to the transport equations for mass, momentum and energy. For our purposes, it is sufficient to think of the filtered fields in the LES equations as cell means. For example, in 1D the filtered density for a cell of width Δ is

$$\bar{\rho}(x,t) = \frac{1}{\Delta}\int_{x-\Delta/2}^{x+\Delta/2} \rho(r,t)\,\mathrm{d}r. \tag{2.1}$$

In FDS, the filter width Δ is equivalent to the local cell size δx and is a key parameter in the submodels for the turbulent viscosity and the reaction time scale discussed later. The practice of taking $\Delta = \delta x$ is called implicit filtering. It is important to appreciate, however, that implicit filtering does not imply dissipative numerics. FDS employs kinetic-energy-conserving central difference schemes for momentum with physically-based closures for the turbulent stress. In what follows, the filter formalism is relaxed (the overline notation is suppressed for clarity) since no explicit filtering operations are performed in the algorithm. A detailed derivation of the formal LES equations is presented in Chapter 4.

2.2 Numerical Grid

FDS is designed to be used by practicing engineers for a variety of fire protection and other thermal flow applications. Therefore, it must be relatively fast and robust, and it must be easy to describe the scenario. This means that the user should only have to specify a small number of numerical parameters, focusing instead on the physical description of the problem. Because the computational domain usually encompasses a volume within a building, or the entire building itself, the most obvious and simplest numerical grid is rectilinear. In fact, because FDS is a large eddy simulation (LES) model, uniform meshing is preferred, and the only numerical parameters chosen by the end user are the three dimensions of the grid. Once established, it is relatively simple to define rectangular obstructions that define the geometry to the level of resolution determined by the grid. These obstructions "snap" to the underlying grid, a very elementary form of an immersed boundary method (IBM).

The governing equations are approximated using second-order accurate finite differences on a collection of uniformly spaced three-dimensional grids. Multiple meshes can be processed in parallel using Message Passing Interface (MPI) libraries. Scalar quantities are assigned to the center of each grid cell; vector components are assigned at the appropriate cell faces. This is what is commonly referred to as a staggered grid [12]. Its main purpose is to avoid "checker-boarding" in pressure-velocity coupling by naturally representing the pressure cell velocity divergence, a very important thermodynamic quantity in the model.

2.3 Mass and Species Transport

The most basic description of the chemistry of fire is a reaction of a hydrocarbon fuel with oxygen that produces carbon dioxide and water vapor. Because fire is a relatively inefficient combustion process involving multiple fuel gases that contain more than just carbon and hydrogen atoms, the number of gas species to keep track of in the simulation is almost limitless. However, to make the simulations tractable, we limit the number of fuels to one, usually, and the number of reactions to just one or two. We also leave open the possibility that the reaction may not proceed for lack of sufficient oxygen in the incoming air stream, as when a fire in a closed compartment extinguishes itself. Even with this simplified approach to the chemistry, we still need to track at least six gas species (Fuel, O_2, CO_2, H_2O, CO, N_2) plus soot particulate. If we assume a single-step reaction, we do not need to solve explicitly seven transport equations. In fact, we only need to solve two – one for the fuel and one for the products. The air is everything that is neither fuel nor

products. Whereas the fuel is a single gas species, the air and products are what are often referred to as "lumped species". A lumped species represents a mixture of gas species that transport together (i.e., the lumped species has a single set of transport properties) and react together, and from the point of view of the numerical model, a lumped species can be treated as a single species. In fact, the mass transport equations make no distinction between a single or lumped species. For example, air is a lumped species that consists of nitrogen, oxygen, and trace amounts of water vapor and carbon dioxide. We use the symbols Z_A, Z_F, and Z_P to denote the mass fractions of air, fuel and products ($Z_A = 1 - Z_F - Z_P$). The lumped species mass fractions are linearly related to the primitive species mass fractions, Y_α; thus, conversion from one to the other is a simple matter of performing a matrix multiplication. For example, the complete combustion of methane:

$$\mathrm{CH_4} + 2\,(\mathrm{O_2} + 3.76\,\mathrm{N_2}) \rightarrow \mathrm{CO_2} + 2\,\mathrm{H_2O} + 7.52\,\mathrm{N_2} \tag{2.2}$$

is expressed as

$$\mathrm{Fuel} + 2\,\mathrm{Air} \rightarrow \mathrm{Products} \tag{2.3}$$

and the primitive species can be recovered from the lumped species via

$$\begin{bmatrix} 0.77 & 0.00 & 0.73 \\ 0.23 & 0.00 & 0.00 \\ 0.00 & 1.00 & 0.00 \\ 0.00 & 0.00 & 0.15 \\ 0.00 & 0.00 & 0.12 \end{bmatrix} \begin{bmatrix} Z_\mathrm{A} \\ Z_\mathrm{F} \\ Z_\mathrm{P} \end{bmatrix} = \begin{bmatrix} Y_{\mathrm{N_2}} \\ Y_{\mathrm{O_2}} \\ Y_{\mathrm{CH_4}} \\ Y_{\mathrm{CO_2}} \\ Y_{\mathrm{H_2O}} \end{bmatrix} \tag{2.4}$$

Notice that the columns of the matrix are the mass fractions of the primitive species within a given lumped species.

The lumped species approach does not change the basic mass transport equations. The equation for total mass is written:

$$\frac{\partial \rho}{\partial t} + \nabla \cdot (\rho \mathbf{u}) = \dot{m}_\mathrm{b}''' \tag{2.5}$$

Note that the source term on the right hand side represents the addition of mass from evaporating droplets or other subgrid-scale particles that represent sprinkler and fuel sprays, vegetation, and any other type of small, unresolvable object. These objects are assumed to occupy no volume; thus they are seen by the governing equations as point sources of mass, momentum, and energy. It is important to note, however, that the evaporated mass species must be one for which an explicit transport equation is solved. For example, water vapor is a product of combustion, but it is also formed by evaporating sprinkler droplets. In cases such as these, there needs to be an explicit transport equation for water vapor to distinguish between that which is formed by combustion and that which is evaporated from the droplets.

The transport equation for each of the lumped species minus one (usually air) has the same form as the transport equation for a single species:

$$\frac{\partial}{\partial t}(\rho Z_\alpha) + \nabla \cdot (\rho Z_\alpha \mathbf{u}) = \nabla \cdot (\rho D_\alpha \nabla Z_\alpha) + \dot{m}_\alpha''' + \dot{m}_{\mathrm{b},\alpha}''' \tag{2.6}$$

Here $\dot{m}_\mathrm{b}''' = \sum_\alpha \dot{m}_{\mathrm{b},\alpha}'''$ is the production rate of species by evaporating droplets or particles. Summing these equations over all species yields the original mass conservation equation because $\sum Z_\alpha = 1$ and $\sum \dot{m}_\alpha''' = 0$ and $\sum \dot{m}_{\mathrm{b},\alpha}''' = \dot{m}_\mathrm{b}'''$, by definition, and because it is assumed that $\sum \rho D_\alpha \nabla Z_\alpha = 0$. This last assertion is not true, in general. However, transport equations are solved for total mass and all but one of the species, implying that the diffusion coefficient of the implicit species is chosen so that the sum of all the diffusive fluxes is zero.

2.4 Low Mach Number Approximation

Rehm and Baum [9] observed that for low speed applications like fire, the spatially and temporally resolved pressure, p, can be decomposed into a "background" pressure, $\overline{p}(z,t)$, plus a perturbation, $\tilde{p}(x,y,z,t)$, with only the background pressure retained in the equation of state (ideal gas law):

$$\overline{p} = \rho T R \sum_{\alpha} \frac{Z_\alpha}{W_\alpha} \equiv \frac{\rho R T}{\overline{W}} \tag{2.7}$$

Note that z is the spatial coordinate in the direction of gravity; thus, the stratification of the atmosphere is included in the background pressure. The perturbation, $\tilde{p}$, drives the fluid motion. This approximation has a number of consequences. First, building compartments connected via a heating, ventilation, and air conditioning (HVAC) system can each maintain individual background pressures. The air flows between compartments can be described in terms of the differences in the background pressures, eliminating the need to solve detailed flow equations within the ventilation ducts.

The second consequence of the low Mach number approximation is that the internal energy, e, and enthalpy, h, may be related in terms of the thermodynamic (background) pressure: $h = e + \overline{p}/\rho$. The energy conservation equation may then be written in terms of the *sensible enthalpy*, h_s:

$$\frac{\partial}{\partial t}(\rho h_\mathrm{s}) + \nabla\cdot(\rho h_\mathrm{s}\mathbf{u}) = \frac{\mathrm{D}\overline{p}}{\mathrm{D}t} + \dot{q}''' - \dot{q}_\mathrm{b}''' - \nabla\cdot\dot{\mathbf{q}}'' \tag{2.8}$$

The term $\dot{q}'''$ is the heat release rate per unit volume from a chemical reaction. The term $\dot{q}_\mathrm{b}'''$ is the energy transferred to subgrid-scale droplets and particles. The term $\dot{\mathbf{q}}''$ represents the conductive, diffusive, and radiative heat fluxes:

$$\dot{\mathbf{q}}'' = -k\nabla T - \sum_{\alpha} h_{\mathrm{s},\alpha}\,\rho\, D_\alpha \nabla Z_\alpha + \dot{\mathbf{q}}_\mathrm{r}'' \tag{2.9}$$

where k is the thermal conductivity and D_α is the diffusivity of species α.

Eq. (2.8) is not solved explicitly. Instead, the velocity divergence is factored out as follows:

$$\nabla\cdot\mathbf{u} = \frac{1}{\rho h_\mathrm{s}}\left[\frac{\mathrm{D}}{\mathrm{D}t}(\overline{p} - \rho h_\mathrm{s}) + \dot{q}''' + \dot{q}_\mathrm{r}''' - \dot{q}_\mathrm{b}''' - \nabla\cdot\dot{\mathbf{q}}''\right] \tag{2.10}$$

The hydrodynamics solver guarantees that Eq. (2.10) is satisfied. It follows that Eq. (2.8) is also satisfied (energy is conserved).

Expanding the material derivatives on the right hand side of Eq. (2.10) produces a fairly complicated expression for the divergence that includes the source and diffusion terms from the mass, species and energy conservation equations. Its importance to the overall algorithm is that it can be computed using only the thermodynamic variables ρ, Z_α, and $\overline{p}$. As will be shown below, the way to advance the flow velocity in time is to first estimate the thermodynamic variables at the next time step, compute the divergence, and then solve an equation for the pressure that will guarantee that the divergence of the updated velocity is identical to that computed solely from the thermodynamic variables.

2.5 Momentum Transport

Noting the vector identity $(\mathbf{u}\cdot\nabla)\mathbf{u} = \nabla|\mathbf{u}|^2/2 - \mathbf{u}\times\omega$ and defining the stagnation energy per unit mass, $H \equiv |\mathbf{u}|^2/2 + \tilde{p}/\rho$, the momentum equation can be written (see Chapter 4 for a detailed derivation)

$$\frac{\partial\mathbf{u}}{\partial t} - \mathbf{u}\times\omega + \nabla H - \tilde{p}\nabla(1/\rho) = \frac{1}{\rho}\Big[(\rho-\rho_0)\mathbf{g} + \mathbf{f}_\mathrm{b} + \nabla\cdot\tau\Big] \tag{2.11}$$

The term, $\mathbf{f}_\mathrm{b}$, represents the drag force exerted by the subgrid-scale particles and droplets. The viscous stress, τ, is closed via gradient diffusion with the turbulent viscosity obtained from the Deardorff eddy viscosity model [13, 14]. It is convenient to write Eq. (2.11) in the form:

$$\frac{\partial \mathbf{u}}{\partial t} + \mathbf{F} + \nabla H = 0 \tag{2.12}$$

so that a Poisson equation for the pressure can be derived by taking its divergence:

$$\nabla^2 H = -\left[\frac{\partial}{\partial t}(\nabla\cdot\mathbf{u}) + \nabla\cdot\mathbf{F}\right] \tag{2.13}$$

Note the appearance of the time derivative of the divergence. This is an important feature of the time marching scheme. Note also that the right hand side of the Poisson equation retains a term that includes the perturbation pressure, $\tilde{p}\nabla(1/\rho)$. This term accounts for the baroclinic torque. It is included on the right hand side of the Poisson equation by using its value from the previous time step. This approximation allows us to solve a separable form of the Poisson equation, for which there are fast, direct solvers that are optimized for uniform grids [15].

2.6 Combustion and Radiation

FDS is described as a "fire model" because it incorporates source terms and boundary conditions that describe the turbulent combustion of gaseous fuel and oxygen, the transport of thermal radiation through hot, soot-laden gases, the thermal decomposition of real materials, the activation of sprinklers and smoke detectors, the transport of water and liquid fuel droplets, and a variety of other features that describe fires inside and outside of buildings.

Combustion and radiation are introduced into the governing equations via the source terms, $\dot{q}'''$ and $\dot{q}'''_\mathrm{r}$, in the energy transport equation. Since the energy equation is not solved explicitly, these terms find their way into the expression for the divergence.

2.6.1 Combustion

For most applications, FDS uses a combustion model based on the mixing-limited, infinitely fast reaction of lumped species. Lumped species are reacting scalar quantities that represent a mixture of species. For example, air is a lumped species which is a mixture of nitrogen, oxygen, water vapor, and carbon dioxide. The reaction of fuel and oxygen is not necessarily instantaneous and complete, and there are several optional schemes that are designed to predict the extent of combustion in under-ventilated spaces.

For an infinitely-fast reaction, reactant species in a given grid cell are converted to product species at a rate determined by a characteristic mixing time, τ_mix. The heat release rate per unit volume is defined by summing the lumped species mass production rates times their respective heats of formation

$$\dot{q}''' = -\sum_\alpha \dot{m}'''_\alpha \Delta h_{\mathrm{f},\alpha} \tag{2.14}$$

Details of τ_mix and $\dot{m}'''_\alpha$ are discussed in Chapter 5.

2.6.2 Radiation

The net contribution from thermal radiation in the energy equation is defined by:

$$\dot{q}'''_r \equiv -\nabla\cdot\dot{\mathbf{q}}''_\mathrm{r}(\mathbf{x}) = \kappa(\mathbf{x})\left[U(\mathbf{x}) - 4\pi I_\mathrm{b}(\mathbf{x})\right] \quad ; \quad U(\mathbf{x}) = \int_{4\pi} I(\mathbf{x},\mathbf{s}')\,d\mathbf{s}' \tag{2.15}$$

where $\kappa(\mathbf{x})$ is the absorption coefficient, $I_b(\mathbf{x})$ is the source term, and $I(\mathbf{x},\mathbf{s})$ is the solution of the radiation transport equation (RTE) for a non-scattering gray gas:

$$\mathbf{s}\cdot\nabla I(\mathbf{x},\mathbf{s}) = \kappa(\mathbf{x})\ [I_\mathrm{b}(\mathbf{x}) - I(\mathbf{x},\mathbf{s})] \tag{2.16}$$

In practical simulations, the spectral dependence of I, I_b, and κ cannot be resolved accurately, nor do we have reliable data for non-ideal fuels typical of real fires. While FDS does have an option to divide the radiation spectrum into a relatively small number of bands and solve a separate RTE for each band, it is usually not necessary because in real fires, soot is the dominant source and sink of thermal radiation and is not particulary sensitive to wavelength. The mean absorption coefficient, κ, is a function of species composition and temperature. Its values are obtained from a narrow-band model called RadCal [16].

The source term, I_b, requires special treatment because of the limited resolution of the underlying numerical grid in the vicinity of flames. In large scale fire simulations, grid cells are typically on the order of tens of centimeters. Flame sheets cannot be resolved, meaning that the computed cell-average temperature can be significantly lower than temperatures one would expect to find in the reacting flame. Consequently, the source term is approximated in grid cells where fuel and oxygen react. Elsewhere, the subgrid temperature field is homogeneous and the source term can be computed directly:

$$\kappa I_\mathrm{b} = \begin{cases} \kappa\sigma T^4/\pi & \text{Outside flame zone,} \quad \dot{q}''' = 0 \\ C\,\kappa\sigma T^4/\pi & \text{Inside flame zone,} \quad \dot{q}''' > 0 \end{cases} \tag{2.17}$$

The constant C is computed at each time step so that the volume integral of Eq. (2.15) over the entire flaming region is approximately equal to the volume integral of $\chi_\mathrm{r}\dot{q}'''$ over that same region. Here, χ_r is an empirical estimate of the *global* fraction of that energy emitted as thermal radiation. Typically, a sooty fire radiates approximately one-third of the total combustion energy.

The radiation equation is solved using a technique similar to a finite volume method for convective transport, thus the name given to it is the Finite Volume Method (FVM). Using approximately 100 discrete angles which are updated over multiple time steps, the finite volume solver requires about 20% of the total CPU time of a calculation, a modest cost given the complexity of radiation heat transfer.

Water droplets can absorb and scatter thermal radiation. This is important in scenarios involving water mist suppression systems, but also plays a role in all sprinkler cases. The absorption and scattering coefficients are based on Mie theory. The scattering from the gaseous species and soot is considered negligible and is not included in the model.

2.7 Solution Procedure

In a given grid cell at the nth time step, we have the density, ρ^n, lumped species mass fractions, Z_α^n, velocity vector, $\mathbf{u}^n$, and the fluctuating stagnation energy per unit mass[1], H^n. In addition, for each compartment in the computational domain, we have a background pressure, $\overline{p}^n$. The temperature is found from the equation of state. These variables are advanced in time using an explicit second-order predictor/corrector scheme. The basic procedure is as follows:

Predictor

1. Estimate ρ, Z_α, and $\overline{p}$ at the next time step with an explicit Euler step. For example, the density is estimated by

$$\frac{\rho^* - \rho^n}{\delta t} + \nabla\cdot\rho^n\mathbf{u}^n = 0 \tag{2.18}$$

[1] Throughout this document H may also be referred to simply as the perturbation pressure.

The asterisk denotes a first order accurate estimate at the next time step. Note that the source term is time-split, as discussed below.

2. Compute the temperature, T^*, from the equation of state.

3. Compute the divergence, $(\nabla\cdot\mathbf{u})^*$, from Eq. (2.10) using the estimated thermodynamic quantities. Note that we use the parentheses to emphasize that an estimate of the velocity field, $\mathbf{u}^*$, at the next time step has not been computed yet, only its divergence.

4. Solve the Poisson equation for the pressure term:

$$\nabla^2 H^n = -\frac{(\nabla\cdot\mathbf{u})^* - \nabla\cdot\mathbf{u}^n}{\delta t} - \nabla\cdot\mathbf{F}^n \tag{2.19}$$

5. Estimate the velocity at the next time step.

$$\frac{\mathbf{u}^* - \mathbf{u}^n}{\delta t} + \mathbf{F}^n + \nabla H^n = 0 \tag{2.20}$$

Note that this procedure guarantees that the divergence of the estimated velocity field, $\nabla\cdot\mathbf{u}^*$, is identically equal to the divergence that is derived from the estimated thermodynamic quantities, $(\nabla\cdot\mathbf{u})^*$, in Step 3.

6. Check that the time step, δt, satisfies the CFL stability condition[2]:

$$\delta t \ \max\left(\frac{|u|}{\delta x}, \frac{|v|}{\delta y}, \frac{|w|}{\delta z}\right) < 1 \tag{2.21}$$

If the time step is too large, it is reduced so that it satisfies the CFL and the procedure returns to the beginning of the time step. If the stability criterion is satisfied, the procedure continues to the corrector step.

Corrector

1. Correct the density at the next time step.

$$\frac{\rho^{**} - \frac{1}{2}(\rho^n + \rho^*)}{\delta t/2} + \nabla\cdot\rho^*\mathbf{u}^* = 0 \tag{2.22}$$

The lumped species mass fractions and background pressure are corrected in a similar way.

2. Compute the temperature, T^{**}, from the equation of state.

3. *Time splitting for mass source terms*. After the corrector step for the transport scheme, source terms are applied to the scalars (for both chemical reactions and Lagrangian particles). The source terms are evaluated using the results from the corrected scalar transport scheme. For example,

$$\frac{(\rho Y_\alpha)_{ijk}^{n+1} - (\rho Y_\alpha)_{ijk}^{**}}{\delta t} = \dot{m}'''_{\alpha,ijk}(\mathbf{Y}^{**}, T^{**}) \tag{2.23}$$

4. With the updated density and composition, compute the final temperature, T^{n+1}, from the equation of state.

[2] In DNS mode, the Von Neumann condition is also checked.

5. Compute the divergence, $(\nabla \cdot \mathbf{u})^{n+1}$, from the corrected thermodynamic quantities.

6. Compute the pressure using the estimated quantities.

$$\nabla^2 H^* = -\left[\frac{(\nabla \cdot \mathbf{u})^{n+1} - \frac{1}{2}(\nabla \cdot \mathbf{u}^* + \nabla \cdot \mathbf{u}^n)}{\delta t/2}\right] - \nabla \cdot \mathbf{F}^* \tag{2.24}$$

7. Correct the velocity at the next time step.

$$\frac{\mathbf{u}^{n+1} - \frac{1}{2}(\mathbf{u}^* + \mathbf{u}^n)}{\delta t/2} + \mathbf{F}^* + \nabla H^* = 0 \tag{2.25}$$

   Note again that the divergence of the corrected velocity field is identically equal to the divergence that was computed in Step 5.

Chapter 3

Mass, Species, and Enthalpy Transport

This chapter describes in detail the equation of state in the low Mach number limit, the finite difference approximation of the mass and species conservation equations, and the role of the flow divergence as a surrogate for the enthalpy transport equation. Due to the use of the low Mach number approximation, the energy conservation equation is not solved explicitly but rather is defined implicitly via the divergence of the flow field, which contains the combustion and radiation source terms.

3.1 The Equation of State

A distinguishing feature of a CFD model is the regime of flow speeds (relative to the speed of sound) for which it is designed. High speed flow codes involve compressibility effects and shock waves. Low speed solvers, however, explicitly eliminate compressibility effects that give rise to acoustic (sound) waves. The Navier-Stokes equations describe the propagation of information at speeds comparable to that of the fluid flow (for fire, approximately 10 m/s), but also at speeds comparable to that of sound waves (for still air, 300 m/s). Solving a discretized form of these equations would require extremely small time steps in order to account for information traveling at the speed of sound, making practical simulations difficult.

Following the work of Rehm and Baum [9], an approximation to the equation of state is made by decomposing the pressure into a "background" component and a perturbation. It is assumed that the background component of pressure can differ from compartment to compartment. If a volume within the computational domain is isolated from other volumes, except via leak paths or ventilation ducts, it is referred to as a "pressure zone" and assigned its own background pressure. The pressure field within the mth zone, for example, is a linear combination of its background component and the flow-induced perturbation:

$$p(\mathbf{x},t) = \overline{p}_m(z,t) + \tilde{p}(\mathbf{x},t) \tag{3.1}$$

Note that the background pressure is a function of z, the vertical spatial coordinate, and the time, t. For most compartment fire applications, $\overline{p}_m$ changes very little with height or time. However, for scenarios where a fire increases the pressure in a closed compartment, or where the HVAC system affects the pressure, or when the height of the domain is significant, $\overline{p}_m$ takes these effects into account [17]. The ambient pressure field is denoted $\overline{p}_0(z)$. Note that the subscript 0 denotes the exterior of the computational domain, not time 0. This is the assumed atmospheric pressure stratification that serves as both the initial and boundary condition for the governing equations.

The purpose of decomposing the pressure is that for low Mach number flows, it can be assumed that the temperature and density are inversely proportional, and thus the equation of state (in the mth pressure zone) can be approximated as

$$\overline{p}_m = \rho T R \sum_\alpha \frac{Z_\alpha}{W_\alpha} = \frac{\rho T R}{\overline{W}} \tag{3.2}$$

Recall from Section 2.3 that Z_α is the mass fraction of lumped species α. The pressure, p, in the state and energy equations is replaced by the background pressure $\overline{p}_m$ to filter out sound waves that travel at speeds that are much faster than typical flow speeds expected in fire applications. The low Mach number assumption serves two purposes. First, the filtering of acoustic waves means that the time step in the numerical algorithm is bound only by the flow speed as opposed to the speed of sound, and second, the modified state equation leads to a reduction in the number of dependent variables in the system of equations by one. The energy equation (2.8) is not explicitly solved; rather, its source terms are included in the expression for the flow divergence, to be discussed later in the chapter. When the velocity field satisfies the specified thermodynamic divergence, the conservative form of the sensible enthalpy equation is satisfied by construction.

The stratification of the atmosphere is derived from the relation

$$\frac{\mathrm{d}\overline{p}_0}{\mathrm{d}z} = -\rho_0(z)\,g \tag{3.3}$$

where ρ_0 is the background density and $g = 9.8\ \mathrm{m/s}$. Using Eq. (3.2), the background pressure can be written as a function of the background temperature, $T_0(z)$,

$$\overline{p}_0(z) = p_\infty \exp\left(-\int_{z_\infty}^{z} \frac{\overline{W}\,g}{R\,T_0(z')}\,\mathrm{d}z'\right) \tag{3.4}$$

where the subscript infinity generally refers to the ground. A linear temperature stratification of the atmosphere may be specified by the user such that $T_0(z) = T_\infty + \Gamma z$ where T_∞ is the temperature at the ground and Γ is the lapse rate (e.g., $\Gamma = -0.0098\ \mathrm{K/m}$ is the *adiabatic lapse rate*). In this case $\overline{p}_0$ and ρ_0 are derived from Eqs. (3.4) and (3.2), respectively. It can then be shown that for $\Gamma \neq 0$ the pressure stratification becomes

$$\overline{p}_0(z) = p_\infty \left(\frac{T_0(z)}{T_\infty}\right)^{\overline{W}g/R\Gamma} \tag{3.5}$$

3.2 Mass and Species Transport

The density and species transport equations are solved using the same basic predictor-corrector scheme. Advection terms are written in flux divergence (conservative) form. In the predictor step, the density in cell ijk at time level $n+1$ is estimated based on information at the nth level

$$\frac{\rho^*_{ijk} - \rho^n_{ijk}}{\delta t} + \nabla\cdot(\overline{\rho}^{\mathrm{FL}}\mathbf{u})^n_{ijk} = 0 \tag{3.6}$$

The quantity $\overline{\rho}^{\mathrm{FL}}$ indicates a *flux limiter* applied to the cell face value, as discussed below in Section 3.2.1. Following the prediction of the velocity and background pressure at time level $n+1$, the density is corrected via

$$\frac{\rho^{n+1}_{ijk} - \frac{1}{2}\left(\rho^n_{ijk} + \rho^*_{ijk}\right)}{\frac{1}{2}\delta t} + \nabla\cdot(\overline{\rho}^{\mathrm{FL}}\mathbf{u})^*_{ijk} = 0 \tag{3.7}$$

The species conservation equations are differenced the same way, with the addition of the diffusion term (including turbulent diffusion[1]):

$$\frac{(\rho Z_\alpha)^*_{ijk} - (\rho Z_\alpha)^n_{ijk}}{\delta t} + \nabla\cdot(\overline{\rho Z_\alpha}^{\mathrm{FL}}\mathbf{u})^n_{ijk} = \nabla\cdot(\rho D_\alpha \nabla Z_\alpha)^n_{ijk} \tag{3.8}$$

[1] In DNS mode, the molecular diffusivity is based on mixture-averaged binary Fickian diffusion. In LES mode, by default, the diffusivity is taken from the molecular and turbulent viscosities divided by the turbulent Schmidt number. That is, to save cost we approximate the molecular plus turbulent diffusivity by $(\mu + \mu_t)/\mathrm{Sc}_t$. Optionally, in LES mode, by setting `RESEARCH_MODE=.TRUE.` on `MISC`, the molecular and turbulent transport coefficients are treated separately, $\rho D_\alpha + \mu_t/\mathrm{Sc}_t$ (at added cost). The same applies for the thermal diffusivity.

at the predictor step, and

$$\frac{(\rho Z_\alpha)^{**}_{ijk} - \frac{1}{2}\left[(\rho Z_\alpha)^{n}_{ijk} + (\rho Z_\alpha)^{*}_{ijk}\right]}{\frac{1}{2}\delta t} + \nabla\cdot(\overline{\rho Z_\alpha}^{\mathrm{FL}}\mathbf{u})^{*}_{ijk} = \nabla\cdot(\rho D_\alpha \nabla Z_\alpha)^{*}_{ijk} \tag{3.9}$$

at the corrector step. The model for the turbulent viscosity μ_t is discussed in Section 4.2. The turbulent Schmidt number is constant with default value $\mathrm{Sc}_t = 0.5$.

Mass source terms due to chemistry, evaporation, or pyrolysis are time split and applied after the corrector step (see Section 3.2.2). If no source terms are present, then $(\rho Z_\alpha)^{n+1}_{ijk} = (\rho Z_\alpha)^{**}_{ijk}$.

3.2.1 Flux Limiters

A *flux limiter* is an interpolation scheme for defining mass fluxes at cell faces. Simple linear interpolation of the cell-centered scalar variables to the cell face would result in a central difference scheme. Such purely centered schemes are known to generate intolerable levels of dispersion error (spurious wiggles) leading to unphysical results such as negative densities or mass fractions outside the range of [0,1]. To address this issue, FDS relies on two schemes: a *flux limiter* (discussed below) that handles the bulk of the problem, and a *flux correction* (see Appendix H) that adds the minimum amount of numerical diffusion to maintain boundedness.

For uniform flow velocity, a fundamental property of the exact solution to the equations governing scalar transport is that the total variation of the scalar field (the sum of the absolute values of the scalar differences between neighboring cells) is either preserved or diminished (never increased). In other words, no new extrema are created. Numerical schemes which preserve this property are referred to as total variation diminishing (TVD) schemes. The practical importance of using a TVD scheme for fire modelling is that such a scheme is able to accurately track coherent vortex structure in turbulent flames and does not develop spurious reaction zones.

FDS employs two second-order TVD schemes as options for scalar transport: Superbee and CHARM. Superbee [18] is recommended for LES because it more accurately preserves the scalar variance for coarse grid solutions that are not expected to be smooth. Due to the gradient steepening applied in Superbee, however, the convergence degrades at small grid spacing for smooth solutions (the method will revert to a stair-step pattern instead of the exact solution). CHARM [19], though slightly more dissipative than Superbee, is convergent, and is therefore the better choice for DNS calculations where the flame front is well resolved.

To illustrate how flux limiters are applied to the scalar transport equations, below we discretize Eq. (3.6) in one dimension:

$$\frac{\rho_i^* - \rho_i^n}{\delta t} + \frac{\overline{\rho}^{\mathrm{FL}}_{i+\frac{1}{2}} u_{i+\frac{1}{2}} - \overline{\rho}^{\mathrm{FL}}_{i-\frac{1}{2}} u_{i-\frac{1}{2}}}{\delta x} = 0 \tag{3.10}$$

Note that the $\pm\frac{1}{2}$ suffixes indicates a face value for a particular cell i. A flux-limited scalar value (density in this case) premultiplies the staggered, face-centered velocity to form the scalar advective flux. Recall that these velocity values are primitive variables in the calculation—they are *not* interpolated. Consider face $i+\frac{1}{2}$ between cells i and $i+1$ and let ϕ denote a general scalar variable, like ρ or ρZ_α. The local (loc) and upstream (up) data variations are

$$\delta\phi_{\mathrm{loc}} = \phi_{i+1} - \phi_i \tag{3.11}$$

$$\delta\phi_{\mathrm{up}} = \begin{cases} \phi_i - \phi_{i-1} & \text{if} \quad u_i > 0 \\ \phi_{i+2} - \phi_{i+1} & \text{if} \quad u_i < 0 \end{cases} \tag{3.12}$$

The limiter function $B(r)$ depends on the upstream-to-local data ratio, $r = \delta\phi_{\mathrm{up}}/\delta\phi_{\mathrm{loc}}$. In FDS, options for the limiter function include [20]:

Flux Limiter	$B(r)$
Central Difference	1
Godunov	0
MINMOD	$\max(0,\min(1,r))$
Superbee [18] (LES default)	$\max(0,\min(2r,1),\min(r,2))$
CHARM [19] (DNS default)	$s(3s+1)/(s+1)^2;\ s=1/r$
MP5 [21]	see below

For the Central Difference, Godunov, MINMOD, and Superbee limiters, the scalar face value is found from

$$\overline{\phi}^{\,\mathrm{FL}}_{i+1/2} = \begin{cases} \phi_i & + \quad B(r)\,\frac{1}{2}\,\delta\phi_{\mathrm{loc}} \quad \text{if} \quad u_i > 0 \\ \phi_{i+1} & - \quad B(r)\,\frac{1}{2}\,\delta\phi_{\mathrm{loc}} \quad \text{if} \quad u_i < 0 \end{cases} \tag{3.13}$$

For CHARM, the face value is given by [22]

$$\overline{\phi}^{\,\mathrm{FL}}_{i+1/2} = \begin{cases} \phi_i & + \quad B(r)\,\frac{1}{2}\,\delta\phi_{\mathrm{up}} \quad \text{if} \quad u_i > 0 \\ \phi_{i+1} & - \quad B(r)\,\frac{1}{2}\,\delta\phi_{\mathrm{up}} \quad \text{if} \quad u_i < 0 \end{cases} \tag{3.14}$$

The MP5 scheme of Suresh and Huynh [21] is based on the keen observation that three points cannot distinguish between extrema and discontinuities. The functional form of the limiter is not as simple as the three-point schemes described above, so we refer the reader to the original paper or the FDS source code for details. But the basic idea behind the method is to use a five-point stencil, three upwind and two downwind, to reconstruct the cell face value, considering both accuracy and monotonicity-preserving constraints. An additional benefit of the MP5 scheme is that it was designed specifically with strong stability-preserving (SSP) Runge-Kutta time discretizations in mind. The predictor-corrector scheme used by FDS is similar to the second-order SSP scheme described in [23].

Notes on Implementation

In practice, we set $r = 0$ initially and only compute r if the denominator is not zero. Note that for $\delta\phi_{loc} = 0$, it does not matter which limiter is used: all the limiters yield the same scalar face value. For CHARM, we set both $r = 0$ and $B = 0$ initially and only compute B if $r > 0$ (this requires data variations to have the same sign). Otherwise, CHARM reduces to Godunov's scheme.

The Central Difference, Godunov, and MINMOD limiters are included for completeness, debugging, and educational purposes. These schemes have little utility for typical FDS applications.

3.2.2 Time Splitting for Mass Source Terms

Following the corrector step of the transport scheme, source terms are applied to the scalars. The source terms are typically related to particle evaporation or combustion, and these processes are computed at the end of the time step. In the case of combustion, the total mass of a grid cell is not changed; rather the species mass fractions change. For particle evaporation, mass is simply added to the cell, particle by particle, and the species mass fractions are adjusted accordingly:

$$(\rho Z_\alpha)^{n+1}_{ijk} = (\rho Z_\alpha)^{**}_{ijk} + \delta t \left(\dot{m}'''_\alpha + \dot{m}'''_{\mathrm{b},\alpha}\right)_{ijk} \tag{3.15}$$

The mean chemical source term, $\dot{m}'''_\alpha$, is discussed in Chapter 5. The bulk subgrid source term, $\dot{m}'''_{\mathrm{b},\alpha}$, is discussed in Chapters 7 and 8 on solid phase pyrolysis and Lagrangian particles, respectively.

3.2.3 Boundary Conditions for Temperature, Species Mass Fraction, and Density

The gas temperature, species mass fractions, and density are computed at the center of each grid cell. At an exterior boundary, or at the boundary of an interior obstruction, these values must be computed at the face of the cell that falls at the boundary interface. In general, the temperature at the boundary, T_w, is computed first, followed by species mass fractions, $Z_{\alpha,\mathrm{w}}$, followed by density, ρ_w. The density is typically determined from the equation of state:

$$\rho_\mathrm{w} = \frac{\overline{p}_m}{R T_\mathrm{w} \sum_\alpha (Z_{\alpha,\mathrm{w}}/W_\alpha)} \tag{3.16}$$

Here, $\overline{p}_m$ denotes the background pressure of the gas phase region.

When necessary, the boundary value is linearly extrapolated one half of a grid cell into the "ghost" cell for use by the gas phase solver. In the sections below, the value at the center of the gas phase cell adjacent to the boundary is denoted with the subscript "g" (for "gas phase", *not* "ghost"), and the value at the boundary by "w" (for "wall").

Solid Boundaries

At a solid boundary, the surface temperature, T_w, is either specified or computed as described in Chapter 7. For an LES calculation, the convective heat flux at the surface is determined via an empirical heat transfer coefficient, h, and the convective heat flux at the boundary is written:

$$k\frac{T_\mathrm{g} - T_\mathrm{w}}{\delta n/2} = h\,(T_\mathrm{g} - T_\mathrm{w}) \tag{3.17}$$

where $\delta n/2$ is the distance between the surface and the center of the adjacent gas phase cell. The convective heat transfer coefficient, h, is described in Section 7.1.2. For a DNS calculation, the convective heat transfer is determined directly from the computed or specified surface temperature.

There is no transfer of mass at a solid boundary; thus, the boundary value for the species mixture α is simply

$$Z_{\alpha,\mathrm{w}} = Z_{\alpha,\mathrm{g}} \tag{3.18}$$

Open Boundaries

The term "open" denotes a non-solid exterior boundary of the computational domain. Gases are allowed to flow freely in and out. At these boundaries, the temperature and species mass fractions take on their respective exterior values if the flow is incoming, and take on their respective values in the grid cell adjacent to the boundary if the flow is outgoing. This is a simple upwind boundary condition.

Specified Mass Flux

Here, the mass flux of species α, $\dot{m}''_\alpha$, is specified or computed as part of the overall solid phase calculation. To determine the mass fraction of species mixture α at the boundary, $Z_{\alpha,f}$, the following equations must be solved iteratively

$$\sum_\alpha \dot{m}''_\alpha = \rho_\mathrm{w} u_n \tag{3.19}$$

$$\dot{m}''_\alpha = u_n \rho_\mathrm{w} Z_{\alpha,\mathrm{w}} - (\rho D_\alpha)_\mathrm{w} \frac{Z_{\alpha,\mathrm{g}} - Z_{\alpha,\mathrm{w}}}{\delta n/2} \tag{3.20}$$

where u_n is the normal component of velocity at the wall pointing into the flow domain and $\delta n/2$ is the distance between the center of the gas cell and the wall. Together with the equation of state, Eqs. (3.19) and

(3.20) are solved iteratively for the unknowns $\rho_{\rm w}$, u_n, and $Z_{\alpha,{\rm w}}$. The surface temperature used in the EOS depends on the thermal boundary condition.

Mesh Interface Boundaries

In simulations involving more than one numerical mesh, information has to be passed between meshes, even when the meshes are being processed by separate computers. If two meshes abut each other, and the mesh cells are aligned and the same size, then one mesh simply uses the density and species mass fractions of the adjacent mesh as the "ghost" cell values. However, in cases where the mesh cells are not the same size, the exchange of information must be done more carefully. Consider a case where two meshes meet:

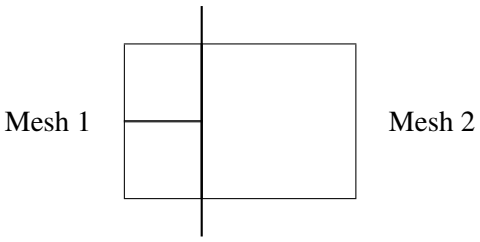

We want the total and species mass fluxes between meshes to be the same. Let the density in cell $(1,j',k')$ of Mesh 2 be denoted $\rho^{(2)}_{1,j'k'}$. Assume that this cell abuts two cells in Mesh 1. The densities in the two abutting cells of Mesh 1 are denoted $\rho^{(1)}_{I,jk}$. Note that j and k are not the same as j' and k'. I is the number of cells in the x direction of Mesh 1. The ghost cell quantities in Mesh 1 have an i index of $I+1$. The ghost cell quantities in Mesh 2 have an i index of 0. We want to assert mass conservation at the mesh interface:

$$\sum_{j,k} u^{(1)}_{I,jk}\,\rho^{(1)}_{{\rm w},jk}\,\delta y^{(1)}\,\delta z^{(1)} = u^{(2)}_{0,j'k'}\,\rho^{(2)}_{{\rm w},j'k'}\,\delta y^{(2)}\,\delta z^{(2)} \tag{3.21}$$

To enforce this condition, we obtain $\rho^{(1)}_{{\rm w},jk}$ on Mesh 1 and $\rho^{(2)}_{{\rm w},j'k'}$ on Mesh 2 from a flux limiter (see Section 3.2.1) once data has been exchanged between meshes. Since only one layer of ghost cells is exchanged, the second upwind data value is linearly extrapolated to maintain second-order accuracy of the interpolated face density.

3.3 The Velocity Divergence

Because of the low Mach number assumption, the velocity divergence (the rate of volumetric expansion) plays an important role in the overall solution scheme. In the FDS algorithm, the divergence is a surrogate for the energy equation. The divergence is factored out of the conservative form of the sensible enthalpy equation (see Appendix B) and when the divergence constraint is satisfied (enforced by the momentum update and solution of the Poisson equation for pressure) the conservative form of the sensible enthalpy equation is satisfied by construction.

For the mth zone, with background pressure $\overline{p}_m$, the divergence may be written as

$$\nabla\cdot\mathbf{u} = D - P\,\frac{\partial\overline{p}_m}{\partial t} \tag{3.22}$$

where

$$P = \frac{1}{\overline{p}_m} - \frac{1}{\rho c_p T} \tag{3.23}$$

and

$$D = \frac{1}{\rho c_p T}\left[\dot{q}''' + \dot{q}_{\mathrm{b}}''' + \dot{q}_{\mathrm{r}}''' - \nabla\cdot\dot{\mathbf{q}}'' - \mathbf{u}\cdot\nabla(\rho h_{\mathrm{s}}) + w\rho_0 g_z\right] + \frac{1}{\rho}\sum_{\alpha}\left(\frac{\overline{W}}{W_\alpha} - \frac{h_{\mathrm{s},\alpha}}{c_p T}\right)\left[\nabla\cdot(\rho D_\alpha \nabla Y_\alpha) - \mathbf{u}\cdot\nabla(\rho Y_\alpha) + \dot{m}_\alpha''' + \dot{m}_{\mathrm{b},\alpha}'''\right] \tag{3.24}$$

3.3.1 Mass and Energy Source Terms

The volumetric source terms in the divergence expression require extended discussion. The heat release rate per unit volume, $\dot{q}'''$, and the mass generation rate of species α per unit volume, $\dot{m}_\alpha'''$, are detailed in Chapter 5, Combustion. The radiative source, $\dot{q}_{\mathrm{r}}'''$, is discussed in Chapter 6, Thermal Radiation. The bulk heat source from Lagrangian particles, $\dot{q}_{\mathrm{b}}'''$, which accounts for convective heat transfer and radiative absorption, is discussed in Chapter 8, Lagrangian Particles. The bulk mass source from Lagrangian particles, $\dot{m}_{\mathrm{b},\alpha}'''$, is also found in Chapter 8.

3.3.2 Diffusion Terms

The thermal and material diffusion terms of Eq. (3.24) are pure second-order central differences. For example, the thermal conduction term is differenced as follows:

$$\begin{aligned}(\nabla\cdot k\nabla T)_{ijk} \quad = \quad & \frac{1}{\delta x}\left[\; k_{i+\frac{1}{2},jk}\;\frac{T_{i+1,jk}-T_{ijk}}{\delta x} \;-\; k_{i-\frac{1}{2},jk}\;\frac{T_{ijk}-T_{i-1,jk}}{\delta x}\;\right] \;+ \\ & \frac{1}{\delta y}\left[\; k_{i,j+\frac{1}{2},k}\;\frac{T_{i,j+1,k}-T_{ijk}}{\delta y} \;-\; k_{i,j-\frac{1}{2},k}\;\frac{T_{ijk}-T_{i,j-1,k}}{\delta y}\;\right] \;+ \\ & \frac{1}{\delta z}\left[\; k_{ij,k+\frac{1}{2}}\;\frac{T_{ij,k+1}-T_{ijk}}{\delta z} \;-\; k_{ij,k-\frac{1}{2}}\;\frac{T_{ijk}-T_{ij,k-1}}{\delta z}\;\right]\end{aligned} \tag{3.25}$$

The thermal conductivity at the cell interface, denoted by the $\frac{1}{2}$ cell index, is the average of its values in the two adjacent cells.

3.3.3 Corrections for Numerical Mixing

The differencing of the convection terms, $\mathbf{u}\cdot\nabla(\rho h_s)$ and $\mathbf{u}\cdot\nabla(\rho Y_\alpha)$, is complex. If not handled carefully, subtle issues related to numerical diffusion in the scalar transport schemes can cause significant conservation errors in the implied energy equation. The proper discretization of these terms is discussed in Appendix B.

3.3.4 Computing the Temperature

The mean cell gas temperature, T, is derived from the density and species mass fractions via the equation of state:

$$T_{ijk} = \frac{\overline{p}_m}{\rho_{ijk} R \sum_{\alpha=0}^{N_s}(Z_{\alpha,ijk}/W_\alpha)} \tag{3.26}$$

3.3.5 Sensible Enthalpy

The sensible enthalpy of the gas is a mass-weighted average of the enthalpies of the lumped species (denoted by α), which are in turn a mass-weighted average of the enthalpies of the individual gas species (denoted by n):

$$h_{\mathrm{s}} = \sum_{\alpha} Z_{\alpha}\, h_{\mathrm{s},\alpha} \quad ; \quad h_{\mathrm{s},\alpha} = \sum_{n} Y_n\, h_{\mathrm{s},n} \quad ; \quad h_{\mathrm{s},n}(T) = \int_{T_0}^{T} c_{p,n}(T')\,\mathrm{d}T' \tag{3.27}$$

The values of $h_{\mathrm{s},n}$ and $c_{p,n}$ for the individual gas species are obtained by table lookup from the NIST-JANAF tables [24]. The values are taken to the nearest degree Kelvin.

3.3.6 Computing the Background Pressure Rise

To describe how the background pressure of the mth pressure zone, $\overline{p}_m$, is updated in time, consider the expression for the divergence written in compact notation:

$$\nabla\cdot\mathbf{u} = D - P\,\frac{\partial \overline{p}_m}{\partial t} \tag{3.28}$$

The terms D and P are defined by Eqs. (3.24) and (3.23), respectively. The subscript m refers to the number of the *pressure zone*; that is, a volume within the computational domain that is allowed to have its own background pressure rise. A closed room within a building, for example, is a pressure zone. The time derivative of the background pressure of the mth pressure zone is found by integrating Eq. (3.28) over the zone volume (denoted by Ω_m):

$$\frac{\partial \overline{p}_m}{\partial t} = \left(\int_{\Omega_m} D\,\mathrm{d}V - \int_{\partial\Omega_m} \mathbf{u}\cdot\mathrm{d}\mathbf{S}\right) \Big/ \int_{\Omega_m} P\,\mathrm{d}V \tag{3.29}$$

Equation (3.29) is essentially a consistency condition, ensuring that blowing air or starting a fire within a sealed compartment leads to an appropriate decrease in the divergence within the volume.

3.3.7 Combining Pressure Zones

In the event that a barrier separating two pressure zones should rupture, Eq. (3.29) is modified so that the pressure in the newly connected zones is driven towards an equilibrium pressure:

$$\overline{p}_{\mathrm{eq}} = \sum_m \left(\overline{p}_m \int_{\Omega_m} P\,\mathrm{d}V\right) \Big/ \sum_m \int_{\Omega_m} P\,\mathrm{d}V \approx \frac{\sum_m V_m}{\sum_m (V_m/\overline{p}_m)} \tag{3.30}$$

Note that

$$\int_{\Omega_m} P\,\mathrm{d}V \approx \frac{V_m}{\gamma \overline{p}_m} \tag{3.31}$$

where V_m is the volume of zone m and γ is the ratio of specific heats. To drive the pressure within the connected zones towards each other, a volume flow, $\dot{V}_m^*$, is applied to each zone. This flow is intended to move gas from zones with the higher pressures towards zones with lower pressures. Eq. (3.29) now becomes:

$$\frac{\partial \overline{p}_{\mathrm{eq}}}{\partial t} - \frac{\overline{p}_m - \overline{p}_{\mathrm{eq}}}{\tau} = \left(\int_{\Omega_m} D\,\mathrm{d}V - \int_{\partial\Omega_m} \mathbf{u}\cdot\mathrm{d}\mathbf{S} - \dot{V}_m^*\right) \Big/ \int_{\Omega_m} P\,\mathrm{d}V \tag{3.32}$$

This equation is solved for $\dot{V}_m^*$. The first term on the left is the change in the equilibrium pressure with time:

$$\frac{\partial \overline{p}_{\mathrm{eq}}}{\partial t} = \left(\sum_m \int_{\Omega_m} D\,\mathrm{d}V - \sum_m \int_{\partial\Omega_m} \mathbf{u}\cdot\mathrm{d}\mathbf{S}\right) \Big/ \sum_m \int_{\Omega_m} P\,\mathrm{d}V \tag{3.33}$$

The summation is over all connected zones, and it is essentially the net change in pressure with time for the entire connected region. If there is any opening to the exterior of the computational domain, this term is set to zero and all connected zone pressures are driven towards ambient. The second term on the left forces the pressure in the mth pressure zone towards the equilibrium. The constant, τ, is a characteristic time for the pressure to come into equilibrium. Its default value is on the order of 1 s. In reality, room pressures typically come into equilibrium very rapidly, but air movements associated with rapid changes in pressure can cause numerical instabilities.

Note: Because of the low Mach number assumption, FDS should not be used for rapid discharge of pressure vessels.

Chapter 4

Momentum Transport and Pressure

This chapter describes the solution of the momentum equation. This consists of three major parts: the LES formulation, the discretization of the flux terms, and the solution of an elliptic partial differential equation for the pressure.

4.1 Large Eddy Simulation (LES)

In this section, we temporarily return to formal LES filter notation and adopt Cartesian tensor index notation (repeated suffixes imply summation) in order to precisely define modeled terms. The LES equations are derived by applying a low-pass filter of width Δ to the DNS equations. The kernel usually associated with finite volume LES is a box filter—grid resolved quantities are physically interpreted as cell means. This interpretation is somewhat misleading (see [25]), but a thorough discussion of filtering is beyond our scope, so the cell mean interpretation will suffice. In FDS, the filter width is taken to be the cube root of the cell volume, $\Delta = V_{\rm c}^{1/3}$, $V_{\rm c} = \delta x\,\delta y\,\delta z$. Then for any continuous field, ϕ, a filtered field is defined as

$$\overline{\phi}(x,y,z,t) \equiv \frac{1}{V_{\rm c}} \int_{x-\delta x/2}^{x+\delta x/2} \int_{y-\delta y/2}^{y+\delta y/2} \int_{z-\delta z/2}^{z+\delta z/2} \phi(x',y',z',t)\,{\rm d}x'\,{\rm d}y'\,{\rm d}z' \tag{4.1}$$

It is also conventional to define a mass-weighted or Favre filter such that $\overline{\rho}\,\widetilde{\phi} \equiv \overline{\rho\phi}$.

4.1.1 The DNS Momentum Equation

In conservative form, the DNS momentum equation for the ith component of velocity is

$$\frac{\partial \rho u_i}{\partial t} + \frac{\partial}{\partial x_j}(\rho u_i u_j) = -\frac{\partial p}{\partial x_i} - \frac{\partial \tau_{ij}}{\partial x_j} + \rho g_i + f_{{\rm d},i} + \dot{m}_{\rm b}''' u_{{\rm b},i} \tag{4.2}$$

In our two-phase formulation, $f_{d,i}$ represents the drag force due to unresolved Lagrangian particles. The bulk source term, $\dot{m}_b''' u_{b,i}$, accounts for the effects of evaporation or pyrolysis. For Eq. (4.2) to be applicable, the grid resolution should be smaller than the Kolmogorov scale, η, the length scale of the smallest turbulent eddies [14],

$$\eta \equiv (\nu^3/\varepsilon)^{1/4} \tag{4.3}$$

Here, ν is the kinematic viscosity and ε is the rate of viscous dissipation (the conversion of kinetic energy to heat by viscosity),

$$\varepsilon \equiv \tau_{ij}\frac{\partial u_i}{\partial x_j} = 2\mu\left(S_{ij}S_{ij} - \frac{1}{3}(\nabla\cdot\mathbf{u})^2\right) \quad ; \quad S_{ij} \equiv \frac{1}{2}\left(\frac{\partial u_i}{\partial x_j} + \frac{\partial u_j}{\partial x_i}\right) \tag{4.4}$$

In fire scenarios, η is usually on the order of one millimeter. DNS is therefore impractical for all but special research flame calculations.

4.1.2 The LES Momentum Equation

For length scales ranging in size from meters to kilometers, the affordable grid resolution for most LES fire calculations ranges from centimeters to meters. The goal of the LES is to evolve the cell mean values of mass, momentum, and energy explicitly, while accounting for the effects that subgrid transport and chemistry have on the mean fields. To this end, we apply the box filter to the DNS equations to obtain the filtered equations. As an example, consider the momentum equation. Applying Eq. (4.1) to Eq. (4.2) results in

$$\frac{\partial \overline{\rho u_i}}{\partial t} + \frac{\partial}{\partial x_j}(\overline{\rho u_i u_j}) = -\frac{\partial \overline{p}}{\partial x_i} - \frac{\partial \overline{\tau}_{ij}}{\partial x_j} + \overline{\rho} g_i + \bar{f}_{\mathrm{d},i} + \overline{\dot{m}'''_{\mathrm{b}} u_{\mathrm{b},i}} \tag{4.5}$$

The cell mean value, $\overline{\rho u_i u_j}$, is not itself a primitive variable in the calculation—we have no way of computing the term under the bar to advance Eq. (4.5) in time. We must, therefore, decompose the terms, and this leads to closure problems.

The next step is simply to apply the Favre filter,

$$\frac{\partial \overline{\rho}\widetilde{u}_i}{\partial t} + \frac{\partial}{\partial x_j}(\overline{\rho}\widetilde{u_i u_j}) = -\frac{\partial \overline{p}}{\partial x_i} - \frac{\partial \overline{\tau}_{ij}}{\partial x_j} + \overline{\rho} g_i + \bar{f}_{\mathrm{d},i} + \overline{\dot{m}'''_{\mathrm{b}}}\widetilde{u}_{\mathrm{b},i} \tag{4.6}$$

The first term is now separable, provided we have a solution for $\overline{\rho}$. But we still have no way to compute the correlation $\widetilde{u_i u_j}$ on the grid. We cannot simply use $\widetilde{u}_i\widetilde{u}_j$ as a substitute (this is the old problem of "the mean of the square does not equal the square of the mean"). Instead, we define the subgrid-scale (SGS) stress:

$$\tau_{ij}^{\mathrm{sgs}} \equiv \overline{\rho}(\widetilde{u_i u_j} - \widetilde{u}_i\widetilde{u}_j) \tag{4.7}$$

Substituting Eq. (4.7) into Eq. (4.6) yields

$$\frac{\partial \overline{\rho}\widetilde{u}_i}{\partial t} + \frac{\partial}{\partial x_j}(\overline{\rho}\widetilde{u}_i\widetilde{u}_j) = -\frac{\partial \overline{p}}{\partial x_i} - \frac{\partial \overline{\tau}_{ij}}{\partial x_j} - \frac{\partial \tau_{ij}^{\mathrm{sgs}}}{\partial x_j} + \overline{\rho} g_i + \bar{f}_{\mathrm{d},i} + \overline{\dot{m}'''_{\mathrm{b}}}\widetilde{u}_{\mathrm{b},i} \tag{4.8}$$

Equation (4.8) is what is typically referred to as the LES momentum equation (analogous to the Cauchy equation—constitutive models have not been applied). All variables are primitive or computable once we find a suitable closure for the subgrid scale stress, τ_{ij}^{sgs}.

Constitutive Relationship

There are a few more modifications we need to make in order to get Eq. (4.8) into shape for FDS. The first is to decompose the SGS stress and apply Newton's law of viscosity as the constitutive relationship for the deviatoric part. Note that $\overline{\tau}_{ij}$ is already the deviatoric part of the viscous stress. We model the total deviatoric stress as

$$\tau_{ij}^{\mathrm{dev}} \equiv \overline{\tau}_{ij} + \tau_{ij}^{\mathrm{sgs}} - \frac{1}{3}\tau_{kk}^{\mathrm{sgs}}\delta_{ij} = -2(\mu + \mu_{\mathrm{t}})\left(\widetilde{S}_{ij} - \frac{1}{3}(\nabla \cdot \widetilde{\mathbf{u}})\delta_{ij}\right) \tag{4.9}$$

Note that δ_{ij} is the Kronecker delta ($\delta_{ij} = 1$ if $i = j$, $\delta_{ij} = 0$ if $i \neq j$). The turbulent viscosity, μ_t, requires modeling, as discussed below.

Modified Pressure Term

In LES of low-Mach flows, the isotropic part of the SGS stress must be absorbed by the pressure term. Define the subgrid kinetic energy as half the trace of the SGS stress,

$$k_{\text{sgs}} \equiv \frac{1}{2}\tau_{kk}^{\text{sgs}} \tag{4.10}$$

and define the modified filtered pressure [14] as

$$\bar{p} \equiv \overline{p} + \frac{2}{3}k_{\text{sgs}} \tag{4.11}$$

Upon substitution of Eqs. (4.9) and (4.11) into Eq. (4.8), we have

$$\frac{\partial \overline{\rho}\widetilde{u}_i}{\partial t} + \frac{\partial}{\partial x_j}(\overline{\rho}\widetilde{u}_i\widetilde{u}_j) = -\frac{\partial \bar{p}}{\partial x_i} - \frac{\partial \tau_{ij}^{\text{dev}}}{\partial x_j} + \overline{\rho}g_i + \bar{f}_{\text{d},i} + \overline{\dot{m}_{\text{b}}'''}\widetilde{u}_{\text{b},i} \tag{4.12}$$

Notice that Eq. (4.12) closely resembles the DNS momentum equation, Eq. (4.2). For this reason, we may relax the filter formalism as we discuss the numerical details of the algorithm. The user should simply understand that in the LES context when we write τ_{ij} we mean precisely τ_{ij}^{dev}, and similarly for pressure in LES p refers to $\bar{p}$.

Bulk Mass Source Term

When writing the momentum equation in non-conservative form, which we will do below, we must account for the introduction of mass from subgrid particles (evaporation of water droplets, for example). Using the continuity equation, Eq. (2.5), we can rewrite Eq. (4.12) as follows:

$$\overline{\rho}\frac{\text{D}\widetilde{u}_i}{\text{D}t} = -\frac{\partial \bar{p}}{\partial x_i} - \frac{\partial \tau_{ij}^{\text{dev}}}{\partial x_j} + \overline{\rho}g_i + \underbrace{\bar{f}_{\text{d},i} + \overline{\dot{m}_{\text{b}}'''}(\widetilde{u}_{\text{b},i} - \widetilde{u}_i)}_{\bar{f}_{\text{b},i}} \tag{4.13}$$

The last term in Eq. (4.13) is absorbed into the bulk subgrid force term, $\bar{f}_{\text{b},i}$, which also accounts for drag, as discussed in Chapter 8 on Lagrangian Particles.

4.1.3 Production of Subgrid Kinetic Energy

The transport equation for the resolved kinetic energy per unit mass, $K \equiv \frac{1}{2}\widetilde{u}_i\widetilde{u}_i$, is derived by dotting the LES momentum equation with the resolved velocity vector. The result is

$$\begin{aligned}
\overline{\rho}\frac{\text{D}K}{\text{D}t} &= -\widetilde{u}_i\frac{\partial \bar{p}}{\partial x_i} - \widetilde{u}_i\frac{\partial \tau_{ij}^{\text{dev}}}{\partial x_j} + (\overline{\rho}g_i + \bar{f}_{b,i})\widetilde{u}_i \\
\overline{\rho}\frac{\text{D}K}{\text{D}t} + \frac{\partial}{\partial x_j}([\bar{p}\delta_{ij} + \tau_{ij}^{\text{dev}}]\widetilde{u}_i) &= \bar{p}\frac{\partial \widetilde{u}_i}{\partial x_i} + \tau_{ij}^{\text{dev}}\frac{\partial \widetilde{u}_i}{\partial x_j} + (\overline{\rho}g_i + \bar{f}_{\text{b},i})\widetilde{u}_i
\end{aligned} \tag{4.14}$$

The terms on the left hand side represent transport. The terms on the right hand side are sources or sinks of kinetic energy. Of particular interest in LES is the *production of subgrid kinetic energy*, buried in the second RHS term. The effect of this term is to transfer energy between the resolved and unresolved scales of motion. In the classical picture of the "energy cascade", the net transfer of energy is from large to small scales, where ultimately the motions are dissipated as heat by viscosity. In LES, however, this term may also be a source of energy, a phenomenon called *backscatter*. An issue that makes designing subgrid closures

for LES challenging is that, far from being the exception, backscatter is ubiquitous and often critical to the formation of large-scale motions (think of subgrid buoyancy-generated turbulence, e.g., the Rayleigh-Taylor instability) [26]. Most simple LES subgrid closures take production of subgrid kinetic energy to be equal to the dissipation of total kinetic energy. Using gradient diffusion for SGS closure, this assumption implies the following:

$$\begin{aligned}
\tau_{ij}^{\mathrm{dev}} \frac{\partial \widetilde{u}_i}{\partial x_j} &= -2(\mu+\mu_{\mathrm{t}}) \left(\widetilde{S}_{ij} - \frac{1}{3}(\nabla \cdot \widetilde{\mathbf{u}}) \delta_{ij} \right) \frac{\partial \widetilde{u}_i}{\partial x_j} \\
&= -2(\mu+\mu_{\mathrm{t}}) \left(\widetilde{S}_{ij} - \frac{1}{3}(\nabla \cdot \widetilde{\mathbf{u}}) \delta_{ij} \right) \widetilde{S}_{ij} \\
&= -2(\mu+\mu_{\mathrm{t}}) \left(\widetilde{S}_{ij}\widetilde{S}_{ij} - \frac{1}{3}(\nabla \cdot \widetilde{\mathbf{u}})^2 \right) = -2\mu \left(S_{ij}S_{ij} - \frac{1}{3}(\nabla \cdot \mathbf{u})^2 \right) \equiv \varepsilon
\end{aligned} \tag{4.15}$$

Using a model kinetic energy spectrum (see [14]), Eq. (4.15) can be used to derive theoretical values for model constants, such as the Smagorinsky constant, discussed below.

4.2 Models for the Turbulent Viscosity

In LES, the "turbulence model" refers to the closure for SGS flux terms. In FDS, *gradient diffusion* is the turbulence model used to close both the SGS momentum and scalar flux terms. We then require a model for the turbulent transport coefficient: the turbulent (or eddy) viscosity or the turbulent (or eddy) diffusivity. The turbulent diffusivity is obtained using a constant Schmidt number (for mass diffusivity) or Prandtl number (for thermal diffusivity), as discussed below, and so the most important transport coefficient is the turbulent viscosity, μ_t. There are several different options available that are described in this section. The Deardorff model, Section 4.2.3, is the default. Its selection as the default was based on comparisons with a wide variety of full-scale experiments.

4.2.1 Constant Coefficient Smagorinsky Model

Following the analysis of Smagorinsky [27], the eddy viscosity can be modeled as follows:

$$\mu_t = \rho\,(C_s\Delta)^2\,|S| \quad ; \quad |S| = \left(2S_{ij}S_{ij} - \frac{2}{3}(\nabla\cdot\mathbf{u})^2\right)^{\frac{1}{2}} \tag{4.16}$$

where $C_s = 0.2$ is a constant and $\Delta = (\delta x\,\delta y\,\delta z)^{1/3}$ is the filter width. This model was used in FDS versions 1 through 5.

4.2.2 Dynamic Smagorinsky Model

For the dynamic Smagorinsky model [28, 29], the coefficient C_s in Eq. (4.16) is no longer taken as a constant, but rather computed based on local flow conditions.

4.2.3 Deardorff's Model

By default, FDS uses a variation of Deardorff's model [30]:

$$\mu_t = \rho\,C_\nu\,\Delta\sqrt{k_{sgs}} \quad ; \quad k_{sgs} = \frac{1}{2}\left((\overline{u}-\hat{u})^2 + (\overline{v}-\hat{v})^2 + (\overline{w}-\hat{w})^2\right) \tag{4.17}$$

where $\overline{u}$ is the average value of u at the grid cell center and $\hat{u}$ is a weighted average of u over the adjacent cells:

$$\overline{u}_{ijk} = \frac{u_{ijk}+u_{i-1,jk}}{2} \quad ; \quad \hat{u}_{ijk} = \frac{\overline{u}_{ijk}}{2} + \frac{\overline{u}_{i-1,jk}+\overline{u}_{i+1,jk}}{4} \tag{4.18}$$

The terms $\hat{v}$ and $\hat{w}$ are defined similarly. The model constant is set to the literature value $C_\nu = 0.1$ [14].

4.2.4 Vreman's Model

Vreman's eddy viscosity model [31] is given by

$$\mu_t = \rho\,c\sqrt{\frac{B_\beta}{\alpha_{ij}\alpha_{ij}}} \tag{4.19}$$

where

$$B_\beta = \beta_{11}\beta_{22} - \beta_{12}^2 + \beta_{11}\beta_{33} - \beta_{13}^2 + \beta_{22}\beta_{33} - \beta_{23}^2 \quad ; \quad \beta_{ij} = \Delta_m^2\alpha_{mi}\alpha_{mj} \tag{4.20}$$

$$\alpha_{ij} = \frac{\partial u_j}{\partial x_i} \tag{4.21}$$

The basic idea behind Vreman's model is to expand the velocity field in a Taylor series and to test filter this field analytically, thus avoiding the expensive explicit test filtering operations necessary in the dynamic model. Therefore, this model is inexpensive. Unlike constant coefficient Smagorinsky, however, Vreman's model is convergent, making it applicable to highly resolved LES calculations.

The model constant may be related to the Smagorinsky constant, $c \approx 2.5 C_s^2$. Since Vreman's model is most applicable to high resolution cases, we base the coefficient off of $C_s = 0.17$, which yields accurate results for highly resolved decaying isotropic turbulence (see the FDS Verification Guide [32]). The default Vreman constant is therefore set to $c = 0.07$.

4.2.5 Thermal Conduction and Gas Species Diffusion

The other diffusive parameters, the thermal conductivity and mass diffusivity, are related to the turbulent viscosity by

$$k_t = \frac{\mu_t c_p}{\mathrm{Pr}_t} \quad ; \quad (\rho D)_t = \frac{\mu_t}{\mathrm{Sc}_t} \tag{4.22}$$

The turbulent Prandtl number Pr_t and the turbulent Schmidt number Sc_t are assumed to be constant for a given scenario. The default value is 0.5 for both.

4.2.6 Numerical Implementation

In the discretized form of the momentum equation, the modeled viscosity is defined at cell centers. For example, the constant coefficient Smagorinsky model takes on the following form:

$$\mu_{ijk} = \rho_{ijk} (C_s \Delta)^2 |S| \tag{4.23}$$

where C_s is an empirical constant, $\Delta = (\delta x \, \delta y \, \delta z)^{\frac{1}{3}}$, and

$$|S|^2 = 2\left(\frac{\partial u}{\partial x}\right)^2 + 2\left(\frac{\partial v}{\partial y}\right)^2 + 2\left(\frac{\partial w}{\partial z}\right)^2 + \left(\frac{\partial u}{\partial y} + \frac{\partial v}{\partial x}\right)^2 + \left(\frac{\partial u}{\partial z} + \frac{\partial w}{\partial x}\right)^2 + \left(\frac{\partial v}{\partial z} + \frac{\partial w}{\partial y}\right)^2 - \frac{2}{3}(\nabla \cdot \mathbf{u})^2 \tag{4.24}$$

The quantity $|S|$ consists of second order spatial differences averaged at cell centers. For example

$$\frac{\partial u}{\partial x} \approx \frac{u_{ijk} - u_{i-1,jk}}{\delta x_i} \tag{4.25}$$

$$\frac{\partial u}{\partial y} \approx \frac{1}{2}\left(\frac{u_{i,j+1,k} - u_{ijk}}{\delta y_{j+\frac{1}{2}}} + \frac{u_{ijk} - u_{i,j-1,k}}{\delta y_{j-\frac{1}{2}}}\right) \tag{4.26}$$

The divergence is described in Section 3.3.2.

The thermal conductivity and material diffusivity of the fluid are related to the viscosity by

$$k_{ijk} = \frac{c_{p,0} \mu_{ijk}}{\mathrm{Pr}_t} \quad ; \quad (\rho D)_{ijk} = \frac{\mu_{ijk}}{\mathrm{Sc}_t} \tag{4.27}$$

where Pr_t is the turbulent Prandtl number and Sc_t is the turbulent Schmidt number, both assumed constant. Note that the specific heat $c_{p,0}$ is that of the dominant species of the mixture. Based on simulations of smoke plumes, C_s is 0.20, Pr_t and Sc_t are 0.5. There are no rigorous justifications for these choices other than through comparison with experimental data [33].

4.2.7 Transport Coefficients for Direct Numerical Simulation (DNS)

There are some flow scenarios where it is possible to use the molecular properties μ, k and D directly. Usually, this means that the numerical grid cells are on the order of 1 mm or less, and the simulation is regarded as a Direct Numerical Simulation (DNS). For a DNS, the viscosity, thermal conductivity and material diffusivity are approximated from kinetic theory because the temperature dependence of each is important in combustion scenarios. The viscosity of the species α is given by

$$\mu_\alpha = \frac{26.69 \times 10^{-7} (W_\alpha T)^{\frac{1}{2}}}{\sigma_\alpha^2 \, \Omega_v} \quad [=] \quad \frac{\text{kg}}{\text{m s}} \tag{4.28}$$

where σ_α is the Lennard-Jones hard-sphere diameter (Å) and Ω_v is the collision integral, an empirical function of the temperature T. The thermal conductivity of species α is given by

$$k_\alpha = \frac{\mu_\alpha \, c_{p,\alpha}}{\text{Pr}} \quad [=] \quad \frac{\text{W}}{\text{m K}} \tag{4.29}$$

where the Prandtl number Pr is 0.7. The viscosity and thermal conductivity of a gas mixture are given by

$$\mu_{\text{DNS}} = \sum_\alpha Y_\alpha \, \mu_\alpha \quad ; \quad k_{\text{DNS}} = \sum_\alpha Y_\alpha \, k_\alpha \tag{4.30}$$

The binary diffusion coefficient of species α diffusing into species β is given by

$$D_{\alpha\beta} = \frac{2.66 \times 10^{-7} \, T^{3/2}}{W_{\alpha\beta}^{\frac{1}{2}} \, \sigma_{\alpha\beta}^2 \, \Omega_D} \quad [=] \quad \frac{\text{m}^2}{\text{s}} \tag{4.31}$$

where $W_{\alpha\beta} = 2(1/W_\alpha + 1/W_\beta)^{-1}$, $\sigma_{\alpha\beta} = (\sigma_\alpha + \sigma_\beta)/2$, and Ω_D is the diffusion collision integral, an empirical function of the temperature, T [34]. It is assumed that nitrogen is the dominant species in any combustion scenario considered here, thus the diffusion coefficient in the species mass conservation equations is that of the given species diffusing into nitrogen

$$(\rho D)_{\alpha,\text{DNS}} = \rho \, D_{\alpha,0} \tag{4.32}$$

where species 0 is nitrogen.

4.3 Simplifying the Momentum Equation

First, we start with the non-conservative form of the momentum equation introduced above (see Eq. 4.13)

$$\rho\left(\frac{\partial \mathbf{u}}{\partial t}+(\mathbf{u}\cdot\nabla)\mathbf{u}\right)+\nabla p=\rho\mathbf{g}+\mathbf{f}_b+\nabla\cdot\tau_{ij} \tag{4.33}$$

Next, we make the following substitutions:

1. Subtract the hydrostatic pressure gradient of the nth pressure zone, $\rho_n(z,t)\mathbf{g}$, from both sides. Note that $\nabla p=\rho_n\mathbf{g}+\nabla\tilde{p}$.
2. Apply the vector identity: $(\mathbf{u}\cdot\nabla)\mathbf{u}=\nabla|\mathbf{u}|^2/2-\mathbf{u}\times\omega$
3. Divide all terms by the density, ρ
4. Decompose the pressure term:
$$\frac{1}{\rho}\nabla\tilde{p}=\nabla\left(\frac{\tilde{p}}{\rho}\right)-\tilde{p}\nabla\left(\frac{1}{\rho}\right)$$
5. Define $H\equiv|\mathbf{u}|^2/2+\tilde{p}/\rho$

Now the momentum equation can be written

$$\frac{\partial \mathbf{u}}{\partial t}-\mathbf{u}\times\omega+\nabla H-\tilde{p}\nabla\left(\frac{1}{\rho}\right)=\frac{1}{\rho}\left[(\rho-\rho_n)\mathbf{g}+\mathbf{f}_\mathrm{b}+\nabla\cdot\tau_{ij}\right] \tag{4.34}$$

It is convenient to write this equation in the form:

$$\frac{\partial \mathbf{u}}{\partial t}+\mathbf{F}+\nabla H=0 \tag{4.35}$$

The vector $\mathbf{F}$ is referred to collectively as the momentum flux terms, and the term ∇H is referred to as the pressure gradient (though, as discussed above, H is not a true "pressure"). The spatial discretization of the momentum equations takes the form

$$\frac{\partial u}{\partial t}+F_{x,ijk}+\frac{H_{i+1,jk}-H_{ijk}}{\delta x}=0 \tag{4.36}$$

$$\frac{\partial v}{\partial t}+F_{y,ijk}+\frac{H_{i,j+1,k}-H_{ijk}}{\delta y}=0 \tag{4.37}$$

$$\frac{\partial w}{\partial t}+F_{z,ijk}+\frac{H_{ij,k+1}-H_{ijk}}{\delta z}=0 \tag{4.38}$$

where H_{ijk} is taken at center of cell ijk, u_{ijk} and $F_{x,ijk}$ are taken at the side of the cell facing in the forward x direction, v_{ijk} and $F_{y,ijk}$ at the side facing in the forward y direction, and w_{ijk} and $F_{z,ijk}$ at the side facing in the forward z (vertical) direction. The flux terms are discretized:

$$F_x=w\,\omega_y-v\,\omega_z-\frac{1}{\rho}\left(f_x+\frac{\partial\tau_{xx}}{\partial x}+\frac{\partial\tau_{xy}}{\partial y}+\frac{\partial\tau_{xz}}{\partial z}\right) \tag{4.39}$$

$$F_y=u\,\omega_z-w\,\omega_x-\frac{1}{\rho}\left(f_y+\frac{\partial\tau_{yx}}{\partial x}+\frac{\partial\tau_{yy}}{\partial y}+\frac{\partial\tau_{yz}}{\partial z}\right) \tag{4.40}$$

$$F_z=v\,\omega_x-u\,\omega_y-\frac{1}{\rho}\left(f_z+\frac{\partial\tau_{zx}}{\partial x}+\frac{\partial\tau_{zy}}{\partial y}+\frac{\partial\tau_{zz}}{\partial z}\right) \tag{4.41}$$

In the definitions to follow, the components of the vorticity $(\omega_x, \omega_y, \omega_z)$ are located at cell edges pointing in the x, y and z directions, respectively. The same is true for the off-diagonal terms of the viscous stress tensor: $\tau_{zy} = \tau_{yz}$, $\tau_{xz} = \tau_{zx}$, and $\tau_{xy} = \tau_{yx}$. The diagonal components of the stress tensor, τ_{xx}, τ_{yy}, and τ_{zz}, and the external force components, f_x, f_y, and f_z, are located at their respective cell faces.

$$F_{x,ijk} = \frac{1}{2}\left(w_{i+\frac{1}{2},jk}\,\omega_{y,ijk} + w_{i+\frac{1}{2},j,k-1}\,\omega_{y,ij,k-1}\right) - \frac{1}{2}\left(v_{i+\frac{1}{2},jk}\,\omega_{z,ijk} + v_{i+\frac{1}{2},j-1,k}\,\omega_{z,i,j-1,k}\right) - \frac{1}{\rho_{i+\frac{1}{2},jk}}\left(f_{x,ijk} + \frac{\tau_{xx,i+1,jk} - \tau_{xx,ijk}}{\delta x} + \frac{\tau_{xy,ijk} - \tau_{xy,i,j-1,k}}{\delta y} + \frac{\tau_{xz,ijk} - \tau_{xz,i,j,k-1}}{\delta z}\right) \tag{4.42}$$

$$F_{y,ijk} = \frac{1}{2}\left(u_{i,j+\frac{1}{2},k}\,\omega_{z,ijk} + u_{i-1,j+\frac{1}{2},k}\,\omega_{z,i-1,jk}\right) - \frac{1}{2}\left(w_{i,j+\frac{1}{2},k}\,\omega_{x,ijk} + w_{i,j+\frac{1}{2},k-1}\,\omega_{x,ij,k-1}\right) - \frac{1}{\rho_{i,j+\frac{1}{2},k}}\left(f_{y,ijk} + \frac{\tau_{yx,ijk} - \tau_{yx,i-1,jk}}{\delta x} + \frac{\tau_{yy,i,j+1,k} - \tau_{yy,ijk}}{\delta y} + \frac{\tau_{yz,ijk} - \tau_{yz,i,j,k-1}}{\delta z}\right) \tag{4.43}$$

$$F_{z,ijk} = \frac{1}{2}\left(v_{ij,k+\frac{1}{2}}\,\omega_{x,ijk} + v_{i,j-1,k+\frac{1}{2}}\,\omega_{x,i,j-1,k}\right) - \frac{1}{2}\left(u_{ij,k+\frac{1}{2}}\,\omega_{y,ijk} + u_{i-1,j,k+\frac{1}{2}}\,\omega_{y,i-1,jk}\right) - \frac{1}{\rho_{ij,k+\frac{1}{2}}}\left(f_{z,ijk} + \frac{\tau_{zx,ijk} - \tau_{zx,i-1,jk}}{\delta x} + \frac{\tau_{zy,ijk} - \tau_{zy,i,j-1,k}}{\delta y} + \frac{\tau_{zz,ij,k+1} - \tau_{zz,ijk}}{\delta z}\right) \tag{4.44}$$

The components of the vorticity vector are:

$$\omega_{x,ijk} = \frac{w_{i,j+1,k} - w_{ijk}}{\delta y} - \frac{v_{ij,k+1} - v_{ijk}}{\delta z} \tag{4.45}$$

$$\omega_{y,ijk} = \frac{u_{ij,k+1} - u_{ijk}}{\delta z} - \frac{w_{i+1,jk} - w_{ijk}}{\delta x} \tag{4.46}$$

$$\omega_{z,ijk} = \frac{v_{i+1,jk} - v_{ijk}}{\delta x} - \frac{u_{i,j+1,k} - u_{ijk}}{\delta y} \tag{4.47}$$

The components of the viscous stress tensor are:

$$\tau_{xx,ijk} = \mu_{ijk}\left(\frac{4}{3}(\nabla\cdot\mathbf{u})_{ijk} - 2\frac{v_{ijk} - v_{i,j-1,k}}{\delta y} - 2\frac{w_{ijk} - w_{ij,k-1}}{\delta z}\right) \tag{4.48}$$

$$\tau_{yy,ijk} = \mu_{ijk}\left(\frac{4}{3}(\nabla\cdot\mathbf{u})_{ijk} - 2\frac{u_{ijk} - u_{i-1,jk}}{\delta x} - 2\frac{w_{ijk} - w_{ij,k-1}}{\delta z}\right) \tag{4.49}$$

$$\tau_{zz,ijk} = \mu_{ijk}\left(\frac{4}{3}(\nabla\cdot\mathbf{u})_{ijk} - 2\frac{u_{ijk} - u_{i-1,jk}}{\delta x} - 2\frac{v_{ijk} - v_{i,j-1,k}}{\delta y}\right) \tag{4.50}$$

$$\tau_{xy,ijk} = \tau_{yx,ijk} = \mu_{i+\frac{1}{2},j+\frac{1}{2},k}\left(\frac{u_{i,j+1,k} - u_{ijk}}{\delta y} + \frac{v_{i+1,jk} - v_{ijk}}{\delta x}\right) \tag{4.51}$$

$$\tau_{xz,ijk} = \tau_{zx,ijk} = \mu_{i+\frac{1}{2},j,k+\frac{1}{2}}\left(\frac{u_{ij,k+1} - u_{ijk}}{\delta z} + \frac{w_{i+1,jk} - w_{ijk}}{\delta x}\right) \tag{4.52}$$

$$\tau_{yz,ijk} = \tau_{zy,ijk} = \mu_{i,j+\frac{1}{2},k+\frac{1}{2}}\left(\frac{v_{ij,k+1} - v_{ijk}}{\delta z} + \frac{w_{i,j+1,k} - w_{ijk}}{\delta y}\right) \tag{4.53}$$

By construction, the divergence defined in Eq. (3.22) is identically equal to the divergence defined by

$$(\nabla\cdot\mathbf{u})_{ijk} = \frac{u_{ijk} - u_{i-1,jk}}{\delta x} + \frac{v_{ijk} - v_{i,j-1,k}}{\delta y} + \frac{w_{ijk} - w_{ij,k-1}}{\delta z} \tag{4.54}$$

The equivalence of the two definitions of the divergence is a result of the form of the discretized equations, the time-stepping scheme, and the direct solution of the Poisson equation for the pressure.

4.4 Velocity Boundary Conditions

4.4.1 Smooth Walls

In finite-volume LES, when the momentum equation is integrated over a cell adjacent to the wall it turns out that the most difficult term to handle is the viscous stress, τ_w, because the wall-normal gradient of the streamwise velocity component cannot be resolved; the SGS stress at the wall is identically zero. We have, therefore, an entirely different situation than exists in the bulk flow at high Reynolds number where the viscous terms are negligible and the SGS stress is of critical importance. The fidelity of the SGS model still influences the wall stress, however, since other components of the SGS tensor affect the value of the near-wall velocity and hence the resulting viscous stress determined by the wall model. FDS models τ_w with a logarithmic velocity profile [14] described below.

An important scaling quantity in the near-wall region is the friction velocity, defined as $u_\tau \equiv \sqrt{\tau_w/\rho}$. From the friction velocity we can define the nondimensional streamwise velocity $u^+ \equiv u/u_\tau$ and nondimensional wall-normal distance $y^+ \equiv y/\delta_\nu$, where $\delta_\nu = \nu/u_\tau = \mu/(\rho u_\tau)$ is the *viscous length scale*. In FDS, the law of the wall is approximated by

$$u^+ = y^+ \qquad \text{for} \quad y^+ < 11.81 \tag{4.55}$$

$$u^+ = \frac{1}{\kappa}\ln y^+ + B \qquad \text{for} \quad y^+ \geq 11.81 \tag{4.56}$$

where $\kappa = 0.41$ is the von Kármán constant and $B = 5.2$. The region $5 < y^+ < 30$, where both viscous and inertial stresses are important, is referred to as the buffer layer. Following the work of Werner and Wengle [35], the solution in this region is approximated by matching the viscous region and log regions at $y^+ = 11.81$.

For the purposes of adapting the log law model to FDS we suppose that the first off-wall velocity component represents the profile sampled at a distance $\delta y/2$ in the wall-normal direction—streamwise components of velocity are stored at the face center on a staggered grid. The density and molecular viscosity are taken as the average of the neighboring cell values and uniform on the cell face where the streamwise velocity component is stored.

4.4.2 Rough Walls

For rough walls FDS employs the log law presented in Pope [14],

$$u^+ = \frac{1}{\kappa}\ln\left(\frac{y}{s}\right) + \tilde{B}(s^+) \tag{4.57}$$

where $s^+ = s/\delta_\nu$ is the roughness length in viscous units and s is the dimensional roughness. The distance to the wall, y, is taken as $\delta y/2$ for the first off-wall grid cell. The parameter $\tilde{B}$ varies with s^+ but attains a constant value $B_2 = 8.5$ in the fully rough limit. In FDS, we implement $\tilde{B}$ as the following piece-wise function:

$$\tilde{B} = \begin{cases} B + (1/\kappa)\ln(s^+) & \text{for} \quad s^+ < 5.83 \\ \tilde{B}_{\max} & \text{for} \quad 5.83 \leq s^+ < 30.0 \\ B_2 & \text{for} \quad s^+ \geq 30.0 \end{cases} \tag{4.58}$$

where $\tilde{B}_{\max} = 9.5$.

4.4.3 Wall Model Implementation

Once u^+ has been determined from the model profile, the stress may be obtained from (the definition of u^+)

$$\tau_w = \rho\left(\frac{u}{u^+}\right)^2 \tag{4.59}$$

Generally, this requires an iterative procedure since τ_w is needed to define δ_ν and hence y^+. The strategy employed in FDS is to first compute τ_w as if the flow is locally laminar (DNS), and if the calculation is an LES the laminar value is used as an initial guess. Testing has shown that three iterations is sufficient to converge the residual error in the profile model to 1%.

4.4.4 Wall Damping of the Turbulent Viscosity

The turbulent viscosity $\nu_\mathrm{t} = \mu_\mathrm{t}/\rho$ may be thought of as a "mixing length" squared divided by a time scale. For example, in the Smagorinsky model the mixing length is $\ell_\mathrm{mix} = C_\mathrm{s}\Delta$ and the time scale is the inverse of the strain rate invariant $1/|S|$. Thus, the turbulent kinematic viscosity has units of length^2/time.

To achieve the correct decay of the Reynolds stresses near a wall, Van Driest [36] proposed the following modification:

$$\ell_\mathrm{mix} = C_\mathrm{s}\Delta\left[1 - \mathrm{e}^{-y^+/A}\right] \tag{4.60}$$

where A is a dimensionless empirical constant equal to 26. The term in brackets is referred to as the *Van Driest damping function*. In FDS, due to difficulties defining a consistent test filter for use with either the Deardorff or the dynamic Smagorinsky turbulence model near the wall, at corners, and inside cavities, the turbulent viscosity of the first off-wall cell is obtained from the Smagorinsky model with Van Driest damping applied to the mixing length as shown in Eq. (4.60) with $y^+ = (\delta y/2)/\delta_\nu$ and $C_\mathrm{s} = 0.2$. See Section 4.4.1 for an explanation of terms. The viscosity near the wall is then given by

$$\nu_\mathrm{t} = \ell_\mathrm{mix}^2\,|S| \tag{4.61}$$

where the strain rate, $|S|$, is defined in Eq. (4.16).

4.5 Time Step and Stability Constraints

In explicit schemes, stability criteria may often be understood in terms of using the time step to maintain physically realizable conditions. Below we examine the necessary conditions for stability in the presence of advection, diffusion, and expansion of the velocity and scalar fields.

4.5.1 The Courant-Friedrichs-Lewy (CFL) Constraint

The well-known CFL constraint given by

$$\mathrm{CFL} = \delta t \frac{\|\mathbf{u}\|}{\delta x} \approx 1 \tag{4.62}$$

places a restriction on the time step due to the advection velocity. Physically, the constraint says that a fluid element should not traverse more than one cell within a time step. For LES, this constraint has the added advantage of keeping the implicit temporal and spatial filters consistent with each other. In other words, in order to resolve an eddy of size δx, the time step needs to be in concert with the CFL. If one were to employ an implicit scheme for the purpose of taking time steps say 10 times larger than the CFL limit, the smallest resolvable turbulent motions would then be roughly 10 times the grid spacing, which would severely limit the benefit of LES. In most cases, if one wishes the simulation to run faster, a better strategy is to coarsen the grid resolution while keeping the CFL ≈ 1.

The exact CFL needed to maintain stability depends on the order (as well as other properties) of the time integration scheme and the choice of velocity norm. Three choices for velocity norm are available in FDS (set on `MISC`):

`CFL_VELOCITY_NORM=0` (default, least restrictive, corresponds to L_∞ norm of velocity vector)

$$\frac{\|\mathbf{u}\|}{\delta x} = \max\left(\frac{|u|}{\delta x}, \frac{|v|}{\delta y}, \frac{|w|}{\delta z}\right) \tag{4.63}$$

`CFL_VELOCITY_NORM=1` (most restrictive, corresponds to L_1 norm of velocity vector)

$$\frac{\|\mathbf{u}\|}{\delta x} = \frac{|u|}{\delta x} + \frac{|v|}{\delta y} + \frac{|w|}{\delta z} \tag{4.64}$$

`CFL_VELOCITY_NORM=2` (L_2 norm of velocity vector)

$$\frac{\|\mathbf{u}\|}{\delta x} = \sqrt{(u/\delta x)^2 + (v/\delta y)^2 + (w/\delta z)^2} \tag{4.65}$$

4.5.2 The Von Neumann Constraint

The Von Neumann constraint is given by

$$\mathrm{VN} = \delta t \max\left[(\mu/\rho), D_\alpha\right] \sum_i \frac{1}{\delta x_i^2} < \frac{1}{2} \tag{4.66}$$

We can understand this constraint in a couple of different ways. First, we could consider the model for the diffusion velocity of species α in direction i, $V_{\alpha,i}Y_\alpha = -D_\alpha \partial Y_\alpha / \partial x_i$, and we would then see that VN is simply a CFL constraint due to diffusive transport.

We can also think of VN in terms of a total variation diminishing (TVD) constraint. That is, if we have variation (curvature) in the scalar field, we do not want to create spurious wiggles that can lead to an

instability by overshooting the smoothing step. Consider the following explicit update of the heat equation for u in 1D. Here subscripts indicate grid indices and ν is the diffusivity.

$$u_i^{n+1} = u_i^n + \frac{\delta t\, \nu}{\delta x^2}\left(u_{i-1}^n - 2u_i^n + u_{i+1}^n\right) \tag{4.67}$$

Very simply, notice that if $\delta t \nu/\delta x^2 = 1/2$ then $u_i^{n+1} = (u_{i-1}^n + u_{i+1}^n)/2$. If the time step is any larger we overshoot the straight line connecting neighboring cell values. Of course, this restriction is only guaranteed to be TVD if the u field is "smooth", else the neighboring cell values may be shifting in the opposite direction. Unfortunately, in LES there is no such guarantee and so the VN constraint can be particularly devilish in generating instabilities. For this reason, some practitioners like to employ implicit methods for the diffusive terms. Note that by default, VN is not checked in LES mode.

4.5.3 Realizable Mass Density Constraint

In an explicit Euler update of the continuity equation, if the time increment is too large the computational cell may be totally drained of mass, which of course is not physical. The constraint $\rho^{n+1} > 0$ therefore leads to the following restriction on the time step:

$$\delta t < \frac{\rho^n}{\overline{\mathbf{u}}^n \cdot \nabla \rho^n + \rho^n \nabla \cdot \mathbf{u}^n} \tag{4.68}$$

We can argue that the case we are most concerned with is when ρ^n is near zero. A reasonable approximation to (4.68) then becomes (time location suppressed, summation over i is implied)

$$\delta t < \frac{\rho}{\overline{u}_i\left(\frac{\rho - 0}{\delta x_i}\right) + \rho \nabla \cdot \mathbf{u}} = \left[\frac{\overline{u}_i}{\delta x_i} + \nabla \cdot \mathbf{u}\right]^{-1} \tag{4.69}$$

Equation (4.69) basically adds the effect of thermal expansion to the CFL constraint and provides a reason to prefer `CFL_VELOCITY_NORM=1` as the basis for the time step restriction.

4.5.4 Realizable Fluid Volume Constraint

Mass conservation tells us that the time rate of change of a fluid element with mass ρV does not change:

$$\frac{\mathrm{d}(\rho V)}{\mathrm{d}t} = 0\,. \tag{4.70}$$

Using continuity, Eq. (4.70) rearranges to

$$\nabla \cdot \mathbf{u} = \frac{1}{V}\frac{\mathrm{d}V}{\mathrm{d}t}\,, \tag{4.71}$$

where $V(t)$ is the time-dependent volume of the fluid element. If $\nabla \cdot \mathbf{u} < 0$, the fluid element is under compression. In fire dynamics this usually occurs due to cooling (heat loss by radiation, for example). Equation (4.71) highlights the physical interpretation of the velocity divergence as the rate of volumetric expansion of the fluid *per unit volume*.

Equation (4.71) also implies a time step constraint. Consider an explicit update of Eq. (4.71) for the fluid volume:

$$V^{n+1} = V^n + \Delta t\, V^n (\nabla \cdot \mathbf{u})^n\,. \tag{4.72}$$

If the fluid element is in compression (the divergence is negative), positivity of the fluid volume requires the time step to be limited by

$$\Delta t < -(\nabla \cdot \mathbf{u})^{-1}. \tag{4.73}$$

Note that this is the analog of the positive mass density constraint when the divergence is positive and provides the rationale for using the absolute value of the divergence $|\nabla \cdot \mathbf{u}|$ in the final version of the CFL constraint shown below.

4.5.5 Heat Transfer Constraint

Note that the heat transfer coefficient, h, has units of W/(m^2 K). Thus, a velocity scale may be formed from $h/(\rho\, c_p)$. Anytime we have a velocity scale to resolve, we have a CFL-type stability restriction. Therefore, the heat transfer stability check loops over all wall cells to ensure $\delta t \leq \delta x \rho\, c_p/h$. This check is an option. It is not done by default.

4.5.6 Adjusting the Time Step

In the default LES mode of operation, the CFL is increased or decreased to remain between 0.8 and 1. To be clear, the CFL constraint is now given by

$$\mathrm{CFL} = \delta t \left(\frac{\|\mathbf{u}\|}{\delta x} + |\nabla \cdot \mathbf{u}| \right) \tag{4.74}$$

In DNS mode, the time step is also adjusted to maintain VN between 0.4 and 0.5. If either the CFL or VN is too large then the new time step is set to 90% of the allowable value. If both CFL and VN are below their minimum values then the current time step is increased by 10%. See the User's Guide [3] for details.

4.6 The Equation for Pressure (Poisson Equation)

An elliptic partial differential equation (known as a Poisson equation) is obtained by taking the divergence of the momentum equation

$$\nabla^2 H = -\frac{\partial(\nabla\cdot\mathbf{u})}{\partial t} - \nabla\cdot\mathbf{F} \quad ; \quad \mathbf{F} = -\mathbf{u}\times\omega - \tilde{p}\nabla\left(\frac{1}{\rho}\right) - \frac{1}{\rho}\Big((\rho-\rho_0)\mathbf{g} + \mathbf{f}_\mathrm{b} + \nabla\cdot\tau_{ij}\Big) \tag{4.75}$$

Note that the perturbation pressure $\tilde{p}$ appears on both sides of Eq. (4.75). The pressure on the right hand side is taken from the previous time step of the overall explicit time-marching scheme. It can be neglected if the baroclinic torque is not important in a given simulation (constant density flows, for example). The pressure on the left hand side (incorporated in the variable H) is solved for directly. The reason for the decomposition of the pressure term is so that the linear algebraic system arising from the discretization of Eq. (4.75) has constant coefficients (i.e., it is *separable*) and can be solved to machine accuracy by a fast, direct (i.e., non-iterative) method that utilizes Fast Fourier Transforms (FFT).

The discretized form of the Poisson equation for the modified pressure, H, is:

$$\begin{aligned}\frac{H_{i+1,jk}-2H_{ijk}+H_{i-1,jk}}{\delta x^2} + \frac{H_{i,j+1,k}-2H_{ijk}+H_{i,j-1,k}}{\delta y^2} + \frac{H_{ij,k+1}-2H_{ijk}+H_{ij,k-1}}{\delta z^2} \\ = -\frac{F_{x,ijk}-F_{x,i-1,jk}}{\delta x} - \frac{F_{y,ijk}-F_{y,i,j-1,k}}{\delta y} - \frac{F_{z,ijk}-F_{z,ij,k-1}}{\delta z} - \frac{\delta}{\delta t}(\nabla\cdot\mathbf{u})_{ijk}\end{aligned} \tag{4.76}$$

The lack of a superscript implies that all quantities are to be evaluated at the same time level. This elliptic partial differential equation is solved using a direct FFT-based solver [15] that is part of a library of routines for solving elliptic PDEs called CRAYFISHPAK[1]. To ensure that the divergence of the fluid is consistent with the definition given in Eq. (3.22), the time derivative of the divergence is defined

$$\frac{\delta}{\delta t}(\nabla\cdot\mathbf{u})_{ijk} \equiv \frac{(\nabla\cdot\mathbf{u})^*_{ijk} - (\nabla\cdot\mathbf{u})^n_{ijk}}{\delta t} \tag{4.77}$$

at the predictor step, and then

$$\frac{\delta}{\delta t}(\nabla\cdot\mathbf{u})_{ijk} \equiv \frac{(\nabla\cdot\mathbf{u})^{n+1}_{ijk} - \frac{1}{2}\left[(\nabla\cdot\mathbf{u})^*_{ijk} + (\nabla\cdot\mathbf{u})^n_{ijk}\right]}{\delta t/2} \tag{4.78}$$

at the corrector step. The thermodynamic divergence is given in Eq. (3.22).

4.6.1 Open Boundary Conditions

An open boundary is where fluid is allowed to flow into or out of the computational domain depending on the local pressure gradient. The boundary condition for the pressure depends on whether the local flow is incoming or outgoing. In either case, it is assumed that the quantity, $H = \tilde{p}/\rho + q^2/2$, remains constant along a streamline. It is also assumed that the pressure perturbation at the boundary is a user-specified input, $\tilde{p}_\mathrm{ext}$, that is zero by default. The Poisson solver for the quantity, H, requires a Dirichlet condition at an open boundary; that is, its value is specified at the border of the computational domain. As an example, consider the boundary, $x = x_\mathrm{min}$. The boundary value of H is given by the following expressions depending on the

[1]CRAYFISHPAK, a vectorized form of the elliptic equation solver FISHPAK, was originally developed at the National Center for Atmospheric Research (NCAR) in Boulder, Colorado.

direction of the flow across the external cell face:

$$H_{\frac{1}{2},jk} = \begin{cases} \dfrac{\tilde{p}_{\text{ext}}}{\rho_{1,jk}} + \dfrac{1}{2}\left(\bar{u}_{1.jk}^2 + \bar{v}_{1,jk}^2 + \bar{w}_{1,jk}^2\right) & \text{outgoing} \\ \dfrac{\tilde{p}_{\text{ext}}}{\rho_\infty} + \dfrac{1}{2}\left(u_\infty^2 + v_\infty^2 + w_\infty^2\right) & \text{incoming} \end{cases} \tag{4.79}$$

The bar over the velocity components indicates an average over the respective faces of the grid cell adjacent to the boundary. The subscript ∞ denotes user-specified far field velocity and density values. Typically, the far field velocity is zero, but for simulations involving an external wind, these values can be specified accordingly.

4.6.2 Solid Boundary Conditions

FDS uses a simple, direct-forcing immersed boundary method (IBM) [37] for block Cartesian geometries. This section discusses the modifications required of the force terms in the momentum equation for IBM.

Direct Poisson solvers are most efficient if the domain is a rectangular region, although other geometries such as cylinders and spheres can be handled almost as easily. For these solvers, a no-flux condition is simple to prescribe at external boundaries. Using the $x = x_{\max}$ boundary as an example:

$$\frac{\partial H}{\partial x} = -F_x - \frac{\partial u}{\partial t} \tag{4.80}$$

where F_x is the x-component of $\mathbf{F}$ at the vent or solid wall, and $\partial u/\partial t$ is the user-specified rate of change in the x-component of velocity. In discretized form, the Poisson solver is supplied with the Neumann boundary condition

$$\frac{H_{I+1,jk} - H_{I,jk}}{\delta x} = -F_{x,I,jk} \tag{4.81}$$

because the normal component of velocity is zero at this boundary from the start of the calculation.

Many practical problems, however, involve more complicated geometries. For building fires, doors and windows within multi-room enclosures are very important features of the simulations. These elements may be included in the overall domain as masked grid cells, but the no-flux condition (4.81) cannot be directly prescribed at the boundaries of these blocked cells. Fortunately, it is possible to exploit the relatively small changes in the pressure from one time step to the next to enforce the no-flux condition. At the start of a time step, the components of the convection/diffusion term $\mathbf{F}$ are computed at all cell faces that do not correspond to walls. At those cell faces that do correspond to solid walls but are not located at the exterior of the computational grid, we prescribe (using the same example as above, but now with $i \neq I$):

$$F_{x,ijk}^n = -\frac{H_{i+1,jk}^{n-1} - H_{ijk}^{n-1}}{\delta x} - \frac{u_{ijk}^b - u_{ijk}^n}{\delta t} \tag{4.82}$$

at the predictor step, and

$$F_{x,ijk}^* = -\frac{H_{i+1,jk}^{*-1} - H_{ijk}^{*-1}}{\delta x} - \frac{u_{ijk}^b - \frac{1}{2}\left(u_{ijk}^* + u_{ijk}^n\right)}{\delta t/2} \tag{4.83}$$

at the corrector step. The no flux condition is enforced at a solid boundary by setting the normal component of the velocity on that boundary to zero. That is, we set $u_{ijk}^b = 0$. If a mass flux exists on the boundary, then $u_{ijk}^b = u_n$ as described in Section 3.2.3.

Note that $*-1$ denotes the pressure term used in the corrector part of the previous time step. In both of these cases, the value of H^n or H^* is not known—it is what we are solving for. Instead, the value of H

from the previous time step is used to estimate the pressure gradient. Equations (4.82) or (4.83) assert that following the solution of the Poisson equation for the pressure, the desired normal component of velocity at the next time step, u^* or u^{n+1}, will be driven towards u^b_{ijk}.

This is approximate because the true value of the velocity time derivative depends on the solution of the pressure equation, but since the most recent estimate of pressure is used, the approximation is fairly good. Also, even though there are small errors in normal velocity at solid surfaces, the divergence of each blocked cell remains exactly zero for the duration of the calculation. In other words, the total flux into a given obstruction is always identically zero, and the error in normal velocity is usually at least several orders of magnitude smaller than the characteristic flow velocity. When implemented as part of a predictor-corrector updating scheme, the no-flux condition at solid surfaces is maintained fairly well. If greater accuracy is required, the Poisson equation can be solved iteratively as the boundary condition (4.82) or (4.83) is updated with each successive approximation of the pressure gradient at the solid wall.

4.6.3 Boundary Conditions at Mesh Interfaces

The time advancement scheme for multiple meshes involves averaging the normal components of velocity at the mesh interface in order to drive them closer into alignment. Because FDS uses a staggered grid, the normal components of velocity co-exist on the mesh interface. Consider two meshes joined side by side in the x direction. The component $u_I \equiv u_{I,jk}$ lives on the right boundary of the left hand mesh, and $u_0 \equiv u_{0,jk}$ lives on the left boundary of the right hand mesh. Ideally, these velocities should be identical, but they are not because of errors associated with solving the pressure on each mesh separately. While the primitive velocity components are indeed unique to a given mesh, for each mesh we may define the discrete "patch-averaged" field $\bar{\mathbf{u}}$ which is identical at all overlapping mesh points. To do this we simply average the coincident values of the normal velocity component at the mesh interfaces. For instance, considering the same side-by-side meshes as before,

$$\bar{u}_I = \bar{u}_0 \equiv \frac{1}{2}\left(u_{I,jk} + u_{0,jk}\right) \tag{4.84}$$

for all patch boundary cells j and k. Here, for simplicity, we are only considering the case in which the cell sizes are equivalent for the adjoining meshes (coarse-fine mesh interfaces are possible).

To see how the new patch-averaged fields are used, consider the predictor step in the time advancement, which may now be written as

$$\mathbf{u}^* = \bar{\mathbf{u}}^n - \delta t\left(\mathbf{F}(\bar{\mathbf{u}}^n) + \nabla H^n\right) \tag{4.85}$$

Note that (4.85) updates a $\bar{\mathbf{u}}$ field to a $\mathbf{u}$ field. In other words, the normal components of velocity at the interface are no longer expected to match because the individual pressure fields do not match exactly at the interface. However, the error introduced in the divergence by the velocity averaging procedure is corrected by the time derivative of divergence in the pressure equation:

$$\nabla^2 H^n = -\left(\frac{\nabla\cdot\mathbf{u}^* - \nabla\cdot\mathbf{u}^n - \nabla\cdot\left(\bar{\mathbf{u}}^n - \mathbf{u}^n\right)}{\delta t}\right) - \mathbf{F}(\bar{\mathbf{u}}^n) \tag{4.86}$$

The extra term in the time derivative, $\nabla\cdot\left(\bar{\mathbf{u}}^n - \mathbf{u}^n\right)$, "corrects" the divergence error. The benefit to averaging the normal components of velocity at mesh interfaces is that $\mathbf{F}$ is the same on each side of the interface, since all force terms are determined using the patch-averaged field. This also means that stress tensors computed at a mesh interface (which are buried in $\mathbf{F}$) are symmetric; this symmetry is a requirement for angular momentum conservation. Thus, the patch-averaging procedure prevents the production of spurious vorticity at mesh interfaces.

4.6.4 Pressure Iteration Scheme

Equation (4.86) corrects the error in the divergence resulting from the averaging of normal velocity components, but it still does not guarantee that the updated velocity components will be equal. To drive the two normal components of velocity closer together, we use the following iterative scheme in the predictor step, again using the x direction interface boundary as an example:

1. Define the pressure term at the mesh interface, H_B, consistent with a Dirichlet boundary condition. Note that the superscript "old" refers to the fact that at this point, the Poisson equation for pressure has not been solved:
$$H_B = \frac{H_I^{\text{old}} + H_1^{\text{old}}}{2} + \frac{\delta x}{4\,\delta t}\left(u_I^{*,\text{old}} - u_0^{*,\text{old}}\right) \tag{4.87}$$
Note also that H is cell-centered; thus, H_I is at the center of the Ith grid cell of the left hand mesh, and H_1 is at the center of the first grid cell of the right hand mesh.

2. Solve the Poisson equation in each mesh separately and exchange values of H_I and H_1.

3. Predict the normal component of velocity at the next time step. Note that the boundary condition for interface pressure term effectively yields the following:
$$u_I^* = \bar{u}_I^n - \frac{u_I^{*,\text{old}} - u_0^{*,\text{old}}}{2} - \delta t\left(F_{x,I}^n + \frac{(H_I^{\text{old}} + H_1^{\text{old}})/2 - H_I}{\delta x/2}\right) \tag{4.88}$$
$$u_0^* = \bar{u}_0^n + \frac{u_I^{*,\text{old}} - u_0^{*,\text{old}}}{2} - \delta t\left(F_{x,0}^n + \frac{H_1 - (H_I^{\text{old}} + H_1^{\text{old}})/2}{\delta x/2}\right) \tag{4.89}$$

4. Repeat this process until $|u_I^* - u_0^*|$ falls below a specified tolerance.

For the corrector step, the procedure is the same, except the boundary condition for the pressure term is:

$$H_B = \frac{H_I^{\text{old}} + H_1^{\text{old}}}{2} + \frac{\delta x}{2\,\delta t}\left(u_I^{n+1,\text{old}} - u_0^{n+1,\text{old}}\right) \tag{4.90}$$

The default velocity tolerance is $|u_I^* - u_0^*| < 0.5\,\delta x$ and the default maximum number of pressure iterations is 10. Both of these parameters can be changed by the user. Details can be found in the FDS User's Guide [3].

Chapter 5

Combustion (Chemically Reacting Flows)

The combustion model determines the mean chemical mass production rate of species α per unit volume, $\dot{m}'''_\alpha$, in the species transport equation, Eq. (2.6). In general, $\dot{m}'''_\alpha$ requires a closure model because the flame thickness is on the order of one millimeter while the grid spacing is typically on the order of tens of centimeters. This chapter describes a partially-stirred batch reactor model for $\dot{m}'''_\alpha$ capable of handling a range of mixing conditions and chemical kinetics. In the non-premixed, fast chemistry limit, which is valid for the vast majority of FDS applications, the reactor model reduces to a simple "mixed is burnt" approximation called the Eddy Dissipation Concept (EDC) [38, 39].

The combustion model also determines the heat release rate for per unit volume, $\dot{q}'''$, which is a quantity of fundamental importance in fire physics and typically the largest contribution to the velocity divergence, Eq. (3.24). Once $\dot{m}'''_\alpha$ has been determined, the heat release rate follows by summing the mass production rates for each species times their respective heats of formation. Details are discussed below in Section 5.2.2.

Before discussing the combustion model, we first discuss of our *lumped species* approach (Section 5.1), which reduces the computational burden of the full chemical system by combining species into groups that transport and react together. In other words, we reduce the number of transport equations we need to solve, which significantly increases the speed of the code. Our basic mixing-controlled, fast chemistry combustion model is presented in Section 5.2.1, followed by details on computing the heat release rate and a simple model for thermal extinction. The model for the mixing time scale (needed in both EDC and the general reactor model) is discussed in Section 5.2.4. In Section 5.2.5, we begin the discussion of our generalized combustion model which is designed to handle both fast and slow chemistry and a range of mixing conditions. For fire, this method holds promise for improved prediction of carbon monoxide and soot. Each computational cell is treated as a partially-stirred batch reactor with a characteristic mixing time. Once reactants are mixed, the reaction rate depends on kinetics. Section 5.2.9 discusses available kinetic mechanisms within FDS, from infinitely fast chemistry (default) to Arrhenius rate laws and reversible reactions.

5.1 Lumped Species Approach

In the typical FDS problem the primitive species are lumped into reacting groups and we consider the simple reaction

$$\text{Fuel} + \text{Air} \rightarrow \text{Products} \tag{5.1}$$

We refer to the Fuel, Air, and Products in Eq. (5.1) as *lumped species*. The lumped species approach is a simplified reaction progress variable approach [40] in which all the progress variables are mass fractions. This avoids any complications related to boundedness and ill-defined initial and boundary conditions.

5.1.1 Relationship between Lumped and Primitive Species

In a simple hydrocarbon reaction, the reactants are the fuel, oxygen, and nitrogen and the products are carbon dioxide, water vapor, and nitrogen. The primitive species mass fractions are given by the composition vector

$$\mathbf{Y} = [Y_{\mathrm{CH_4}}\ Y_{\mathrm{O_2}}\ Y_{\mathrm{N_2}}\ Y_{\mathrm{CO_2}}\ Y_{\mathrm{H_2O}}]^T \tag{5.2}$$

Lumped species are groups of primitive species which only exist in the flow in certain proportions. For example, Air can be assumed to be a lumped species composed of 21 % O_2, 79 % N_2 by volume, plus trace amounts of water vapor and carbon dioxide. The key assumption made in lumping primitive species is that the new species groups transport (implying equal diffusivities) and react together.

In terms of primitive species, a one-step methane reaction may be written as

$$\mathrm{CH_4} + 2\,\mathrm{O_2} + 7.52\,\mathrm{N_2} \rightarrow \mathrm{CO_2} + 2\,\mathrm{H_2O} + 7.52\,\mathrm{N_2} \tag{5.3}$$

This is equivalent to

$$9.52\underbrace{(0.21\,\mathrm{O_2} + .79\,\mathrm{N_2})}_{\text{Air, } Z_0} + \underbrace{\mathrm{CH_4}}_{\text{Fuel, } Z_1} \rightarrow 10.52\underbrace{(0.095\,\mathrm{CO_2} + 0.19\,\mathrm{H_2O} + 0.715\,\mathrm{N_2})}_{\text{Products, } Z_2} \tag{5.4}$$

where 9.52 moles of Air react with 1 mole of Fuel to produce 10.52 moles of Products. Notice that the primitive species have been grouped by volume fraction into lumped species and the lumped species stoichiometric coefficients are the sum of the primitive species coefficients from Eq. (5.3). Note that 9.52×0.21 is only approximately equal to 2. In practice the atom balance requires machine precision. To alleviate this issue, FDS internally normalizes the lumped species volume fractions and makes any necessary adjustments to the specified lumped stoichiometric coefficients. The lumped species mass fractions are denoted Z_i, $i = 0, 1, ..., N_Z$, where N_Z is the number of tracked species. The Background species, Z_0, is found from $Z_0 = 1 - \sum_{i=1}^{N_Z} Z_i$. In the case of Eq. (5.4), two transport equations are solved (Fuel and Products).

The linear transformation from lumped species to primitive species is given by

$$\mathbf{Y} = A\mathbf{Z} \tag{5.5}$$

where A is the transformation matrix (N_y rows $\times$ $(N_z + 1)$ columns). Each column of A represents a different lumped species. The elements of A are the mass fractions for each primitive species in a given lumped species:

$$a_{\alpha i} = \frac{\upsilon_{\alpha i} W_\alpha}{\sum_\beta \upsilon_{\beta i} W_\beta} \tag{5.6}$$

where $\upsilon_{\alpha i}$ are the volume fractions of primitive species α in lumped species i and W_α are the molecular weights. If we want the primitive species in Eq. (5.4) and, as an example, say we have $\mathbf{Z} = [0.3\ 0.2\ 0.5]^T$, we can transform from lumped species to primitive species via

$$\mathbf{Y} = \begin{bmatrix} Y_{\mathrm{O_2}} \\ Y_{\mathrm{N_2}} \\ Y_{\mathrm{CH_4}} \\ Y_{\mathrm{CO_2}} \\ Y_{\mathrm{H_2O}} \end{bmatrix} = \begin{bmatrix} 0.2330 & 0 & 0 \\ 0.7670 & 0 & 0.7248 \\ 0 & 1 & 0 \\ 0 & 0 & 0.1514 \\ 0 & 0 & 0.1238 \end{bmatrix} \begin{bmatrix} 0.3 \\ 0.2 \\ 0.5 \end{bmatrix} = \begin{bmatrix} 0.0699 \\ 0.5925 \\ 0.2000 \\ 0.0757 \\ 0.0619 \end{bmatrix} \tag{5.7}$$

To transform back to lumped species from primitive species we can use:

$$\mathbf{Z} = B\mathbf{Y} \quad ; \quad B = (A^T A)^{-1} A^T \tag{5.8}$$

provided A has full rank and $\mathbf{Y}$ is realizable (i.e., the forward transformation is also possible).

5.1.2 Default Hydrocarbon Combustion Chemistry

The default reaction equation in FDS, known as "simple chemistry," is defined as follows:

$$\nu_0 \underbrace{\left(\upsilon_{O_2,0}\,O_2 + \upsilon_{N_2,0}\,N_2 + \upsilon_{H_2O,0}\,H_2O + \upsilon_{CO_2,0}\,CO_2\right)}_{\text{Background, } Z_0} + \nu_1 \underbrace{C_mH_nO_aN_b}_{\text{Fuel, } Z_1} \longrightarrow$$
$$\nu_2 \underbrace{\left(\upsilon_{CO_2,2}\,CO_2 + \upsilon_{H_2O,2}\,H_2O + \upsilon_{N_2,2}\,N_2 + \upsilon_{CO,2}\,CO + \upsilon_{S,2}\,\text{Soot}\right)}_{\text{Products, } Z_2} \quad (5.9)$$

Here, the volume fraction of primitive species α in lumped species i is denoted by $\upsilon_{\alpha i}$ and the stoichiometric coefficients for the lumped species i are denoted by ν_i.

Carbon monoxide and soot yields are zero by default. The user can specify the CO and soot yields (y_{CO} and y_S respectively). The CO yield, and similarly for soot, is the mass of CO produced per mass of fuel reacted:

$$y_{CO} = \frac{\text{mass CO in Products}}{\text{mass of Fuel reacted}} \quad (5.10)$$

In this reaction system, Air (Background) is lumped species 0, Fuel is lumped species 1, and Products is lumped species 2. To find the stoichiometric coefficients of CO and soot within the products lumped species, FDS uses

$$\nu_2 \upsilon_{CO,2} = -\nu_1 \frac{W_1}{W_{CO}} y_{CO} \quad (5.11)$$

$$\nu_2 \upsilon_{S,2} = -\nu_1 \frac{W_1}{W_S} y_S \quad (5.12)$$

The remaining coefficients come from an atom balance.

Example Consider a methane–air reaction where methane has a specified CO yield of $y_{CO} = 0.1$ and a Soot yield of $y_S = 0.01$. The default FDS reaction system lumps these species into Products. Note that, by default, Air is primarily composed of oxygen and nitrogen but includes trace amounts of carbon dioxide and water vapor. For this reaction the transformation matrix, A, is

	Air	Fuel	Products
CH_4	0.000000	1.000000	0.000000
N_2	0.763017	0.000000	0.720373
O_2	0.231163	0.000000	0.000000
CO_2	0.000592	0.000000	0.143067
CO	0.000000	0.000000	0.005589
H_2O	0.005228	0.000000	0.130412
C	0.000000	0.000000	0.000559

The preceding table shows that the addition of carbon monoxide and soot increases the number of primitive species in the reaction from five to seven. The number of lumped species, however, remains at three—the composition of Products has changed to include to the two additional species. Note that FDS prints the A matrix in the `CHID.out` file so that the user can double check the reaction system.

5.2 Turbulent Combustion

5.2.1 Mixing-Controlled Fast Chemistry (Default)

For the vast majority of FDS applications the "mixed is burnt" assumption is adequate to model the reaction system and the mean chemical source term for Fuel is modeled using the Eddy Dissipation Concept (EDC) of Magnussen and Hjertager [38, 39]:

$$\dot{m}_{\rm F}''' = -\rho \frac{\min(Z_{\rm F}, Z_{\rm A}/s)}{\tau_{\rm mix}} \tag{5.13}$$

Here, $Z_{\rm F}$ and $Z_{\rm A}$ are the lumped mass fractions of Fuel and Air, respectively, and s is the mass stoichiometric coefficient for Air. The quantity $\tau_{\rm mix}$ is a time scale for mixing which must be modeled (see Section 5.2.4). The EDC model therefore states that the rate of fuel consumption is proportional to both the local limiting reactant concentration and the local rate of mixing. As we will see below, the EDC model is a limiting case of a generalized partially-stirred batch reactor model in which all the reactants are initially unmixed and the rate of chemical kinetics is infinite.

5.2.2 Heat Release Rate

The heat release per unit volume is found by summing the species mass production rates times the respective heats of formation:

$$\dot{q}''' \equiv -\sum_{\alpha} \dot{m}_{\alpha}''' \Delta h_{{\rm f},\alpha} \tag{5.14}$$

To maintain code stability, it is sometimes necessary to put an upper bound on the local heat release rate per unit volume. A scaling analysis of pool fires by Orloff and de Ris [41] suggests that the spatial average of the heat release rate of a fire is approximately 1200 kW/m^3. FDS uses a less restrictive upper bound on the local heat release rate per unit volume:

$$\dot{q}'''_{\rm upper} = 200/\delta x + 2500 \quad {\rm kW/m^3} \tag{5.15}$$

The value of 200 kW/m^2 is an empirically derived upper bound on the heat release rate per unit area of flame sheet and δx is the characteristic cell size (m).

5.2.3 Extinction

Subgrid-scale modeling of gas phase suppression and extinction is still an area of active research in the combustion community. The physical mechanisms underlying these phenomena are complex, and even simplified models still rely on an accurate prediction of the flame temperature and local strain rate, neither of which is readily available in an LES calculation.

A limitation of the mixing-controlled reaction model described above is that it assumes fuel and oxygen always react regardless of the local conditions for temperature, dilution, or strain. For large-scale, well-ventilated fires, this approximation is usually sufficient. However, if a fire is in an under-ventilated compartment, or if a suppression agent like water mist or CO_2 is introduced, or if the strain between the fuel and oxidizing streams is high, burning may not occur.

FDS uses simple empirical rules—which ignore strain—to predict local extinction within a certain grid cell based on resolved species concentrations and the mean cell temperature. The default FDS extinction model consists of two parts (shown below) based on the concept of a *critical flame temperature* [42]. If either criterion fails, then there is no chemical reaction and $\dot{m}_{\alpha}''' = 0$ and $\dot{q}''' = 0$ for that time step.

Basic Extinction Model

1. If the cell temperature is below the auto-ignition temperature (AIT) for all fuels in the cell then combustion is suppressed. The auto-ignition temperature for each fuel is zero by default; thus, the user does not need to specify an ignition source.

2. If the potential combustion heat release from a *local pocket of stoichiometric fuel-air-product (hereafter "reactant") mixture* cannot raise the temperature of that mixture above an empirically determined critical flame temperature, T_{CFT}, then combustion is suppressed. Consider the simple reaction $\mathrm{Fuel} + \mathrm{Air} \rightarrow \mathrm{Products}$. The local mass fractions of lumped species Fuel, Air, and Products in the cell at the beginning of the combustion time step are $[Z_{\mathrm{F}}, Z_{\mathrm{A}}, Z_{\mathrm{P}}]$ and s is the mass stoichiometric coefficient for Air (mass of Air required per mass of Fuel consumed). Based on the limiting reactant, the masses in the local reactant mixture are defined as follows (take 1 kg as a basis; the hat $\hat{}$ indicates a reactant mixture value):

$$\hat{Z}_{\mathrm{F}} = \min(Z_{\mathrm{F}}, Z_{\mathrm{A}}/s) \tag{5.16}$$

$$\hat{Z}_{\mathrm{A}} = s\,\hat{Z}_{\mathrm{F}} \tag{5.17}$$

   The stoichiometric mixture value for the product diluents is defined such that the following ratio holds:

$$\frac{\hat{Z}_{\mathrm{P}}}{\hat{Z}_{\mathrm{A}}} = \frac{\overbrace{Z_{\mathrm{F}} - \hat{Z}_{\mathrm{F}}}^{\text{unburned fuel}} + Z_{\mathrm{P}}}{Z_{\mathrm{A}}} \tag{5.18}$$

   In other words, within the reactant mixture we lump unburned fuel in with any products or diluents and keep the ratio of diluent to air constant.

   Another way to say this is that excess fuel to acts as a diluent, but excess air does *not*. Hence, a large computational cell which is mostly air with a small amount of fuel (and no additional diluents) is likely to burn, whereas a cell which is mostly fuel with very little air will not burn.

   Once the local reactant mixture has been determined, the extinction criterion is given by

$$\hat{Z}_{\mathrm{F}}\,(h_{\mathrm{F}}(T) + \Delta h_{\mathrm{c,F}}) + \hat{Z}_{\mathrm{A}}\,h_{\mathrm{A}}(T) + \hat{Z}_{\mathrm{P}}\,h_{\mathrm{P}}(T) < \hat{Z}_{\mathrm{F}}\,h_{\mathrm{F}}(T_{\mathrm{CFT}}) + \hat{Z}_{\mathrm{A}}\,h_{\mathrm{A}}(T_{\mathrm{CFT}}) + \hat{Z}_{\mathrm{P}}\,h_{\mathrm{P}}(T_{\mathrm{CFT}}) \tag{5.19}$$

   where T is the initial mean cell temperature and T_{CFT} is the critical flame temperature. If the inequality Eq. (5.19) is true, then combustion is suppressed—the heat of combustion is not sufficient to raise the product mixture above its critical flame temperature.

Alternative Extinction Model In addition to the extinction model described above, there is the option to select a simpler extinction model based on the limiting oxygen concentration. Details of this model are discussed in Appendix D.

5.2.4 Reaction Time Scale Model

In this section we provide an expression for the mixing time based on the local state of the flow field. The basic idea behind the model we propose here is to consider the three physical processes of diffusion, subgrid-scale (SGS) advection, and buoyant acceleration and to take the fastest of these processes (locally) as the controlling flow time scale [43].

It is important to consider the behavior of an SGS model as the LES filter width (cell size) varies. The mixing times for diffusion, SGS advection, and buoyant acceleration scale differently with filter width and

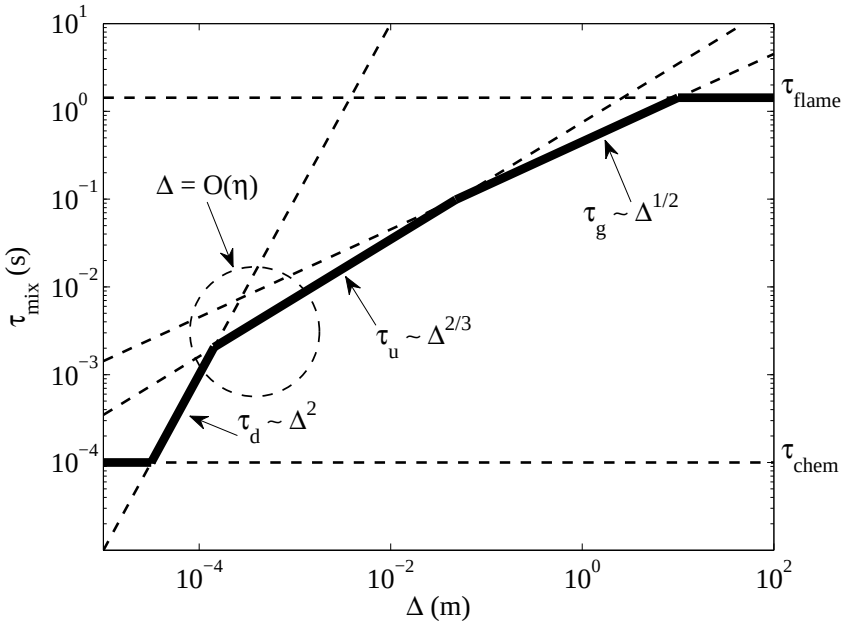

Figure 5.1: Reaction time scale model.

if we look to the limits of the filter scales an interesting picture emerges. Referring to Fig. 5.1, let us move from left to right along the horizontal axis following the thick black line which represents our time scale model for a hypothetical flow condition. First, notice that the reaction time scale must be greater than or equal to the chemical time scale, τ_{chem}, which, though usually small, is finite. At a slightly larger scale, we expect the mixing time to vary as the square of the filter width because the mixing is controlled by molecular diffusion. In this regime, denoted τ_d, the numerical solution is a DNS and this scaling law is valid while Δ is less than the Kolmogorov scale, η, the length scale of the smallest turbulent eddies (for this discussion we assume the Schmidt number (Sc) is of order unity). For a sufficiently high Reynolds number flow (such that an inertial subrange exists), as the filter width increases beyond the Kolmogorov scale we encounter a regime, marked τ_u, where turbulent advection controls the rate of mixing and the mixing time varies as the two-thirds power of the filter width [14]. This is the regime where most LES submodels are valid (It is important to appreciate that fire differs from turbulent combustion in that the assumption of locally high Re is frequently invalid).

Now, let us imagine what should happen to the mixing time as the filter width increases beyond the inertial subrange to a length scale larger than the height of the flame itself (actually a possibility in wildfire modeling). We would *not* expect the inertial range scaling to continue up through the so-called "energy-containing" range of turbulent length scales. Rather, for fires we expect buoyant acceleration to control the mixing at these relatively coarse scales. A time scale based on a constant acceleration goes as the square root of the filter width, as shown by the regime marked τ_g in the diagram. This shift in scaling may appear minor given the log-log nature of the plot, but the effect of the acceleration-based time scale is indeed significant for large cell sizes. Finally, note that the flame height presents a limit to the reaction time scale, here denoted τ_{flame}, since all fuel must be consumed within a single cell.

Of course, the relative importance of the physical processes will depend on the flow. For example, if gravity is weak, the τ_g line shifts up and may not affect the reaction time before the flame time scale is reached. If the flow is highly turbulent, the inertial range scaling may be more dominant, which would be indicated by a lowering of the τ_u line. Or, for highly turbulent jet flames τ_{flame} may be reached before the

acceleration time scale has any effect. Perhaps more typical for low strain fires, if an inertial subrange does not exist (if the Reynolds number is too low relative to the Froude number), then the τ_u line in Fig. 5.1 moves up out of the picture and we are left with diffusion and buoyancy to control the mixing.

The bold solid line in Fig. 5.1 is mathematically represented by

$$\tau_{mix} = \max(\tau_{chem}, \min(\tau_d, \tau_u, \tau_g, \tau_{flame})) \tag{5.20}$$

The mathematical details of the submodels are as follows:

$$\tau_d = \frac{\Delta^2}{D_F} \tag{5.21}$$

$$\tau_u = \frac{\Delta}{\sqrt{2k_{sgs}}} \tag{5.22}$$

$$\tau_g = \sqrt{2\Delta/g} \tag{5.23}$$

where D_F is the diffusivity of the fuel species. Note that k_{sgs} is the unclosed subgrid kinetic energy per unit mass which by default is taken from the model for the turbulent viscosity (see Section 4.2). The acceleration time scale τ_g is the time required to travel a distance Δ starting from rest under a constant acceleration, $g = 9.81$ m/s^2.

5.2.5 Partially-Stirred Batch Reactor Model

Modeling chemical reactions in turbulent flow is mathematically challenging because the length and time scales associated with the reactions may be orders of magnitude below what can be spatially and temporally resolved by the simulation. When the fuel and oxidizer are initially unmixed (diffusion flame) and the kinetics are fast compared with mixing, the simple Eddy Dissipation Concept (EDC) model [38, 39] is sufficient. However, for more complex reactions—such as carbon monoxide and soot formation—where reaction and mixing time scales may overlap, we require a more generalized approach.

To this end, we have developed a simple mixing environment method to close the mean chemical source term, $\dot{m}'''_\alpha$, in Eq. (2.6). For pure diffusion flames our method is similar to EDC, but the method is not limited to diffusion flames. Each computational cell is thought of as a partially stirred batch reactor. At the start of a time step, each cell has an initial concentration of species (reactants, products, inerts) that exist with some degree of mixing. By default, each cell is completely unmixed at the start of a time step (corresponding to a diffusion flame). Generally, the rate of mixing is dominated by turbulence. The mixing time, τ_{mix}, was discussed in Section 5.2.4. Once mixed, species can react based on specified kinetic parameters—reactions may be infinitely fast or governed by an Arrhenius rate law (Section 5.2.11).

At the start of the integration of the reactor model, the species transport equations have been solved and we know the mean cell concentrations of all reactants in our chemical system. In this section, for simplicity we will work in terms of primitive species mass fractions.

5.2.6 A Simple Subgrid Environment

The cell mean mass fraction of α, a function of time, is denoted $\widetilde{Y}_\alpha(t)$. The local concentration at any point within the cell exists in one of two states: completely unmixed or completely mixed. Let $\hat{Y}_\alpha(t)$ denote the mass fraction of α in the mixed reactor zone, initially equal to the cell mean, $\hat{Y}_\alpha(0) = \widetilde{Y}^0_\alpha \equiv \widetilde{Y}_\alpha(0)$. With $\psi_\alpha \in [0,1]$ representing the sample space for the composition, the subgrid probability density function (PDF) may be written as

$$f(\psi_\alpha; t) = w_1\delta(0-\psi_\alpha) + w_2\delta(1-\psi_\alpha) + w_3\delta(\hat{Y}_\alpha[t]-\psi_\alpha) \tag{5.24}$$

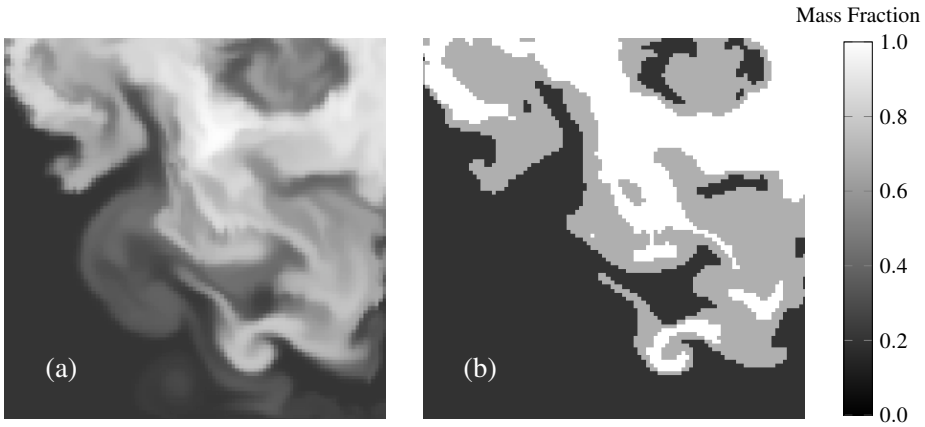

Figure 5.2: Subgrid environment at an instant in time in a hypothetical computational cell (batch reactor). (a) Well-resolved scalar field, highly unmixed, after turbulent transport. (b) Idealized subgrid environment: the local mass fraction is either 0, 1, or equal to a mixed mean. In the present model, the gray region is called the "mixed reactor zone" and evolves in time (in volume and composition) during the integration of the batch reactor.

where $\delta(x)$ is the Dirac delta function. In other words, if we look at a specific point, the mass fraction of species α may only be 0, 1, or equal to the mixed zone value, $\hat{Y}_\alpha$ (see Fig. 5.2). The weights w_i must satisfy integral constraints on the cell: $\int f(\psi_\alpha;t)\,\mathrm{d}\psi_\alpha = 1$, $\int f(\psi_\alpha;t)\,\psi_\alpha\,\mathrm{d}\psi_\alpha = \widetilde{Y}_\alpha(t)$.

For convenience, we define the *unmixed fraction*, $\zeta(t)$, as the fraction of mass within the cell existing as either 0 or 1. To satisfy the integral constraints, the PDF weights are set to

$$w_1 = \zeta\,(1-\widetilde{Y}_\alpha^0) \tag{5.25}$$

$$w_2 = \zeta\,\widetilde{Y}_\alpha^0 \tag{5.26}$$

$$w_3 = 1-\zeta \tag{5.27}$$

As shown in Appendix F, the unmixed fraction evolves by the following simple ODE

$$\frac{\mathrm{d}\zeta}{\mathrm{d}t} = -\frac{\zeta}{\tau_{\mathrm{mix}}} \tag{5.28}$$

with the solution

$$\zeta(t) = \zeta_0\,\mathrm{e}^{-t/\tau_{\mathrm{mix}}} \tag{5.29}$$

The initial condition ζ_0 may be specified, modeled algebraically, or taken from the update of a passive scalar transport equation. Currently, FDS takes $\zeta_0 = 1$ as default for LES mode (diffusion flame) and $\zeta_0 = 0$ as default for DNS (it is assumed that the mixing time scale is well-resolved).

5.2.7 Mean Chemical Source Term

At any point in time, the composition of the computational cell may be determined by combining the unmixed and mixed portions:

$$\widetilde{Y}_\alpha(t) = \zeta(t)\,\widetilde{Y}_\alpha^0 + (1-\zeta(t))\,\hat{Y}_\alpha(t) \tag{5.30}$$

Differentiating (5.30) in time and using (5.28) we see that our model for the chemical source term needed in (2.6) is given by

$$\dot{m}'''_\alpha = \rho \frac{\mathrm{d}\widetilde{Y}_\alpha}{\mathrm{d}t} = \rho \left[\frac{\zeta}{\tau_{\mathrm{mix}}} (\hat{Y}_\alpha - \widetilde{Y}^0_\alpha) + (1-\zeta) \frac{\mathrm{d}\hat{Y}_\alpha}{\mathrm{d}t} \right] \tag{5.31}$$

Note that the unmixed fraction is comparable to the *complement* of the fraction of "reacting fine structures" in other EDC formulations [44, 45], but in our model this fraction evolves in time. A comparison between our model and that of Panjwani et al. [45] is developed further in Appendix G.

An alternate derivation of (5.30) and (5.31) in terms of moments of the transport equation for the PDF (5.24) is given in Appendix F. This derivation highlights that the implicit mixing model is a *variant of* the 'interaction by exchange with the mean' or IEM model [46], which we refer to as the 'interaction by exchange with the mixed mean' or IEMM.

5.2.8 Evolution of the Composition in the Mixed Reactor Zone

Since (5.31) was obtained by differentiating (5.30) and we are ultimately interested in integrating over an LES times step Δt to obtain the final cell composition, it turns out to be easier and more accurate to simply work in terms of (5.30). Thus, the problem is reduced to finding a solution for $\hat{Y}_\alpha(t)$, since the solution $\zeta(t)$ is known from (5.29).

The composition in the mixed reactor zone changes by two processes: mixing (mass is transferred from the unmixed zone to the mixed zone) and chemical reaction. As a consequence of the time splitting scheme, the total mass within the reactor (computational cell) is constant over a time step. We denote this mass by ρV_{c}, where ρ is the initial cell mass density and V_{c} is the cell volume. The unmixed mass is denoted $U(t)$ and the mixed mass is denoted $M(t)$. Given (5.29), the following equations describe the cell mass evolution:

$$\rho V_{\mathrm{c}} = U(t) + M(t) \tag{5.32}$$

$$U(t) = \zeta(t)\, \rho V_{\mathrm{c}} \tag{5.33}$$

$$M(t) = (1-\zeta(t))\, \rho V_{\mathrm{c}} \tag{5.34}$$

Within the mixed reactor zone, let $m_\alpha(t)$ denote the mass of species α. The mass fraction of α in the mixed zone may then be written as

$$\hat{Y}_\alpha(t) \equiv \frac{m_\alpha(t)}{M(t)} \tag{5.35}$$

This concentration is important because Arrhenius rate laws are based on the mixed composition only.

The ODE governing the mixed species mass is

$$\begin{aligned} \frac{\mathrm{d}m_\alpha}{\mathrm{d}t} &= \hat{Y}_\alpha \frac{\mathrm{d}M}{\mathrm{d}t} + M \frac{\mathrm{d}\hat{Y}_\alpha}{\mathrm{d}t} \\ &= -\widetilde{Y}^0_\alpha \frac{\mathrm{d}U}{\mathrm{d}t} + M \frac{\mathrm{d}\hat{Y}_\alpha}{\mathrm{d}t} \\ &= \rho V_{\mathrm{c}} \left[\frac{\zeta\, \widetilde{Y}^0_\alpha}{\tau_{\mathrm{mix}}} + (1-\zeta) \frac{\mathrm{d}\hat{Y}_\alpha}{\mathrm{d}t} \right] \end{aligned} \tag{5.36}$$

The first term on the RHS accounts for mixing. The second term represents chemical kinetics. Note that in the second step we have utilized the fact that the unmixed composition remains constant (at the initial cell mean) throughout the time step. The third step follows from (5.28), (5.33), and (5.34).

5.2.9 Time Integration for Mixing and Reaction

In this section, we discuss the numerical solution of (5.36). Let Δt^k represent the kth sub-time step in the integration (less than or equal to the LES time step δt); $t^k = 0$ at the start of the reactor integration. The integration is time split such that *mixing is done first, followed by reaction*. A simple explicit update of (5.36) over the sub-time interval t^k to $t^k + \Delta t^k$ is given by

$$m_\alpha^* = m_\alpha(t^k) - [\zeta(t^k + \Delta t^k) - \zeta(t^k)]\,\widetilde{Y}_\alpha^0\,\rho V_c \tag{5.37}$$

$$\hat{Y}_\alpha^* = m_\alpha^*/M^* \tag{5.38}$$

$$\hat{Y}_\alpha(t^k + \Delta t^k) = \hat{Y}_\alpha^* + \Delta\hat{Y}_\alpha^* \tag{5.39}$$

The superscript * indicates a post-mixing value. The first step, (5.37), is an analytical solution for the mixing step (first term in (5.36)), obtained using (5.29). The mixing time scale τ_{mix}, needed in (5.29), is computed once per LES time step using (5.20) and held constant during the reactor integration. The mixed mass, $M^* = M(t^k + \Delta t^k)$, is evaluated at the end of the subinterval using (5.34). For fast chemistry, we take only one sub-step ($\Delta t^{k=1} = \delta t$).

The method to determine $\Delta\hat{Y}_\alpha^*$ (the change in mass fraction of α due to chemical reaction) in (5.39) depends on the complexity of the reaction system. Below we first discuss the simplest case of infinitely fast chemistry. Then we discuss finite-rate chemistry.

At the end of the time integration, the mixed zone composition, $\hat{Y}_\alpha(\delta t)$, is combined with the unmixed mass in (5.30) to obtain the final cell composition.

5.2.10 Infinitely Fast Chemistry (Default)

Single Reaction

For a single reaction, the change in fuel is based on the limiting reactant [39]:

$$\Delta\hat{Y}_F = -\min\left(\hat{Y}_F, \hat{Y}_\alpha \frac{\nu_F W_F}{\nu_\alpha W_\alpha}\right) \quad ; \quad \text{for all reactants, } \alpha \tag{5.40}$$

The minimum is taken in Eq. (5.40) to ensure that the reactant species mass fractions remain realizable.

Multiple Reactions

For multiple reactions with infinitely fast chemistry, a more general boundedness correction algorithm is used. In this formulation, the change in fuel is simply the amount of the fuel present

$$\Delta\hat{Y}_F = -\hat{Y}_F \tag{5.41}$$

Discussion of how this algorithm is used to maintain realizability is in Section 5.2.13.

5.2.11 Finite-Rate Chemistry (Arrhenius Reaction)

Consider a simple one-step forward reaction:

$$a\mathrm{A} + b\mathrm{B} \rightarrow c\mathrm{C} + d\mathrm{D} \tag{5.42}$$

The rate expression for species A with a mixed zone concentration of C_A in mol/L and rate constant k is

$$\frac{\mathrm{d}C_A}{\mathrm{d}t} = -k\,C_A^a\,C_B^b \tag{5.43}$$

Consider a set of N_r reactions with fuel F. The reaction rate (mol/(L · s)) for F in the ith reaction is

$$r_{\mathrm{F},i} = -k_i \prod C_\alpha^{a_{\alpha,i}} \tag{5.44}$$

For the ith Arrhenius reaction, the rate constant, k_i, depends on the temperature, T, the temperature exponent, n_i, the pre-exponential factor, A_i, and the activation energy, E_i:

$$k_i = A_i \, T^{n_i} \, \mathrm{e}^{-E_i/RT} \tag{5.45}$$

Note that the units of E are J/mol and units of A are dependent upon the order of the reaction and take the appropriate form to ensure the units of Eq. (5.44) are correct.

The reaction rate for species α of the ith reaction is based on the ratio of stoichiometric coefficients:

$$r_{\alpha,i} = \left(\frac{\nu_{\alpha,i}}{\nu_{F,i}} \right) r_{\mathrm{F},i} \tag{5.46}$$

The change in concentration for species α within the mixed reactor zone is then:

$$\frac{\mathrm{d}C_\alpha}{\mathrm{d}t} = \sum_i r_{\alpha,i} \tag{5.47}$$

FDS only transports lumped species and only lumped species can be consumed or created. Note, however, that any of the primitive species may participate in a reaction rate law.

It is more convenient for FDS to work in terms of mass fractions, Y_α. The concentration (mol/L) and mass fractions (kg α/kg) are related by $C_\alpha = Y_\alpha \rho / W_\alpha$. To simplify the calculations within FDS, density and molecular weight are pulled out of the product of the concentrations on the right hand side of Eq. (5.44) and calculated with the other constants to form A':

$$A_i' = A_i \, \rho^{\Sigma a_\alpha} \prod W_\alpha^{-a_{\alpha,i}} \tag{5.48}$$

Using A_i', the rate becomes

$$r_{F,i}' = -A_i' \, T^{n_i} \, \mathrm{e}^{-E_i/RT} \prod Y_\alpha^{a_{\alpha,i}} \tag{5.49}$$

The reaction rate on a mass basis for species α in the ith reaction is

$$r_{\alpha,i}' = \left(\frac{\nu_{\alpha,i} W_\alpha}{\nu_{F,i} W_F} \right) r_{F,i}' \tag{5.50}$$

Last, the rate of change in composition for species α (kg α/(m^3 · s)) in the mixed reactor zone becomes

$$\frac{\mathrm{d}\hat{Y}_\alpha}{\mathrm{d}t} = \frac{1}{\rho} \sum_i r_{\alpha,i}' \tag{5.51}$$

See Section 5.2.13 for a discussion on the algorithm used to ensure species remain realizable.

Time Integration for Finite-Rate Chemistry

For reactions other than single step, mixing controlled chemistry, a fourth-order explicit integrator with error control is used. The time integration follows the procedure outlined in Eqs. (5.37) and (5.39), but multiple subiterations are generally needed and the change in composition over the subinterval in the mixed reactor zone, $\Delta\hat{Y}_\alpha^*$, is usually obtained by integrating an Arrhenius rate law (we say "usually" because a combination of fast and finite-rate chemistry is permissible). More detail on the numerical methods of the integrator, including a method to combat stiff chemistry, can be found in Appendix E.

5.2.12 Change in Species Compositions

Using the change in fuel concentration for each of the i reactions, the change in each species α is given by

$$\Delta\hat{Y}_\alpha = \sum_i \left(\frac{\nu_{\alpha,i} W_\alpha}{\nu_{\mathrm{F},i} W_{\mathrm{F},i}} \right) \Delta\hat{Y}_{\mathrm{F},i} \tag{5.52}$$

5.2.13 Maintaining Species Boundedness

To maintain realizable species mass fractions ($0 \leq \hat{Y}_\alpha \leq 1$), a predictor-corrector scheme is used

$$\hat{Y}_\alpha^p = \hat{Y}_\alpha^k + \Delta\hat{Y}_\alpha \tag{5.53}$$

$$\hat{Y}_\alpha^{k+1} = \hat{Y}_\alpha^k + \Delta\hat{Y}_\alpha \beta \tag{5.54}$$

After computing the predicted values, a boundedness correction, β, is applied to the change in species vector, $\Delta\hat{Y}_\alpha$, to determine the corrected values. Here β is defined as

$$\beta = \begin{cases} \dfrac{\hat{Y}_\alpha^k}{|\hat{Y}_\alpha^p| + \hat{Y}_\alpha^k} & \hat{Y}_\alpha^p \leq 0 \\ \dfrac{1 - \hat{Y}_\alpha^k}{\hat{Y}_\alpha^p - \hat{Y}_\alpha^k} & \hat{Y}_\alpha^p > 1 \end{cases} \quad ; \quad \text{take minimum value over all } \alpha \text{ species} \tag{5.55}$$

Example: Infinitely Fast Chemistry, Oxygen-limited, Methane Combustion

Consider a single step methane oxidation reaction

$$\mathrm{CH_4} + 2\,\mathrm{O_2} \rightarrow \mathrm{CO_2} + 2\,\mathrm{H_2O} \tag{5.56}$$

where the initial mass fractions of species are 30% methane, 30% oxygen, and 40% nitrogen by mass. In this example, the conditions are oxygen-limited. This means that the only way for all of the fuel to be consumed would be to have a negative mass fraction of oxygen. This is not physical. As a result, we follow Eq. (5.40) and find change in fuel concentration by the limiting reactant:

$$\Delta\hat{Y}_\mathrm{F} = -\min\left(0.3, 0.3\frac{(-1)(16)}{(-2)(32)}\right) = -0.075 \tag{5.57}$$

An alternative method is to follow the predictor-corrector scheme discussed in Section 5.2.13. First we find the change in fuel concentration

$$\Delta\hat{Y}_\mathrm{F} = -0.3 \tag{5.58}$$

and the corresponding change is oxygen

$$\Delta\hat{Y}_{\mathrm{O_2}} = -0.3\left(\frac{(-2)(32)}{(-1)(16)}\right) = -1.2 \tag{5.59}$$

Following Eq. (5.53), the updated reaction concentrations are $\hat{Y}_\mathrm{F}^p = 0$ and $\hat{Y}_{\mathrm{O_2}}^p = -0.9$. The boundedness correction factor is then calculated:

$$\beta = \frac{0.3}{0.9 + 0.3} = 0.25 \tag{5.60}$$

Multiplying β by the change in fuel results

$$\Delta\hat{Y}_\mathrm{F} = (-0.3)(0.25) = -0.075 \tag{5.61}$$

which is the same result as found by Eq. (5.57).

Example: Infinitely Fast Chemistry, Oxygen-limited, Methane-Propane Combustion

Consider the case where there are two, single step hydrocarbon oxidization reactions

$$\text{Reaction 1} \qquad \mathrm{CH_4 + 2\,O_2 \rightarrow CO_2 + 2\,H_2O} \tag{5.62}$$

$$\text{Reaction 2} \qquad \mathrm{C_3H_8 + 5\,O_2 \rightarrow 3\,CO_2 + 4\,H_2O} \tag{5.63}$$

The initial composition of a premixed reactor is 30% methane, 40% propane, and 30% oxygen by mass.

Lumped Species Approach

One way to solve this problem is to use a lumped species approach; combine the methane and propane into a new fuel known as 'My Fuel.' In this example, the initial volume fractions of methane and propane are 0.673 and 0.327, respectively. 'My Fuel' can then be defined as

$$\text{My Fuel} = (0.673\,\mathrm{CH_4} + 0.327\,\mathrm{C_3H_8}) = \mathrm{C_{1.65}H_{5.31}} \tag{5.64}$$

The molecular weight of this lumped fuel is 25.21 g/mol. Based on the lumped fuel composition, a single reaction can be constructed

$$\mathrm{C_{1.65}H_{5.31} + 2.98\,O_2 \rightarrow 1.65\,CO_2 + 2.66\,H_2O} \tag{5.65}$$

On a mass basis, the reactor is 70 % fuel, with with 43 % of that mass methane and 57 % propane. Following Eq. (5.40) yields a change in fuel of

$$\Delta\hat{Y}_\mathrm{F} = -\min\left(0.7, 0.3\frac{(-1)(25.21)}{(-2.98)(32)}\right) = -0.0793 \tag{5.66}$$

The change in fuel for each species is based on each fuel's mass fraction in the lumped fuel

$$\Delta\hat{Y}_{\mathrm{F},1} = (-0.0793)(0.43) = -0.0339 \tag{5.67}$$

$$\Delta\hat{Y}_{\mathrm{F},2} = (-0.0793)(0.57) = -0.0452 \tag{5.68}$$

Primitive Species Approach

An alternative method is to process each reaction independently and use the boundedness correction algorithm (Section 5.2.13). The first step is to compute the change in fuel for each reaction

$$\Delta\hat{Y}_{\mathrm{F},1} = -0.3 \tag{5.69}$$

$$\Delta\hat{Y}_{\mathrm{F},2} = -0.4 \tag{5.70}$$

and the equivalent change in oxygen

$$\Delta\hat{Y}_{\mathrm{O_2},1} = -0.3\left(\frac{(-2)(32)}{(-1)(16)}\right) = -1.2 \tag{5.71}$$

$$\Delta\hat{Y}_{\mathrm{O_2},2} = -0.4\left(\frac{(-5)(32)}{(-1)(44)}\right) = -1.45 \tag{5.72}$$

The updated reaction concentrations are then

$$\hat{Y}^p_{\mathrm{F},1} = 0.3 - 0.3 = 0 \tag{5.73}$$

$$\hat{Y}^p_{\mathrm{F},2} = 0.4 - 0.4 = 0 \tag{5.74}$$

$$\hat{Y}^p_{\mathrm{O_2}} = 0.3 - 1.2 - 1.45 = -2.35 \tag{5.75}$$

The resulting boundedness correction factor is found to be

$$\beta = \frac{0.3}{2.35 + 0.3} = 0.113 \tag{5.76}$$

Applying the β correction to the change in fuel for each reaction results in the same values are Eqs. (5.67) and (5.68)

$$\Delta\hat{Y}_{\mathrm{F},1} = (-0.3)(0.113) = -0.0339 \tag{5.77}$$

$$\Delta\hat{Y}_{\mathrm{F},2} = (-0.4)(0.113) = -0.0452 \tag{5.78}$$

Chapter 6

Thermal Radiation

Gas phase thermal conduction and radiation are represented by the divergence of the heat flux vector in the energy equation, $\nabla \cdot \dot{\mathbf{q}}''$. This chapter describes the equations that govern the radiative component, $\dot{\mathbf{q}}_{\mathrm{r}}''$.

6.1 Radiation Transport Equation

The Radiative Transport Equation (RTE) for an absorbing, emitting, and scattering medium is [47]

$$\mathbf{s}\cdot\nabla I_\lambda(\mathbf{x},\mathbf{s}) = \underbrace{-\kappa(\mathbf{x},\lambda)\,I_\lambda(\mathbf{x},\mathbf{s})}_{\text{Energy loss by absorption}} - \underbrace{\sigma_{\mathrm{s}}(\mathbf{x},\lambda)\,I_\lambda(\mathbf{x},\mathbf{s})}_{\text{Energy loss by scattering}} + \underbrace{B(\mathbf{x},\lambda)}_{\text{Emission source term}} + \underbrace{\frac{\sigma_{\mathrm{s}}(\mathbf{x},\lambda)}{4\pi}\int_{4\pi}\Phi(\mathbf{s}',\mathbf{s})\,I_\lambda(\mathbf{x},\mathbf{s}')\,d\mathbf{s}'}_{\text{In-scattering term}} \tag{6.1}$$

where $I_\lambda(\mathbf{x},\mathbf{s})$ is the radiation intensity at wavelength, λ; $\mathbf{s}$ is the direction vector of the intensity; and $\kappa(\mathbf{x},\lambda)$ and $\sigma_{\mathrm{s}}(\mathbf{x},\lambda)$ are the local absorption and scattering coefficients, respectively. $B(\mathbf{x},\lambda)$ is the emission source term, describing how much heat is emitted by the local mixture of gas, soot and droplets/particles. The integral on the right hand side describes the in-scattering from other directions. The in-scattering and scattering terms are detailed in Section 6.3.

In practical simulations, the spectral dependence of the RTE cannot be resolved accurately. Instead, the radiation spectrum is divided into a relatively small number of bands and a separate RTE is derived for each band. For instance, the band specific RTE for a non-scattering gas is

$$\mathbf{s}\cdot\nabla I_n(\mathbf{x},\mathbf{s}) = B_n(\mathbf{x}) - \kappa_n(\mathbf{x})\,I_n(\mathbf{x},\mathbf{s}),\;\; n = 1\ldots N \tag{6.2}$$

where I_n is the intensity integrated over the band n, and κ_n is the appropriate mean absorption coefficient for the band. When the intensities corresponding to the bands are known, the total intensity is calculated by summing over all the bands

$$I(\mathbf{x},\mathbf{s}) = \sum_{n=1}^{N} I_n(\mathbf{x},\mathbf{s}) \tag{6.3}$$

6.1.1 Radiation Source Term

The emission source term for radiation band n is

$$B_n(\mathbf{x}) = \kappa_n(\mathbf{x})\,I_{\mathrm{b},n}(\mathbf{x}) \tag{6.4}$$

where $I_{b,n}$ is the fraction of the blackbody radiation at temperature $T(\mathbf{x})$:

$$I_{b,n}(\mathbf{x}) = F_n(\lambda_{\min}, \lambda_{\max})\, \sigma T(\mathbf{x})^4/\pi \tag{6.5}$$

and σ is the Stefan-Boltzmann constant. The calculation of factors F_n is explained in Ref. [48]. The measurement of the absorption coefficients, κ_n, is discussed in Appendix C.

Even with a reasonably small number of bands, solving multiple RTEs is very time consuming. Fortunately, in most large-scale fire scenarios soot is the most important combustion product controlling the thermal radiation from the fire and hot smoke. As the radiation spectrum of soot is continuous, it is possible to assume that the gas behaves as a gray medium. The spectral dependence is then lumped into one absorption coefficient ($N = 1$) and the source term is given by the blackbody radiation intensity [49]

$$I_b(\mathbf{x}) = \frac{\sigma T(\mathbf{x})^4}{\pi} \tag{6.6}$$

This is the default mode of FDS. For optically thin flames, however, where the yield of soot is small compared to the yields of CO_2 and water vapor, the gray gas assumption can lead to an over-prediction of the emitted radiation. From a series of numerical experiments using methane as the fuel, it has been found that six bands ($N = 6$) provide an accurate representation of the most important radiation bands of the fuel, CO_2, and water vapor [50]. Table 6.1 through Table 6.9 list the band limits for various fuel species. The location of the bands have been adjusted to accommodate most of the features of the fuels spectra. If the absorption of the fuel is known to be important, separate bands can be reserved for fuel, increasing the total number of bands, N. The number of additional bands depends on the fuel, as discussed in Appendix C.

6.1.2 Radiation Contribution to Energy Equation

The radiant heat flux vector $\dot{\mathbf{q}}''_r$ is defined

$$\dot{\mathbf{q}}''_r(\mathbf{x}) = \int_{4\pi} \mathbf{s}'\, I(\mathbf{x}, \mathbf{s}')\, \mathrm{d}\mathbf{s}' \tag{6.7}$$

The gas phase contribution to the radiative loss term in the energy equation is (under the gray gas assumption)

$$-\nabla\cdot\dot{\mathbf{q}}''_r(\mathbf{x})(\mathrm{gas}) = \kappa(\mathbf{x})\,[U(\mathbf{x}) - 4\pi I_b(\mathbf{x})] \quad ; \quad U(\mathbf{x}) = \int_{4\pi} I(\mathbf{x}, \mathbf{s}')\, \mathrm{d}\mathbf{s}' \tag{6.8}$$

For N bands, the gas phase contribution to the radiative loss term in the energy equation is

$$-\nabla\cdot\dot{\mathbf{q}}''_r(\mathbf{x})(\mathrm{gas}) = \sum_{n=1}^{N} \kappa(\mathbf{x})\, U_n(\mathbf{x}) - 4\pi B_n(\mathbf{x}) \quad ; \quad U_n(\mathbf{x}) = \int_{4\pi} I_n(\mathbf{x}, \mathbf{s}')\, \mathrm{d}\mathbf{s}' \tag{6.9}$$

In words, the net radiant energy gained by a grid cell is the difference between that which is absorbed and that which is emitted.

Table 6.1: Limits of the spectral bands for methane (CH_4).

ω (1/cm)	10000		3800		3400	2400	2174		1000	50
6 Band Model	1		2		3	4	5		6	
Major Species	Soot CO_2, H_2O		CO_2 H_2O, Soot		CH_4 Soot	CO_2 Soot	H_2O,CH_4 Soot		H_2O CO_2	
λ (μm)	1.00		2.63		2.94	4.17	4.70		10.0	200

Table 6.2: Limits of the spectral bands for ethane (C_2H_6).

ω (1/cm)	10000		3800		3350	2550		1650		1090		50
6 Band Model	1		2		3	4			5		6	
Major Species	Soot CO_2, H_2O		CO_2 H_2O, Soot		C_2H_6 Soot	CO_2 CO, H_2O, Soot			C_2H_6 H_2O, Soot		H_2O CO_2, C_2H_6	
λ (μm)	1.00		2.63		2.99	3.92		6.06		9.17		200

Table 6.3: Limits of the spectral bands for ethylene (C_2H_4).

ω (1/cm)	10000		3800		3375	2800		1650		780	50
6 Band Model	1		2		3	4			5		6
Major Species	Soot CO_2, H_2O		CO_2 H_2O, Soot		C_2H_4 Soot	CO_2 CO, H_2O, Soot			C_2H_4 H_2O, Soot		H_2O CO_2
λ (μm)	1.00		2.63		2.96	3.57		6.06		12.82	200

Table 6.4: Limits of the spectral bands for propylene (C_3H_6).

ω (1/cm)	10000		3800		3250	2600	1950		1175	50
6 Band Model	1		2		3	4		5	6	
Major Species	Soot CO_2, H_2O		CO_2 H_2O, Soot		C_3H_6 Soot	CO_2 CO, Soot		C_3H_6 H_2O, Soot	C_3H_6, H_2O CO_2	
λ (μm)	1.00		2.63		3.08	3.85	5.13		8.51	200

Table 6.5: Limits of the spectral bands for propane (C_3H_8).

ω (1/cm)	10000		3800		3350	2550		1650		1175	50
6 Band Model	1		2		3	4			5		6
Major Species	Soot CO_2, H_2O		CO_2 H_2O, Soot		C_3H_8 Soot	CO_2 CO, H_2O, Soot			C_3H_8 H_2O, Soot		H_2O CO_2
λ (μm)	1.00		2.63		2.99	3.92		6.06		8.51	200

Table 6.6: Limits of the spectral bands for heptane (C_7H_{16}).

ω (1/cm)	10000	3800	3250	2550	1775	1100	50
6 Band Model	1	2	3	4	5	6	
Major Species	Soot CO_2, H_2O	CO_2 H_2O, Soot	C_7H_{16} Soot	CO_2 CO, Soot	C_7H_{16} H_2O, Soot	H_2O CO_2	
λ (μm)	1.00	2.63	3.08	3.92	5.63	9.09	200

Table 6.7: Limits of the spectral bands for toluene (C_7H_8).

ω (1/cm)	10000	3800	3200	2550	2050	1200	50
6 Band Model	1	2	3	4	5	6	
Major Species	Soot CO_2, H_2O	CO_2 H_2O, Soot	C_7H_8 Soot	CO_2 CO, Soot	C_7H_8 H_2O, Soot	C_7H_8, H_2O CO_2	
λ (μm)	1.00	2.63	3.12	3.92	4.88	8.33	200

Table 6.8: Limits of the spectral bands for methanol (CH_3OH).

ω (1/cm)	10000	3825	3200	2600	1675	1125	50
6 Band Model	1	2	3	4	5	6	
Major Species	Soot CO_2, H_2O	CH_3OH CO_2, Soot	CH_3OH Soot	CO_2 CO, Soot	CH_3OH H_2O, Soot	CH_3OH, H_2O CO_2	
λ (μm)	1.00	2.61	3.12	3.85	5.97	8.89	200

Table 6.9: Limits of the spectral bands for methyl methacrylate (MMA).

ω (1/cm)	10000	3800	3250	2650	2050	1250	50
6 Band Model	1	2	3	4	5	6	
Major Species	Soot CO_2, H_2O	CO_2 H_2O, Soot	MMA Soot	CO_2 CO, Soot	MMA H_2O, Soot	MMA, H_2O CO_2	
λ (μm)	1.00	2.63	3.08	3.77	4.88	8.00	200

6.1.3 Correction of the Emission Source Term

In calculations of limited spatial resolution, the source term, I_b, defined in Eq. (6.6) requires special treatment in the flaming region of the fire. Typical FDS calculations use grid cells that are tens of centimeters in size, and consequently the computed temperatures constitute a bulk average for a given grid cell and are considerably lower than the maximum temperature in a diffusion flame. Because of its fourth-power dependence on the temperature, the source term must be modeled in those grid cells where combustion occurs. Elsewhere, the computed temperature is used directly to compute the source term. It is assumed that this "flaming region" is where the local heat release rate is non-zero, $\dot{q}''' > 0$. In this region, the global radiative fraction model is used. The emission source term is multiplied by a corrective factor, C:

$$I_{\mathrm{b,f}}(\mathbf{x}) = C\,\frac{\sigma\,T(\mathbf{x})^4}{\pi} \quad ; \quad C = \frac{\sum_{\dot{q}'''_{ijk}>0}\left(\chi_\mathrm{r}\,\dot{q}'''_{ijk} + \kappa_{ijk}\,U_{ijk}\right)\,\mathrm{d}V}{\sum_{\dot{q}'''_{ijk}>0}\left(4\,\kappa_{ijk}\,\sigma\,T^4_{ijk}\right)\,\mathrm{d}V} \tag{6.10}$$

When the source term defined in Eq. (6.10) is substituted into Eq. (6.8), the net radiative emission from the flaming region becomes the desired fraction of the total heat release rate.

The radiative fraction, χ_r, is a useful quantity in fire science. It is the nominal fraction of the combustion energy that is emitted as thermal radiation. For most combustibles, χ_r is between 0.3 and 0.4 [51]. However, in Eq. (6.10), χ_r is interpreted as the fraction of energy radiated from the flaming region. For a small fire with a base diameter less than approximately 1 m, the local χ_r is approximately equal to its global counterpart. However, as the fire increases in size, the global value will typically decrease due to a net re-absorption of the thermal radiation by the increasing smoke mantle [52].

6.2 Numerical Method

This section describes how $\nabla\cdot\dot{\mathbf{q}}''_\mathrm{r}$ (the radiative loss term) is computed at all gas-phase cells, and how the the radiative heat flux $\dot{q}''_\mathrm{r}$ is computed at solid boundaries.

6.2.1 Angular Discretization

To obtain the discretized form of the RTE, the unit sphere is divided into a finite number of solid angles. The coordinate system used to discretize the solid angle is shown in Figure 6.1. The discretization of the solid

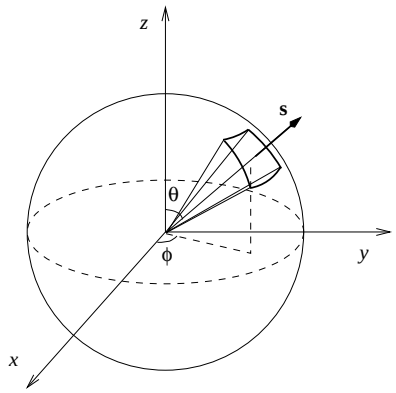

Figure 6.1: Coordinate system of the angular discretization.

angle is done by dividing first the polar angle, θ, into N_θ bands, where N_θ is an even integer. Each θ-band is then divided into $N_\phi(\theta)$ parts in the azimuthal (ϕ) direction. $N_\phi(\theta)$ must be divisible by 4. The numbers N_θ and $N_\phi(\theta)$ are chosen to give the total number of angles N_Ω as close to the value defined by the user as possible. N_Ω is calculated as

$$N_\Omega = \sum_{i=1}^{N_\theta} N_\phi(\theta_i) \tag{6.11}$$

The distribution of the angles is based on empirical rules that try to produce equal solid angles $\delta\Omega^l = 4\pi/N_\Omega$. The number of θ-bands is

$$N_\theta = 1.17\, N_\Omega^{1/2.26} \tag{6.12}$$

rounded to the nearest even integer. The number of ϕ-angles on each band is

$$N_\phi(\theta) = \max\left\{4, 0.5 N_\Omega \left[\cos(\theta^-) - \cos(\theta^+)\right]\right\} \tag{6.13}$$

rounded to the nearest integer that is divisible by 4. θ^- and θ^+ are the lower and upper bounds of the θ-band, respectively. The discretization is symmetric with respect to the planes $x = 0$, $y = 0$, and $z = 0$. This symmetry has three important benefits: First, it avoids the problems caused by the fact that the first-order upwind scheme, used to calculate intensities on the cell boundaries, is more diffusive in non-axial directions than axial. Second, the treatment of the mirror boundaries becomes very simple, as will be shown later. Third, it avoids so called "overhang" situations, where $\mathbf{s}\cdot\mathbf{i}$, $\mathbf{s}\cdot\mathbf{j}$ or $\mathbf{s}\cdot\mathbf{k}$ changes sign inside the control angle. These "overhangs" would make the resulting system of linear equations more complicated.

In the axially symmetric case these "overhangs" cannot be avoided, and a special treatment, developed by Murthy and Mathur [53], is applied. In these cases $N_\phi(\theta_i)$ is kept constant, and the total number of angles is $N_\Omega = N_\theta \times N_\phi$. In addition, the angle of the vertical slice of the cylinder is chosen to be the same as $\delta\phi$.

6.2.2 Spatial Discretization

The grid used for the RTE solver is the same as for the hydrodynamic solver. The radiative transport equation (6.2) is solved using techniques similar to those for convective transport in finite volume methods for fluid flow [54]; thus, the name given to it is the Finite Volume Method (FVM). More details of the model implementation are included in Ref. [55].

The thermal radiation spectrum is first divided into bands, as described in section 6.1. The procedure outlined below is applied for each band of a wide band model, and thus the subscript n has been removed for clarity. The unit sphere is then discretized, as described in section 6.2.1. Finally, the computational domain is divided into numerical grid as described in section 2.2. In each grid cell, a discretized equation is derived by integrating Eq. (6.2) over the volume of cell ijk and the control angle $\delta\Omega^l$, to obtain

$$\int_{\delta\Omega^l}\int_{V_{ijk}} \mathbf{s}'\cdot\nabla I(\mathbf{x}',\mathbf{s}')\,\mathrm{d}\mathbf{x}'\,\mathrm{d}\mathbf{s}' = \int_{\delta\Omega^l}\int_{V_{ijk}} \kappa(\mathbf{x}')\,\left[I_\mathrm{b}(\mathbf{x}') - I(\mathbf{x}',\mathbf{s}')\right]\,\mathrm{d}\mathbf{x}'\,\mathrm{d}\mathbf{s}' \tag{6.14}$$

The volume integral on the left hand side is replaced by a surface integral over the cell faces using the divergence theorem.

$$\int_{\delta\Omega^l}\int_{A_{ijk}} \left(\mathbf{s}'\cdot\mathbf{n}'\right) I(\mathbf{x}',\mathbf{s}')\,\mathrm{d}\mathbf{n}'\,\mathrm{d}\mathbf{s}' = \int_{\delta\Omega^l}\int_{V_{ijk}} \kappa(\mathbf{x}')\,\left[I_\mathrm{b}(\mathbf{x}') - I(\mathbf{x}',\mathbf{s}')\right]\,\mathrm{d}\mathbf{x}'\,\mathrm{d}\mathbf{s}' \tag{6.15}$$

Assuming that the radiation intensity $I(\mathbf{x},\mathbf{s})$ is constant on each of the cell faces, the surface integral can be approximated by a sum over the cell faces. Assuming further that $I(\mathbf{x},\mathbf{s})$ is constant within the volume V_{ijk} and over the angle $\delta\Omega^l$, and that $\kappa(\mathbf{x}')$ and $I_\mathrm{b}(\mathbf{x}')$ are constants within the volume V_{ijk}, we obtain

$$\sum_{m=1}^{6} A_m\, I^l_m \int_{\Omega^l} (\mathbf{s}'\cdot\mathbf{n}_m)\,\mathrm{d}\mathbf{s}' = \kappa_{ijk}\left[I_{\mathrm{b},ijk} - I^l_{ijk}\right]\, V_{ijk}\,\delta\Omega^l \tag{6.16}$$

where

I^l_{ijk}	radiant intensity in direction l
I^l_m	radiant intensity at cell face m
$I_{b,ijk}$	radiant blackbody Intensity in cell
$\delta\Omega^l$	solid angle corresponding to direction l
V_{ijk}	volume of cell ijk
A_m	area of cell face m
$\mathbf{n}_m$	unit normal vector of the cell face m

Note that while the intensity is assumed constant within the angle $\delta\Omega^l$, its direction covers the angle $\delta\Omega^l$ exactly.The local incident radiation intensity is

$$U_{ijk} = \sum_{l=1}^{N_\Omega} I^l_{ijk}\,\delta\Omega^l \tag{6.17}$$

In Cartesian coordinates[1], the normal vectors $\mathbf{n}_m$ are the base vectors of the coordinate system and the integrals over the solid angle do not depend on the physical coordinate, but the direction only. These integrals are denoted as

$$D^l_m = \int_{\Omega^l} (\mathbf{s}' \cdot \mathbf{n}_m)\,\mathrm{d}\mathbf{s}' \tag{6.18}$$

and the discrete equation becomes

$$\sum_{m=1}^{6} A_m\, I^l_m\, D^l_m = \kappa_{ijk}\left[I_{\mathrm{b},ijk} - I^l_{ijk}\right]\, V_{ijk}\,\delta\Omega^l \tag{6.19}$$

The cell face intensities, I^l_m appearing on the left hand side of (6.19) are calculated using a first order upwind scheme. Consider, for example, a control angle having a direction vector $\mathbf{s}$. If the radiation is traveling in the positive x-direction, i.e., $\mathbf{s}\cdot\mathbf{i} \geq 0$, the intensity on the upwind side, I^l_{xu} is assumed to be the intensity in the neighboring cell, $I^l_{i-1\,jk}$, and the intensity on the downwind side is the (unknown) intensity in the cell itself I^l_{ijk}. The discrete RTE can now be written using the upwind intensities I^l_{xu}, I^l_{yu} and I^l_{zu} and I^l_{ijk}:

$$\begin{aligned} &A_x\, I^l_{xu}\, D^l_{xu} + A_x\, I^l_{ijk}\, D^l_{xd} + \\ &A_y\, I^l_{yu}\, D^l_{yu} + A_y\, I^l_{ijk}\, D^l_{yd} + \\ &A_z\, I^l_{zu}\, D^l_{zu} + A_z\, I^l_{ijk}\, D^l_{zd} \\ &\qquad = \kappa_{ijk}\, I_{\mathrm{b},ijk} V_{ijk}\,\delta\Omega^l - \kappa_{ijk}\, I^l_{ijk} V_{ijk}\,\delta\Omega^l \end{aligned} \tag{6.20}$$

where the D-terms on the LHS are integrals (6.18) evaluated on upwind and downwind sides of the cell. In the rectilinear mesh, $D^l_{xu} = -D^l_{xd}$ and the equation can be simplified further. In addition, the integrals over

[1] In the axisymmetric case equation (6.16) becomes a little bit more complicated, as the cell face normal vectors $\mathbf{n}_m$ are not always constant. However, the computational efficiency can still be retained.

the solid angle can be calculated analytically

$$D_x^l = \int_{\Omega^l} (\mathbf{s}^l \cdot \mathbf{i})\, \mathrm{d}\Omega = \int_{\delta\phi}\int_{\delta\theta} (\mathbf{s}^l \cdot \mathbf{i}) \sin\theta \;\mathrm{d}\theta\,\mathrm{d}\phi = \int_{\delta\phi}\int_{\delta\theta} \cos\phi \sin\theta \sin\theta \;\mathrm{d}\theta\,\mathrm{d}\phi$$
$$= \frac{1}{2}\left(\sin\phi^+ - \sin\phi^-\right)\left[\Delta\theta - \left(\cos\theta^+\sin\theta^+ - \cos\theta^-\sin\theta^-\right)\right] \tag{6.21}$$
$$D_y^l = \int_{\Omega^l} (\mathbf{s}^l \cdot \mathbf{j})\, \mathrm{d}\Omega = \int_{\delta\phi}\int_{\delta\theta} \sin\phi \sin\theta \sin\theta \;\mathrm{d}\theta\,\mathrm{d}\phi$$
$$= \frac{1}{2}\left(\cos\phi^- - \cos\phi^+\right)\left[\Delta\theta - \left(\cos\theta^+\sin\theta^+ - \cos\theta^-\sin\theta^-\right)\right] \tag{6.22}$$
$$D_z^l = \int_{\Omega^l} (\mathbf{s}^l \cdot \mathbf{k})\, \mathrm{d}\Omega = \int_{\delta\phi}\int_{\delta\theta} \cos\theta \sin\theta \;\mathrm{d}\theta\,\mathrm{d}\phi$$
$$= \frac{1}{2}\Delta\phi\left[\left(\sin\theta^+\right)^2 - \left(\sin\theta^-\right)^2\right] \tag{6.23}$$
$$\delta\Omega^l = \int_{\Omega^l} \mathrm{d}\Omega = \int_{\delta\phi}\int_{\delta\theta} \sin\theta \;\mathrm{d}\theta\,\mathrm{d}\phi \tag{6.24}$$

Equation (6.20) for the unknown intensity I_{ijk}^l is written in the form

$$a_{ijk}^l I_{ijk}^l = a_x^l I_{xu}^l + a_y^l I_{yu}^l + a_z^l I_{zu}^l + b_{ijk}^l \tag{6.25}$$

where

$$a_{ijk}^l = A_x|D_x^l| + A_y|D_y^l| + A_z|D_z^l| + \kappa_{ijk}\, V_{ijk}\delta\Omega^l \tag{6.26}$$

$$a_x^l = A_x|D_x^l| \tag{6.27}$$
$$a_y^l = A_y|D_y^l| \tag{6.28}$$
$$a_z^l = A_z|D_z^l| \tag{6.29}$$
$$b_{ijk}^l = \kappa_{ijk}\, I_{\mathrm{b},ijk}\, V_{ijk}\, \delta\Omega^l \tag{6.30}$$

Here $\mathbf{i}$, $\mathbf{j}$ and $\mathbf{k}$ are the base vectors of the Cartesian coordinate system. θ^+, θ^-, ϕ^+ and ϕ^- are the upper and lower boundaries of the control angle in the polar and azimuthal directions, respectively, and $\Delta\theta = \theta^+ - \theta^-$ and $\Delta\phi = \phi^+ - \phi^-$.

The solution method of (6.20) is based on an explicit marching sequence [56]. The marching direction depends on the propagation direction of the radiation intensity. As the marching is done in the "downwind" direction, the "upwind" intensities in all three spatial directions are known, and the intensity I_{ijk}^l can be solved directly from an algebraic equation. In the first cell to be solved, all the upwind intensities are determined from solid or gas phase boundaries. In theory, iterations are needed if the reflections or scattering are important, or if the scenario is optically very thick. Currently, no iterations are made.

6.2.3 Boundary Conditions

The boundary condition for the radiation intensity leaving a gray diffuse wall is given as

$$I_{\mathrm{w}}(\mathbf{s}) = \frac{\varepsilon\,\sigma\,T_{\mathrm{w}}^4}{\pi} + \frac{1-\varepsilon}{\pi}\int_{\mathbf{s}'\cdot\mathbf{n}_{\mathrm{w}}<0} I_{\mathrm{w}}(\mathbf{s}')\,|\mathbf{s}'\cdot\mathbf{n}_{\mathrm{w}}|\;\mathrm{d}\mathbf{s}' \tag{6.31}$$

where $I_{\mathrm{w}}(\mathbf{s})$ is the intensity at the wall, ε is the emissivity, and T_w is the wall surface temperature. In discretized form, the boundary condition on a solid wall is given as

$$I_{\mathrm{w}}^l = \frac{\varepsilon\,\sigma\,T_{\mathrm{w}}^4}{\pi} + \frac{1-\varepsilon}{\pi}\sum_{D_{\mathrm{w}}^{l'}<0} I_{\mathrm{w}}^{l'}\,|D_{\mathrm{w}}^{l'}| \tag{6.32}$$

where $D_{\mathrm{w}}^{l'} = \int_{\Omega^{l'}} (\mathbf{s}\cdot\mathbf{n}_{\mathrm{w}})\,\mathrm{d}\Omega$. The constraint $D_{\mathrm{w}}^{l'} < 0$ means that only the "incoming" directions are taken into account when calculating the reflection. The *net* radiative heat flux on the wall is

$$\dot{q}_{\mathrm{r}}'' = \sum_{l=1}^{N_\Omega} I_{\mathrm{w}}^{l} \int_{\delta\Omega^{l}} (\mathbf{s}'\cdot\mathbf{n}_{\mathrm{w}})\,\mathrm{d}\mathbf{s}' = \sum_{l=1}^{N_\Omega} I_{\mathrm{w}}^{l} D_{n}^{l} \tag{6.33}$$

where the coefficients D_n^l are equal to $\pm D_x^l$, $\pm D_y^l$ or $\pm D_z^l$, and can be calculated for each wall element at the start of the calculation.

The open boundaries are treated as black walls, where the incoming intensity is the blackbody intensity of the ambient temperature. On mirror boundaries the intensities leaving the wall are calculated from the incoming intensities using a predefined connection matrix:

$$I_{\mathrm{w},ijk}^{l} = I^{l'} \tag{6.34}$$

Computationally intensive integration over all the incoming directions is avoided by keeping the solid angle discretization symmetric on the x, y and z planes. The connection matrix associates one incoming direction l' to each mirrored direction on each wall cell.

6.3 Absorption and Scattering of Thermal Radiation by Droplets/Particles

The attenuation of thermal radiation by liquid droplets and particles is an important consideration, especially for water mist systems [57]. Droplets and particles attenuate thermal radiation through a combination of scattering and absorption [58]. The radiation-spray interaction must therefore be solved for both the accurate prediction of the radiation field and for the particle energy balance. If the gas phase absorption and emission in Eq. (6.1) are temporarily neglected for simplicity, the radiative transport equation becomes

$$\mathbf{s}\cdot\nabla I_\lambda(\mathbf{x},\mathbf{s}) = -\Big[\kappa_{\mathrm{p}}(\mathbf{x},\lambda)+\sigma_{\mathrm{p}}(\mathbf{x},\lambda)\Big] I_\lambda(\mathbf{x},\mathbf{s}) + \kappa_{\mathrm{p}}(\mathbf{x},\lambda)\, I_{\mathrm{b,p}}(\mathbf{x},\lambda) + \frac{\sigma_{\mathrm{p}}(\mathbf{x},\lambda)}{4\pi}\int_{4\pi}\Phi(\mathbf{s},\mathbf{s}')\, I_\lambda(\mathbf{x},\mathbf{s}')\,\mathrm{d}\mathbf{s}' \tag{6.35}$$

where κ_{p} is the particle absorption coefficient, σ_{p} is the particle scattering coefficient and $I_{\mathrm{b,p}}$ is the emission term of the particles. $\Phi(\mathbf{s}',\mathbf{s})$ is a scattering phase function that gives the scattered intensity fraction from direction $\mathbf{s}'$ to $\mathbf{s}$.

6.3.1 Absorption and Scattering Coefficients

Radiation absorption and scattering by particles depends on their cross sectional areas and radiative material properties. For simplicity, we assume that the particles are spherical in shape, in which case the cross sectional area of a particle is πr^2, where r is the particle radius. If the local number density distribution of particles at location $\mathbf{x}$ is denoted by $n(r(\mathbf{x}))$, the local absorption and scattering coefficients within a spray/particle cloud can be calculated from:

$$\kappa_{\mathrm{p}}(\mathbf{x},\lambda) = \int_0^\infty n(r(\mathbf{x}))\, Q_{\mathrm{a}}(r,\lambda)\,\pi r^2\,\mathrm{d}r \tag{6.36}$$

$$\sigma_{\mathrm{p}}(\mathbf{x},\lambda) = \int_0^\infty n(r(\mathbf{x}))\, Q_{\mathrm{s}}(r,\lambda)\,\pi r^2\,\mathrm{d}r \tag{6.37}$$

where Q_{a} and Q_{s} are the absorption and scattering efficiencies, respectively. For the computation of the spray/particle cloud radiative properties, spherical particles are assumed and the radiative properties of the individual particles are computed using Mie theory.

Based on Refs. [59] and [60], the real particle size distribution inside a grid cell is modeled as a mono-disperse suspension whose diameter corresponds to the Sauter mean (d_{32}) diameter of the poly-disperse spray. This assumption leads to a simplified expression of the radiative coefficients

$$\kappa_{\mathrm{p}}(\mathbf{x},\lambda) = A_{\mathrm{p}}(\mathbf{x})\, Q_{\mathrm{a}}(r_{32},\lambda) \tag{6.38}$$

$$\sigma_{\mathrm{p}}(\mathbf{x},\lambda) = A_{\mathrm{p}}(\mathbf{x})\, Q_{\mathrm{s}}(r_{32},\lambda) \tag{6.39}$$

These expressions are functions of the total cross sectional area per unit volume of the droplets, A_{p}, which is computed simply by summing the cross sectional areas of all the droplets within a cell and dividing by the cell volume. For practical reasons, a relaxation factor of 0.5 is used to smooth slightly the temporal variation of A_{p}.

6.3.2 Approximating the In-Scattering Integral

An accurate computation of the in-scattering integral on the right hand side of Eq. (6.35) would be extremely time consuming and require a prohibitive amount of memory because the individual intensities in each location would have to be stored. Instead, a simplified form of Eq. (6.35) can be derived:

$$\mathbf{s}\cdot\nabla I_{\lambda}(\mathbf{x},\mathbf{s}) = -\left[\kappa_{\mathrm{p}}(\mathbf{x},\lambda)+\overline{\sigma}_{\mathrm{p}}(\mathbf{x},\lambda)\right] I_{\lambda}(\mathbf{x},\mathbf{s}) + \kappa_{\mathrm{p}}(\mathbf{x},\lambda)\, I_{\mathrm{b,p}}(\mathbf{x},\lambda) + \frac{\overline{\sigma}_{\mathrm{p}}(\mathbf{x},\lambda)}{4\pi} U(\mathbf{x},\lambda) \tag{6.40}$$

where $U(\mathbf{x})$ is the total intensity integrated over the unit sphere and $\overline{\sigma}_{\mathrm{p}}$ is an effective scattering coefficient. The derivation of Eq. (6.40) is given in Appendix J. This simplified equation can be integrated over the spectrum to get the band specific RTE's. The procedure is exactly the same as that used for the gas phase RTE. After the band integrations, the spray RTE for band n becomes:

$$\mathbf{s}\cdot\nabla I_{n}(\mathbf{x},\mathbf{s}) = -\left[\kappa_{\mathrm{p},n}(\mathbf{x})+\overline{\sigma}_{\mathrm{p},n}(\mathbf{x})\right] I_{n}(\mathbf{x},\mathbf{s}) + \kappa_{\mathrm{p},n}(\mathbf{x})\, I_{\mathrm{b,p},n}(\mathbf{x}) + \frac{\overline{\sigma}_{\mathrm{p},n}(\mathbf{x})}{4\pi} U_{n}(\mathbf{x}) \tag{6.41}$$

where the source function is based on the average particle temperature within a cell.

6.3.3 Forward Fraction of Scattering

The effective scattering coefficient in Eq. (6.40) is defined:

$$\overline{\sigma}_{\mathrm{p}}(\mathbf{x},\lambda) = \frac{4\pi}{4\pi-\delta\Omega^{l}}\Big(1-\chi_{\mathrm{f}}(\mathbf{x},\lambda)\Big)\,\sigma_{\mathrm{p}}(\mathbf{x},\lambda) \tag{6.42}$$

where χ_{f} is the fraction of the total intensity originally within the solid angle $\delta\Omega^{l}$ that is scattered into the same angle, $\delta\Omega^{l}$. The computation of χ_{f} has been derived in Ref. [61]. It can be shown that here χ_{f} becomes:

$$\chi_{\mathrm{f}}(r,\lambda) = \frac{1}{\delta\Omega^{l}}\int_{\mu^{l}}^{1}\int_{\mu^{l}}^{1}\int_{\mu_{\mathrm{p},0}}^{\mu_{\mathrm{p},\pi}} \frac{P_0(\theta_{\mathrm{p}},\lambda)}{\left[(1-\mu^2)(1-\mu'^2)-(\mu_{\mathrm{p}}-\mu\mu')^2\right]^{1/2}}\,\mathrm{d}\mu_{\mathrm{p}}\,\mathrm{d}\mu\,\mathrm{d}\mu' \tag{6.43}$$

where μ_{p} is a cosine of the scattering angle θ_{p} and $P_0(\theta_{\mathrm{p}},\lambda)$ is a single droplet scattering phase function

$$P_0(\theta_{\mathrm{p}},\lambda) = \frac{\lambda^2\left(|S_1(\theta_{\mathrm{p}})|^2+|S_2(\theta_{\mathrm{p}})|^2\right)}{2\,Q_{\mathrm{s}}(r,\lambda)\pi r^2} \tag{6.44}$$

$S_1(\theta_{\mathrm{p}})$ and $S_2(\theta_{\mathrm{p}})$ are the scattering amplitudes, given by Mie-theory. The integration limit, μ^{l}, is a cosine of the polar angle defining the boundary of the symmetric control angle, $\delta\Omega^{l}$

$$\mu^{l} = \cos(\theta^{l}) = 1-\frac{2}{N_{\Omega}} \tag{6.45}$$

The limits of the innermost integral are

$$\mu_{\mathrm{p},0} = \mu\mu' + \sqrt{1-\mu^2}\sqrt{1-\mu'^2} \quad ; \quad \mu_{\mathrm{p},\pi} = \mu\mu' - \sqrt{1-\mu^2}\sqrt{1-\mu'^2} \tag{6.46}$$

6.3.4 Solution Procedure

The absorption and scattering coefficients, κ_p and $\overline{\sigma}_p$ are not repeatedly calculated during the simulation. Instead, they are tabulated at the beginning of the simulation for each band and a range of different Sauter mean diameters, r_{32}. The averaged quantities, now functions r_{32} only, are stored in one-dimensional arrays. During the simulation, the local properties are found by table look-up.

In the band integration of κ_p and $\overline{\sigma}_p$, a constant "radiation" temperature, T_{rad}, is used to provide the wavelength weighting (Planck function). T_{rad} should be selected to represent a typical radiating flame temperature. A value of 1173 K is used by default.

The absorption and scattering efficiencies, Q_a and Q_s, and the scattering phase function $P_0(\theta_p, \lambda)$, are calculated using the MieV code developed by Wiscombe [62]. The spectral properties of the particles can be specified in terms of a wavelength-dependent complex refractive index. Pre-compiled data are included for water and a generic hydrocarbon fuel based on diesel fuel and heptane. For water, the values of the imaginary part of the complex refractive index (related to the absorption coefficient) are taken from Ref. [63], and a value of 1.33 is used for the real part. For fuel, the droplet spectral properties are taken from Ref. [64], which includes measurements of the refractive index of a diesel fuel and a comparison of the values with those of heptane. The diesel properties are used for the real part of the refractive index. For the complex part, the heptane properties are used to avoid the uncertainty associated with different types of diesel fuels. Usually, the radiative properties of the particle cloud are more sensitive to the particle size and concentration than to values of the refractive index.

6.3.5 Heat absorbed by droplets

The droplet contribution to the radiative loss term is

$$-\nabla\cdot\dot{\mathbf{q}}_r''(\mathbf{x})(\text{droplets}) = \kappa_p(\mathbf{x})\left[U(\mathbf{x}) - 4\pi I_{b,p}(\mathbf{x})\right] \tag{6.47}$$

For each individual droplet, the radiative heating/cooling power is computed as

$$\dot{q}_r = \frac{m_p}{\rho_p(\mathbf{x})}\kappa_p(\mathbf{x})\left[U(\mathbf{x}) - 4\pi I_{b,p}(\mathbf{x})\right] \tag{6.48}$$

where m_p is the mass of the droplet and $\rho_p(\mathbf{x})$ is the total density of droplets in the cell.

Chapter 7

Solid Phase

FDS assumes that solid surfaces consist of multiple layers, with each layer composed of multiple material components that can undergo multiple thermal degradation reactions. Heat conduction is assumed only in the direction normal to the surface. Each reaction can produce multiple gas and solid species. This chapter describes the heat conduction equation for solid materials, plus the various coefficients, source terms, and boundary conditions, including the computation of the convective heat flux $\dot{q}''_{\rm c}$ at solid boundaries.

7.1 The Heat Conduction Equation for a Solid

The one-dimensional heat conduction equation for the solid phase temperature $T_{\rm s}(x,t)$ is applied in the direction x pointing into the solid (the point $x = 0$ represents the surface)[1]

$$\rho_{\rm s} c_{\rm s} \frac{\partial T_{\rm s}}{\partial t} = \frac{\partial}{\partial x}\left(k_{\rm s}\frac{\partial T_{\rm s}}{\partial x}\right) + \dot{q}'''_{\rm s} \tag{7.2}$$

Section 7.1.3 describes the component-averaged material properties, $k_{\rm s}$ and $\rho_{\rm s} c_{\rm s}$. The source term, $\dot{q}'''_{\rm s}$, consists of chemical reactions and radiative absorption:

$$\dot{q}'''_{\rm s} = \dot{q}'''_{\rm s,c} + \dot{q}'''_{\rm s,r} \tag{7.3}$$

Section 7.2 describes the term $\dot{q}'''_{\rm s,c}$, which is essentially the heat production (loss) rate given by the pyrolysis models for different types of solid and liquid fuels. Section 7.1.1 describes the term $\dot{q}'''_{\rm s,r}$, the radiative absorption and emission in depth.

The boundary condition on the front surface of a solid obstruction is

$$-k_{\rm s}\frac{\partial T_{\rm s}}{\partial x}(0,t) = \dot{q}''_{\rm c} + \dot{q}''_{\rm r} \tag{7.4}$$

where $\dot{q}''_{\rm c}$ is the convective and $\dot{q}''_{\rm r}$ the radiative flux. If the radiation is assumed to penetrate in depth, the surface radiation term, $\dot{q}''_{\rm r}$, is set to 0. Section 7.1.2 describes the convective heat transfer to the solid surface.

On the back surface, there are two possible boundary conditions: (1) if the back surface is assumed to be open either to an ambient void or to another part of the computational domain, the back side boundary

[1] In cylindrical and spherical coordinates, the heat conduction equation is written

$$\rho_{\rm s} c_{\rm s} \frac{\partial T_{\rm s}}{\partial t} = \frac{1}{r}\frac{\partial}{\partial r}\left(r\,k_{\rm s}\frac{\partial T_{\rm s}}{\partial r}\right) + \dot{q}'''_{\rm s} \quad ; \quad \rho_{\rm s} c_{\rm s} \frac{\partial T_{\rm s}}{\partial t} = \frac{1}{r^2}\frac{\partial}{\partial r}\left(r^2\,k_{\rm s}\frac{\partial T_{\rm s}}{\partial r}\right) + \dot{q}'''_{\rm s} \tag{7.1}$$

FDS offers the user these options for cases where the obstruction surface is not flat, but rather cylindrical or spherical in shape. This option is useful in describing the behavior of small, complicated "targets" like cables or heat detection devices.

condition is similar to that of the front side, or (2) if the back side is assumed to be perfectly insulated, an adiabatic condition is used

$$-k_s \frac{\partial T_s}{\partial x} = 0 \tag{7.5}$$

The numerical solution of the solid phase heat equation is presented in detail in Appendix L.

7.1.1 Radiation Heat Transfer to Solids

If it is assumed that the thermal radiation from the surrounding gases is absorbed within an infinitely thin layer at the surface of the solid obstruction, then the net radiative heat flux is the sum of incoming and outgoing components, $\dot{q}''_r = \dot{q}''_{r,in} - \dot{q}''_{r,out}$:

$$\dot{q}''_{r,in} = \varepsilon \int_{\mathbf{s}'\cdot\mathbf{n}_w<0} I_w(\mathbf{s}') \, |\mathbf{s}'\cdot\mathbf{n}_w| \, d\Omega \tag{7.6}$$

$$\dot{q}''_{r,out} = \varepsilon \sigma T_w^4 \tag{7.7}$$

However, many common materials are not opaque; thus, the radiation penetrates the material to some finite depth. The radiative transport within the solid (or liquid) can be described as a source term in Eq. (7.2). A "two-flux" model based on the Schuster-Schwarzschild approximation [48] assumes the radiative intensity is constant inside the "forward" and "backward" hemispheres. The transport equation for the intensity in the "forward" direction is

$$\frac{1}{2}\frac{dI^+(x)}{dx} = \kappa_s \left(I_b - I^+(x)\right) \tag{7.8}$$

where x is the distance from the material surface and κ_s is the component-averaged absorption coefficient:

$$\kappa_s = \sum_{\alpha=1}^{N_m} X_\alpha \, \kappa_{s,\alpha} \tag{7.9}$$

A corresponding formula can be given for the "backward" direction. Multiplying Eq. 7.8 by π gives us the "forward" radiative heat flux into the solid

$$\frac{1}{2}\frac{d\dot{q}^+_r(x)}{dx} = \kappa_s \left(\sigma T_s^4 - \dot{q}^+_r(x)\right) \tag{7.10}$$

The radiative source term in the heat conduction equation is the sum of the "forward" and "backward" flux gradients

$$\dot{q}'''_{s,r}(x) = \frac{d\dot{q}^+_r(x)}{dx} + \frac{d\dot{q}^-_r(x)}{dx} \tag{7.11}$$

The boundary condition for Eq. 7.10 at the solid (or liquid) surface is given by

$$\dot{q}^+_r(0) = \dot{q}''_{r,in} + (1-\varepsilon)\,\dot{q}^-_r(0) \tag{7.12}$$

where $\dot{q}^-_r(0)$ is the "backward" radiative heat flux at the surface. In this formulation, the surface emissivity and the internal absorption are assumed constant.

The two-flux model has not been adapted for cylindrical or spherical geometry.

7.1.2 Convective Heat Transfer to Solids

The calculation of the convective heat flux depends on whether one is performing a direct numerical simulation (DNS) or a large eddy simulation (LES). For DNS, the convective heat transfer is calculated directly from the resolved gas and solid phase variables. For LES, there are a variety of empirical options.

Direct Numerical Simulation

In a DNS calculation, the convective heat flux to a solid surface $\dot{q}''_c$ is obtained directly from the gas temperature gradient at the boundary

$$\dot{q}''_c = -k\,\frac{\partial T}{\partial n} = -k\frac{T_w - T_g}{\delta n/2} \tag{7.13}$$

where k is the thermal conductivity of the gas, n is the spatial coordinate pointing into the solid, δn is the normal grid spacing, T_g is the gas temperature in the center of the first gas phase cell, and T_w is the wall surface temperature.

Empirical Natural/Forced Convection Model

In an LES calculation, the convective heat transfer coefficient, h, is based on a combination of natural and forced convection correlations:

$$\dot{q}''_c = h\,(T_g - T_w) \quad \mathrm{W/m^2} \quad ; \quad h = \max\left[\,C\,|T_g - T_w|^{\frac{1}{3}}\,,\ \frac{k}{L}\,\mathrm{Nu}\right] \quad \mathrm{W/(m^2\cdot K)} \tag{7.14}$$

where C is a empirical coefficient for natural convection (1.52 for a horizontal plate and 1.31 for a vertical plane or cylinder) [65], L is a characteristic length related to the size of the physical obstruction, and k is the thermal conductivity of the gas. The Nusselt number (Nu) depends on the geometric and flow characteristics. For many flow regimes, it has the form:

$$\mathrm{Nu} = C_1 + C_2\,\mathrm{Re}^n\,\mathrm{Pr}^m \quad ; \quad \mathrm{Re} = \frac{\rho|\mathbf{u}|L}{\mu} \quad ; \quad \mathrm{Pr} \approx 0.7 \tag{7.15}$$

For planar and cylindrical surfaces, the default values are $C_1 = 0$, $C_2 = 0.037$, $n = 0.8$, $m = 0.33$, and $L = 1$ m. For spherical surfaces, the default values are $C_1 = 2$, $C_2 = 0.6$, $n = 0.5$, $m = 0.33$, and $L = D$, the diameter of the sphere. Note that for a sphere, the coefficient for natural convection, C, is assumed to be zero. It is possible to change these values for a particular application, but it is not possible to find a set of parameters that is appropriate for the wide variety of scenarios considered. Various correlations for planes, cylinders, and spheres can be found in Refs. [65, 66].

Optional Near-Wall Model

This section describes an optional model for the heat transfer coefficient which may be more appropriate for well-resolved LES calculations. This model has been validated for low Reynolds number heated channel flow [67] and has been used in a model to predict upper layer temperature in airplane cargo compartments [68].

Wall models aim to mimic the sudden change from molecular to turbulent transport close to the walls using algebraic formulations without resolving the smallest length scales. The theory follows dimensional analysis based on the idea that shear at the wall is constant. Accordingly, non-dimensional velocity can be defined as a function of non-dimensional length scale. In FDS, the wall model for velocity is implemented based on the law of the wall with a semi-log fit connecting the limits of the viscous and log regions (see Section 4.4).

By analogy to the near-wall model for velocity, the non-dimensional temperature is defined as

$$T^+ = \frac{T_g - T_w}{T_\tau} \tag{7.16}$$

where T_g is the first off-wall gas-phase cell temperature. The model profile is given by

$$T^+ = \mathrm{Pr}\, y^+ \qquad \text{for} \quad y^+ \le 11.81 \tag{7.17}$$

$$T^+ = \frac{\mathrm{Pr}_t}{\kappa} \ln y^+ + B_T \qquad \text{for} \quad y^+ \ge 11.81 \tag{7.18}$$

where Pr and Pr_t are the molecular and turbulent Prandtl numbers ($\mathrm{Pr}_t = 0.5$ by default in FDS), and $\kappa = 0.41$ is the von Kármán constant. The temperature scale, T_τ, is defined by

$$T_\tau \equiv \frac{\dot{q}''_c}{\rho c_p u_\tau} \tag{7.19}$$

where $\dot{q}''_c$, ρ, and c_p are the convective heat flux at the wall, the gas density, and the specific heat, respectively.

The second term, B_T, on the right hand side of Eq. 7.18 is a function of the molecular Prandtl number and can be determined experimentally. Mathematically, this term is the integration constant stemming from the relation between velocity and temperature gradients. Physically, it represents the resistance to the heat and momentum transport close to the wall. FDS uses the experimental correlation proposed by Kader [69]

$$B_T = (3.85\,\mathrm{Pr}^{1/3} - 1.3)^2 + 2.12 \ln \mathrm{Pr} \tag{7.20}$$

The convective heat transfer coefficient (h) is obtained from the definition of h and T^+:

$$h = \frac{\dot{q}''_c}{(T_g - T_w)} = \frac{\rho c_p u_\tau}{T^+} \tag{7.21}$$

7.1.3 Component-Averaged Thermal Properties

The conductivity and volumetric heat capacity of the solid are defined as

$$k_s = \sum_{\alpha=1}^{N_m} X_\alpha\, k_{s,\alpha} \quad ; \quad \rho_s c_s = \sum_{\alpha=1}^{N_m} \rho_{s,\alpha}\, c_{s,\alpha} \tag{7.22}$$

where N_m is the number of material components forming the solid, X_α is the volume fraction of component α, and $\rho_{s,\alpha}$ is the *component density:*

$$\rho_{s,\alpha} = \rho_s Y_\alpha \tag{7.23}$$

where ρ_s is the density of the composite material and Y_α is the mass fraction of component α. The solid density is the sum of the component densities

$$\rho_s = \sum_{\alpha=1}^{N_m} \rho_{s,\alpha} \tag{7.24}$$

and the volume fraction of component α is computed as

$$X_\alpha = \frac{\rho_{s,\alpha}}{\rho_\alpha} \Bigg/ \sum_{\alpha'=1}^{N_m} \frac{\rho_{s,\alpha'}}{\rho_{\alpha'}} \tag{7.25}$$

where ρ_α is the true density of material α. Multi-component solids are defined by specifying the mass fractions, Y_α, and densities, ρ_α, of the individual components of the composite.

7.2 Pyrolysis Models

This section describes how solid phase reactions and the chemical source term in the solid phase heat conduction equation, $\dot{q}'''_{s,c}$, are modeled. This is commonly referred to as the "pyrolysis model," but it actually can represent any number of reactive processes, including evaporation, charring, and internal heating.

7.2.1 Specified Heat Release Rate

Often the intent of a fire simulation is merely to predict the transport of smoke and heat from a *specified* fire. In other words, the heat release rate is a specified input, not something the model predicts. In these instances, the desired HRR is translated into a mass flux for fuel at a given solid surface, which can be thought of as the surface of a burner:

$$\dot{m}''_{\mathrm{f}} = \frac{f(t)\ \dot{q}''_{\mathrm{user}}}{\Delta H_{\mathrm{c}}} \tag{7.26}$$

Usually, the user specifies a desired heat release rate per unit area, $\dot{q}''_{\mathrm{user}}$, plus a time ramp, $f(t)$, and the mass loss rate is computed accordingly.

7.2.2 Solid Fuels

Solids can undergo simultaneous reactions under the following assumptions:

- instantaneous release of gas species
- local thermal equilibrium between the solid and gaseous components
- no condensation of gaseous products
- no porosity effects[2]

Each material component may undergo several competing reactions, and each of these reactions may produce some other solid component (residue) and gaseous species according to specified yield coefficients. These coefficients should sum to 1, but yields summing to less than 1 can account for products that are not explicitly included in the simulation.

The local density of material component α evolves in time according to the solid phase species conservation equation

$$\frac{\partial}{\partial t}\left(\frac{\rho_{\mathrm{s},\alpha}}{\rho_{\mathrm{s}}(0)}\right) = -\sum_{\beta=1}^{N_{\mathrm{r},\alpha}} r_{\alpha\beta} + S_{\alpha} \tag{7.27}$$

where $N_{\mathrm{r},\alpha}$ is the number of reactions for material α, $r_{\alpha\beta}$ is the rate of reaction β in units of 1/s, and $\rho_{\mathrm{s}}(0)$ is the initial density of the material layer. S_{α} is the production rate of material component α as a result of the reactions of the other components. The reaction rates are functions of solid and gas phase conditions and calculated as a combination of Arrhenius and power functions:

$$r_{\alpha\beta} = \underbrace{\left(\frac{\rho_{\mathrm{s},\alpha}}{\rho_{\mathrm{s}}(0)}\right)^{n_{\mathrm{s},\alpha\beta}}}_{\text{Reactant dependency}}\ \underbrace{A_{\alpha\beta}\ \exp\left(-\frac{E_{\alpha\beta}}{RT_{\mathrm{s}}}\right)}_{\text{Arrhenius function}}\ \underbrace{\left[X_{\mathrm{O_2}}(x)\right]^{n_{\mathrm{O_2},\alpha\beta}}}_{\text{Oxidation function}}\ \underbrace{\max\left[0, S_{\mathrm{thr},\alpha,\beta}(T_{\mathrm{s}} - T_{\mathrm{thr},\alpha\beta})\right]^{n_{\mathrm{t},\alpha\beta}}}_{\text{Power function}} \tag{7.28}$$

The first term describes the dependence of the reaction rate on the concentration of the reactant itself, with $n_{\mathrm{s},\alpha\beta}$ being the partial reaction order. The second term is the Arrhenius function which is commonly used

[2] Although porosity is not explicitly included in the model, it is possible to account for it because the volume fractions defined by Eq. (7.25) need not sum to unity, in which case the thermal conductivity and absorption coefficient are effectively reduced.

to describe the reaction kinetics, i.e. the dependence of the reaction rate on the material temperature. The chapter on pyrolysis in the FDS Verification Guide describes methods for determining the kinetic parameters $A_{\alpha\beta}$ and $E_{\alpha\beta}$ using bench-scale measurement techniques.

The third term can be used to describe the dependence on the local oxygen concentration $X_{O_2}(x)$ and the heterogeneous reaction order, $n_{O_2,\alpha\beta}$. The oxygen concentration profile within practical materials depends on the competetion between diffusion and reactive consumption. As FDS does not solve for the transport of gaseous species within concensed phase materials, a simple exponential profile is assumed and the user is expected to specify the characteristic depth at which oxygen would be present. The local oxygen volume fraction at depth x is calculated from the gas phase (first grid cell) oxygen volume fraction $X_{O_2,g}$ as

$$X_{O_2}(x) = X_{O_2,g} \exp(-x/L_{g,\alpha\beta}) \tag{7.29}$$

where $L_{g,\alpha\beta}$ is the characteristic depth of oxygen diffusion. Specifying $L_{g,\alpha\beta} = 0$ means that the reaction takes place only at the surface of the material.

The fourth term is the power function where $T_{thr,\alpha\beta}$ is a threshold temperature that can be used to dictate that the reaction must not occur below ($S_{thr,\alpha,\beta} = +1$) or above ($S_{thr,\alpha,\beta} = -1$) a user-specified temperature. By default, the fourth term is deactivated ($S_{thr,\alpha,\beta} = +1, T_{thr,\alpha\beta} = 0$ K).

Note that the solid species conservation equation 7.27 and the reaction rate equation 7.28 are inconsistent with the common practice of chemical kinetics convention, where the unit of the reaction rate is usually kg/(m$^3 \cdot$ s) or mol/(m$^3 \cdot$ s). The current form can be obtained by dividing a more conventional reaction rate equation by $\rho_s(0)$. This form is very close to the form used in [70] with the exception that initial layer density $\rho_s(0)$ is used for scaling instead of the instantaneous value.

The production term S_α is the sum over all the reactions where the solid residue is material α

$$S_\alpha = \sum_{\alpha'=1}^{N_m} \sum_{\beta=1}^{N_{r,\alpha'}} \nu_{\alpha,\alpha'\beta}\, r_{\alpha'\beta} \qquad \text{(where Residue}_{\alpha'\beta} = \text{Material}_\alpha\text{)} \tag{7.30}$$

where $\nu_{\alpha,\alpha'\beta}$ is the yield of component α from reaction β of component α'. The volumetric production rate of each gas species, γ, is

$$\dot{m}'''_\gamma = \rho_s(0) \sum_{\alpha=1}^{N_m} \sum_{\beta=1}^{N_{r,\alpha}} \nu_{\gamma,\alpha\beta}\, r_{\alpha\beta} \tag{7.31}$$

It is assumed that the gases are transported instantaneously to the surface, where the mass fluxes are given by[3]

$$\dot{m}''_\gamma = \int_0^L \dot{m}'''_\gamma(x)\, \mathrm{d}x \tag{7.33}$$

where L is the thickness of the solid. The chemical source term in the heat conduction equation is

$$\dot{q}'''_{s,c}(x) = -\rho_s(0) \sum_{\alpha=1}^{N_m} \sum_{\beta=1}^{N_{r,\alpha}} r_{\alpha\beta}(x) H_{r,\alpha\beta} \tag{7.34}$$

where $H_{r,\alpha\beta}$ is the heat of reaction.

[3] In cylindrical and spherical coordinates, the mass fluxes are

$$\dot{m}''_\gamma = \frac{1}{R_{out}} \int_{R_{in}}^{R_{out}} \dot{m}'''_\gamma(x)\, r\, \mathrm{d}r \;\; ; \;\; \dot{m}''_\gamma = \frac{1}{R_{out}^2} \int_{R_{in}}^{R_{out}} \dot{m}'''_\gamma(x)\, r^2\, \mathrm{d}r \tag{7.32}$$

7.2.3 Phase Change Reactions

To describe freezing or melting of liquids, the two phases are separated by a sharp interface at the constant phase-change temperature, T_f. The location of the phase boundary x_f is governed by the equation

$$k_{\mathrm{s},1}\frac{\partial T_{\mathrm{s},1}}{\partial x} - k_{\mathrm{s},2}\frac{\partial T_{\mathrm{s},2}}{\partial x} = \rho_\mathrm{s} H_{\mathrm{r},\alpha\beta}\frac{\partial x_\mathrm{f}}{\partial t} \tag{7.35}$$

where 1 and 2 refer to the materials on the two sides of the boundary. In the context of the fixed-grid finite-difference method, it is more convenient to allow a small deviation from T_f and solve for the amount of mass reacting during the time step, Δt, from the energy required to convert the mass from one phase to the other

$$\dot{m}'''\Delta t = \frac{\rho_\mathrm{s} c_\mathrm{s}(T_\mathrm{s} - T_\mathrm{f})}{H_{\mathrm{r},\alpha\beta}} \tag{7.36}$$

This reaction can be implemented by setting $T_{\mathrm{thr},\alpha\beta} = T_\mathrm{f}$ and $A_{\alpha\beta} = c_\mathrm{s}$ and turning on a specific *phase-change reaction* mode. The reaction rate given by Eq. 7.28 is then divided by the factor $H_{\mathrm{r},\alpha\beta}\Delta t$.

7.2.4 Liquid Fuels

The rate at which liquid fuel evaporates when burning is a function of the liquid temperature and the concentration of fuel vapor above the pool surface. According to the Clausius-Clapeyron relation, the volume fraction of the fuel vapor above the surface is a function of the liquid boiling temperature

$$X_{\mathrm{F},\ell} = \exp\left[-\frac{h_\mathrm{v} W_\mathrm{F}}{R}\left(\frac{1}{T_\mathrm{s}} - \frac{1}{T_\mathrm{b}}\right)\right] \tag{7.37}$$

where h_v is the heat of vaporization, W_F is the molecular weight of the fuel gas, T_s is the surface temperature, and T_b is the boiling temperature of the fuel [71]. The evaporation rate of the fuel is governed by Stefan diffusion [72]:

$$\dot{m}'' = h_\mathrm{m}\frac{\overline{p}_m W_\mathrm{F}}{R T_\mathrm{g}}\ln\left(\frac{X_{\mathrm{F,g}} - 1}{X_{\mathrm{F},\ell} - 1}\right) \quad ; \quad h_\mathrm{m} = \frac{\mathrm{Sh}\, D_{\ell,\mathrm{g}}}{L} \tag{7.38}$$

where $\overline{p}_m$ is the pressure, T_g is the temperature, and $X_{\mathrm{F,g}}$ is the volume fraction of fuel vapor in the grid cell adjacent to the pool surface. The Sherwood number is given by

$$\mathrm{Sh} = 0.037\,\mathrm{Sc}^{\frac{1}{3}}\mathrm{Re}^{\frac{4}{5}} \quad ; \quad \mathrm{Sc} = 0.6 \quad ; \quad \mathrm{Re} = \frac{\rho\,||\mathbf{u}||\,L}{\mu} \tag{7.39}$$

The Reynolds number is calculated based on conditions in the cell adjacent to the surface. The length scale, L, used in calculating the Reynolds number is 1 m unless otherwise specified and is the same length scale used for the convective heat transfer calculation.

For simplicity, the liquid fuel itself is treated like a thermally-thick solid for the purpose of computing the heat conduction. There is no computation of the convection of the liquid within the pool.

7.2.5 Shrinking and Swelling Materials

The layer thickness is updated according to the ratio of the instantaneous material density and the density of the material in its pure form. In case of several material components, the amount of swelling and shrinking is determined by the maximum and sum of these ratios, respectively. In each time step, the size of each condensed phase cell is multiplied by the following factor:

$$\delta = \begin{cases} \max_\alpha\left(\frac{\rho_{\mathrm{s},\alpha}}{\rho_\alpha}\right) & \text{if } \max_\alpha\left(\frac{\rho_{\mathrm{s},\alpha}}{\rho_\alpha}\right) \geq 1 \\ \sum_\alpha\left(\frac{\rho_{\mathrm{s},\alpha}}{\rho_\alpha}\right) & \text{if } \max_\alpha\left(\frac{\rho_{\mathrm{s},\alpha}}{\rho_\alpha}\right) < 1 \end{cases} \tag{7.40}$$

Correspondingly, the densities are divided by the factor δ to conserve mass.

7.3 Aerosol Deposition

By default, FDS assumes that soot is transported just like all other gaseous species. That is, the soot particles are small enough that their settling velocity is small compared to the fire-driven flows of the gas containing the soot. Near surfaces, however, other mechanisms can affect the soot, which results in its deposition onto surfaces. The removal of soot via deposition can impact the visibility for egress and the time for smoke detectors to activate. In forensic fire reconstructions, the amount of soot deposited on surfaces can be correlated to post-fire observations. The deposition of particulates is also important for computing the dispersion characteristics of aerosol toxicants like ash, radionuclides, or other particulate matter.

However, there is an option to treat any gas phase species as an aerosol that can be deposited on surfaces. Aerosol deposition is determined by applying an empirical deposition velocity to aerosols near surfaces. There are a number of phenomena that cause deposition: thermophoresis (where temperature gradients push the aerosol towards or away from the surface), gravitational settling, diffusive deposition (where the aerosols move along the boundary layer concentration gradient), and turbulent deposition (essentially impact deposition due to a turbulent boundary layer). Other phenomena, such as electrical fields, can also result in deposition but are not considered in FDS due to their relatively small contribution in compartment fire scenarios.

The total aerosol deposition velocity to surfaces, $u_{\rm dep}$, is determined by assuming the deposition phenomena are independent, computing a deposition velocity for each mechanism, and then summing them [73]

$$u_{\rm dep} = u_{\rm g} + u_{\rm th} + u_{\rm dt} \tag{7.41}$$

where $u_{\rm g}$ is the gravitational settling velocity (for cells near upward-facing surfaces), $u_{\rm th}$ is the thermophoretic velocity, and $u_{\rm dt}$ is the combined diffusion-turbulence velocity. If the aerosol is located in a gas-phase cell adjacent to a wall, then the aerosol (represented by the subscript α) is removed from the gas-phase and deposited onto the surface by imposing the following boundary condition

$$\dot{m}''_{{\rm dep},\alpha} = \rho Y_\alpha \, u_{\rm dep} \tag{7.42}$$

Using this boundary condition, the aerosol surface density that accumulates on surfaces is tracked, and the amount of aerosol that deposits to a surface is removed from the adjacent gas-phase cell. Note that the subscript α refers to a species that contains soot or aerosol, whereas the subscript 'a' in the remainder of the section refers to the condensed phase soot or aerosol properties, such as mass or density.

7.3.1 Gravitational Settling

The gravitational settling velocity is given by [74]

$$u_{\rm g} = g m_{\rm a} \frac{\rm Cn}{6\pi \chi_{\rm d} \mu r_{\rm a}} \tag{7.43}$$

where $m_{\rm a}$ is the particle mass, $\chi_{\rm d}$ is a shape factor, μ is the dynamic viscosity of air, r_a is the particle radius, and Cn is the Cunningham slip correction factor given by [75]

$${\rm Cn} = 1 + 1.25\ {\rm Kn} + 0.41\ {\rm Kn}\ {\rm e}^{-0.88/{\rm Kn}} \tag{7.44}$$

where Kn is the particle Knudsen number given by the ratio of the mean free path of the gas to the particle radius. The mean free path of a gas is proportional to its temperature, thus Kn is computed as [76]

$${\rm Kn} = \frac{\lambda}{r_{\rm a}} \frac{T_{\rm g}}{T_\infty} \tag{7.45}$$

where λ is the mean free path of gas molecules and is 0.065 μm at a temperature of 25 °C and atmospheric pressure.

For each aerosol species in the gas phase, a gravitational settling velocity is calculated and imposed on the convective term (in the z-direction) in the species transport equation (Eq. 3.6). This approach is similar to the drift flux model for smoke transport described in Hu et al. [77]. The gravitational settling velocity is also included in the total deposition velocity to deposit aerosols onto upward-facing flat surfaces, as described above.

7.3.2 Thermophoretic Deposition

The thermophoretic velocity is computed as

$$u_{\text{th}} = \frac{K_{\text{th}} \nu}{T_{\text{g}}} \frac{\mathrm{d}T}{\mathrm{d}x} \tag{7.46}$$

This requires the wall temperature gradient, which is only resolved in a DNS simulation. For an LES simulation, the temperature gradient is computed from the wall heat transfer coefficient.

$$\frac{\mathrm{d}T}{\mathrm{d}x} = \frac{h\left(T_{\text{g}} - T_{\text{w}}\right)}{k_{\text{g}}} \tag{7.47}$$

K_{th} is the thermophoretic velocity coefficient and is calculated using the following correlation [78]

$$K_{\text{th}} = \frac{2C_{\text{s}}\left(\alpha + C_{\text{t}}\,\text{Kn}\right)\,\text{Cn}}{\left(1+3C_{\text{m}}\,\text{Kn}\right)\left(1+2\alpha+2C_{\text{t}}\,\text{Kn}\right)} \tag{7.48}$$

where $C_{\text{s}} = 1.17$ is the thermal slip coefficient, α is the ratio of the gas conductivity to the particle conductivity, $C_{\text{m}} = 1.14$ is the momentum accommodation coefficient, and $C_{\text{t}} = 2.18$ is the thermal accommodation coefficient.

7.3.3 Turbulent Deposition

The diffusion-turbulence deposition velocity depends upon the flow regime (diffusion, diffusion-impaction, or inertia-moderated). The deposition velocity for these regimes is given below [79].

$$u_{\text{dt}} = \begin{cases} 0.086\,\text{Sc}^{-0.7}\,u_\tau & \tau^+ < 0.2 \\ 3.5\times10^{-4}\,\tau^{+2}\,u_\tau & 0.2 < \tau^+ < 22.9 \\ 0.17\,u_\tau & \tau^+ > 22.9 \end{cases} \tag{7.49}$$

where Sc is the particle Schmidt number, or the ratio of the kinematic viscosity to the Brownian diffusion coefficient of the particle (ν/D_{B}), u_τ is the wall friction velocity computed by the wall model, and τ^+ is the dimensionless stopping distance given by [80]

$$\tau^+ = \frac{\rho_{\text{a}}\left(2r_{\text{a}}\right)^2}{18\mu^2}\,u_\tau^2\,\rho_{\text{g}} \tag{7.50}$$

Chapter 8

Lagrangian Particles

Lagrangian particles are used to represent a wide variety of objects that cannot be resolved on the numerical grid. Liquid droplets are the most common example. This chapter outlines the treatment of the transport, size distribution, and mass, momentum and energy transfer to and from Lagrangian particles.

8.1 Particle Transport in the Gas Phase

In the gas phase momentum equation, Eq. (4.33), the force term $\mathbf{f}_\mathrm{b}$ represents the momentum transferred from particles to the gas. It is obtained by summing the force transferred from each particle in a grid cell and dividing by the cell volume, V:

$$\mathbf{f}_\mathrm{b} = \frac{1}{V}\sum\left[\frac{1}{2}\rho C_\mathrm{d} A_\mathrm{p}(\mathbf{u}_\mathrm{p}-\mathbf{u})|\mathbf{u}_\mathrm{p}-\mathbf{u}| - \frac{\mathrm{d}m_\mathrm{p}}{\mathrm{d}t}(\mathbf{u}_\mathrm{p}-\mathbf{u})\right] \tag{8.1}$$

where C_d is the drag coefficient, A_p is the particle cross-sectional area, r_p is the particle radius, $\mathbf{u}_\mathrm{p}$ is the particle velocity, m_p is the particle mass, $\mathbf{u}$ is the gas velocity, and ρ is the gas density. The particle acceleration is given by

$$\frac{\mathrm{d}\mathbf{u}_\mathrm{p}}{\mathrm{d}t} = \mathbf{g} - \frac{1}{2}\frac{\rho C_\mathrm{d} A_\mathrm{p}}{m_\mathrm{p}}(\mathbf{u}_\mathrm{p}-\mathbf{u})|\mathbf{u}_\mathrm{p}-\mathbf{u}| \tag{8.2}$$

The particle position, $\mathbf{x}_\mathrm{p}$, is determined from the equation

$$\frac{\mathrm{d}\mathbf{x}_\mathrm{p}}{\mathrm{d}t} = \mathbf{u}_\mathrm{p} \tag{8.3}$$

The exact solution procedure of the above model is presented in Appendix I. The drag coefficient (default based on a sphere) is a function of the local Reynolds number that is based on the particle diameter, D

$$C_\mathrm{d} = \begin{cases} 24/\mathrm{Re}_D & \mathrm{Re}_D < 1 \\ 24\left(0.85 + 0.15\,\mathrm{Re}_D^{0.687}\right)/\mathrm{Re}_D & 1 < \mathrm{Re}_D < 1000 \\ 0.44 & 1000 < \mathrm{Re}_D \end{cases} \tag{8.4}$$

$$\mathrm{Re}_D = \frac{\rho\,|\mathbf{u}_\mathrm{p}-\mathbf{u}|\,2r_\mathrm{p}}{\mu(T)} \tag{8.5}$$

where $\mu(T)$ is the dynamic viscosity of air at temperature T. For cylindrical particles,

$$C_\mathrm{d} = \begin{cases} 10/\mathrm{Re}_D^{0.8} & \mathrm{Re}_D < 1 \\ 10\left(0.6+0.4\mathrm{Re}_D^{0.8}\right)/\mathrm{Re}_D & 1 < \mathrm{Re}_D < 1000 \\ 1 & 1000 < \mathrm{Re}_D \end{cases} \tag{8.6}$$

Additional corrections are made to account for drag reduction due to the wake effect [81] and deformation of the droplet [82].

8.1.1 Drag Reduction

Typically, Lagrangian particle models only consider two-way coupling between the gas and particles. This means that each particle interacts with the carrier fluid individually. Momentum lost from a particle is added to the fluid and vice versa. If the spray is dense enough, however, the individual particles influence each other through aerodynamic interactions. These effects cannot be captured by the current Eulerian-Lagrangian model for two reasons. First, the Lagrangian particles occupy no volume in the Eulerian space. Second, the separation lengths would be of sub-grid scale in most practical simulations. The aerodynamic interactions start to have an effect when the average particle spacing is less than 10 diameters [83, 84]. This corresponds to a particle volume fraction, α, of approximately 0.01. Volume fractions as high as this can sometimes be achieved inside water mist sprays. If the spray is even more dense, particle-particle collisions or four-way coupling would need to be considered.

In a configuration where two particles with the same diameter are directly in line, the reduction of the drag force on the second particle can be modeled by the following [81]:

$$C_\mathrm{d} = C_{\mathrm{d},0}\frac{F}{F_0} \tag{8.7}$$

where $C_{\mathrm{d},0}$ is the single particle drag coefficient and F/F_0 is the hydrodynamic force ratio of the trailing particle to an isolated particle:

$$\frac{F}{F_0} = W\left[1+\frac{\mathrm{Re}}{16}\frac{1}{(L/D-1/2)^2}\exp\left(-\frac{\mathrm{Re}}{16}\frac{1}{(L/D-1/2)}\right)\right] \tag{8.8}$$

where Re is the single particle Reynolds number, L is the distance between the particles, and W is the non-dimensional, non-disturbed wake velocity at the center of the trailing particle

$$W = 1-\frac{C_{\mathrm{d},0}}{2}\left[1-\exp\left(-\frac{\mathrm{Re}}{16}\frac{1}{(L/D-1/2)}\right)\right] \tag{8.9}$$

This model assumes that the spheres are traveling directly in-line with each other. As such, this provides an upper bound for the strength of the aerodynamic interactions between two particles of the same size. The separation distance L/D between particle centers is calculated from the local particle volume fraction and local average particle diameter $\bar{D}$

$$L/D = \bar{D}(\pi/6\alpha)^{\frac{1}{3}} \tag{8.10}$$

Here, local quantities are averaged over a single computational cell.

In reality, the spray is not monodisperse and the separation distance between the interacting particles varies. In the simulation, the drag reduction factor in Eq. 8.7 is only used when the local droplet volume fraction exceeds 1×10^{-5}. The drag reduction model is turned on by default.

An alternative approach to drag reduction was provided by Prahl et al. [83] who studied the interaction between two solid spheres in steady or pulsating flow by detailed numerical simulations. According to their study, the above correlation under-estimates the drag reduction significantly at small drop-to-drop distances. The inflow pulsations were found to reduce the effect of the drag reduction. At large distances, the two results are similar, the Ramírez-Muñoz correlation showing more drag reduction. This is not surprising since the velocity profile of a fully developed axi-symmetric wake behind an axi-symmetric body is used in developing the drag reduction correction in Eqs. 8.8 and 8.9. At short distances, the wake is not fully developed and the assumption does not hold.

8.2 Liquid Droplet Size Distribution

The cumulative volume distribution for a liquid spray is represented by a combination of lognormal and Rosin-Rammler distributions [85]:

$$F_{\rm v}(D) = \begin{cases} \frac{1}{\sqrt{2\pi}} \int_0^D \frac{1}{\sigma D'} \exp\left(-\frac{[\ln(D'/D_{\rm v,0.5})]^2}{2\sigma^2}\right) \, {\rm d}D' & (D \le D_{\rm v,0.5}) \\ 1 - \exp\left(-0.693 \left(\frac{D}{D_{\rm v,0.5}}\right)^{\gamma}\right) & (D_{\rm v,0.5} < D) \end{cases} \tag{8.11}$$

where $D_{\rm v,0.5}$ is the median volumetric droplet diameter (i.e., half the mass is carried by droplets with diameters of $D_{\rm v,0.5}$ or less), and γ and σ are empirical constants equal to approximately 2.4 and 0.6, respectively.[1] Alternatively, the user may specify any form of size distribution using the tabulated input data.

The median droplet diameter is a function of the sprinkler orifice diameter, operating pressure, and geometry. Research at Factory Mutual has yielded a correlation for the median droplet diameter [86]

$$\frac{D_{\rm v,0.5}}{d} \propto {\rm We}^{-\frac{1}{3}} \tag{8.12}$$

where d is the orifice diameter of the nozzle. The orifice Weber number, the ratio of inertial forces to surface tension forces, is given by

$${\rm We} = \frac{\rho_{\rm p} u_{\rm p}^2 d}{\sigma} \tag{8.13}$$

where $\rho_{\rm p}$ is the liquid density, $u_{\rm p}$ is the discharge velocity, and σ is the liquid surface tension (72.8×10^{-3} N/m at 20 °C for water). The discharge velocity can be computed from the mass flow rate, a function of the operating pressure and orifice coefficient known as the K-factor. FM reports that the constant of proportionality in Eq. (8.12) appears to be independent of flow rate and operating pressure. Three different sprinklers were tested in their study with orifice diameters of 16.3 mm, 13.5 mm, and 12.7 mm, and the constants were approximately 4.3, 2.9, and 2.3, respectively. The strike plates of the two smaller sprinklers were notched, while that of the largest sprinkler was not [86].

In real sprinkler systems, the operating pressure is affected by the number of open nozzles. Typically, the pressure in the piping is high when the first sprinkler activates, and decreases when more and more sprinkler heads are activated. The pipe pressure has an effect on flow rate, droplet velocity and droplet size distribution. FDS does not predict the variation of pipe pressure; it should be specified by the user. The following dependencies are used to update the droplet boundary conditions for mass flow, droplet speed, and median diameter:

$$\dot{m}_{\rm p} \propto p^{1/2} \quad ; \quad u_{\rm p} \propto p^{1/2} \quad ; \quad D_{\rm v,0.5} \propto p^{-1/3} \tag{8.14}$$

[1] The Rosin-Rammler and lognormal distributions are smoothly joined if $\sigma = 2/(\sqrt{2\pi}\,(\ln 2)\,\gamma) = 1.15/\gamma$.

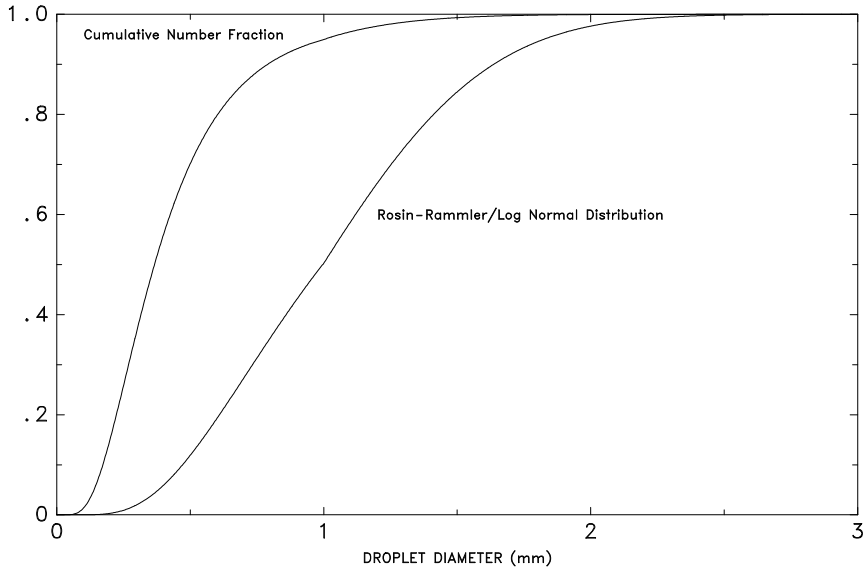

Figure 8.1: Cumulative Volume Fraction and Cumulative Number Fraction functions of the droplet size distribution from a typical industrial-scale sprinkler. The median volumetric diameter, $D_{\mathrm{v},0.5}$, is 1 mm, $\sigma = 0.6$ and $\gamma = 2.4$.

The droplet diameters are randomly chosen from the given size distribution. The cumulative number fraction (CNF), F_{n}, is determined from the cumulative volume fraction, F_{v}, as follows

$$F_{\mathrm{n}}(D) = \int_0^D \frac{F'_{\mathrm{v}}(D')}{D'^3}\,\mathrm{d}D' \Bigg/ \int_0^\infty \frac{F'_{\mathrm{v}}(D')}{D'^3}\,\mathrm{d}D' \quad ; \quad F'_{\mathrm{v}} \equiv \frac{\mathrm{d}F_{\mathrm{v}}}{\mathrm{d}D} \tag{8.15}$$

Figure 8.1 displays the Rosin-Rammler/lognormal function and the resulting cumulative number fraction.

The selection of droplet diameters makes use of a stratified sampling technique to ensure that the droplets span the entire range of sizes, even with a relatively small number of droplets. Without the stratification, the tails of the distribution can be poorly represented. The procedure for selecting droplet sizes is as follows:

1. Suppose that the mass flow rate of the liquid is $\dot{m}$, that the time interval for droplet insertion is δt, and that the number of droplets inserted each time interval is N.

2. Divide the droplet diameter range into a number of bins of equal width (7 by default).

3. Randomly choose N integers, n_i, ranging from 1 to the total number of bins.

4. Choose N uniformly distributed real numbers between 0 and 1 and calculate N random droplet diameters:

$$D_i = F_{\mathrm{n}}^{-1}\left[F_{\mathrm{n}}(D_{n_i,\min}) + \mathscr{U}(0,1)\left(F_{\mathrm{n}}(D_{n_i,\max}) - F_{\mathrm{n}}(D_{n_i,\min})\right)\right] \tag{8.16}$$

   where $\mathscr{U}(0,1)$ is a uniformly distributed real number between 0 and 1 and $D_{n_i,\min}$ and $D_{n_i,\max}$ are the minimum and maximum diameters of bin n_i.

5. Compute weighting constants for each droplet $C_i = F_{\mathrm{n}}(D_{n_i,\max}) - F_{\mathrm{n}}(D_{n_i,\min})$.

6. Compute a global weighting constant, C, to maintain the overall mass balance:

$$\dot{m}\,\delta t = C\sum_{i=1}^{N} C_i\,\frac{4}{3}\pi\rho_{\mathrm{p}}\left(\frac{D_i}{2}\right)^3 \tag{8.17}$$

The mass and heat transferred from each droplet will be multiplied by the weighting factor C.

8.3 Spray Initialization

The droplets are introduced into the simulation along a spherical surface whose diameter is a specified stand-off distance from the nozzle orifice. It is assumed that the droplets have fully atomized by this stage. The longitude of the initial droplet position, $0 \le \theta < 2\pi$, is randomly chosen from a uniform distribution. The latitude, $0 \le \phi < \pi$, is randomly selected from the following distribution:

$$f(\phi) = \exp\left[-\beta\left(\frac{\phi-\phi_{\min}}{\phi_{\max}-\phi_{\min}}\right)^2\right] \tag{8.18}$$

Note that $\phi = 0$ is the south pole of the sphere. The spread parameter, β, is 5 by default. All the droplets are given the same initial speed in the direction of the surface normal.

8.4 Heating and Evaporation of Liquid Droplets

Liquid droplets can represent either discrete airborne spheres or elements of the thin liquid film that forms on wetted solids. These film "droplets" are still individually tracked as Lagrangian particles, but the heat and mass transfer coefficients are different. In the discussion to follow, the term "droplets" will be used to describe either form.

Over the course of a time step of the gas phase solver, the droplets in a given grid cell evaporate to form the gas species α. The evaporation rate is a function of the liquid equilibrium vapor mass fraction, $Y_{\alpha,\ell}$, the local gas phase vapor mass fraction, $Y_{\alpha,\mathrm{g}}$, the (assumed uniform) droplet temperature, T_{p}, and the local gas temperature, T_{g}. The subscript "g" refers to the average of the quantity in the cell occupied by the droplet. The subscript "p" refers to the liquid droplet. If the droplet is attached to a solid, T_{s} is the surface temperature. The mass and energy transfer between the gas and the liquid can be described by the following set of equations [87]

$$\frac{\mathrm{d}m_{\mathrm{p}}}{\mathrm{d}t} = -A_{\mathrm{p}}\,h_{\mathrm{m}}\,\rho_{\mathrm{g}}\,(Y_{\alpha,\ell}-Y_{\alpha,\mathrm{g}}) \tag{8.19}$$

$$\frac{\mathrm{d}T_{\mathrm{p}}}{\mathrm{d}t} = \frac{1}{m_{\mathrm{p}}\,c_{\mathrm{p}}}\left[A_{\mathrm{p}}\,h\,(T_{\mathrm{g}}-T_{\mathrm{p}}) + \dot{q}_{\mathrm{r}} + \frac{\mathrm{d}m_{\mathrm{p}}}{\mathrm{d}t}\,h_{\mathrm{v}}\right] \tag{8.20}$$

Here, m_{p} is the mass of the liquid droplet (or that fraction of the surface film associated with the formerly airborne droplet), A_{p} is the surface area of the liquid droplet, h_{m} is the mass transfer coefficient to be discussed below, ρ_{g} is the gas density, c_{p} is the liquid specific heat, h is the heat transfer coefficient between the droplet and the gas, $\dot{q}_{\mathrm{r}}$ is the rate of radiative heating of the droplet, and h_{v} is the latent heat of vaporization of the liquid. The vapor mass fraction of the gas, $Y_{\alpha,\mathrm{g}}$, is obtained from the gas phase mass transport equations, and the liquid equilibrium vapor mass fraction is obtained from the Clausius-Clapeyron equation

$$X_{\alpha,\ell} = \exp\left[\frac{h_{\mathrm{v}}\,W_\alpha}{R}\left(\frac{1}{T_{\mathrm{b}}}-\frac{1}{T_{\mathrm{p}}}\right)\right] \quad ; \quad Y_{\alpha,\ell} = \frac{X_{\alpha,\ell}}{X_{\alpha,\ell}\,(1-W_{\mathrm{a}}/W_\alpha)+W_{\mathrm{a}}/W_\alpha} \tag{8.21}$$

where $X_{\alpha,\ell}$ is the equilibrium vapor *volume* fraction, W_α is the molecular weight of the gaseous species α, W_a is the molecular weight of air, R is the universal gas constant, and T_b is the boiling temperature of the liquid at standard atmospheric pressure.

Mass and heat transfer between liquid and gas are described with analogous empirical correlations. The mass transfer coefficient, h_m, is described by the empirical relationships [66]:

$$h_\mathrm{m} = \frac{\mathrm{Sh}\, D_{\ell\mathrm{g}}}{L} \quad ; \quad \mathrm{Sh} = \begin{cases} 2 + 0.6\, \mathrm{Re}_D^{\frac{1}{2}}\, \mathrm{Sc}^{\frac{1}{3}} & \text{droplet} \\ \\ 0.037\, \mathrm{Re}_L^{\frac{4}{5}}\, \mathrm{Sc}^{\frac{1}{3}} & \text{film} \end{cases} \tag{8.22}$$

Sh is the Sherwood number, $D_{\ell\mathrm{g}}$ is the binary diffusion coefficient between the liquid vapor and the surrounding gas (usually assumed air), L is a length scale equal to either the droplet diameter or 1 m for a surface film, Re_D is the Reynolds number of the droplet (based on the diameter, D, and the relative air-droplet velocity), Re_L is the Reynolds number based on the length scale L, and Sc is the Schmidt number ($\nu / D_{\ell\mathrm{g}}$, assumed 0.6 for all cases).

An analogous relationship exists for the heat transfer coefficient [66]:

$$h = \frac{\mathrm{Nu}\, k}{L} \quad ; \quad \mathrm{Nu} = \begin{cases} 2 + 0.6\, \mathrm{Re}_D^{\frac{1}{2}}\, \mathrm{Pr}^{\frac{1}{3}} & \text{gas-droplet} \\ \\ 0.037\, \mathrm{Re}_L^{\frac{4}{5}}\, \mathrm{Pr}^{\frac{1}{3}} & \text{gas-film} \end{cases} \tag{8.23}$$

Nu is the Nusselt number, k is the thermal conductivity of the gas, and Pr is the Prandtl number (assumed 0.7 for all cases). In cases where the droplet is actually a portion of the liquid film attached to a solid surface, half of the droplet mass is heated or cooled by the solid surface and half is heated or cooled by the gas.

The exchange of mass and energy between liquid droplets and the surrounding gases (or solid surfaces) is computed droplet by droplet. After the temperature of each droplet is computed, the appropriate amount of vaporized liquid is added to the given mesh cell, and the cell gas temperature is reduced slightly based on the energy lost to the droplet.

Equation (8.20) is solved semi-implicitly over the course of a gas phase time step as follows:

$$\frac{T_\mathrm{p}^{n+1} - T_\mathrm{p}^n}{\delta t} = \frac{1}{m_\mathrm{p}\, c_\mathrm{p}} \left[A_\mathrm{p}\, h \left(T_\mathrm{g} - \frac{T_\mathrm{p}^{n+1} + T_\mathrm{p}^n}{2} \right) - A_\mathrm{p}\, h_\mathrm{m}\, \rho_\mathrm{g} \left(\frac{Y_{\alpha,\ell}^{n+1} + Y_{\alpha,\ell}^n}{2} - Y_{\alpha,\mathrm{g}} \right) h_\mathrm{v} \right] \tag{8.24}$$

The equilibrium vapor mass fraction, $Y_{\alpha,\ell}^n$, is computed using T_p^n via Eq. (8.21), and its value at the next time step is approximated via

$$Y_{\alpha,\ell}^{n+1} \approx Y_{\alpha,\ell}^n + \left(\frac{\mathrm{d}Y_{\alpha,\ell}}{\mathrm{d}T_\mathrm{p}} \right)^n \left(T_\mathrm{p}^{n+1} - T_\mathrm{p}^n \right) \tag{8.25}$$

where the derivative of $Y_{\alpha,\ell}$ with respect to temperature is obtained via the chain rule:

$$\frac{\mathrm{d}Y_{\alpha,\ell}}{\mathrm{d}T_\mathrm{p}} = \frac{\mathrm{d}Y_{\alpha,\ell}}{\mathrm{d}X_{\alpha,\ell}} \frac{\mathrm{d}X_{\alpha,\ell}}{\mathrm{d}T_\mathrm{p}} = \frac{W_\mathrm{a}/W_\alpha}{(X_{\alpha,\ell}(1 - W_\mathrm{a}/W_\alpha) + W_\mathrm{a}/W_\alpha)^2} \frac{h_\mathrm{v} W_\alpha}{R\, T_\mathrm{p}^2} \exp\left[\frac{h_\mathrm{v}\, W_\alpha}{R} \left(\frac{1}{T_\mathrm{b}} - \frac{1}{T_\mathrm{p}} \right) \right] \tag{8.26}$$

The amount of evaporated liquid is given by

$$\delta m_\mathrm{p} = -\delta t\, A_\mathrm{p}\, h_m\, \rho_\mathrm{g} \left[Y_{\alpha,\ell}^n + \frac{1}{2} \left(\frac{\mathrm{d}Y_{\alpha,\ell}}{\mathrm{d}T_\mathrm{p}} \right)^n \left(T_\mathrm{p}^{n+1} - T_\mathrm{p}^n \right) - Y_{\alpha,\mathrm{g}} \right] \tag{8.27}$$

The amount of heat extracted from the gas is

$$\delta q = \delta t\, A_\mathrm{p}\, h \left(T_\mathrm{g} - \frac{T_\mathrm{p}^n + T_\mathrm{p}^{n+1}}{2} \right) \tag{8.28}$$

8.5 Fire Suppression by Water

The previous sections describe heat transfer from a liquid droplet to a gas, a solid, or both. Although there is some uncertainty in the values of the respective heat transfer coefficients, the fundamental physics are fairly well understood. However, when the droplets encounter burning surfaces, simple heat transfer correlations become more difficult to apply. The reason for this is that the water is not only cooling the surface and the surrounding gas, but it is also changing the pyrolysis rate of the fuel. If the surface of the fuel is planar, it is possible to characterize the decrease in the pyrolysis rate as a function of the decrease in the total heat feedback to the surface. Unfortunately, most fuels of interest in fire applications are multi-component solids with complex geometry at scales unresolvable by the computational grid.

8.5.1 Droplet Transport on a Surface

When a liquid droplet hits a solid horizontal surface, it is assigned a random horizontal direction and moves at a fixed velocity until it reaches the edge, at which point it drops straight down at the same fixed velocity. This "dripping" velocity has been measured for water to be on the order of 0.5 m/s [88, 89]. While attached to a surface, the "droplet" is assumed to form a thin film of liquid that transfers heat to the solid, and heat and mass to the gas. The film thickness, δ, is given by

$$\delta = \max\left(\delta_{\min}, \sum \frac{4}{3}\frac{\pi r_{\rm p}^3}{A}\right) \tag{8.29}$$

where A is the area of the wall cell to which the droplet is attached. It is assumed that the minimum film thickness, $\delta_{\min}$, is 1×10^{-5} m. This prevents a very small amount of liquid from spreading across the entire cell width. It is also assumed that the liquid is opaque with regard to thermal radiation.

8.5.2 Reduction of Pyrolysis Rate due to Water

To date, most of the work in this area has been performed at Factory Mutual. An important paper on the subject is by Yu *et al.* [90]. The authors consider dozens of rack storage commodity fires of different geometries and water application rates, and characterize the suppression rates in terms of a few global parameters. Their analysis yields an expression for the total heat release rate from a rack storage fire after sprinkler activation

$$\dot{Q} = \dot{Q}_0\, \mathrm{e}^{-k(t-t_0)} \tag{8.30}$$

where $\dot{Q}_0$ is the total heat release rate at the time of application t_0, and k is a fuel-dependent constant. This analysis is based on global water flow and burning rates. Equation (8.30) accounts for both the cooling of non-burning surfaces as well as the decrease in heat release rate of burning surfaces. In the FDS model, the cooling of unburned surfaces and the reduction in the heat release rate are computed locally. Thus, it is awkward to apply a global suppression rule. However, the exponential nature of suppression by water is observed both locally and globally, thus it is assumed that the local heat release rate per unit area can be expressed in the form [88, 89]

$$\dot{q}''(t) = \dot{q}_0''(t)\, \mathrm{e}^{-\int k(t)\,\mathrm{d}t} \tag{8.31}$$

where $\dot{q}_0''(t)$ is the burning rate per unit area of the fuel when no water is applied and $k(t)$ is a linear function of the local water mass per unit area, $m_{\rm w}''$, expressed in units of kg/m^2,

$$k(t) = a\, m_{\rm w}''(t) \quad \mathrm{s}^{-1} \tag{8.32}$$

Note that a is an empirical constant that is dependent on the material properties of the solid fuel and its geometrical configuration.

8.6 Using Lagrangian Particles to Model Complex Objects

There are many real objects that participate in a fire that cannot be modeled easily as solid obstructions that conform to the rectilinear mesh. For example, electrical cables, dry brush, tree branches, and so on, are potential fuels that cannot be well-represented as solid cubes, not only because the geometry is wrong, but also because the solid restricts the movement of hot gases through the complex collection of objects. Additionally objects such as window screens also impose flow restrictions but are typically not resolvable in an engineering calculation. As a potential remedy for the problem, these objects can be modeled as discrete particles that are either spheres, cylinders or small sheets. Each particle can be assigned a surface type in much the same way as is done for solid obstructions that conform to the numerical grid. The particle is assumed to be thermally-thick, but for simplicity the heat conduction within the particle is assumed to be one-dimensional in either a cylindrical, spherical or cartesian coordinate system.

It is assumed that the particles interact with the surrounding gas via an additional source term in the energy conservation equation. For a grid cell with indices ijk, the source term is:

$$\dot{q}'''_{\mathrm{r},ijk} \equiv (-\nabla\cdot\dot{\mathbf{q}}''_{\mathrm{r}})_{ijk} = \sum \kappa_{\mathrm{p}} \left(U_{ijk} - 4\sigma T_{\mathrm{p}}^4\right) \tag{8.33}$$

where the summation is over all the particles within the cell. The effective absorption coefficient for a single particle is given by

$$\kappa_{\mathrm{p}} = \frac{A}{4\,\delta x\,\delta y\,\delta z} \tag{8.34}$$

where A is the surface area of the particle and $\delta x\,\delta y\,\delta z$ is the volume of the cell. The net radiative heat flux onto the surface of the particle is

$$\dot{q}''_{\mathrm{r,p}} = \varepsilon\left(\frac{U_{ijk}}{4} - \sigma T_{\mathrm{p}}^4\right) \tag{8.35}$$

8.6.1 Porous Media (Screens, Metal Meshes, and Similar Materials)

Catwalk grating, expanded metal mesh, window screens, and similar thin porous materials are commonly found in buildings. For a typical calculation, the dimensions of the holes in the porous material and the material surrounding them are going to be much smaller than the grid size. There is, therefore, no easy way to model these materials using solid obstructions. Lagrangian particles can; however, be used to represent both the drag and the mass of these materials. Lagrangian particles arranged in a plane can represent a window screen, for example. By modifying the particle drag law, the particles can impose drag appropriate for a thin porous material. The pressure drop across a screen of thickness l is given by [91]:

$$\frac{\Delta p}{l} = \frac{\mu}{K}u + \rho\frac{Y}{\sqrt{K}}u^2 \tag{8.36}$$

where K is a permeability constant, Y is an inertial constant, u is the velocity normal to the screen, ρ is the density, and μ is the viscosity of the gas. K and Y are functions of the screen porosity (free area/total area), ϕ:

$$K = 3.44\times10^{-9}\;\phi^{1.6}\;\;\mathrm{m}^2 \quad ; \quad Y = 0.043\,\phi^{2.13} \tag{8.37}$$

The force vector $\mathbf{f}_{\mathrm{b}}$ in Eq. (4.33) represents the momentum transferred from the screen to the gas:

$$\mathbf{f}_{\mathrm{b}} = l\left(\frac{\mu}{K} + \rho\frac{Y}{\sqrt{K}}|\mathbf{u}|\right)\left(\frac{u}{\delta x}, \frac{v}{\delta y}, \frac{w}{\delta z}\right) \tag{8.38}$$

This force term essentially spreads the pressure drop over the width of a grid cell.

8.7 Turbulent Dispersion

The effect of subgrid-scale turbulent fluid motion on the velocity and position of a Lagrangian particle may be accounted for using a random walk model [92]. The position of a tracer particle obeys the stochastic differential equation

$$\mathrm{d}\mathbf{x}^* = \left[\tilde{\mathbf{u}} + \frac{1}{\bar{\rho}}\nabla(\bar{\rho}\,D_t)\right]\mathrm{d}t + \sqrt{2D_t}\,\mathrm{d}\mathbf{W} \tag{8.39}$$

where $\mathbf{x}^*$ denotes the particle position (an asterisk signifies a particle property), $\tilde{\mathbf{u}}$ is the resolved LES velocity, D_t is the turbulent diffusivity (taken from an eddy viscosity model, for example), and $\mathbf{W}$ is an independent Wiener process. Notice that if no turbulent diffusion exists, the particle follows the resolved flow. The term added to the resolved velocity accounts for the deterministic mean drift and the random walk term (Wiener process) accounts for the reorientation effect of unresolved turbulent motion.

For those unfamiliar with stochastic differential equations, the Wiener process may be understood numerically as $\mathrm{dW}(t) = (\delta t)^{1/2}\,\zeta(t)$ in the limit $\delta t \to 0$, where $\zeta(t)$ is an independent standardized Gaussian random variable [14]. In FDS, $\zeta(t)$ are generated from a Box-Muller transform [93].

Chapter 9

Fire Detection Devices

FDS predicts the thermal environment resulting from a fire, but it relies on empirical models that describe the activation of various fire detection devices. These models are described in this section.

9.1 Sprinklers

The temperature of the sensing element (or "link") of an automatic fire sprinkler is estimated from the differential equation put forth by Heskestad and Bill [94], with the addition of a term to account for the cooling of the link by water droplets in the gas stream from previously activated sprinklers

$$\frac{\mathrm{d}T_l}{\mathrm{d}t} = \frac{\sqrt{|\mathbf{u}|}}{\mathrm{RTI}}(T_g - T_l) - \frac{C}{\mathrm{RTI}}(T_l - T_m) - \frac{C_2}{\mathrm{RTI}}\beta|\mathbf{u}| \tag{9.1}$$

where $\mathbf{u}$ is the gas velocity, RTI is the response time index, T_l is the link temperature, T_g is the gas temperature in the neighborhood of the link, T_m is the temperature of the sprinkler mount (assumed ambient), and β is the volume fraction of (liquid) water in the gas stream. The sensitivity of the sprinkler link is characterized by its RTI value. The amount of heat conducted away from the link by the mount is indicated by the "C-Factor", C. The RTI and C-Factor are determined experimentally. The constant C_2 has been empirically determined by DiMarzo and co-workers [95, 96, 97] to be 6×10^6 K/(m/s)$^{1/2}$, and its value is relatively constant for different types of sprinklers.

The algorithm for heat detector activation is exactly the same as for sprinkler activation, except there is no accounting for conductive losses or droplet cooling. Note that neither the sprinkler nor heat detector models account for thermal radiation.

9.2 Heat Detectors

As far as FDS is concerned, a heat detector is just a sprinkler with no water spray. In other words, the activation of a heat detector is governed by Eq. (9.1), but with just the first term on the right hand side:

$$\frac{\mathrm{d}T_l}{\mathrm{d}t} = \frac{\sqrt{|\mathbf{u}|}}{\mathrm{RTI}}(T_g - T_l) \tag{9.2}$$

Both the RTI and activation temperature are determined empirically.

9.3 Smoke Detectors

An informative discussion of the issues associated with smoke detection can be found in the SFPE Handbook chapter "Design of Detection Systems," by Schifiliti, Meacham, and Custer [98]. The authors point out that the difficulty in modeling smoke detector activation stems from a number of issues: (1) the production and transport of smoke in the early stage of a fire are not well-understood, (2) detectors often use complex response algorithms rather than simple threshold or rate-of-change criteria, (3) detectors can be sensitive to smoke particle number density, size distribution, refractive index, composition, etc., and (4) most computer models, including FDS, do not provide detailed descriptions of the smoke besides its bulk transport. This last point is the most important. At best, in its present form, FDS can only calculate the velocity and smoke concentration of the ceiling jet flowing past the detector. Regardless of the detailed mechanism within the device, any activation model included within FDS can only account for the entry resistance of the smoke due to the geometry of the detector. Issues related to the effectiveness of ionization or photoelectric detectors cannot be addressed by FDS.

Consider the simple idealization of a "spot-type" smoke detector. A disk-shaped cover lined with a fine mesh screen forms the external housing of the device, which is usually mounted on the ceiling. Somewhere within the device is a relatively small sensing chamber where the smoke is actually detected in some way. A simple model of this device has been proposed by Heskestad [98]. He suggested that the mass fraction of smoke in the sensing chamber of the detector Y_c lags behind the mass fraction in the external free stream Y_e by a time period $\delta t = L/u$, where u is the free stream velocity and L is a length characteristic of the detector geometry. The change in the mass fraction of smoke in the sensing chamber can be found by solving the following equation:

$$\frac{\mathrm{d}Y_c}{\mathrm{d}t} = \frac{Y_e(t) - Y_c(t)}{L/\mathbf{u}} \tag{9.3}$$

The detector activates when Y_c rises above a detector-specific threshold.

A more detailed model of smoke detection involving two filling times rather than one has also been proposed. Smoke passing into the sensing chamber must first pass through the exterior housing, then it must pass through a series of baffles before arriving at the sensing chamber. There is a time lag associated with the passing of the smoke through the housing and also the entry of the smoke into the sensing chamber. Let δt_e be the characteristic filling time of the entire volume enclosed by the external housing. Let δt_c be the characteristic filling time of the sensing chamber. Cleary *et al.* [99] suggested that each characteristic filling time is a function of the free-stream velocity u outside the detector

$$\delta t_e = \alpha_e u^{\beta_e} \quad ; \quad \delta t_c = \alpha_c u^{\beta_c} \tag{9.4}$$

The α and β parameters are empirical constants related to the specific detector geometry. Suggested values for these parameters are listed in the FDS User's Guide [3]. The change in the mass fraction of smoke in the sensing chamber Y_c can be found by solving the following equation:

$$\frac{\mathrm{d}Y_c}{\mathrm{d}t} = \frac{Y_e(t - \delta t_e) - Y_c(t)}{\delta t_c} \tag{9.5}$$

where Y_e is the mass fraction of smoke outside of the detector in the free-stream. A simple interpretation of the equation is that the concentration of the smoke that enters the sensing chamber at time t is that of the free-stream at time $t - \delta t_e$.

An analytical solution for Eq. (9.5) can be found, but it is more convenient to simply integrate it numerically as is done for sprinklers and heat detectors. Then, the predicted mass fraction of smoke in the sensing chamber $Y_c(t)$ can be converted into an expression for the percent obscuration per unit length by computing:

$$\text{Obscuration} = \left(1 - \mathrm{e}^{-K_m \rho Y_c l}\right) \times 100 \ \ \% \text{ per length } l \tag{9.6}$$

where K_m is the mass extinction coefficient, ρ is the density of the external gases in the ceiling jet, and l is the unit of length over which the light is attenuated[1]. For most flaming fuels, a suggested value for K_m is 8700 m^2/kg $\pm$ 1100 m^2/kg at a wavelength of 633 nm [100].

The SFPE Handbook [98] has references to various studies on smoke detection and suggested values for the characteristic length L. FDS includes the one-parameter Heskestad model as a special case of the four-parameter Cleary model. For the Cleary model, the user must specify α_e, β_e, α_c, and β_c, whereas for the Heskestad model, only $L = \alpha_c$ needs to be specified. Equation (9.5) is still used, with $\alpha_e = 0$ and $\beta_e = \beta_c = -1$. Proponents of the four-parameter model claim that the two filling times are needed to better capture the behavior of detectors in a very slow free-stream ($u < 0.5$ m/s). Rather than declaring one model better than another, the algorithm included in FDS allows the user to pick these various parameters, and in doing so, pick whichever model the user feels is appropriate [101].

Additionally, FDS can model the behavior of beam and aspiration smoke detectors. For a beam detector, the user specifies the emitter and receiver positions and the total obscuration at which the detector will alarm. FDS will then integrate the obscuration over the path length using the predicted soot concentration in each grid cell along the path:

$$\text{Obscuration} = \left(1 - \mathrm{e}^{-K_m \int \rho Y_s \, \mathrm{d}l}\right) \times 100 \ \ \% \tag{9.7}$$

where the integration is carried out over the path of the beam.

For an aspiration detector, the user specifies the sampling locations, the flow rate at each location, the transport time from each sampling point to the detector, the flow rate of any bypass flow, and the total obscuration at which the detector alarms. FDS computes the soot concentration at the detector by weighting the predicted soot concentrations at the sampling locations with their flow rates after applying the appropriate time delay. See the FDS User's Guide [3] for details.

[1] Typically, the activation criterion for a spot-type smoke detector is listed as a percent obscuration per foot or per meter. For the former, $l = 0.3048$ m and for the latter, $l = 1$ m.

Chapter 10

Heating, Ventilation, and Air Conditioning (HVAC)

HVAC systems are found throughout the built environment. During a fire, HVAC ducts can serve as a path for heat and combustion products to be moved through a building and the ducts can serve as a supply of fresh air. In some facilities, such as data centers and clean rooms, fire detection devices are placed inside of HVAC ducts. HVAC systems may also serve as part of the fire protection system for a building when used to exhaust smoke or maintain stairwell pressurization.

FDS has relatively simple fixed flow boundary conditions for velocity or mass flux, and it has a simple pressure boundary condition. While these can adequately represent very simple HVAC features, they cannot model an entire multi-room system. There is no coupling of the mass, momentum, and energy solutions amongst the multiple inlets and outlets comprising the HVAC network. To address this limitation, an HVAC network solver has been added to FDS.

The reader may find it useful to review similar work in coupling CFD to a 1-D nodal model for analysis of ventilation in tunnel fires [102, 103].

10.1 Governing Equations

The overall HVAC solver is based on the MELCOR [104] thermal hydraulic solver. MELCOR is a computer program for simulating accidents in nuclear power plant containment buildings. The Fire and Smoke Simulator (FSSIM) [105], a network fire model, has shown prior success in using the MELCOR solver to model fire spread and smoke movement in the presence of complex ventilation systems, and the FDS implementation of the MELCOR solver is largely based on the implementation found in FSSIM. The coupling of the HVAC solver to the remainder of the FDS computation is in part based upon approaches taken in GOTHIC [106], another containment analysis code that couples CFD-like features for large containment volumes with a network model for piping and ventilation.

The MELCOR solver uses an explicit solver for the conservation equations of mass and energy combined with an implicit solver for the conservation of momentum equation. An HVAC system is represented as a network of nodes and ducts. A node represents where a duct joins with the FDS computational domain or where multiple ducts are joined such as at a tee joint. A duct segment in the network represents any continuous flow path not interrupted by a node and as such may include multiple fittings (elbows, expansions, or contractions, etc.) and may have varying area over its length. The current implementation of the model does not account for mass storage within an HVAC network. The nodal conservation equations of mass,

energy, and momentum (in that order) are:

$$\sum_j \rho_j u_j A_j = 0 \tag{10.1}$$

$$\sum_j \rho_j u_j A_j h_j = 0 \tag{10.2}$$

$$\rho_j L_j \frac{\mathrm{d}u_j}{\mathrm{d}t} = (p_i - p_k) + (\rho g \Delta z)_j + \Delta p_j - \frac{1}{2} K_j \rho_j \left|u_j\right| u_j \tag{10.3}$$

where u is the duct velocity, A is the duct area, and h is the enthalpy of the fluid in the duct. The subscript j indicates a duct segment, the subscripts i and k indicate nodes (where one or more ducts join or where a duct terminates in a compartment). ΔP is a fixed source of momentum (a fan or blower), L is the length of the duct segment, and K is the friction loss of the duct segment.

Since nodes have no volume, the mass and energy conservation equations require that what flows into a node must also flow out. In the momentum equation the terms on the right hand side consist of the pressure gradient between the upstream and the downstream node, the buoyancy head, pressure rise due to an external source (e.g., a fan or blower), and the pressure losses due to wall friction or the presence of duct fittings.

10.2 Solution Procedure

The momentum equation (10.3) is non-linear with respect to velocity due to the loss term. Additionally, the pressure difference between two nodes in the network is impacted by the pressure change at all nodes coupled to that duct either directly (part of the same duct network) or indirectly (connected to the same compartment as another duct network). Solving the momentum equation, requires accounting for both of these. This is done with the following discretization:

$$u_j^{n+1} = u_j^n + \frac{\Delta t^n}{\rho_j L_j} \left[(\tilde{p}_i^n - \tilde{p}_k^n) + (\rho g \Delta z)_j^{n-1} + \Delta p_j^{n-1} - \frac{1}{2} K_j \left(\left| u_j^{n-} + u_j^{n+} \right| u^n - \left| u_j^{n+} \right| u_j^{n-} \right) \right] \tag{10.4}$$

The superscripts $n+$ and $n-$ on the velocity are used to linearize the flow loss in a duct to avoid a non-linear differential equation for velocity. The $n+$ superscript is the prior iteration value and the $n-$ is either the prior iteration value or zero if flow reversal occurred between iterations. This approach is used to speed convergence when duct flows are near zero to avoid large changes in K if the forward and reverse losses are markedly different. Note that the node pressures are not expressed as P_i^n, but rather as $\tilde{p}_i^n$. This indicates an extrapolated pressure at the end of the current time step rather than the actual pressure at the end of the time step. The pressure in a compartment is a function of the mass and energy flowing in and out. If that compartment is connected to other compartments by doors or other openings, then the pressure is also dependent upon flows into and out those other compartments. Those mass and energy flows include both those being predicted by the HVAC model and those being predicted by the CFD model. For example, in Fig. 10.1, the un-shaded compartments have pressure solutions that are dependent upon the flows predicted by both the HVAC model and the CFD model and all of those compartments need to be included in the extrapolated pressure for those compartments. Since the two models are not fully coupled, the extrapolated pressure is an estimate of the pressure at the end of the time step based upon the pressure rise for the prior time step.

The extrapolated pressure for a compartment can be determined by using Eq. (3.29) and correcting the integral over velocity for the current solution of all interdependent HVAC flows into or out of an FDS

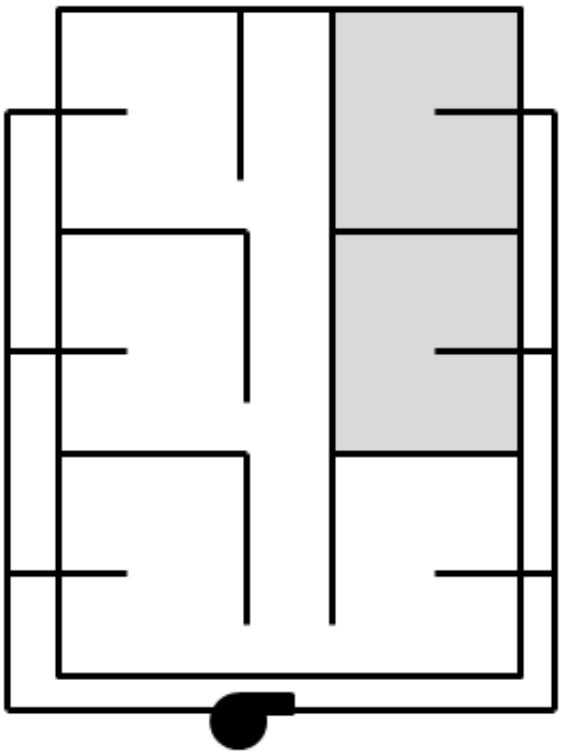

Figure 10.1: Illustration of interdependent pressure solutions. All unshaded compartments have pressures that are dependent upon each other.

pressure zone:

$$\tilde{p}_i^n = p_i^{n-1} + \left(\frac{\mathrm{d}p_i^{n-1}}{\mathrm{d}t} + \frac{\sum_j u_j^{n-1} A_j^{n-1} - \sum_j u_j^n A_j^n}{\int_{\Omega_m} P \, \mathrm{d}V} \right) \Delta t^n = \tilde{p}_i^{*n} - \frac{\sum_j u_j^n A_j^n}{\int_{\Omega_m} P \, \mathrm{d}V}) \Delta t^n \tag{10.5}$$

If the summation term for the velocities being predicted in this timestep is removed from Eq. (10.5) and placed on the left hand side of Eq. (10.4) and the remaining terms of Eq. (10.5) are placed on the right hand side we obtain the following:

$$u_j^n \left(1 + \frac{K_j}{2L_j} \left| u_j^{n-} + u_j^{n+} \right| \right) - \frac{\Delta t^{n2}}{\rho_j L_j} \frac{\sum_{j \in i} u_j^n A_j^n - \sum_{j \in k} u_j^n A_j^n}{\int_{\Omega_m} P \, \mathrm{d}V} =$$
$$u_j^{n-1} + \frac{\Delta t^{n2}}{\rho_j L_j} (\tilde{p}_i^{*n} - \tilde{p}_k^{*n} + (\rho g \Delta z)_j + \Delta p_j) + \frac{K_j}{2L_j} \left| u_j^{n+} \right| \left| u_j^{n-} \right| \tag{10.6}$$

If node i or node k for duct j in Eq. (10.6) is an internal duct node, then extrapolated pressures are not computed and the actual node pressure is solved for. Applying Eq. (10.6) to each duct results in a linear set of equations. Adding additional equations to the set for the mass conservation at internal duct nodes, results in complete set of equations. The solution scheme is as follows:

1. Determine the boundary conditions at all points where the HVAC network joins the FDS computational domain using the previous time step values.

2. Compute the extrapolated pressures for each pressure zone using the previous iteration (previous time step if the first iteration).

3. Assemble the linear set of equations for conservation of momentum and conservation of mass.

4. Solve the equation and check the solution for errors in mass conservation, flow reversal over the time step, and the magnitude of change in the velocity solution for each duct. If any convergence check fails, the solution is re-iterated with new extrapolated pressures. Density and enthalpy values are taken as the upwind values in each iteration. After each iteration, the temperature and density of each node are update using the velocity and pressure solution. The node temperature is computed by summing the enthalpy flows into the node and computing the average temperature that represents the total enthalpy. Density is then updated using the equation of state and the new temperature.

10.2.1 Filtration

Filters have two effects on the flow in an HVAC network. First, a filter causes a flow loss whose magnitude depends on the loading of the filter. Second, a filter removes mass from flow going through the filter as a function of the filter's efficiency. Filter losses are evaluated using the filter loading at the start of each time step. This loss is applied to the upstream duct. The filter loss is computed as a function of the total filter loading using either a linear ramp or a user defined table. The total loading of the filter is determined by summing the mass of each species trapped times a weighting factor for that species.

The filter is assumed to remove a fixed fraction (the filter's efficiency) of the species being trapped by the filter. Each species can be given its own removal efficiency. Eq. (10.1) for a filter is therefore given as:

$$u_{\text{out}}\,\rho_{\text{out}}\,A_{\text{out}} = u_{\text{in}}\,\rho_{\text{in}}\,A_{\text{in}} - \sum_j u_{\text{in}}\,\rho_{\text{in}}\,A_{\text{in}}\,Y_{j,\text{in}}\,E_j = u_{\text{in}}\,\rho_{\text{in}}\,A_{\text{in}}\left(1 - \sum_j Y_{j,\text{in}}\,E_j\right) \tag{10.7}$$

where j is a species being filtered and E_j is its removal efficiency.

10.2.2 Node Losses

Some nodes in the modeled HVAC system will represent items such as tees. Flow through such a node will result in a flow loss. However, as seen in Eq. (10.6), flow loss terms appear only in the equations for a duct. This means that losses that are physically associated with a node must be expressed numerically as equivalent losses in the ducts attached to the node. The losses also need to be applied in a manner that represents the flow conditions within the node. For example, if a tee has flow into one leg and out of two legs, it would not make sense to apply the loss to the upstream leg as there would be no way to distinguish losses due to any changes of the flow splitting in the downstream legs. Loss terms are applied as follows:

1. If there is no flow at the node, then each duct connected to the node is assigned the average of all the losses for flows to the duct from all other ducts.

2. If there is flow into only one connected duct, then each outflowing duct is assigned the flow loss for flow from the inlet duct to the outlet duct.

3. If there is flow out of only one connected duct, then each inflowing duct is assigned the flow loss for flow from the inlet duct to the outlet duct corrected for any change in duct area from inlet to outlet (node losses are input as a function of the downstream duct area).

4. If there is flow into multiple ducts and out of multiple ducts, then each outgoing duct is given the average loss from the inflowing ducts weighted by the volume flow.

10.2.3 Duct Losses

The total flow loss in the duct, K, is the sum of fitting losses in the duct (e.g. elbows, expansion/reduction, orifice plates) plus losses due to wall friction. Wall friction losses are modeled as follows:

$$K = \frac{fL}{D} \tag{10.8}$$

where D is the duct diameter. f is determined from the Colebrook equation. However, since this equation does not have an analytical solution, an approximation by Zigrang and Sylvester is used [107].

$$\frac{1}{\sqrt{f}} = -2\log_{10}\left(\frac{\varepsilon/D}{3.7} - \frac{4.518}{\mathrm{Re}_D}\log_{10}\left(\frac{6.9}{\mathrm{Re}_D} + \left(\frac{\varepsilon/D}{3.7}\right)^{1.11}\right)\right) \tag{10.9}$$

where ε is the absolute roughness of the duct.

10.2.4 Heating and Coiling Coils

A duct can contain a heating or cooling coil. These either add or remove heat from the mass flowing in a duct. This enthalpy change is then added to the duct enthalpy flow at the downstream node prior to computing the node temperature. Two models are available. The first model is a constant heat model that adds or removes heat at a fixed rate as long as the coil is operating. The second model is an effectiveness type heat exchanger model in which four parameters are specified: the enthalpy of the working fluid ($c_{p,\mathrm{fl}}$), the temperature of the working fluid, (T_{fl}), the mass flow rate of the working fluid ($\dot{m}_{\mathrm{fl}}$), and the effectiveness (η). The rate of enthalpy change is then computed as follows:

$$T_{\mathrm{out}} = \frac{\dot{m}_{\mathrm{duct}}\, c_{p,\mathrm{duct,in}}\, T_{\mathrm{duct,in}} + \dot{m}_{\mathrm{fl}}\, c_{p,\mathrm{fl}}\, T_{\mathrm{fl}}}{\dot{m}_{\mathrm{duct}}\, c_{p,\mathrm{duct,in}} + \dot{m}_{\mathrm{fl}}\, c_{p,\mathrm{fl}}} \tag{10.10}$$

$$\dot{q}_{\mathrm{coil}} = \dot{m}_{\mathrm{fl}} c_{p,\mathrm{fl}} \left(T_{\mathrm{fl}} - T_{\mathrm{out}}\right) \eta \tag{10.11}$$

10.3 Leakage

With rare exceptions, walls, floors, and ceilings are not air tight. Gaps around windows and doors and openings for electrical, mechanical, and other systems provide small flow paths through obstructions. These flow paths can be modeled as an equivalent HVAC system where each leakage path is a single duct. The area of the duct is total leakage area and the terminal nodes of the duct can be considered the entire area of the surfaces defined as participating in that flow path.

10.4 Coupling the HVAC solver to FDS

10.4.1 Boundary Conditions for the HVAC Solver

Prior to updating the HVAC solution, the inlet conditions at each duct node are determined by summing the mass and energy of the gas cells next to duct node and averaging the pressure. The total mass and energy along with the average pressure are then used to determine the average temperature.

$$\bar{\rho}_i = \frac{\sum_j \rho_j A_j}{\sum_j A_j} \quad ; \quad \bar{Y}_{\alpha,i} = \frac{\sum_j Y_{\alpha,j}\,\rho_j A_j}{\sum_j \rho_j A_j} \quad ; \quad \bar{P}_i = \frac{\sum_j P_j A_j}{\sum_j A_j} \tag{10.12}$$

$$\bar{h}_i = \frac{\sum_j \rho_j A_j c_p(T_j, Y_j)}{\sum_j \rho_j A_j} \quad ; \quad \bar{T}_i = \frac{\bar{h}_i}{c_p(\bar{T}_i, \bar{Y}_i)} \tag{10.13}$$

where i is a duct node and j are the gas cells adjacent to the node.

10.4.2 Boundary Conditions for the FDS Hydrodynamic Solver

For wall cells containing inflow from an HVAC duct that is not leakage flow, the surface temperature, T_w, is set to the value in the connected duct. If the flow is a leakage flow, then T_w is computed based on the thermal properties assigned to the surface (see Chapter 7) . The remaining wall boundary conditions are computed as follows:

$$\dot{m}''_\alpha = Y_{\alpha,d}\,\dot{m}'' \quad ; \quad \dot{m}'' = \frac{u_d\,\rho_d\,A_d}{A_v} \tag{10.14}$$

where the subscript d is the attached duct and A_v is the total area of the vent (which in the case of leakage flow is the total area of all surfaces for that leak path).

$$u_w = \frac{\dot{m}''}{\rho_w} \quad ; \quad \rho_w = \frac{p\,\overline{W}}{R\,T_w} \tag{10.15}$$

$$Y_{\alpha,w} = \frac{\dot{m}''_\alpha + \frac{2\,\rho_w\,D\,Y_{\alpha,\mathrm{gas}}}{\delta n}}{\frac{2\,\rho_w\,D}{\delta n} + u_w\,\rho_w} \tag{10.16}$$

The above three equations are solved iteratively with a limit of 20 iterations (typically only one or two iterations are needed).

For wall cells with outflow to an HVAC duct, the wall boundary conditions are set to gas cell values except for a leakage flow where the temperature is computed based on the thermal properties assigned to the surface.

Bibliography

[1] American Society for Testing and Materials, West Conshohocken, Pennsylvania. *ASTM E 1355-04, Standard Guide for Evaluating the Predictive Capabilities of Deterministic Fire Models*, 2004. v

[2] K. McGrattan, S. Hostikka, R. McDermott, J. Floyd, C. Weinschenk, and K. Overholt. *Fire Dynamics Simulator, Technical Reference Guide*. National Institute of Standards and Technology, Gaithersburg, Maryland, USA, and VTT Technical Research Centre of Finland, Espoo, Finland, sixth edition, September 2013. Vol. 1: Mathematical Model; Vol. 2: Verification Guide; Vol. 3: Validation Guide; Vol. 4: Configuration Management Plan. v

[3] K. McGrattan, S. Hostikka, R. McDermott, J. Floyd, C. Weinschenk, and K. Overholt. *Fire Dynamics Simulator, User's Guide*. National Institute of Standards and Technology, Gaithersburg, Maryland, USA, and VTT Technical Research Centre of Finland, Espoo, Finland, sixth edition, September 2013. v, 36, 40, 88, 89

[4] H.C. Hottel. Stimulation of Fire Research in the United States After 1940 (A Historical Account). *Combustion Science and Technology*, 39:1–10, 1984. 1

[5] W.W. Jones. A Review of Compartment Fire Models. NBSIR 83-2684, National Bureau of Standards (now NIST), Gaithersburg, Maryland, 1983. 1

[6] J. Quintiere. A Perspective on Compartment Fire Growth. *Combustion Science and Technology*, 39:11–54, 1984. 1

[7] G.P. Forney and W.F. Moss. Analyzing and Exploiting Numerical Characteristics of Zone Fire Models. *Fire Science and Technology*, 14:49–60, 1994. 1

[8] S.V. Patankar. *Numerical Heat Transfer and Fluid Flow*. Hemisphere Publishing, New York, 1980. 2

[9] R.G. Rehm and H.R. Baum. The Equations of Motion for Thermally Driven, Buoyant Flows. *Journal of Research of the NBS*, 83:297–308, 1978. 2, 8, 13, 111

[10] E.S. Oran and J.P. Boris. *Numerical Simulation of Reactive Flow*. Elsevier Science Publishing Company, New York, 1987. 2

[11] K. McGrattan, S. Hostikka, R. McDermott, J. Floyd, C. Weinschenk, and K. Overholt. *Fire Dynamics Simulator, Technical Reference Guide, Volume 3: Validation*. National Institute of Standards and Technology, Gaithersburg, Maryland, USA, and VTT Technical Research Centre of Finland, Espoo, Finland, sixth edition, September 2013. 5

[12] F. H. Harlow and J. E. Welch. Numerical calculation of time-dependent viscous incompressible flow of fluid with a free surface. *Phys. Fluids*, 8:2182, 1965. 6

[13] J.W. Deardorff. Stratocumulus-capped mixed layers derived from a three-dimensional model. *Boundary-Layer Meteorol.*, 18:495–527, 1980. 9

[14] Stephen B. Pope. *Turbulent Flows*. Cambridge University Press, 2000. 9, 23, 25, 26, 27, 32, 46, 85, 131

[15] R.A. Sweet. Direct Methods for the Solution of Poisson's Equation on a Staggered Grid. *Journal of Computational Physics*, 12:422–428, 1973. 9, 37

[16] W. Grosshandler. RadCal: A Narrow Band Model for Radiation Calculations in a Combustion Environment. NIST Technical Note 1402, National Institute of Standards and Technology, Gaithersburg, Maryland, 1993. 10, 115, 116

[17] H.R. Baum and K.B. McGrattan. Simulation of Large Industrial Outdoor Fires. In *Fire Safety Science – Proceedings of the Sixth International Symposium*. International Association for Fire Safety Science, 2000. 13

[18] P.L. Roe. Characteristics-based schemes for the euler equations. *Ann. Rev. Fluid Mech.*, 18:337, 1986. 15, 16, 135

[19] G. Zhou. *Numerical simulations of physical discontinuities in single and multi-fluid flows for arbitrary Mach numbers*. PhD thesis, Chalmers Univ. of Tech., Goteborg, Sweden, 1995. 15, 16, 135

[20] E.F. Toro. *Riemann Solvers and Numerical Methods for Fluid Dynamics: A Practical Introduction*. Springer, 2nd edition, 1999. 15, 135

[21] A. Suresh and H.T. Huynh. Accurate Monotonicity-Preserving Schemes with Runge-Kutta Time Stepping. *Journal of Computational Physics*, 136:83–99, 1997. 16

[22] A. Kempf. *Large-Eddy Simulation of Non-Premixed Turbulent Flames*. PhD thesis, Technischen Universität Darmstadt, 2003. 16

[23] S. Gottlieb, C.-W. Shu, and E. Tadmor. Strong Stability-Preserving High-Order Time Discretization Methods. *SIAM Review*, 43(1):89–112, 2001. 16

[24] Jr. M.W. Chase. NIST-JANAF Thermochemical Tables, Fourth Edition. *J. Physical and Chemical Reference Data*, Monograph No. 9, 1998. 20

[25] R. McDermott, A. Kerstein, R. Schmidt, and P. Smith. Characteristics of 1D spectra in finite-volume large-eddy simulations with one-dimensional turbulence subgrid closure. In *58th Annual Meeting of the American Physical Society, Division of Fluid Dynamics*, Chicago, Illinois, November 2005. 23

[26] U. Piomelli, W.H. Cabot, P. Moin, and S. Lee. Subgrid-scale backscatter in turbulent and transitional flows . *Physics of Fluids A*, 3(7):1766–1771, 1991. 26

[27] J. Smagorinsky. General Circulation Experiments with the Primitive Equations. I. The Basic Experiment. *Monthly Weather Review*, 91(3):99–164, March 1963. 27

[28] M. Germano, U. Piomelli, P. Moin, and W.H. Cabot. A Dynamic Subgrid-Scale Eddy Viscosity Model. *Physics of Fluids A*, 3(7):1760–1765, 1991. 27

[29] P. Moin, K. Squires, W. Cabot, and S. Lee. A dynamic subgrid-scale model for compressible turbulence and scalar transport. *Phys. Fluids A*, 3(11):2746–2757, 1991. 27

[30] J.W. Deardorff. Numerical Investigation of Neutral and Unstable Planetary Boundary Layers. *Journal of Atmospheric Sciences*, 29:91–115, 1972. 27

[31] B. Vreman. An eddy-viscosity subgrid-scale model for turbulent shear flow: Algebraic theory and applications. *Phys. Fluids*, 16(10):3670–3681, 2004. 27

[32] K. McGrattan, S. Hostikka, R. McDermott, J. Floyd, C. Weinschenk, and K. Overholt. *Fire Dynamics Simulator, Technical Reference Guide, Volume 2: Verification*. National Institute of Standards and Technology, Gaithersburg, Maryland, USA, and VTT Technical Research Centre of Finland, Espoo, Finland, sixth edition, September 2013. 28, 142

[33] W. Zhang, N. Ryder, R.J. Roby, and D. Carpenter. Modeling of the Combustion in Compartment Fires Using Large Eddy Simulation Approach. In *Proceedings of the 2001 Fall Technical Meeting, Eastern States Section*. Combustion Institute, Pittsburgh, Pennsylvania, December 2001. 28

[34] B.E. Poling, J.M. Prausnitz, and J.P. O'Connell. *The Properties of Gases and Liquids*. McGraw-Hill, New York, 5th edition, 2000. 29

[35] H. Werner and H. Wengle. Large-eddy simulation of turbulent flow over and around a cube in a plate channel. In *8th Symposium on Turbulent Shear Flows*, pages 155–168, Munich, Germany, 1991. Technische University Munich. 32

[36] D.C. Wilcox. *Turbulence Modeling for CFD*. DCW Industries, Inc., 2nd edition, 1998. 33

[37] E.A. Fadlun, R. Verzicco, P. Orlandi, and J. Mohd-Yusof. Combined Immersed-Boundary Finite-Difference Methods for Three-Dimensional Complex Flow Simulations. *Journal of Computational Physics*, 161:35–60, 2000. 38

[38] B.F. Magnussen and B.H. Hjertager. On Mathematical Modeling of Turbulent Combustion with Special Emphasis on Soot Formation and Combustion. In *Proceedings of the Sixteenth Symposium (International) on Combustion*, pages 719–729. Combustion Institute, Pittsburgh, Pennsylvania, 1977. 41, 44, 47

[39] T. Poinsot and D. Veynante. *Theoretical and Numerical Combustion*. R.T. Edwards, Inc., Philadelphia, Pennsylvania, 2nd edition, 2005. 41, 44, 47, 50, 133

[40] R.O. Fox. *Computational Models for Turbulent Reacting Flows*. Cambridge Univ Pr, 2003. 41

[41] L. Orloff and J. De Ris. Froude Modeling of Pool Fires. In *Proceedings of the Nineteenth Symposium (International) on Combustion*, pages 885–895. Combustion Institute, Pittsburgh, Pennsylvania, 1982. 44

[42] C. Beyler. *SFPE Handbook of Fire Protection Engineering*, chapter Flammability Limits of Premixed and Diffusion Flames. National Fire Protection Association, Quincy, Massachusetts, 4th edition, 2008. 44

[43] R. McDermott, K. McGrattan, and J. Floyd. A simple reaction time scale for under-resolved fire dynamics. In *Fire Safety Science – Proceedings of the 10th International Symposium*, pages 809–820, University of Maryland, College Park, Maryland, USA, 2011. 45

[44] Z. Chen, J. Wen, B. Xu, and S. Dembele. Extension of the eddy dissipation concept and smoke point soot model to the les frame for fire simulations. in review. 49, 133

[45] B. Panjwani, I. Ertesvåg, K. E. Rian, and A. Gruber. Subgrid Combustion modeling for large eddy simulation (LES) of turbulent combustion using eddy dissipation concept. In J. C. F. Pereira and A Sequeira, editors, *V European Conference on Computational Fluid Dynamics*, Lisbon, Portugal, 14-17 June 2010. ECCOMAS. 49, 133, 134

[46] C. Dopazo and E. E. O'Brien. Approach to autoignition of turbulent mixture. *Acta Astronaut.*, 1:1239–1266, 1974. 49, 131

[47] R Viskanta and M P Menguc. Radiation Heat Transfer in Combustion Systems. *Progress in Energy and Combustion Science*, 13:97–160, 1987. 55

[48] R. Siegel and J. R. Howell. *Thermal Radiation Heat Transfer*. Taylor & Francis, New York, 4th edition, 2002. 56, 68

[49] C.B. Ludwig, W. Malkmus, J.E. Reardon, and J.A.L. Thomson. Handbook of Infrared Radiation From Combustion Gases. Nasa sp-3080, National Aeronautics and Space Administration, Office of Management, Scientific and Technical Information Program, 1973. 56, 118

[50] S. Hostikka, K.B. McGrattan, and A. Hamins. Numerical Modeling of Pool Fires using Large Eddy Simulation and Finite Volume Method for Radiation. In *Fire Safety Science – Proceedings of the Seventh International Symposium*, pages 383–394. International Association for Fire Safety Science, 2002. 56

[51] C.L. Beyler. *SFPE Handbook of Fire Protection Engineering*, chapter Fire Hazard Calculations for Large Open Hydrocarbon Fires. National Fire Protection Association, Quincy, Massachusetts, 4th edition, 2008. 59

[52] N. Takahashi, H. Koseki, and T. Hirano. Temporal and Spatial Characteristics of Radiation from Large Pool Fires. *Bulletin of Japanese Association of Fire Science and Engineering*, 49(1):27–33, 1999. 59

[53] J.Y. Murthy and S.R. Mathur. Radiative Heat Transfer in Axisymmetric Geometries Using an Unstructured Finite-Volume Method. *Numerical Heat Transfer, Part B*, 33:397–416, 1998. 60

[54] G.D. Raithby and E.H. Chui. A Finite-Volume Method for Predicting Radiant Heat Transfer in Enclosures with Participating Media. *Journal of Heat Transfer*, 112(2):415–423, 1990. 60

[55] S. Hostikka. Development of fire simulation models for radiative heat transfer and probabilistic risk assessment. VTT Publications 683, VTT Technical Research Centre of Finland, Espoo, Finland, 2008. 60

[56] S.H. Kim and K.Y. Huh. Assessment of The Finite-Volume Method and The Discrete Ordinate Method for Radiative Heat Transfer In a Three-Dimensional Rectangular Enclosure. *Numerical Heat Transfer, Part B*, 35:85–112, 1999. 62

[57] T. Ravigururajan and M. Beltran. A Model for Attenuation of Fire Radiation Through Water Droplets. *Fire Safety Journal*, 15:171–181, 1989. 63

[58] A. Tuntomo, C. Tien, and S. Park. Optical Constants of Liquid Hydrocarbon Fuels. *Combustion Science and Technology*, 84:133–140, 1992. 63

[59] A. Collin, P. Boulet, G. Parent, and D. Lacroix. Numerical simulation of a water spray - Radiation attenuation related to spray dynamics. *International Journal of Thermal Sciences*, 46:856–868, September 2007. 64

[60] S. Maruyama, H. Nakai, A. Sakurai, and A. Komiya. Evaluation method for radiative heat transfer in polydisperse water droplets. *Journal of Quantitative Spectroscopy and Radiative Transfer*, 109:1–15, January 2008. 64

[61] W. Yang, T. Parker, H.D. Ladouceur, and R.J. Kee. The Interaction of Thermal Radiation and Water Mist in Fire Suppression. *Fire Safety Journal*, 39:41–66, 2004. 64

[62] W.J. Wiscombe. Improved Mie Scattering Algorithms. *Applied Optics*, 19(9):1505–1509, 1980. 65

[63] G.M. Hale and M.R. Querry. Optical constants of water in the 200 nm to 200 *mu*m wavelength region. *Applied Optics*, 12(3):555–563, 1973. 65

[64] L.A. Dombrovsky, S.S. Sazhin, S.V. Mikhalovsky, R. Wood, and M.R. Heikal. Spectral properties of diesel fuel droplets. *Fuel*, 82:15–22, 2003. 65

[65] J.P. Holman. *Heat Transfer*. McGraw-Hill, New York, 7th edition, 1990. 69

[66] F. P. Incropera and D. P. De Witt. *Fundamentals of Heat and Mass Transfer*. John Wiley and Sons, New York, 4th edition, 1996. 69, 82

[67] H.W. Park, K. Moon, E. Oztekin, R. McDermott, C. Lee, and J.-I. Choi. Near-Wall Modeling for Large Eddy Simulation of Convective Heat Transfer in Turbulent Boundary Layers. In *65th Annual Meeting of the APS Division of Fluid Dynamics*, San Diego, CA, November 18-20 2012. American Physical Society. 69

[68] E.S. Oztekin, D. Blake, and R. Lyon. Numerical simulations of a small fire in an aircraft cargo compartment. In *FM Global Open Source CFD Fire Modeling Workshop*, Norwood, MA, May 10 2012. 69

[69] B.A. Kader. Temperature and concentration profiles in fully turbulent boundary layers. *International Journal of Heat and Mass Transfer*, 24:1541–1544, 1981. 70

[70] C. Lautenberger and C. Fernandez-Pello. Generalized pyrolysis model for combustible solids. *Fire Safety Journal*, 44:819–839, 2009. 72

[71] K. Prasad, C. Li, K. Kailasanath, C. Ndubizu, R. Ananth, and P.A. Tatem. Numerical modelling of methanol liquid pool fires. *Combustion Theory and Modelling*, 3:743–768, 1999. 73

[72] R. Taylor and R. Krishna. *Multicomponent Mass Transfer*. Wiley-Interscience, 1993. 73

[73] N. Bixler. VICTORIA 2.0: A Mechanistic Model for Radionuclide Behavior in a Reactor Coolant System Under Severe Accident Conditions. NUREG/CR 6131, US Nuclear Regulatory Commission, Washington, DC, 1998. 74

[74] C. Davies. *Aerosol Science*. Academic Press, London, 1966. 74

[75] E. Cunningham. On the Velocity of Steady Fall of Spherical Particles. *Proc. Roy. Soc. A*, 83:357, 1910. 74

[76] M. Sippola and W. Nazaroff. Particle Deposition from Turbulent Flow: Review of Published Research and Its Applicability to Ventilation Ducts in Commercial Buildings. LBNL Report 51432, Lawrence Berkeley National Laboratory, Berkeley, California, 2002. 74

[77] X. Hu, Z. Wang, F. Jia, E.R. Galea, and M.K. Patel. Simulating Smoke Transport in Large Scale Enclosure Fires Using a Multi-Particle-Size Model. In *Fire Safety Science – Proceedings of the 10th International Symposium*, pages 445–458, University of Maryland, College Park, Maryland, USA, 2011. 75

[78] J. Brock. On the Theory of Thermal Forces Acting on Aerosol Particles. *J. Coll. Sci.*, 17:768–780, 1962. 75

[79] D. McCoy and T. Hanratty. Rate of Deposition of Droplets in Annular Two-Phase Flow. *Int. J. Multiphase Flow*, 3:319–331, 1977. 75

[80] W. Ludwig, K. Lehtinen, J. Pyykonen, D. Brown, J. Paraled, J. Jokiniemi, and R. Gamble. CFD Simulation on Aerosol Impaction and Deposition Analysis in a Passive Containment Condenser. In *8th International Conference on Nuclear Engineering*. American Society of Mechanical Engineers, 2000. 75

[81] J. Ramírez-Muñoz, A. Soria, and E. Salinas-Rodríguez. Hydrodynamic force on interactive spherical particles due to the wake effect. *International journal of multiphase flow*, 33(7):802–807, 2007. 78

[82] E. Loth. Quasi-steady shape and drag of deformable bubbles and drops. *International Journal of Multiphase Flow*, 34(6):523–546, June 2008. 78

[83] L Prahl, A Holzer, D Arlov, J Revstedt, M Sommerfeld, and L Fuchs. On the interaction between two fixed spherical particles. *International Journal of Multiphase Flow*, 33(7):707–725, 2007. 78, 79

[84] L. Prahl, A. Jadoon, and J. Revstedt. Interaction between two spheres placed in tandem arrangement in steady and pulsating flow. *International Journal of Multiphase Flow*, 35(10):963–969, 2009. 78

[85] T.S. Chan. Measurements of Water Density and Droplet Size Distributions of Selected ESFR Sprinklers. *Journal of Fire Protection Engineering*, 6(2):79–87, 1994. 79

[86] H.Z. Yu. Investigation of Spray Patterns of Selected Sprinklers with the FMRC Drop Size Measuring System. In *Fire Safety Science – Proceedings of the First International Symposium*, pages 1165–1176. International Association For Fire Safety Science, 1986. 79

[87] N. Cheremisinoff. *Encyclopedia of Fluid Mechanics, Volume 3: Gas-Liquid Flows*. Gulf Publishing Company, Houston, Texas, 1986. 81

[88] A. Hamins and K.B. McGrattan. Reduced-Scale Experiments to Characterize the Suppression of Rack Storage Commodity Fires. NISTIR 6439, National Institute of Standards and Technology, Gaithersburg, Maryland, 1999. 83

[89] A. Hamins and K.B. McGrattan. Reduced-Scale Experiments on the Water Suppression of a Rack-Storage Commodity Fire for Calibration of a CFD Fire Model. In *Fire Safety Science – Proceedings of the Seventh International Symposium*, pages 457–468. International Association for Fire Safety Science, 2002. 83

[90] H.Z. Yu, J.L. Lee, and H.C. Kung. Suppression of Rack-Storage Fires by Water. In *Fire Safety Science – Proceedings of the Fourth International Symposium*, pages 901–912. International Association For Fire Safety Science, 1994. 83

[91] T. Bartzanas, T. Boulard, and C. Kittas. Numerical simulation of the airflow and temperature distribution in a tunnel greenhouse equipped with insect-proof screens in the openings. *Computers and Electronics in Agriculture*, 34:207–221, 2002. 84

[92] V. Raman, H. Pitsch, and R.O. Fox. Hybrid large-eddy simulation/Lagrangian filtered-density-function approach for simulating turbulent combustion. *Combustion and Flame*, 143:56–78, 2005. 85

[93] G.E.P Box and M.E. Muller. A Note on the Generation of Random Normal Deviates. *The Annals of Mathematical Statistics*, 29(2):610–611, 1958. 85

[94] G. Heskestad and R.G. Bill. Quantification of Thermal Responsiveness of Automatic Sprinklers Including Conduction Effects. *Fire Safety Journal*, 14:113–125, 1988. 87

[95] P. Ruffino and M. di Marzo. Temperature and Volumetric Fraction Measurements in a Hot Gas Laden with Water Droplets. *Journal of Heat Transfer*, 125(2):356–364, April 2003. 87

[96] P. Ruffino and M. di Marzo. The Effect of Evaporative Cooling on the Activation Time of Fire Sprinklers. In *Fire Safety Science – Proceedings of the Seventh International Symposium*, pages 481–492. International Association for Fire Safety Science, 2002. 87

[97] F. Gavelli, P. Ruffino, G. Anderson, and M. di Marzo. Effect of Minute Water Droplets on a Simulated Sprinkler Link Thermal Response. NIST GCR 99-776, National Institute of Standards and Technology, Gaithersburg, Maryland, July 1999. 87

[98] P.J. DiNenno, editor. *SFPE Handbook of Fire Protection Engineering*. National Fire Protection Association, Quincy, Massachusetts, 3rd edition, 2002. 88, 89

[99] T. Cleary, A. Chernovsky, W. Grosshandler, and M. Anderson. Particulate Entry Lag in Spot-Type Smoke Detectors. In *Fire Safety Science – Proceedings of the Sixth International Symposium*, pages 779–790. International Association for Fire Safety Science, 1999. 88

[100] G.W. Mulholland and C. Croarkin. Specific Extinction Coefficient of Flame Generated Smoke. *Fire and Materials*, 24:227–230, 2000. 89

[101] R.J. Roby, S.J. Olenick, W. Zhang, D.J. Carpenter, M.S. Klassen, and J.L. Torero. A Smoke Detector Algorithm for Large Eddy Simulation Modeling. NIST GCR 07-911, National Institute of Standards and Technology, Gaithersburg, Maryland, 2007. 89

[102] F. Colella, G. Rein, J. Torero, and R. Borchiellini. A novel multiscale methodology for simulating tunnel ventilation flows during fires. *Fire Technology*, 2010. 91

[103] F. Colella, G. Rein, V. Verda, and R. Borchiellini. Multiscale modeling of transient flows from fire and ventilation in long tunnels. *Computers and Fluids*, 51:16–29, 2011. 91

[104] R. Gaunt *et al.* MELCOR Computer Code Manuals: Reference Manuals Version 1.8.5, Volume 2, Rev. 2. NUREG/CR-6119, US Nuclear Regulatory Commission, Washington, DC, 2000. 91

[105] J. Floyd, S. Hunt, F. Williams, and P. Tatem. Fire and Smoke Simulator (FSSIM) Version 1: Theory Manual. NRL/MR/6180-04-8765, U.S. Naval Research Laboratory, Washington, DC, 2004. 91

[106] T. George et al. GOTHIC Containment Analysis Package Users Manual. NAI 8907-02, Numerical Applications, Inc., Richland, WA, 2006. 91

[107] D. Zigrang and N. Sylvester. A Review of Explicit Friction Factor Equations. *Transactions of the ASME*, 107:280–283, 1985. 95

[108] C.L. Tien. Thermal Radiation Properties of Gases. In J.P. Hartnett and T.F. Irvine, editors, *Advances in Heat Transfer*, volume 5, pages 253–324. Academic Press, New York, 1968. 115, 116

[109] S.S. Penner. *Quantitative molecular spectroscopy and gas emissivities*. Addison-Wesley Publishing Company, Reading, Massachusetts, USA, 1959. 115, 116

[110] Peter J. Mohr, Barry N. Taylor, and David B. Newell. CODATA recommended values of the fundamental physical constants: 2010. *Reviews of Modern Physics*, 84:1527–1605, 2012. 115

[111] K. Wakatsuki. *High Temperature Radiation Absorption of Fuel Molecules And An Evaluation of Its Influence on Pool Fire Modeling* . PhD thesis, University of Maryland, College Park, Maryland, 2005. 117, 118, 119, 120, 121, 122

[112] LA Lorne Matheson. The intensity of infrared absorption bands. *Physical Review*, 40(5):813–828, June 1932. 117

[113] Gerhard Herzberg. *Molecular Spectra and Molecular Structure: II, Infrared and Raman Spectra of Polyatomic Molecules*. D. Van Nostrand Company, Inc., New York, fourth pri edition, 1949. 117, 118, 119, 120, 121

[114] Editor: Russell D. Johnson III. NIST Computational Chemistry Comparison and Benchmark Database, 2011. 120, 121

[115] Michael F. Modest. *Radiative Heat Transfer, Second Edition*. Academic Press, 2003. 122

[116] David R Mott and Elaine S Oran. Chemeq2: A solver for the stiff ordinary differential equations of chemical kinetics. Technical report, DTIC Document, 2001. 127

[117] P. Moin. *Fundamentals of Engineering Numerical Analysis*. Cambridge University Press, 2001. 128

[118] S.R. Turns. *An Introduction to Combustion*. McGraw-Hill, New York, 2nd edition, 1996. 133

[119] B. Lilleberg, B. Panjwani, and I. S. Ertesvag. Large Eddy Simulation of Methane Diffusion Flame: Comparison of Chemical Kinetics Mechanisms. In *ICNAAM, Numerical Analysis and Applied Mathematics, International Conference*, volume III, pages 2158–2161. American Institute of Physics, 2010. 133

[120] M. Herrmann, G. Blanquart, and V. Raman. Flux corrected finite-volume scheme for preserving boundedness in large-eddy simulations. AIAA Paper 2005-25009, 2005. 135

[121] J.M. Suo-Anttila, T.K. Blanchat, A.J. Ricks, and A.L. Brown. Characterization of thermal radiation spectra in 2 m pool fires. *Proceedings of the Combustion Institute*, 32(2):2567–2574, 2009. 145, 146

[122] K. Wakatsuki, G. Jackson, J. Kim, A. Hamins, M. Nyden, and S. Fuss. Determination of planck mean absorption coefficients for hydrocarbon fuels. *Combustion Science and Technology*, 180:616–630, 2008. 145

[123] S.I. Stoliarov, S. Crowley, R.E. Lyon, and G.T. Linteris. Prediction of the burning rates of non-charring polymers. *Combustion and Flame*, 156:1068–1083, 2009. 145

[124] P.T. Tsilingiris. Comparative evaluation of the infrared transmission of polymer films. *Energy Conversion and Management*, 44:2839–2856, 2003. 145

[125] B. Broeckmann and H Schecker. Heat transfer mechanisms and boilover in burning oil-water systems. *Journal of Loss Prevention in the Process Industries*, 8(3):137–147, 1995. 145

[126] S.S. Sazhin, P.A. Krutitskii, W.A. Abdelghaffar, E.M. Sazhina, S.V. Mikhalovsky, S.T. Meikle, and M.R. Heikal. Transient heating of diesel fuel droplets. *International Journal of Heat and Mass Transfer*, 47(14-16):3327–3340, 2004. 145

[127] G.V. Madhav and R.P. Chhabra. Drag on non-spherical particles in viscous fluids. *International Journal of Mineral Processing*, 43(1-2):15–29, 1994. 145

[128] S.S. Manohar, A.K. Kulkarni, and S.T. Thynell. In-depth absorption of externally incident radiation in nongray media. *Journal of Heat Transfer*, 117:146–151, February 1995. 145

[129] P.J. Linstrom and W.G. Mallard. Evaluated Infrared Reference Spectra. WebBook. NIST Chemistry WebBook, NIST Standard Reference Database Number 69. 145

[130] J.E. Bertie, R.N. Jones, Y. Apelblat, and C.D Keefe. Infrared intensities of liquids XXV: Dielectric constants, molar polarizabilities and integrated intensities of liquid toluene at 25 °C between 4800 and 400 cm^{-1}. *Journal of Molecular Structure*, 750(1-3):78–93, 2005. 145

[131] J.E. Bertie, R.N. Jones, Y. Apelblat, and C.D Keefe. Infrared Intensities of Liquids XIII: Accurate Optical Constants and Molar Absorption Coefficients Between 6500 and 435 cm^{-1} of Toluene at 25 °C, from Spectra Recorded in Several Laboratories. *Applied Spectroscopy*, 48:127–143, January 1994. 145, 146

[132] J.E. Bertie, S.L. Zhang, H.H. Eysel, S. Baluja, and M.K Ahmed. Infrared Intensities of Liquids XI: Infrared Refractive Indices from 8000 to 2 cm^{-1}, Absolute Integrated Intensities, and Dipole Moment Derivatives of Methanol at 25 °C. *Applied Spectroscopy*, 47:1100–1115, August 1993. 145, 146

[133] J.E. Bertie, R.N. Jones, and C.D Keefe. Infrared Intensities of Liquids XII: Accurate Optical Constants and Molar Absorption Coefficients Between 6225 and 500 cm^{-1} of Benzene at 25 °C, from Spectra Recorded in Several Laboratories. *Applied Spectroscopy*, 47(7):891–911, 1993. 145, 146

[134] J.E. Bertie and Z Lan. Infrared Intensities of Liquids XX: The Intensity of the OH Stretching Band of Liquid Water Revisited, and the Best Current Values of the Optical Constants of H2O (l) at 25 °C between 15,000 and 1 cm^{-1}. *Applied Spectroscopy*, 50(8):1047–1057, 1996. 145, 146

Appendix A

Nomenclature

A_p	droplet/particle surface area
$A_{\alpha\beta}$	pre-exponential factor for solid phase Arrhenius reaction
B	emission source term
C	sprinkler C-factor; coefficient of natural convection
C_d	drag coefficient
C_m	momentum accommodation coefficient
Cn	Cunningham slip correction factor
C_s	Smagorinsky constant (LES); thermal slip coefficient
C_t	thermal accommodation coefficient
c	solid material specific heat; speed of light in vacuum
c_p	constant-pressure specific heat
D	droplet/particle diameter
D_α	diffusion coefficient
$D_{\mathrm{v},0.5}$	median volumetric droplet diameter
E	activation energy
$\mathbf{f}_\mathrm{b}$	external force vector (excluding gravity)
g	acceleration of gravity
$\mathbf{g}$	gravity vector, normally $(0, 0, -g)$
H	total pressure divided by the density (Bernoulli integral)
$H_{\mathrm{r},\alpha\beta}$	heat of reaction for a solid phase reaction
h	heat transfer coefficient; Planck constant
$h_{\mathrm{s},\alpha}$	sensible enthalpy of species α
h^0_α	heat of formation of species α
I	radiation intensity per unit of solid angle
I_b	radiation blackbody intensity per unit of solid angle
$I_{b,\lambda}$	spectral radiation blackbody intensity as function of wavelength per unit of solid angle
$I_{b,\omega}$	spectral radiation blackbody intensity as function of wavenumber per unit of solid angle
k	thermal conductivity; suppression decay factor
k_B	Boltzmann constant
Kn	Knudsen number
K_th	thermophoretic velocity coefficient
L	characteristic length; surface thickness
$\dot{m}'''_{\mathrm{b},\alpha}$	mass production rate per unit volume of species α by evaporating droplets/particles
$\dot{m}'''_\alpha$	mass production rate per unit volume of species α by chemical reactions

$\dot{m}''_{\mathrm{w}}$	water mass flux
m''_{w}	water mass per unit area
n_{s}	partial reaction order for solid
$n_{\mathrm{O_2}}$	partial reaction order for oxygen
Nu	Nusselt number
Pr	Prandtl number
p	pressure
$\overline{p}_0$	atmospheric pressure profile
$\overline{p}_m$	background pressure of mth pressure zone
$\tilde{p}$	pressure perturbation
$\dot{\mathbf{q}}''$	heat flux vector
$\dot{q}'''$	heat release rate per unit volume
$\dot{q}''_{\mathrm{r}}$	radiative heat flux
$\dot{q}''_{\mathrm{c}}$	convective heat flux
$\dot{Q}$	total heat release rate
$\dot{Q}^*$	fire Froude number
R	universal gas constant
Re	Reynolds number
r_{p}	particle/droplet radius
$r_{\alpha\beta}$	solid phase reaction rate
RTI	Response Time Index of a sprinkler
$\mathbf{s}$	unit vector in direction of radiation intensity
Sc	Schmidt number
Sh	Sherwood number
S_α	solid component production rate
T	temperature
t	time
U	integrated radiant intensity; optical pathlength
$\mathbf{u} = (u, v, w)$	velocity vector
W_α	molecular weight of gas species α
$\overline{W}$	molecular weight of the gas mixture
We	Weber number
$\mathbf{x} = (x, y, z)$	position vector
X_α	volume fraction of species α
Y_α	mass fraction of species α
$\bar{Y}_\alpha$	mean mass fraction of species α
$\hat{Y}_\alpha$	mass fraction of species α in mixed zone of a computation cell
$Y^\infty_{\mathrm{O_2}}$	mass fraction of oxygen in the ambient
Y_{F}	mass fraction of fuel
y_{s}	soot yield
Z_α	species mixture α

Greek Letters

α	ratio of gas conductivity to the particle conductivity; integrated band intensity
γ	ratio of specific heats; Rosin-Rammler exponent; spectral fine structure parameter of narrow band
Δ	LES filter width
Δh	heat of combustion

Δh_{O_2}	energy released per unit mass oxygen consumed
$\Delta h_{f,\alpha}$	heat of formation of species α
δ	film thickness; scaling factor of thickness and density
ε	dissipation rate; emissivity
κ	absorption coefficient; von Karman constant
λ	mean free path of gas molecules; wavelength of thermal radiation
μ	dynamic viscosity
ν	frequency of the thermal radiation
ν_α	stoichiometric coefficient, species α
ν_s	yield of solid residue in solid phase reaction
$\nu_{g,\gamma}$	yield of gaseous species γ in solid phase reaction
ρ	density
$\bar{\tau}_\omega$	mean spectral transmissivity of a narrow band centered in ω
τ_{ij}	viscous stress tensor
ϕ	porosity
χ	shape factor
χ_r	radiative loss fraction
σ	Stefan-Boltzmann constant; constant in droplet size distribution; surface tension
σ_p	particle scattering coefficient
σ_s	scattering coefficient
τ^+	dimensionless stopping distance
ω	wavenumber of thermal radiation
$\omega = (\omega_x, \omega_y, \omega_z)$	vorticity vector
Ω	solid angle

Subscripts

0	initial value
a	air
b	bulk phase property; boiling
B	Brownian
c	convective
d	drag
e	effective properties
g	gas
ijk	gas phase cell indices
n	band properties
p	particle/droplet
p	pressure
r	radiative
s	solid; sensible; soot
w	wall
α	gas species index
β	index of reaction
λ	wavelength
ω	wavenumber

Appendix B

A Velocity Divergence Constraint for Large-Eddy Simulation of Low-Mach Flows

The equations governing the evolution of a low-Mach, variable density fluid—first introduced by Rehm and Baum in 1978 [9]—are continuity, species concentration (mass fraction), momentum, energy (sensible enthalpy), and the ideal gas equation of state:

$$\frac{\partial \rho}{\partial t} + \nabla \cdot (\rho \mathbf{u}) = 0 \tag{B.1}$$

$$\frac{\partial \rho Y_\alpha}{\partial t} + \nabla \cdot (\rho Y_\alpha \mathbf{u}) = \nabla \cdot (\rho D_\alpha \nabla Y_\alpha) + \dot{m}'''_\alpha \tag{B.2}$$

$$\frac{\partial \rho \mathbf{u}}{\partial t} + \nabla \cdot (\rho \mathbf{u}\mathbf{u}) = -\nabla \tilde{p} - \nabla \cdot \tau + (\rho - \rho_0)\mathbf{g} \tag{B.3}$$

$$\frac{\partial \rho h_s}{\partial t} + \nabla \cdot (\rho h_s \mathbf{u}) = \frac{\mathrm{D}\bar{p}}{\mathrm{D}t} + \dot{q}''' - \nabla \cdot \dot{\mathbf{q}}'' \tag{B.4}$$

$$\rho = \frac{\bar{p}\overline{W}}{RT} \tag{B.5}$$

In this appendix, starting from the conservative form of the sensible enthalpy transport equation, we derive a numerically consistent velocity divergence constraint for use in large-eddy simulation (LES) of low-Mach flows. The result accounts for numerical transport of mass and energy, which is difficult to eliminate in relatively coarse, engineering LES calculations when total variation diminishing (TVD) scalar transport schemes are employed. Without the correction terms derived here, unresolved (numerical) mixing of gas species with different heat capacities and molecular weights may lead to erroneous mixture temperatures and ultimately to an imbalance in the energy budget.

B.1 The Divergence Constraint

As mentioned, the present work stems from attempts to understand and correct an energy budget imbalance that became evident after implementing both temperature-dependent specific heats and TVD scalar transport. One of the revelations of this work has been that the choice of starting point for deriving the divergence constraint naturally leads to two different forms of the divergence expression. While these forms are mathematically equivalent, they lead to two completely different—and yet completely plausible—numerical formulations.

B.1.1 From Continuity

Starting from the continuity equation, we can factor out the velocity divergence leaving the material derivative of the density:

$$\nabla \cdot \mathbf{u} = -\frac{1}{\rho}\frac{\mathrm{D}\rho}{\mathrm{D}t} \tag{B.6}$$

Using the ideal gas law and differentiating the equation of state leads to

$$\begin{aligned}\nabla \cdot \mathbf{u} = &\left(\frac{1}{\rho c_p T} - \frac{1}{\bar{p}}\right)\frac{\mathrm{D}\bar{p}}{\mathrm{D}t} \\ &+ \frac{1}{\rho c_p T}\left[\dot{q}''' - \nabla \cdot \dot{\mathbf{q}}''\right] \\ &+ \frac{1}{\rho}\sum_{\alpha}\left(\frac{\overline{W}}{W_\alpha} - \frac{h_{s,\alpha}}{c_p T}\right)\left[\nabla \cdot (\rho D_\alpha \nabla Y_\alpha) + \dot{m}_\alpha'''\right]\end{aligned} \tag{B.7}$$

B.1.2 From Sensible Enthalpy

Alternatively, we may factor the velocity divergence from the sensible enthalpy transport equation:

$$\nabla \cdot \mathbf{u} = \frac{1}{\rho h_s}\left[\frac{\mathrm{D}}{\mathrm{D}t}(\bar{p} - \rho h_s) + \dot{q}''' - \nabla \cdot \dot{\mathbf{q}}''\right] \tag{B.8}$$

From this starting point, (arguably) the natural result for the divergence expression is

$$\begin{aligned}\nabla \cdot \mathbf{u} = &\frac{1}{\rho c_p T}\frac{\mathrm{D}\bar{p}}{\mathrm{D}t} - \frac{1}{\bar{p}}\frac{\partial \bar{p}}{\partial t} \\ &+ \frac{1}{\rho c_p T}\left[\dot{q}''' - \nabla \cdot \dot{\mathbf{q}}'' - \mathbf{u} \cdot \nabla(\rho h_s)\right] \\ &+ \frac{1}{\rho}\sum_{\alpha}\left(\frac{\overline{W}}{W_\alpha} - \frac{h_{s,\alpha}}{c_p T}\right)\left[\nabla \cdot (\rho D_\alpha \nabla Y_\alpha) - \mathbf{u} \cdot \nabla(\rho Y_\alpha) + \dot{m}_\alpha'''\right]\end{aligned} \tag{B.9}$$

B.1.3 Comparison

Notice the subtle differences between the first, second, and third lines of (B.7) and (B.9). The first lines differ by $(\mathbf{u} \cdot \nabla \bar{p})/\bar{p}$. In (B.9), the second and third lines each contain an extra term accounting for advection of enthalpy and mass, respectively, $\mathbf{u} \cdot \nabla(\rho h_s)$ and $\mathbf{u} \cdot \nabla(\rho Y_\alpha)$. Using (B.1)-(B.5), it can be shown that (B.7) and (B.9) are mathematically equivalent.

B.1.4 The Discrete Divergence

The *conservative form* of the sensible enthalpy transport equation—which derives its name from the flux divergence form of the mean transport term on the left hand side—is

$$\frac{\partial(\rho h_s)}{\partial t} + \underbrace{\nabla \cdot (\rho h_s \mathbf{u})}_{\text{mean transport}} = \frac{\mathrm{D}\bar{p}}{\mathrm{D}t} + \dot{q}''' - \nabla \cdot \dot{\mathbf{q}}''. \tag{B.10}$$

This form is called conservative because, by Gauss's theorem, the integral of the discrete flux divergence over the domain is equivalent to the surface integral of the flux over the boundary of the domain. For

a periodic domain the integral is zero—*flow in* must equal *flow out*. The key to guaranteeing discrete conservation of sensible enthalpy is to first discretize the mean transport term. Below an overline will denote a slope-limiting interpolation operator. As discussed in Section B.2, this operator is specially designed to be consistent with flux-limited, total variation diminishing (TVD) transport for the conservative form of the mean transport term.

Expanding the mean transport term and rearranging (B.10) in terms of the discrete divergence yields

$$\nabla\cdot\mathbf{u} = \frac{1}{\rho h_s}\left[-\left(\frac{\partial(\rho h_s)}{\partial t} + \overline{\mathbf{u}\cdot\nabla(\rho h_s)}\right) + \frac{\mathrm{D}\bar{p}}{\mathrm{D}t} + \dot{q}''' - \nabla\cdot\dot{\mathbf{q}}''\right]. \tag{B.11}$$

The numerical details of $\overline{\mathbf{u}\cdot\nabla(\rho h_s)}$ are the key to assuring discrete conservation (see Section B.2). Mathematically, (B.11) is equivalent to (B.8). Numerically, however, (B.11) accounts for the critical details of the TVD transport scheme.

Most of the complexity in the divergence expression is buried in the time derivative term, $\partial(\rho h_s)/\partial t$. Using (B.1)-(B.5), it can be shown that (B.11) expands to yield (B.9).

B.2 Factoring the Discrete Flux Divergence

Below we show the numerical decomposition of the enthalpy flux divergence for cell i in 1D. The operator $\delta(\ )/\delta x$ denotes a central difference. Density ρ and sensible enthalpy h_s are stored at cell centers indexed by i, $i+1$, etc. Velocity u is stored at the cell face and indexed by $i+\frac{1}{2}$, etc. Here an overline applied to a face value ($i\pm\frac{1}{2}$ suffix) denotes a flux limiter, which is basically a special interpolation of the scalar field to the cell face. The purpose of the flux limiter is to prevent spurious oscillations in the scalar solution. Such oscillations must be avoided because they may lead to boundedness violations and instability.

In decomposing the flux divergence, our goal is to break the term into two parts as follows:

$$\begin{aligned}\left[\frac{\delta(\rho h_s u)}{\delta x}\right]_i &= \frac{\overline{(\rho h_s)}_{i+\frac{1}{2}}u_{i+\frac{1}{2}} - \overline{(\rho h_s)}_{i-\frac{1}{2}}u_{i-\frac{1}{2}}}{\delta x} \\ &= (\rho h_s)_i \underbrace{\frac{u_{i+\frac{1}{2}} - u_{i-\frac{1}{2}}}{\delta x}}_{\nabla\cdot\mathbf{u}} + \underbrace{\frac{\Delta_{i+\frac{1}{2}}u_{i+\frac{1}{2}} + \Delta_{i-\frac{1}{2}}u_{i-\frac{1}{2}}}{\delta x}}_{\overline{\mathbf{u}\cdot\nabla(\rho h_s)}}\end{aligned} \tag{B.12}$$

Here $\Delta_{i+\frac{1}{2}}$ represents a limited slope of the scalar data (ρh_s in this case) at the face $i+\frac{1}{2}$. The slope limiters for cell i are defined such that

$$(\rho h_s)_i + \Delta_{i+\frac{1}{2}} = \overline{(\rho h_s)}_{i+\frac{1}{2}} \tag{B.13}$$

$$(\rho h_s)_i - \Delta_{i-\frac{1}{2}} = \overline{(\rho h_s)}_{i-\frac{1}{2}} \tag{B.14}$$

Note that while scalar face values are unique to the face $\left[\overline{(\rho h_s)}_{i+\frac{1}{2}} = \overline{(\rho h_s)}_{i+1-\frac{1}{2}}\right]$, the limited slopes are not ($\Delta_{i+\frac{1}{2}} \neq \Delta_{i+1-\frac{1}{2}}$).

B.2.1 Example: Pure Upwinding

Suppose all $u > 0$ in 1D, a wind from left to right. For Godunov's scheme (first-order upwinding) the limited slopes would be computed as follows:

$$\begin{aligned}\Delta_{i+\frac{1}{2}} &= \overline{(\rho h_s)}_{i+\frac{1}{2}} - (\rho h_s)_i \\ &= (\rho h_s)_i - (\rho h_s)_i \\ &= 0\end{aligned} \tag{B.15}$$

$$\begin{aligned}\Delta_{i-\frac{1}{2}} &= (\rho h_s)_i - \overline{(\rho h_s)}_{i-\frac{1}{2}} \\ &= (\rho h_s)_i - (\rho h_s)_{i-1}\end{aligned} \tag{B.16}$$

The cell-average advection term therefore becomes

$$\overline{\mathbf{u}\cdot\nabla(\rho h_s)} = u_{i-\frac{1}{2}}\left[\frac{(\rho h_s)_i - (\rho h_s)_{i-1}}{\delta x}\right] \tag{B.17}$$

B.2.2 Example: Central Differencing

For central differencing the limited slopes would be computed as follows:

$$\begin{aligned}\Delta_{i+\frac{1}{2}} &= \overline{(\rho h_s)}_{i+\frac{1}{2}} - (\rho h_s)_i \\ &= \frac{1}{2}\left[(\rho h_s)_i + (\rho h_s)_{i+1}\right] - (\rho h_s)_i \\ &= \frac{1}{2}\left[(\rho h_s)_{i+1} - (\rho h_s)_i\right]\end{aligned} \tag{B.18}$$

$$\begin{aligned}\Delta_{i-\frac{1}{2}} &= (\rho h_s)_i - \overline{(\rho h_s)}_{i-\frac{1}{2}} \\ &= (\rho h_s)_i - \frac{1}{2}\left[(\rho h_s)_{i-1} + (\rho h_s)_i\right] \\ &= \frac{1}{2}\left[(\rho h_s)_i - (\rho h_s)_{i-1}\right]\end{aligned} \tag{B.19}$$

The cell-average advection term therefore becomes

$$\overline{\mathbf{u}\cdot\nabla(\rho h_s)} = \frac{1}{2}u_{i+\frac{1}{2}}\left[\frac{(\rho h_s)_{i+1} - (\rho h_s)_i}{\delta x}\right] + \frac{1}{2}u_{i-\frac{1}{2}}\left[\frac{(\rho h_s)_i - (\rho h_s)_{i-1}}{\delta x}\right] \tag{B.20}$$

B.2.3 General Implementation: Using Flux Limiters

The examples above are for illustration purposes only. In general, we first compute the flux-limited face values and obtain the limited slopes from (B.13) and (B.14). The cell-average advection term is then computed from the second underbrace in (B.12).

Appendix C

Absorption Coefficients

For the calculation of the gray or band-mean absorption coefficients, κ_n, a narrow-band model, RADCAL [16], has been implemented in FDS. RADCAL computes the spectral properties of the radiation participating species at discrete values of the spectrum (expressed either in wavenumber ω or in wavelength λ) and temperature, and returns two alternative mean absorption coefficients for each spectral band, n. The first coefficient is the Planck mean coefficient [108]

$$\kappa_n(P,T) = \frac{\pi}{\sigma T^4} \int_{\lambda_{\min}}^{\lambda_{\max}} I_{\mathrm{b},\lambda}(T) \sum_i 100 \bar{\kappa}_i(\lambda,T) P_i \, \mathrm{d}\lambda \tag{C.1}$$

where λ is the wavelength, expressed in units of μm, P_i is the partial pressure of participating species i, in units of atm, and $\bar{\kappa}_i$ is the spectral absorption coefficient of participating species i, in units of $\mathrm{atm}^{-1}\mathrm{cm}^{-1}$. Note that the temperature used in the calculation of κ_n is the local gas temperature; thus, $\kappa_n(P,T)$ is a function of the gas phase temperature and partial pressure and is independent of the pathlength. Its units are 1/m. The factor 100 is introduced to convert $\bar{\kappa}_i$ from $\mathrm{atm}^{-1}\mathrm{cm}^{-1}$ to $\mathrm{atm}^{-1}\mathrm{m}^{-1}$

The source term $I_{\mathrm{b},\lambda}(T)$ is the *Planck blackbody distribution law* which expresses the equilibrium rate of radiant energy emitted from a blackbody at temperature, T, and as function of wavelength, λ. Formally, the monochromatic blackbody radiant energy emitted at a wavelength λ is given by [109]

$$I_{\mathrm{b},\lambda}(T)\,\mathrm{d}\lambda = \frac{2hc^2\lambda^{-5}}{\exp\left(\dfrac{hc}{k_{\mathrm{B}}\lambda T}\right) - 1}\,\mathrm{d}\lambda \tag{C.2}$$

Here, h is the Planck constant (6.626×10^{-34} J·s), c is the speed of light in vacuum (2.998×10^{8} m/s), and k_{B} is the Boltzmann constant (1.381×10^{-23} J/K) [110]. $I_{\mathrm{b},\lambda}(T)$ is in units of $\mathrm{W/m^2/str/m}$; the wavelengths are converted from μm to m.

The second coefficient is the so-called *path mean* or *effective* absorption coefficient, $\kappa_{\mathrm{e},n}(T)$ which is defined according to the following equation

$$\int_{\lambda_{\min}}^{\lambda_{\max}} I(\lambda,L,T,T_{\mathrm{rad}})\,\mathrm{d}\lambda = \frac{\sigma}{\pi}\left[\left(1-\mathrm{e}^{-\kappa_{\mathrm{e},n}(T)L}\right)T^4 + \mathrm{e}^{-\kappa_{\mathrm{e},n}(T)L}T_{\mathrm{rad}}^4\right] \tag{C.3}$$

where L is the path length and T_{rad} is the effective temperature of flame radiation. RADCAL calculates the left hand integral by calculating the intensity leaving a uniform gas layer of equivalent thickness L, bounded by a black wall at temperature T_{rad}, for a large number of narrow spectral bands. By default in FDS, the pathlength, L, is five times the characteristic cell size of the simulation, limited by a maximum value of 10 m. It can also be specified by the user. If $T = T_{\mathrm{rad}}$ the intensity does not depend on $\kappa_{\mathrm{e},n}$. The value $\kappa_{\mathrm{e},n}(T_{\mathrm{rad}})$ is therefore interpolated from the neighbouring temperatures.

In cases with only one band (N=1), the smaller of the two absorption coefficients is used:

$$\kappa_n = \min\left(\kappa_n(P,T), \kappa_{e,n}(T)\right) \tag{C.4}$$

If $N > 1$ or $L = 0$, $\kappa_n = \kappa_n(P,T)$. Note that the spectral data within RADCAL are used whenever the gas mixture contains water vapor, fuel or combustion products, regardless of the number of radiation bands N.

Note on wavenumber, wavelength, and frequency: some confusion might arise when dealing with the various quantities describing the wave nature of radiation. These quantities are wavenumber ω, wavelength λ, and frequency denoted here ν. Most users may be familiar with the frequency ν, in units of *hertz*, Hz, representing the number of cycles per second. While this unit is preferred for radiation waves of low energy such as radio waves, wavelength and wavenumber are preferred for waves of higher energy. Wavenumber and wavelength are related to frequency through [109]

$$\lambda = c/\nu \text{ and } \omega = \nu/c \tag{C.5}$$

where c is the speed of light in a vacuum. The wavelength, λ, represents the distance traveled by the wave during one cycle, assuming it travels at the speed of light in a vacuum. Its units are commonly expressed in μm. Wavenumber, ω, is the reciprocal of the wavelength. It represents the number of cycles per unit length. In most infrared spectroscopic work, it is expressed in units of cm^{-1}. This is the unit used in the sections below. One can easily switch from wavenumber in units of cm^{-1} to wavelength in units of μm using the relation

$$\lambda\ \mu\text{m} = 10000/\omega\ \text{cm}^{-1} \tag{C.6}$$

Finally, the user who wishes to express the Planck blackbody distribution law as a function of wavenumber should take caution when performing the change of variables. One should start by expressing that the radiant energy emitted at a wavelength λ is the same as the radiant energy emitted at the corresponding wavenumber ω [108]

$$I_{b,\lambda}(T)\,d\lambda = -I_{b,\omega}(T)\,d\omega \tag{C.7}$$

the negative sign is introduced because ω is the reciprocal of λ. Since $\lambda = 1/\omega$, it comes

$$\frac{d\lambda}{d\omega} = -\frac{1}{\omega^2} \tag{C.8}$$

Equation C.7, can be rewritten using Eq. C.2 as

$$I_{b,\omega}(T)\,d\omega = \frac{2hc^2\omega^3}{\exp\left(\dfrac{hc\,\omega}{k_B T}\right) - 1}\,d\omega \tag{C.9}$$

$I_{b,\omega}(T)$ is in units of W/m/str/m^{-1}; the wavenumbers are converted from cm^{-1} to m^{-1}. The user who wishes to analyze the fuel bands presented below (given in wavenumber) with the Planck blackbody distribution law should use Eq. C.9 but should NOT use Eq. C.2 with $\lambda = 1/\omega$.

A combination of molecular models and data tables are used to compute the spectral radiative properties of the radiation participating species. The original version of RADCAL includes spectral properties of CO_2, H_2O, CO, and CH_4 that are either modeled through quantitative molecular spectroscopy derivations or tabulated from the fitting of experimental data into appropriate statistical narrow band models [16]. The original RADCAL data have been supplemented with new tabulated experimental data for the following fuels:

- Ethylene: C_2H_4

- Ethane: C_2H_6
- Propylene: C_3H_6
- Propane: C_3H_8
- Toluene: C_7H_8
- *n*-Heptane: C_7H_{16}
- Methanol: CH_3OH
- Methyl Methacrylate: $C_5H_8O_2$

These new data have been obtained through FTIR measurements for wavenumbers between 700 cm^{-1} and 4000 cm^{-1} [111]. A useful quantity to compare the relative importance of the different IR bands is provided by the integrated band intensity, α_i, defined for the ith participating species as [112]:

$$\alpha_i(T) = \int_{\omega_{min}}^{\omega_{max}} \bar{\kappa}_i(\omega', T)\ \mathrm{d}\omega' \tag{C.10}$$

whose units are $atm^{-1}cm^{-2}$. The value of the spectral absorption coefficient, $\bar{\kappa}_i$, is averaged over a narrow band whose spectral width, $\Delta\omega$, varies from 5 cm^{-1} for $\omega < 1100$ cm^{-1}, to 25 cm^{-1} for 1100 $cm^{-1} \leq \omega <$ 5000 cm^{-1}, and to 50 cm^{-1} for 5000 $cm^{-1} \leq \omega$.

The subsections below briefly describe the molecular bands where the species are active for each of the gas-phase radiative species, and provide for most of them the integrated band intensity of their most important bands at the indicated temperature. Outside these bands, the species are transparent. At the start of a simulation, the absorption coefficients are calculated using RADCAL and then tabulated as a function of species concentration and temperature. During the simulation, the local absorption coefficient is interpolated from the table of values. The contributions of individual species are summed to the the total absorption coefficient.

Carbon Dioxide: CO_2

Carbon dioxide is a linear molecule and has four vibrational modes, but only two fundamental IR vibration frequencies [113]. It has five distinct bands that are included in RADCAL, see Table C.1. The strongest

Table C.1: Spectral bands of CO_2 included in RADCAL.

Band #	Bounds (cm^{-1})		Method
1	500	880	tabulated
2	880	1100	modeled
3	1975	2475	modeled
4	3050	3800	modeled
5	4550	5275	modeled

band in the CO_2 spectrum is Band 3. At 300 K, it has an integrated band intensity of 2963 $atm^{-1}cm^{-2}$. The tabulated data were obtained from experiments with temperatures ranging from 300 K to 2400 K using the Goody statistical narrow band model.

Carbon Monoxide: CO

Carbon Monoxide is a diatomic molecule and as such, it has only one vibrational mode [113]. RADCAL includes one distinct band, see Table C.2. It corresponds to the stretching of the triple bond C ≡ O. The

Table C.2: Spectral bands of CO included in RADCAL.

Band #	Bounds (cm^{-1})		Method
1	1600	2400	modeled

first overtone (centered at $\omega \approx 4260\ cm^{-1}$) is not accounted for; its integrated band intensity is negligible at standard temperature and pressure. At 295 K, the integrated band intensity of Band 1 is 260 $atm^{-1}cm^{-2}$. The statistical narrow band model associated with CO is the Goody model. Recommended temperatures of use range from 295 K to 2500 K.

Water Vapor: H_2O

Due to the non-linearity of its molecular structure, the IR spectrum of water vapor is complex and broad [113]. In RADCAL, water vapor spectrum from 50 cm^{-1} to 9300 cm^{-1} is considered. Data in RADCAL are provided by Ludwig *et al.* [49]. Experimental data have been fitted using the statistical Goody narrow band model. The strongest bands at standard temperature and pressure are located in the ranges $[50-2100]\ cm^{-1}$: $\alpha = 300\ atm^{-1}cm^{-2}$, and $[3000-4000]\ cm^{-1}$: $\alpha = 220\ atm^{-1}cm^{-2}$.

Methane: CH_4

Methane is a spherical top molecule of tetrahedral shape with the carbon atom occupying the center of the tetrahedron [113]. It belongs to the point group T_d. The methane IR spectrum is the result of the vibration-rotation modes of the C – H groups. It has nine vibrational modes, but due to its symmetry, this translates into only two distinct IR active fundamental vibration frequencies. In RADCAL, the methane IR spectrum is divided into three distinct bands (fundamentals + degenerates), see Table C.3. The strongest

Table C.3: Spectral bands of CH_4 included in RADCAL.

Band #	Bounds (cm^{-1})		Method	Assignment	$\alpha(T = 296\ K)$ ($atm^{-1}cm^{-2}$)
1	1150	1600	tabulated	C – H Bend	237
2	2700	3250	tabulated	C – H Stretch	212
3	3400	5000	modeled	C – H Stretch	

bands are Bands 1 and 2 which at standard temperature and pressure have an integrated band intensity of 237 $atm^{-1}cm^{-2}$ and 212 $atm^{-1}cm^{-2}$, respectively. The tabulated data were obtained from high resolution FTIR experiments with temperatures varying from 300 K to 1400 K [111]. The spectral absorption coefficients were obtained assuming the FTIR measurements to be in the weak line regime and applying the Beer-Lambert Law to the experimental spectral transmissivity.

Ethylene: C_2H_4

Ethylene is a molecule with a plane symmetrical form and belongs to the point group D_{2h} [113]. The ethylene IR spectrum is the result of the vibration-rotation modes of the C = C, CH, and CH_2 groups. It

has 12 vibrational modes. In RADCAL, its IR spectrum is divided into four distinct bands, see Table C.4. Band 1 is the strongest absorbing band. All the ethylene IR spectral absorption data were obtained from high

Table C.4: Spectral bands of C_2H_4 included in RADCAL.

Band #	Bounds (cm^{-1})		Method	Assignment	$\alpha(T = 296\ K)$ ($atm^{-1}cm^{-2}$)
1	780	1250	tabulated	CH_2 Bend	366
2	1300	1600	tabulated	CH_2 Bend	43
3	1750	2075	tabulated	C = C Stretch	20
4	2800	3400	tabulated	C – H Stretch	183

resolution FTIR experiments with temperatures varying from 296 K to 801 K [111]. The spectral absorption coefficients were obtained by fitting the experimental spectral transmissivity of a homogeneous column of isothermal ethylene with a total pressure of 1 atm using the Goody model.

Ethane: C_2H_6

Ethane has a three-fold axis of symmetry and belongs to the point group D_{3d} [113]. The ethane IR spectrum is the result of the vibration-rotation modes of the C – C, CH, and CH_2 groups. It has 18 vibrational modes; its IR spectrum is divided into three distinct bands, see Table C.5. Band 3 corresponds to the stretching of

Table C.5: Spectral bands of C_2H_6 included in RADCAL.

Band #	Bounds (cm^{-1})		Method	Assignment	$\alpha(T = 296\ K)$ ($atm^{-1}cm^{-2}$)
1	730	1095	tabulated	CH_3 Rock	29
2	1250	1700	tabulated	CH Bend	64
3	2550	3375	tabulated	CH Stretch	761

CH and is the strongest absorbing band. At standard temperature and pressure, its integrated band intensity is more than 10 times the value of Band 2, and more than 20 times the value of Band 1. All the ethane IR spectral absorption data were obtained from high resolution FTIR experiments with temperatures varying from 296 K to 1000 K [111]. The spectral absorption coefficients were obtained by fitting the experimental spectral transmissivity of a homogeneous column of isothermal ethane with a total pressure of 1 atm using the Elsasser model.

Propylene: C_3H_6

Propylene has only one plane of symmetry and belongs to the point group C_s [113]. The propylene IR spectrum is the result of the vibration-rotation modes of the C – C, C = C, CH, CH_2, and CH_3 groups. It has 21 vibrational modes; its IR spectrum is divided into three distinct bands, see Table C.6. Band 3 corresponds to the stretching of CH and is the strongest of all Propylene absorbing bands. All the propylene IR spectral absorption data were obtained from high resolution FTIR experiments with temperatures varying from 296 K to 1003 K [111]. The spectral absorption coefficients were obtained by fitting the experimental spectral transmissivity of a homogeneous column of isothermal propylene with a total pressure of 1 atm using the Goody model.

Table C.6: Spectral bands of C_3H_6 included in RADCAL.

Band #	Bounds (cm^{-1})		Method	Assignment	$\alpha(T = 296\ K)$ ($atm^{-1}cm^{-2}$)
1	775	1150	tabulated	C – C Stretch, CH_3 Rock	296
2	1225	1975	tabulated	C = C Stretch, CH Bend	271
3	2650	3275	tabulated	CH Stretch	509

Propane: C_3H_8

Propane has two planes of symmetry and two axes of rotation. It belongs to the point group C_{2v} [113]. The propane IR spectrum is the result of the vibration-rotation modes of the C – C, CH_2, CH_3 groups. It has 27 vibrational modes; its IR spectrum is divided into two distinct bands, see Table C.7. Band 2 corresponds to

Table C.7: Spectral bands of C_3H_8 included in RADCAL.

Band #	Bounds (cm^{-1})		Method	Assignment	$\alpha(T = 295\ K)$ ($atm^{-1}cm^{-2}$)
1	1175	1675	tabulated	CH_3 Bending	121
2	2550	3375	tabulated	CH_3, CH_2 Stretch	1186

the stretching of CH_3 and CH_2 and is the strongest of all propane absorbing bands. For similar conditions, Band 1 has a much lower integrated band intensity. All the propane IR spectral absorption data were obtained from high resolution FTIR experiments with temperatures varying from 295 K to 1009 K [111]. The spectral absorption coefficients were obtained by fitting the experimental spectral transmissivity of a homogeneous column of isothermal propane with a total pressure of 1 atm using the Goody model.

Toluene: C_7H_8

Toluene has only one plane of symmetry. It belongs to the point group C_s [114]. The toluene IR spectrum is the result of the vibration-rotation modes of the C = C, CH, and CH_3 groups. It has 39 vibrational modes. For ease of modeling using statistical narrow band models, its IR spectrum has been divided into five distinct bands, see Table C.8. Band 5 corresponds to the stretching of CH_3 and CH, and it is the strongest absorbing

Table C.8: Spectral bands of C_7H_8 included in RADCAL.

Band #	Bounds (cm^{-1})		Method	Assignment	$\alpha(T = 300\ K)$ ($atm^{-1}cm^{-2}$)
1	700	805	tabulated	CH Bending	237
2	975	1175	tabulated	CH Bending	40
3	1275	1650	tabulated	CH_3 Bending	166
4	1650	2075	tabulated	C = C Stretching	101
5	2675	3225	tabulated	CH_3, CH Stretching	510

band. All the toluene IR spectral absorption data were obtained from high resolution FTIR experiments with temperatures varying from 300 K to 795 K [111]. The spectral absorption coefficients were obtained by fitting the experimental spectral transmissivity of a homogeneous column of isothermal toluene with a total pressure of 1 atm using the Goody model.

***n*-Heptane:** C_7H_{16}

n-heptane has two planes of symmetry and two axes of rotation. It belongs to the point group C_{2v} [114]. The *n*-heptane IR spectrum results from the vibration-rotation modes of the $C-C$, CH_2, and CH_3 groups. It has 63 vibrational modes. For ease of modeling using statistical narrow band models, its IR spectrum has been divided into two distinct bands, see Table C.9. Band 2 corresponds to the stretching of CH_3 and CH_2

Table C.9: Spectral bands of C_7H_{16} included in RADCAL.

Band #	Bounds (cm^{-1})		Method	Assignment	$\alpha(T = 293\ K)$ ($atm^{-1}cm^{-2}$)
1	1100	1800	tabulated	CH_2, CH_3 Bending	298
2	2250	3275	tabulated	CH_2, CH_3 Stretching	3055

groups, and is the strongest absorbing band. All the *n*-heptane IR spectral absorption data were obtained from high resolution FTIR experiments with temperatures varying from 293 K to 794 K [111]. The spectral absorption coefficients were obtained by fitting the experimental spectral transmissivity of a homogeneous column of isothermal *n*-heptane with a total pressure of 1 atm using the Goody model.

Methanol: CH_3OH

Methanol has only one plane of symmetry. It belongs to the point group C_s [113]. The methanol IR spectrum results from the vibration-rotation modes of the $C-O$, OH, and CH_3 groups. It has 12 vibrational modes. For ease of modeling using statistical narrow band models, its IR spectrum has been divided into four distinct bands, see Table C.10. Band 3 corresponds to the stretching of the CH_3 group and is the strongest absorbing

Table C.10: Spectral bands of CH_3OH included in RADCAL.

Band #	Bounds (cm^{-1})		Method	Assignment	$\alpha(T = 293\ K)$ ($atm^{-1}cm^{-2}$)
1	825	1125	tabulated	$C-O$ Stretching	593
2	1125	1700	tabulated	CH_3, OH Bending	197
3	2600	3225	tabulated	CH_3 Stretching	684
4	3525	3850	tabulated	OH Stretching	112

band. All the methanol IR spectral absorption data were obtained from high resolution FTIR experiments with temperatures varying from 293 K to 804 K [111]. The spectral absorption coefficients were obtained by fitting the experimental spectral transmissivity of a homogeneous column of isothermal methanol with a total pressure of 1 atm using the Goody model.

Methyl Methacrylate: $C_5H_8O_2$

Methyl Methacrylate or MMA has the most complex IR spectrum of all the fuels presented above. With 15 atoms, it has 39 vibrational modes [114]. The MMA IR spectrum results from the vibration-rotation modes of the $C-O$, $C=O$, $C=C$, CH_2, and CH_3 groups. For ease of modeling using statistical narrow band models, its IR spectrum has been divided into six distinct bands, see Table C.11. Band 3 corresponds to the stretching of the $C-O$ group and has the highest integrated band intensity. All the MMA IR spectral absorption data were obtained from high resolution FTIR experiments with temperatures varying from 396 K

Table C.11: Spectral bands of $C_5H_8O_2$ included in RADCAL.

Band #	Bounds (cm^{-1})		Method	Assignment	$\alpha(T = 396\,K)$ ($atm^{-1}cm^{-2}$)
1	750	875	tabulated	CH_2 Bending	42
2	875	1050	tabulated	CH_2 Bending	131
3	1050	1250	tabulated	$C-O$ Stretching	800
4	1250	1550	tabulated	CH_3 Bending	490
5	1550	1975	tabulated	$C=C, C=O$ Stretching	538
6	2650	3275	tabulated	CH_2, CH_3 Stretching	294

to 803 K [111]. The spectral absorption coefficients were obtained by fitting the experimental spectral transmissivity of a homogeneous column of isothermal MMA with a total pressure of 1 atm using the Goody model.

Statistical Narrow Band Models

This section briefly describes the statistical models used to obtain most of the tabulated species IR spectral absorption coefficients at different temperatures, $\bar{\kappa}_i(\omega, T)$. Narrow band models are used in lieu of line-by-line models to represent the IR spectra of radiating species in engineering applications. In the narrow band approach, the whole spectrum is divided into small spectral bands (typically several cm^{-1}), and different statistical approaches are used to compute the average radiative properties over these narrow bands. Two main models are presented below: the Elsasser model and the Goody model. Both models assume Lorentz lines.

The Elsasser model assumes all the lines to have the same shape, same strength, and to be equally spaced from each other. In this model, the spectral transmissivity, $\bar{\tau}_\omega$, of a homogeneous isothermal column filled with only some gas of species i, at a total pressure P_T and with an optical pathlength $U = P_i L$ (L being the column physical length and P_i the ith participating radiating species partial pressure), is given by the expression [115]:

$$\bar{\tau}_\omega = 1 - \mathrm{erf}\left(\frac{\sqrt{\pi}\,\bar{\kappa}_i U}{\sqrt{1 + \dfrac{\pi\,\bar{\kappa}_i U}{4\,\bar{\gamma}_i P_T}}} \right) \tag{C.11}$$

where $\bar{\gamma}_i$ is the spectral fine structure parameter of the narrow band. Its units are in atm^{-1}. $\bar{\kappa}_i$ is the spectral absorption coefficient of the narrow band. Its units are in $atm^{-1}cm^{-1}$. The Goody model assumes all the lines to have the same shape, but to be randomly spaced within the narrow band, and their line strength follows an exponential distribution. For this model, the spectral transmissivity is given by the expression [115]:

$$\bar{\tau}_\omega = \exp\left(-\frac{\bar{\kappa}_i U}{\sqrt{1 + \dfrac{\bar{\kappa}_i U}{4\,\bar{\gamma}_i P_T}}} \right) \tag{C.12}$$

For both models, the two narrow band spectral quantities of the ith species ($\bar{\kappa}_i$ and $\bar{\gamma}_i$) are obtained either from line-by-line calculations or by fitting experimental data.

Note: For all the tabulated data, a linear interpolation of $\bar{\kappa}_i$ and $\bar{\gamma}_i$ in temperature and/or in wavenumber is performed by RADCAL when necessary. If the temperature sought is out of the tabulated data range, then the data at the nearest temperature are used.

Appendix D

A Simple Model of Flame Extinction

Frederick W. Mowrer, Department of Fire Protection Engineering, University of Maryland

A diffusion flame immersed in a vitiated atmosphere will extinguish before consuming all the available oxygen from the atmosphere. The classic example of this behavior is a candle burning within an inverted jar. This same concept has been applied within FDS to determine the conditions under which the local ambient oxygen concentration will no longer support a diffusion flame. In this appendix, the critical adiabatic flame temperature concept is used to estimate the local ambient oxygen concentration at which extinction will occur.

Consider a control volume characterized by a bulk temperature, T_m, a mass, m, an average specific heat, $\overline{c_p}$, and an oxygen mass fraction, Y_{O_2}. Complete combustion of the oxygen within the control volume would release a quantity of energy given by:

$$Q = m\hat{Y}_{O_2}\left(\frac{\Delta H}{r_{O_2}}\right) \tag{D.1}$$

where $\Delta H/r_{O_2}$ has a relatively constant value of approximately 13100 kJ/kg for most fuels of interest for fire applications.[1] Under adiabatic conditions, the energy released by combustion of the available oxygen within the control volume would raise the bulk temperature of the gases within the control volume by an amount equal to:

$$Q = m\overline{c_p}(T_f - T_m) \tag{D.2}$$

The average specific heat of the gases within the control volume can be calculated based on the composition of the combustion products as:

$$\overline{c_p} = \frac{1}{(T_f - T_m)}\sum_{\alpha}\int_{T_m}^{T_f} c_{p,\alpha}(T)\,dT \tag{D.3}$$

To simplify the analysis, the combustion products are assumed to have an average specific heat over the temperature range of interest. The relationship between the oxygen mass fraction within the control volume and the adiabatic temperature rise of the control volume is evaluated by equating Eqs. (D.1) and (D.2):

$$\hat{Y}_{O_2,lim} = \frac{\overline{c_p}(T_f - T_m)}{\Delta H/r_{O_2}} \tag{D.4}$$

If $\hat{Y}_{O_2} < \hat{Y}_{O_2,lim}$ then combustion is not allowed and $\Delta\hat{Y}_F$ is set to 0.

As an example, the critical adiabatic flame temperature can be assumed to have a constant value of approximately 1700 K for hydrocarbon diffusion flames, as suggested by Beyler[2]. The combustion products

[1] C. Huggett, "Estimation of the Rate of Heat Release by Means of Oxygen Consumption," *Fire and Materials*, Vol. 12, pp. 61-65, 1980.

[2] C. Beyler, "Flammability Limits of Premixed and Diffusion Flames," *SFPE Handbook of Fire Protection Engineering* (3rd Ed.), National Fire Protection Association, Quincy, MA, 2003.

can have an average specific heat of 1.2 kJ/(kg · K) which is a value similar to that of nitrogen, the primary component of the products. Then, the relationship between the limiting oxygen mass fraction and the bulk temperature of a control volume is given by:

$$\hat{Y}_{O_2,lim} = \frac{\overline{c_p}(T_{CFT} - T_m)}{\Delta H / r_{O_2}} \approx \frac{1.2\,(1700 - T_m)}{13100} \tag{D.5}$$

For a control volume at a temperature of 300 K, i.e., near room temperature, the limiting oxygen mass fraction would evaluate to $\hat{Y}_{O_2,lim} = 0.128$. This value is consistent with the measurements of Morehart, Zukoski and Kubota[3] who measured the oxygen concentration at extinction of flames by dilution of air with combustion products. They found that flames self-extinguished at oxygen concentrations of 12.4 % to 14.3 %. Note that their results are expressed as volume, not mass, fractions. Beyler's chapter in the SFPE Handbook references other researchers who measured oxygen concentrations at extinction ranging from 12 % to 15 %.

[3] Morehart, J., Zukoski, E., and Kubota, T., "Characteristics of Large Diffusion Flames Burning in a Vitiated Atmosphere," *Third International Symposium on Fire Safety Science*, Elsevier Science Publishers, pp. 575-583, 1991.

Appendix E

Numerical Methods for Integration of Complex Chemistry

To solve the system of ordinary differential equations used for complex chemistry (e.g., multi-step reactions, reversible reactions), FDS uses a second-order Runge-Kutta (RK2) scheme as the foundation for its numerical integrator. As discussed below, the scheme is augmented with Richardson extrapolation, which increases the accuracy to fourth-order and provides a means of error control. The general procedure of using an explicit integration scheme with an error controller to maintain stability and speed is similar to that of Mott and Oran [116].

Our goal is to integrate the ODE

$$\frac{\mathrm{d}Y}{\mathrm{d}t} = f(Y) \tag{E.1}$$

where $f(Y)$ represents a reaction rate law and Y is a species mass fraction (temperature dependence of the rate law is frozen at the initial condition). The total time interval is the FDS time step, δt, and the iteration substep is Δt. The RK2 scheme is given by

$$\begin{aligned} Y^* &= Y^k + \Delta t^k f(Y^k) \\ Y^{k+1} &= \frac{1}{2}\left(Y^k + Y^* + \Delta t^k f(Y^*)\right) \end{aligned} \tag{E.2}$$

Here k is the iteration index. The number of sub-time intervals is determined by an error controller, as described below. This second-order scheme is an improvement upon the first-order explicit scheme used for simple chemistry. To maintain stability for stiff problems, however, an intractable number of time steps may be required.

Richardson Extrapolation

To overcome this issue, we use Richardson extrapolation. Richardson extrapolation increases the order of accuracy and provides a means of error control. Suppose you have an exact solution A represented by a numerical approximation using the interval h such that the error, $A - A(h)$, can be represented by a polynomial expansion of h. For two different intervals h and $h/2$ we may write

$$A_1 = A(h) + \underbrace{a_1(h) + a_2(h)^2 + O(h^3)}_{O(h)} \tag{E.3}$$

$$A_2 = A\left(\frac{h}{2}\right) + \underbrace{a_1\left(\frac{h}{2}\right) + a_2\left(\frac{h}{2}\right)^2 + O(h^3)}_{O(h)} \tag{E.4}$$

Here the subscript on A represents subdivisions of the time step h, where A_1 takes $h/1$ steps, A_2 takes $h/2$ steps, and so on. The a_1 terms can be eliminated by subtracting Eq. (E.3) from two times Eq. (E.4):

$$A = 2A_2 - A_1 = 2A\left(\frac{h}{2}\right) - A(h) + \underbrace{a_2\left(\frac{h}{2}\right)^2 + O(h^3)}_{O(h^2)} \tag{E.5}$$

which results in a solution with a higher order of error.

This same technique is applied to the second-order Runge-Kutta scheme with three sub-intervals: h, $h/2$, and $h/4$. Because the RK2 scheme was initially second-order, the three-step Richardson extrapolation gives a fourth-order solution [117]:

$$A = \frac{4A_4 - A_2}{3} + O(h^4) \tag{E.6}$$

In Eq. (E.6), A represents the time updated value of the species concentrations in the mixed reactor zone, $\hat{Y}_\alpha$, as found in Eq. (5.39).

Error Control

In addition to increasing the order of the error in the numerical scheme, Richardson extrapolation also provides an estimate of the error value. This estimate is calculated via a Taylor expansion:

$$error \approx \frac{1}{15}\left(\frac{4A_4 - A_2}{3} - \frac{4A_2 - A_1}{3}\right) \tag{E.7}$$

The time step (Δt_{new}) required to maintain the specified/acceptable error (err_tol) can be calculated by using the local error ($error$), the current time step (Δt), and the order of error within the numerical integration scheme, in this case fourth-order:

$$\Delta t_{new} = \Delta t\left(\frac{err\_tol}{error}\right)^{1/4} \tag{E.8}$$

Eq. (E.8) indicates that if the error estimate is large relative to the tolerance, then the new time step decreases; whereas if the error is small, then the new time step increases. This dynamic time stepping scheme improves computational efficiency because it allows the integrator to take the largest time step possible bounded by either the error tolerance or the global simulation time step, thus minimizing the total number of integration steps required.

A Total Variation Scheme for Stiff Chemistry

The stiffness associated with a flame front is handled by the error controller and variable time stepping discussed above. The scheme discussed in this section automatically detects chemical equilibrium, the explicit integration of which is also a stiff problem. Even with error control, the numerical solution may exhibit numerical fluctuations between the bounds of the error tolerance. This is an undesirable condition which often occurs in cases with competing or reversible reactions.

If the values are fluctuating around a fixed value bounded by the error tolerance, the integrator is doing extra work by continuing to calculate every fluctuation within a time step. To minimize the computational expense, a total variation (TV) scheme has been developed. This scheme examines the differences in species mass fractions at four consecutive sub-time steps. Within this four point stencil, there are three differences for each species mass fraction. The TV scheme compares the absolute value of the sum of the differences

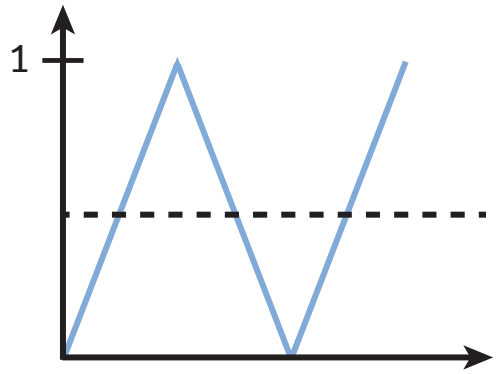

Figure E.1: Illustration of a quantity fluctuating between 0 and 1 about a fixed value.

to the sum of the absolute values of the differences. For a monotonic function, the following condition must hold:

$$\sum_{i=1}^{4} |Y(i+1) - Y(i)| = |\sum_{i=1}^{4} (Y(i+1) - Y(i))| \tag{E.9}$$

The reader unfamiliar with the concept of "data variation" should stop and think about this for a moment. It says that, regardless of other complexities, the monotonicity constraint (no fluctuations) is sufficient to guarantee the condition stated in Eq. (E.9). The corollary is that if Eq. (E.9) does not hold, then we are guaranteed to have some level of fluctuation.

The condition which corresponds to the extreme case of repeating fluctuations between the error tolerance bounds for our four point stencil is

$$\sum_{i=1}^{4} |Y(i+1) - Y(i)| = 3\,|\sum_{i=1}^{4} (Y(i+1) - Y(i))| \tag{E.10}$$

This is illustrated in Fig. E.1, which shows a quantity fluctuating between 0 and 1 about a fixed point. We can compare the sum of the absolute value of the differences between the four points,

$$\sum_{i=1}^{4} |Y(i+1) - Y(i)| = |1-0| + |0-1| + |1-0| = 3 \tag{E.11}$$

to the absolute value of the sum of the differences,

$$|\sum_{i=1}^{4} (Y(i+1) - Y(i))| = |(1-0) + (0-1) + (1-0)| = 1 \tag{E.12}$$

The ratio of Eq. (E.11) and Eq. (E.12) is 3, which indicates that this data is fluctuating. For the implementation of this scheme in FDS, instead of comparing directly to 3, we use 2.9 because floating point division might not return a value of exactly 3. If fluctuations have been identified, then the values at the fourth point in the stencil are frozen and become the final values at the end of an integration time step. This prevents unnecessary sub-time steps being taken by the integrator. Because the error controller is bounding the solution, any one of the values within the stencil is also within the error tolerance and is therefore acceptable.

Appendix F

The Unmixed Fraction

Moments of the PDF Transport Equation

As discussed by Pope [14], the PDF (5.24) evolves by the Fokker-Planck equation:

$$\frac{\partial f}{\partial t} = -\frac{\partial}{\partial \psi_\alpha}\left(f \left\langle \frac{\partial Y_\alpha}{\partial t} \middle| \psi_\alpha \right\rangle \right). \tag{F.1}$$

The term on the right in angled brackets is a conditional mean. Here it is modeled using a variant of IEM [46] which we call 'interaction by exchange with the mixed mean' or IEMM. When including chemical reaction, the conditional mean is modeled by

$$\left\langle \frac{\partial Y_\alpha}{\partial t} \middle| \psi_\alpha \right\rangle = \frac{1}{\tau_{\text{mix}}}(\hat{Y}_\alpha - \psi_\alpha) + \frac{\mathrm{d}\hat{Y}_\alpha}{\mathrm{d}t}. \tag{F.2}$$

Using (F.2), the zeroth moment of (F.1) yields (5.30). The zeroth and first moments of (F.1) combine to yield the model for the chemical source term (5.31), once multiplied by density.

Derivation of First Moment Equation

$$\int \psi_\beta \left[\frac{\partial f}{\partial t} = -\frac{\partial}{\partial \psi_\alpha}\left(f \left\langle \frac{\partial Y_\alpha}{\partial t} \middle| \psi_\alpha \right\rangle \right) \right] \mathrm{d}\psi_\beta \tag{F.3}$$

LHS:

$$\int \left[\frac{\partial f \psi_\beta}{\partial t} - f \underbrace{\frac{\partial \psi_\beta}{\partial t}}_{0} \right] \mathrm{d}\psi_\beta = \frac{\mathrm{d}\widetilde{Y}_\beta}{\mathrm{d}t} \tag{F.4}$$

RHS:

$$\int -\psi_\beta \frac{\partial}{\partial \psi_\alpha}\left(f \left\{ \frac{1}{\tau_{\text{mix}}}(\hat{Y}_\alpha - \psi_\alpha) + \frac{\mathrm{d}\hat{Y}_\alpha}{\mathrm{d}t} \right\} \right) \mathrm{d}\psi_\beta = \\ - \underbrace{\int \frac{\partial}{\partial \psi_\alpha}\left[\psi_\beta f\{\ \} \right] \mathrm{d}\psi_\beta}_{0 \text{ by Pope Exercise 12.1 [14]}} + \int f\{\ \} \underbrace{\frac{\partial \psi_\beta}{\partial \psi_\alpha}}_{\delta_{\alpha\beta}} \mathrm{d}\psi_\beta \tag{F.5}$$

$$
\begin{aligned}
&= \frac{1}{\tau_{\text{mix}}}(\hat{Y}_\beta - \widetilde{Y}_\beta) + (1-\zeta)\frac{\mathrm{d}\hat{Y}_\beta}{\mathrm{d}t} \\
&= \frac{1}{\tau_{\text{mix}}}(\hat{Y}_\beta - [\zeta\widetilde{Y}^0_\beta + (1-\zeta)\hat{Y}_\beta]) + (1-\zeta)\frac{\mathrm{d}\hat{Y}_\beta}{\mathrm{d}t} \\
&= \frac{\zeta}{\tau_{\text{mix}}}(\hat{Y}_\beta - \widetilde{Y}^0_\beta) + (1-\zeta)\frac{\mathrm{d}\hat{Y}_\beta}{\mathrm{d}t}
\end{aligned} \tag{F.6}
$$

Evolution of the Unmixed Fraction

Equation (5.28) may be derived as follows. Differentiating (5.30) in time we get

$$
\begin{aligned}
\frac{\mathrm{d}\widetilde{Y}_\alpha}{\mathrm{d}t} &= \widetilde{Y}^0_\alpha\frac{\mathrm{d}\zeta}{\mathrm{d}t} + (1-\zeta)\frac{\mathrm{d}\hat{Y}_\alpha}{\mathrm{d}t} - \hat{Y}_\alpha\frac{\mathrm{d}\zeta}{\mathrm{d}t} \\
&= -\frac{\mathrm{d}\zeta}{\mathrm{d}t}(\hat{Y}_\alpha - \widetilde{Y}^0_\alpha) + (1-\zeta)\frac{\mathrm{d}\hat{Y}_\alpha}{\mathrm{d}t}
\end{aligned} \tag{F.7}
$$

Comparing (F.7) with (F.6) we see that during the reactor step the unmixed fraction evolves by

$$
\frac{\mathrm{d}\zeta}{\mathrm{d}t} = -\frac{\zeta}{\tau_{\text{mix}}}. \tag{F.8}
$$

Note that while (5.31) invokes (F.8) in its derivation, (F.6) does not—it is an independent derivation that relies on the choice of mixing model, in this case a variant of IEM as shown in (F.2).

Appendix G

Limiting Behavior of the PaSR Model

G.1 Burke-Schumann Solution

When the reactants are initially completely mixed ($\zeta_0 = 0$) and the chemical kinetics are infinitely fast for a single step reaction, Fuel + Air $\rightarrow$ Products, the present model reduces to the Burke-Schumann solution (see, e.g., [118]), where the cell mean mixture fraction is given by

$$\widetilde{Z} = \widetilde{Y}_{\mathrm{F}} + \left(\frac{1}{1+s}\right)\widetilde{Y}_{\mathrm{P}}. \tag{G.1}$$

G.2 Basic EDC

When the reactants are initially unmixed ($\zeta_0 = 1$) and the kinetics are infinitely fast, our model reduces to the Eddy Dissipation Concept (EDC) as described in [39]. First, write (5.31) for Fuel (F) with $\zeta = 1$:

$$\dot{m}'''_{\mathrm{F}} = \rho \frac{1}{\tau_{\mathrm{mix}}}(\hat{Y}_{\mathrm{F}} - \widetilde{Y}^0_{\mathrm{F}}). \tag{G.2}$$

For infinitely fast kinetics, the Fuel composition in the mixed zone is

$$\hat{Y}_{\mathrm{F}} = \begin{cases} 0 & \text{if} \quad \widetilde{Y}^0_{\mathrm{F}} \le \widetilde{Y}^0_{\mathrm{A}}/s \quad \text{(excess Air)}, \\ \widetilde{Y}^0_{\mathrm{F}} - \widetilde{Y}^0_{\mathrm{A}}/s & \text{if} \quad \widetilde{Y}^0_{\mathrm{F}} > \widetilde{Y}^0_{\mathrm{A}}/s \quad \text{(excess Fuel)}. \end{cases} \tag{G.3}$$

Using (G.3) in (5.13) we recover the basic EDC model:

$$\dot{m}'''_{\mathrm{F}} = -\rho \frac{\min(\widetilde{Y}^0_{\mathrm{F}}, \widetilde{Y}^0_{\mathrm{A}}/s)}{\tau_{\mathrm{mix}}}. \tag{G.4}$$

G.3 Extended EDC

When the unmixed fraction is held constant ($\zeta = \zeta_0$), our formulation may be cast as an extended EDC model with the mixed reactor zone treated as a perfectly stirred reactor (PSR). Previous authors [44, 45, 119] have referred to the mixed reactor zone as the "fine structure region." In the notation of [45], the extended EDC reaction rate model, comparable to (5.31) in this paper, is given by

$$\rho \frac{\mathrm{d}\widetilde{Y}_\alpha}{\mathrm{d}t} = \rho \frac{\gamma_\lambda^2 \chi}{\tau^\star} \left(Y^0_\alpha - Y^\star_\alpha\right), \tag{G.5}$$

where γ_λ is the "ratio between the mass of the fine structure and the total mass of the subgrid structure" and χ is the probability of fine structure burning [45]; in practice, both quantities are between 0 and 1. The reactor residence time is denoted $\tau^\star$, clearly comparable to our mixing time scale, and the fine structure mass fraction is $Y_\alpha^\star$, clearly comparable to our mixed zone mass fraction $\hat{Y}_\alpha$. Panjwani et al. [45] refer to Y_α^0 as the mass fraction of the "surrounding state," thus equivalent to our initial cell mean $\widetilde{Y}_\alpha^0$.

Appendix H

Scalar Boundedness Correction

Second-order central differencing of the advection term in the scalar transport equation leads to dispersion errors (spurious wiggles) and these errors, if left untreated, can lead to scalar fields which are physically not realizable, e.g., negative densities. To prevent this, FDS employs a boundedness correction to the scalar fields after the explicit transport step. The correction, which we describe below, acts locally and effectively adds the minimum amount of diffusion necessary to prevent boundedness violations. This correction does not make the scalar transport scheme total variation diminishing (TVD); it only serves to correct for boundedness. Similar schemes are employed by others (e.g., [120]).

By default, FDS employs a TVD transport scheme (Superbee [18] for LES and CHARM [19] for DNS). These TVD schemes are applied during the transport step and each can be shown to be TVD in one dimension under certain CFL constraints. However, except for Godunov's scheme, the TVD proofs do not extend to three dimensions [20]. Still, these schemes do a much better job than pure central differencing at mitigating dispersion error. Note that even though TVD schemes are applied, FDS still checks for boundedness in case any small violations are not prevented by the flux limiter.

A simple case

For simplicity we start by considering a minimum boundedness violation for density in 1-D. That is, somewhere we have $\rho < \rho_{\min}$. Let ρ_i^* denote the resulting density from the explicit transport step for cell i with volume V_i. Our goal is to find a correction $\delta\rho_i$ which:

(a) satisfies boundedness, $\rho_i = \rho_i^* + \delta\rho_i \geq \rho_{\min}$ for all i

(b) conserves mass, $\sum_i \delta\rho_i V_i = 0$

(c) minimizes data variation, $\sum_i |\delta\rho_i|$ (i.e., we change the field as little as possible)

The basic idea is to apply a linear smoothing operator, $\mathscr{L}$, to the density field in regions where boundedness violations have occurred. So, the correction may be viewed as an explicit diffusion step applied to the uncorrected field with diffusion coefficient c:

$$\rho = \rho^* + c\,\mathscr{L}(\rho^*) \tag{H.1}$$

To make matters simple, let us envision for the moment that the density in cell i is negative but that the densities in cells $i-1$ and $i+1$ are both safely in bounds (this actually is what happens most of the time with dispersion error). We therefore want a correction that takes mass away from $i-1$ and $i+1$ and moves it to i to make up the deficit. We know that for cell i the minimum change in mass and therefore the minimum

correction that will satisfy boundedness is $\delta\rho_i = \rho_{\min} - \rho_i^*$. The operator $\mathscr{L}$ takes the form of the standard discrete Laplacian. The correction for cell i is simply

$$\begin{aligned}\rho_i &= \rho_i^* + \delta\rho_i \\ &= \rho_i^* + \rho_{\min} - \rho_i^* \\ &= \rho_i^* + c_i(\rho_{i-1}^* - 2\rho_i^* + \rho_{i+1}^*)\end{aligned} \tag{H.2}$$

Comparing the second and third lines, we find that the diffusion coefficient is given by

$$c_i = \frac{\rho_{\min} - \rho_i^*}{\rho_{i-1}^* - 2\rho_i^* + \rho_{i+1}^*} \tag{H.3}$$

Based on the third line of (H.2), the correction for cell i may be thought of as the sum of the two mass fluxes from its neighboring cells. The change in mass of cell i is $\delta m_i = \delta\rho_i V_i$ and is balanced by changes in mass for cells $i-1$ and $i+1$:

$$\begin{aligned}\delta m_{i-1} &= -c_i\,(\rho_{i-1}^* - \rho_i^*)\,V_i \\ \delta m_{i+1} &= -c_i\,(\rho_{i+1}^* - \rho_i^*)\,V_i\end{aligned}$$

In this case the sum of the mass corrections is zero, as desired:

$$\begin{aligned}\sum_{j=i-1}^{i+1} \delta m_j &= \delta\rho_{i-1}V_{i-1} + \delta\rho_i V_i + \delta\rho_{i+1}V_{i+1} \\ &= -c_i\,(\rho_{i-1}^* - \rho_i^*)\,V_i + c_i\,(\rho_{i-1}^* - 2\rho_i^* + \rho_{i+1}^*)\,V_i - c_i\,(\rho_{i+1}^* - \rho_i^*)\,V_i \\ &= 0\end{aligned}$$

Realistic cases

The discussion above was to provide a simple case for understanding the basic idea behind the correction method. In a realistic case we must account for multi-dimensional aspects of the problem and for the possibility that neighboring cells may both be out of bounds. Consider a grid cell whose density is outside the specified range. Denote this cell with a "c" for center. Its volume is V_c and density is ρ_c^*, obtained from the transport scheme. Let the subscript "n" denote any of the six neighboring cells (in other words, only include cells which share a face with cell c). We want to correct any boundedness violations for the cell c by shifting mass to or from its neighboring cells n:

$$\rho_c = \rho_c^* + \delta\rho_c \quad ; \quad \rho_n = \rho_n^* + \delta\rho_n \tag{H.4}$$

We first define the total amount of mass we wish to shift:

$$m_c = |\rho_c^* - \rho_{\text{cut}}|\,V_c \tag{H.5}$$

where ρ_{cut} is the appropriate upper or lower bound of the density. The amount of mass each neighboring cell can accommodate without falling outside the range is:

$$m_n = \left|\min\left[\rho_{\max}, \max[\rho_{\min}, \rho_n^*]\right] - \rho_{\text{cut}}\right| V_n \tag{H.6}$$

The correction terms that guarantee mass conservation ($V_c\,\delta\rho_c = -\sum V_n\,\delta\rho_n$) are:

$$\delta\rho_c = \pm\min\left[m_c, \sum m_n\right]/V_c \quad ; \quad \delta\rho_n = \mp\min\left[\frac{m_c}{\sum m_n}, 1\right] m_n/V_n \tag{H.7}$$

Next, to correct species mass fractions that are out of bounds, we follow the exact same procedure.

$$Z_c = Z_c^* + \delta Z_c \quad ; \quad Z_n = Z_n^* + \delta Z_n \tag{H.8}$$

We define the amount of species mass we wish to shift:

$$m_c = |Z_c^* - Z_{\text{cut}}| \, \rho_c V_c \tag{H.9}$$

where Z_{cut} is either 0 or 1. The amount of species mass each neighboring cell can accommodate without falling outside the range is:

$$m_n = \left| \min \left[1, \max[0, Z_n^*] \right] - Z_{\text{cut}} \right| \rho_n V_n \tag{H.10}$$

The correction terms that guarantee mass conservation ($V_c \, \rho_c \, \delta Z_c = -\sum V_n \, \rho_n \, \delta Z_n$) are:

$$\delta Z_c = \pm \min \left[m_c, \sum m_n \right] / (\rho_c V_c) \quad ; \quad \delta Z_n = \mp \min \left[\frac{m_c}{\sum m_n}, 1 \right] m_n / (\rho_n V_n) \tag{H.11}$$

Appendix I

Fluid-Particle Momentum Transfer

The trajectories of Lagrangian particles in FDS could be calculated with Forward Euler (FE) time integration. However, Forward Euler extracts momentum from the cell corresponding to each particle's initial position and this may cause large changes in the flow field and ultimately instability unless the time step is extremely small. Consequently, a stable, single-step approximate solution is developed and is implemented in FDS.

Two effects are neglected in this formulation. The first is the effect of the change in droplet mass between time steps. The droplet's evaporation is not coupled to this model. This is justified because the change in droplet mass per time step is small. The second neglected effect is the change in drag coefficient between time steps. This is justified because of the large uncertainties in the drag coefficients. Modeling the time derivative of the drag coefficient would not improve accuracy beyond these uncertainties, but it would slow down the code.

Relative velocities

Let m_p denote the particle mass, $\mathbf{u}$ the particle velocity, A_p the particle cross-sectional area, C_d the particle drag coefficient, ρ the fluid mass density, $\mathbf{U}$ the fluid velocity around the particle, V_g the volume occupied by the fluid in a cell, $M \equiv \rho V_\mathrm{g}$ the fluid mass of a cell, n_p the number of particles in a cell, $M_\mathrm{p} \equiv M/n_\mathrm{p}$ the average fluid mass per particle in a cell, and $\mathbf{g}$ the gravitational acceleration vector.

The equations of motion of the particles and fluid are formulated as follows from Newton's second law,

$$m_\mathrm{p}\frac{\mathrm{d}\mathbf{u}}{\mathrm{d}t} = -\frac{1}{2}\rho C_\mathrm{d} A_\mathrm{p}(\mathbf{u}-\mathbf{U})|\mathbf{u}-\mathbf{U}| + m_\mathrm{p}\mathbf{g} \tag{I.1}$$

$$M_\mathrm{p}\frac{\mathrm{d}\mathbf{U}}{\mathrm{d}t} = \frac{1}{2}\rho C_\mathrm{d} A_\mathrm{p}(\mathbf{u}-\mathbf{U})|\mathbf{u}-\mathbf{U}|\,. \tag{I.2}$$

Note that the fluid Eq. (I.2) does not include a gravity term. This gravity term is included in the Navier-Stokes equations; including it here would be redundant. Also note that lift is not included here.

If we define $\mathbf{u}_\mathrm{r} \equiv \mathbf{u} - \mathbf{U}$ as the relative velocity between the fluid and the particle, we can find a single equation for the relative velocity by dividing both equations by their respective masses (i.e., m_p and M_p) and then subtracting the second from the first. This result is

$$\frac{\mathrm{d}\mathbf{u}_\mathrm{r}}{\mathrm{d}t} = -\frac{1}{2}\rho C_\mathrm{d} A_\mathrm{p}\left(\frac{1}{m_\mathrm{p}} + \frac{1}{M_\mathrm{p}}\right)\mathbf{u}_\mathrm{r}|\mathbf{u}_\mathrm{r}| + \mathbf{g}\,. \tag{I.3}$$

The equation above can be written in short as

$$\frac{\mathrm{d}\mathbf{u}_\mathrm{r}}{\mathrm{d}t} = -K_\mathrm{p}\mathbf{u}_\mathrm{r}|\mathbf{u}_\mathrm{r}| + \mathbf{g} \quad ; \quad K_\mathrm{p} \equiv \frac{1}{2}\rho C_\mathrm{d} A_\mathrm{p}\left(\frac{1}{m_\mathrm{p}} + \frac{1}{M_\mathrm{p}}\right). \tag{I.4}$$

Note that the p subscripts have been dropped in $\mathbf{u}_\mathrm{r}$ terms for convenience. The p subscript also will be dropped from some other variables later as convenient.

This is the drag equation, which has no solution in terms of elementary functions. Our solution approach first finds a solution neglecting gravity and then adds in a series for the gravity terms. $\mathbf{u}_\mathrm{r} \equiv \mathbf{u}_\mathrm{d} + \mathbf{u}_\mathrm{g}$ is the decomposition of $\mathbf{u}_\mathrm{r}$. The velocities $\mathbf{u}_\mathrm{r}$ and $\mathbf{u}_\mathrm{d}$ both have the same initial condition, $\mathbf{u}_\mathrm{r}(0) \equiv \mathbf{u}_\mathrm{p}(0) - \mathbf{U}_\mathrm{p}(0)$. And $\mathbf{u}_\mathrm{d}$ satisfies the drag equation without gravity, specifically

$$\frac{\mathrm{d}\mathbf{u}_\mathrm{d}}{\mathrm{d}t} = -K_\mathrm{p}\mathbf{u}_\mathrm{d}|\mathbf{u}_\mathrm{d}|\,. \tag{I.5}$$

The solution subject to these initial conditions is

$$\mathbf{u}_\mathrm{d} = \frac{\mathbf{u}(0) - \mathbf{U}(0)}{1 + \beta_\mathrm{p} t} \quad ; \quad \beta_\mathrm{p} \equiv K_\mathrm{p}|\mathbf{u}_\mathrm{r}(0)|\,. \tag{I.6}$$

We can decompose $\mathbf{u}_\mathrm{r}$ to find a series solution for $\mathbf{u}_\mathrm{g}$. The function $\mathbf{u}_\mathrm{g}$ can be written $\mathbf{u_g} = \mathbf{u}_\mathrm{r} - \mathbf{u}_\mathrm{d}$. So the differential equation for $\mathbf{u}_\mathrm{g}$ is

$$\frac{\mathrm{d}\mathbf{u}_\mathrm{g}}{\mathrm{d}t} = -K_\mathrm{p}(\mathbf{u}_\mathrm{r}|\mathbf{u}_\mathrm{r}| - \mathbf{u}_\mathrm{d}|\mathbf{u}_\mathrm{d}|) + \mathbf{g} \quad ; \quad \mathbf{u}_\mathrm{g}(0) = \mathbf{u}_\mathrm{r}(0) - \mathbf{u}_\mathrm{d}(0) = 0\,. \tag{I.7}$$

The Taylor series for $\mathbf{u}_\mathrm{g}$ about $t = 0$ is

$$\mathbf{u}_\mathrm{g} = \mathbf{u}_\mathrm{g}(0) + t\frac{\mathrm{d}\mathbf{u}_\mathrm{g}}{\mathrm{d}t}(0) + \frac{t^2}{2}\frac{\mathrm{d}^2\mathbf{u}_\mathrm{g}}{\mathrm{d}t^2}(0) + \frac{t^3}{6}\frac{\mathrm{d}^3\mathbf{u}_\mathrm{g}}{\mathrm{d}t^3}(0) + \cdots\,. \tag{I.8}$$

The task now is to find the derivatives of $\mathbf{u}_\mathrm{g}$ at $t = 0$. The first derivative, $\mathrm{d}\mathbf{u}_\mathrm{g}/\,\mathrm{d}t(0)$, can be seen to be $\mathbf{g}$ by inspection, as we would expect from the solution without drag. The second derivative is more complicated, and we find that

$$\frac{\mathrm{d}^2\mathbf{u}_\mathrm{g}}{\mathrm{d}^2t} = -K_\mathrm{p}\frac{\mathrm{d}}{\mathrm{d}t}(\mathbf{u}_\mathrm{r}|\mathbf{u}_\mathrm{r}| - \mathbf{u}_\mathrm{d}|\mathbf{u}_\mathrm{d}|) + \frac{\mathrm{d}\mathbf{g}}{\mathrm{d}t} = -K_\mathrm{p}\left(|\mathbf{u}_\mathrm{r}|\frac{\mathrm{d}\mathbf{u}_\mathrm{r}}{\mathrm{d}t} + \mathbf{u}_\mathrm{r}\frac{\mathrm{d}|\mathbf{u}_\mathrm{r}|}{\mathrm{d}t} - |\mathbf{u}_\mathrm{d}|\frac{\mathrm{d}\mathbf{u}_\mathrm{d}}{\mathrm{d}t} - \mathbf{u}_\mathrm{d}\frac{\mathrm{d}|\mathbf{u}_\mathrm{d}|}{\mathrm{d}t}\right),$$

$$\frac{\mathrm{d}^2\mathbf{u}_\mathrm{g}}{\mathrm{d}^2t}(0) = -K_\mathrm{p}\left(|\mathbf{u}_\mathrm{r}(0)|\frac{\mathrm{d}\mathbf{u}_\mathrm{r}}{\mathrm{d}t}(0) + \mathbf{u}_\mathrm{r}(0)\frac{\mathrm{d}|\mathbf{u}_\mathrm{r}|}{\mathrm{d}t}(0) - |\mathbf{u}_\mathrm{d}(0)|\frac{\mathrm{d}\mathbf{u}_\mathrm{d}}{\mathrm{d}t}(0) - \mathbf{u}_\mathrm{d}(0)\frac{\mathrm{d}|\mathbf{u}_\mathrm{d}|}{\mathrm{d}t}(0)\right). \tag{I.9}$$

The values of $\mathrm{d}\mathbf{u}_\mathrm{r}/\,\mathrm{d}t(0)$ and $\mathrm{d}\mathbf{u}_\mathrm{d}/\,\mathrm{d}t(0)$ are

$$\frac{\mathrm{d}\mathbf{u}_\mathrm{r}}{\mathrm{d}t}(0) = -K_\mathrm{p}\mathbf{u}_\mathrm{r}(0)|\mathbf{u}_\mathrm{r}(0)| + \mathbf{g}\,,$$
$$\frac{\mathrm{d}\mathbf{u}_\mathrm{d}}{\mathrm{d}t}(0) = -K_\mathrm{p}\mathbf{u}_\mathrm{r}(0)|\mathbf{u}_\mathrm{r}(0)|\,.$$

The derivative of the L_2 norm must now be found. It can be shown that for an arbitrary vector $\mathbf{a}$,

$$\frac{\mathrm{d}|\mathbf{a}|}{\mathrm{d}t} = \left(\frac{\mathbf{a}}{|\mathbf{a}|}\right)\cdot\frac{\mathrm{d}\mathbf{a}}{\mathrm{d}t}\,.$$

The derivatives of the vector norms can be written as

$$\frac{\mathrm{d}|\mathbf{u}_\mathrm{r}|}{\mathrm{d}t} = \left(\frac{\mathbf{u}_\mathrm{r}}{|\mathbf{u}_\mathrm{r}|}\right)\cdot\frac{\mathrm{d}\mathbf{u}_\mathrm{r}}{\mathrm{d}t} = \left(\frac{\mathbf{u}_\mathrm{r}(0)}{|\mathbf{u}_\mathrm{r}(0)|}\right)\cdot(-K_\mathrm{p}\mathbf{u}_\mathrm{r}(0)|\mathbf{u}_\mathrm{r}(0)| + \mathbf{g})\,, \tag{I.10}$$

$$\frac{\mathrm{d}|\mathbf{u}_\mathrm{d}|}{\mathrm{d}t} = \left(\frac{\mathbf{u}_\mathrm{d}}{|\mathbf{u}_\mathrm{d}|}\right)\cdot\frac{\mathrm{d}\mathbf{u}_\mathrm{d}}{\mathrm{d}t} = \left(\frac{\mathbf{u}_\mathrm{r}(0)}{|\mathbf{u}_\mathrm{r}(0)|}\right)\cdot(-K_\mathrm{p}\mathbf{u}_\mathrm{r}(0)|\mathbf{u}_\mathrm{r}(0)|)\,. \tag{I.11}$$

Once all of this is written out and expanded, the second derivative of $\mathbf{u}_\mathrm{g}$ at $t=0$ is

$$\frac{\mathrm{d}^2\mathbf{u}_\mathrm{g}}{\mathrm{d}^2t}(0) = -K_\mathrm{p}\left[\mathbf{u}_\mathrm{r}(0)\left(\frac{\mathbf{u}_\mathrm{r}(0)\cdot\mathbf{g}}{|\mathbf{u}_\mathrm{r}(0)|}\right)+\mathbf{g}|\mathbf{u}_\mathrm{r}(0)|\right] = -\beta_\mathrm{p}\left[\mathbf{u}_\mathrm{r}(0)\left(\frac{\mathbf{u}_\mathrm{r}(0)\cdot\mathbf{g}}{|\mathbf{u}_\mathrm{r}(0)|^2}\right)+\mathbf{g}\right]. \tag{I.12}$$

This has a term parallel to the initial relative velocity and a term parallel to the gravitational acceleration vector.

Assembling all these terms, $\mathbf{u}_\mathrm{g}$ can be found to be

$$\mathbf{u}_\mathrm{g} = \mathbf{g}t - \frac{\beta_\mathrm{p}t^2}{2}\left[\mathbf{u}_\mathrm{r}(0)\left(\frac{\mathbf{u}_\mathrm{r}(0)\cdot\mathbf{g}}{|\mathbf{u}_\mathrm{r}(0)|^2}\right)+\mathbf{g}\right]+O(t^3). \tag{I.13}$$

Assembling Eqs. (I.6) and (I.13), the solution for $\mathbf{u}_\mathrm{r}$ is

$$\mathbf{u}_\mathrm{r} = \frac{\mathbf{u}_\mathrm{r}(0)}{1+\beta_\mathrm{p}t}+\mathbf{g}t-\frac{\beta_\mathrm{p}t^2}{2}\left[\mathbf{u}_\mathrm{r}(0)\left(\frac{\mathbf{u}_\mathrm{r}(0)\cdot\mathbf{g}}{|\mathbf{u}_\mathrm{r}(0)|^2}\right)+\mathbf{g}\right]+O(t^3) \quad ; \quad \beta_\mathrm{p}\equiv K_\mathrm{p}|\mathbf{u}_\mathrm{r}(0)|. \tag{I.14}$$

Particle velocities and positions

The results of the previous section are not directly useful unless $\mathbf{U}(t)$ is known. $\mathbf{U}(t)$ can be found via the conservation of momentum and this leads to a solution for the particle velocities and positions.

The fluid and particles can gain or lose momentum due to gravity. Drag forces exchange momentum between the fluid and particle, which does not change the total momentum of the system. As gravity is the only force that can change momentum, the time derivative of the fluid-particle system momentum is $m_\mathrm{p}\mathbf{g}$ by Newton's second law, so we can write

$$m_\mathrm{p}\mathbf{u}+M_\mathrm{p}\mathbf{U} = m_\mathrm{p}\mathbf{u}(0)+M_\mathrm{p}\mathbf{U}(0)+m_\mathrm{p}\mathbf{g}t, \tag{I.15}$$

$$\mathbf{u}+\alpha_\mathrm{p}\mathbf{U} = \mathbf{u}(0)+\alpha_\mathrm{p}\mathbf{U}(0)+\mathbf{g}t \quad ; \quad \alpha_\mathrm{p}\equiv\frac{M_\mathrm{p}}{m_\mathrm{p}}. \tag{I.16}$$

Solving for $\mathbf{U}$ leads to

$$\mathbf{U}+\frac{\mathbf{u}_\mathrm{r}(0)}{1+\beta_\mathrm{p}t}+\mathbf{u}_\mathrm{g}+\alpha_\mathrm{p}\mathbf{U} = \mathbf{u}(0)+\alpha_\mathrm{p}\mathbf{U}(0)+\mathbf{g}t,$$

$$\mathbf{U} = \frac{\mathbf{u}(0)+\alpha_\mathrm{p}\mathbf{U}(0)+\mathbf{g}t-\mathbf{u}_\mathrm{g}}{1+\alpha_\mathrm{p}}-\frac{\mathbf{u}_\mathrm{r}(0)}{(1+\beta_\mathrm{p}t)(1+\alpha_\mathrm{p})}. \tag{I.17}$$

Eq. (I.17) can be substituted into Eq. (I.14) to get the solution for $\mathbf{u}$.

$$\begin{aligned}\mathbf{u} &= \mathbf{U}+\frac{\mathbf{u}(0)-\mathbf{U}(0)}{1+\beta_\mathrm{p}t}+\mathbf{u}_\mathrm{g}\\ &= \frac{\mathbf{u}(0)+\alpha_\mathrm{p}\mathbf{U}(0)+\mathbf{g}t-\mathbf{u}_\mathrm{g}}{1+\alpha_\mathrm{p}}-\frac{\mathbf{u}(0)-\mathbf{U}(0)}{(1+\beta_\mathrm{p}t)(1+\alpha_\mathrm{p})}+\frac{\mathbf{u}(0)-\mathbf{U}(0)}{1+\beta_\mathrm{p}t}+\mathbf{u}_\mathrm{g}\\ &= \frac{\mathbf{u}(0)}{1+\beta_\mathrm{p}t}+\frac{(\mathbf{u}(0)+\alpha_\mathrm{p}\mathbf{U}(0))\beta_\mathrm{p}t}{(1+\beta_\mathrm{p}t)(1+\alpha_\mathrm{p})}+\frac{\mathbf{g}t+\alpha_\mathrm{p}\mathbf{u}_\mathrm{g}}{1+\alpha_\mathrm{p}}\end{aligned}$$

$$\mathbf{u} = \frac{\mathbf{u}(0)}{1+\beta_\mathrm{p}t}+\frac{(\mathbf{u}(0)+\alpha_\mathrm{p}\mathbf{U}(0))\beta_\mathrm{p}t}{(1+\beta_\mathrm{p}t)(1+\alpha_\mathrm{p})}+\mathbf{g}t-\frac{\alpha_\mathrm{p}\beta_\mathrm{p}t^2}{2(1+\alpha_\mathrm{p})}\left[\mathbf{u}_\mathrm{r}(0)\left(\frac{\mathbf{u}_\mathrm{r}(0)\cdot\mathbf{g}}{|\mathbf{u}_\mathrm{r}(0)|^2}\right)+\mathbf{g}\right]+O(t^3) \tag{I.18}$$

Integrating Eq. (I.18) leads to an equation for the particle positions,

$$\mathbf{x} = \mathbf{x}_p(0)+\left(\frac{\mathbf{u}(0)+\alpha_\mathrm{p}\mathbf{U}(0)}{1+\alpha_\mathrm{p}}\right)t-\frac{\alpha_\mathrm{p}(\mathbf{u}(0)-\mathbf{U}(0))}{\beta_\mathrm{p}(1+\alpha_\mathrm{p})}\ln(\beta_\mathrm{p}t+1)+\frac{\mathbf{g}t^2}{2}-\frac{\alpha_\mathrm{p}\beta_\mathrm{p}t^3}{6(1+\alpha_\mathrm{p})}\left[\mathbf{u}_\mathrm{r}(0)\left(\frac{\mathbf{u}_\mathrm{r}(0)\cdot\mathbf{g}}{|\mathbf{u}_\mathrm{r}(0)|^2}\right)+\mathbf{g}\right]+O(t^4). \tag{I.19}$$

Implementation in FDS

The following solutions are used to advance the particle positions forward in time by Δt much like a normal finite-difference scheme. The exact solution is used for the case without drag.

$$\mathbf{u}^{n+1} = \frac{\mathbf{u}^n}{1+\beta_\mathrm{p}\Delta t} + \frac{(\mathbf{u}^n + \alpha_\mathrm{p}\mathbf{U}^n)\beta_\mathrm{p}\Delta t}{(1+\beta_\mathrm{p}\Delta t)(1+\alpha_\mathrm{p})} + \mathbf{g}\Delta t - \frac{\alpha_\mathrm{p}\beta_\mathrm{p}(\Delta t)^2}{2(1+\alpha_\mathrm{p})}\left[\mathbf{u}_\mathrm{r}^n\left(\frac{\mathbf{u}_\mathrm{r}^n\cdot\mathbf{g}}{|\mathbf{u}_\mathrm{r}^n|^2}\right)+\mathbf{g}\right] \tag{I.20}$$

$$\mathbf{x}^{n+1} = \mathbf{x}^n + \left(\frac{\mathbf{u}^n + \alpha_\mathrm{p}\mathbf{U}^n}{1+\alpha_\mathrm{p}}\right)\Delta t + \frac{\alpha_\mathrm{p}(\mathbf{u}^n - \mathbf{U}^n)}{\beta_\mathrm{p}(1+\alpha_\mathrm{p})}\ln(\beta_\mathrm{p}\Delta t + 1) + \frac{\mathbf{g}(\Delta t)^2}{2} \tag{I.21}$$

$$\alpha_\mathrm{p} \equiv \frac{\rho V_\mathrm{g}}{m_\mathrm{p} n_\mathrm{p}}$$

$$\beta_\mathrm{p} \equiv \frac{1}{2}\rho C_\mathrm{d} A_\mathrm{p}\left(\frac{1}{m_\mathrm{p}} + \frac{1}{M_\mathrm{p}}\right)|\mathbf{u}_\mathrm{r}(0)|$$

At first glance, the theoretical accuracy of the original equation for $\mathbf{x}^{n+1}$, Eq. (I.19), appears to be $O(\Delta t^3)$. But computation reveals it is actually $O(\Delta t^2)$. This is due to the velocity error reducing the overall accuracy of the position solution. The Δt^3 term, therefore, may be dropped from Eq. (I.19) without loss of accuracy. More details about this are available in the Lagrangian Particles chapter in the FDS Verification Guide [32].

Appendix J

Simplifications of the Radiation Transport Equation

Antti Paajanen, VTT, Finland

The Radiation Transport Equation (RTE) for particles is given by Eq. (6.35) and repeated here:

$$\mathbf{s}\cdot\nabla I_\lambda(\mathbf{x},\mathbf{s}) = -\Big[\kappa_\mathrm{p}(\mathbf{x},\lambda)+\sigma_\mathrm{p}(\mathbf{x},\lambda)\Big] I_\lambda(\mathbf{x},\mathbf{s}) + \kappa_\mathrm{p}(\mathbf{x},\lambda)\, I_{\mathrm{b,p}}(\mathbf{x},\lambda) + \frac{\sigma_\mathrm{p}(\mathbf{x},\lambda)}{4\pi}\int_{4\pi}\Phi(\mathbf{s},\mathbf{s}')\, I_\lambda(\mathbf{x},\mathbf{s}')\,\mathrm{d}\mathbf{s}' \quad \text{(J.1)}$$

An accurate computation of the in-scattering integral on the right hand side of Eq. (J.1) would be extremely time consuming and require a prohibitive amount of memory because the individual intensities in each location would have to be stored. The in-scattering integral can be approximated by dividing the total 4π solid angle into a "forward angle," $\delta\Omega^l$, and an "ambient angle," $\delta\Omega^* = 4\pi - \delta\Omega^l$. For compatibility with the FVM solver, $\delta\Omega^l$ is set equal to the control angle given by the angular discretization. However, it is assumed to be symmetric around the center of the control angle. Within $\delta\Omega^l$ the intensity is $I_\lambda(\mathbf{x},\mathbf{s})$ and elsewhere it is approximated as

$$U^*(\mathbf{x},\lambda) = \frac{U(\mathbf{x},\lambda) - \delta\Omega^l\, I_\lambda(\mathbf{x},\mathbf{s})}{\delta\Omega^*} \quad \text{(J.2)}$$

where $U(\mathbf{x})$ is the total intensity integrated over the unit sphere. The in-scattering integral in Eq. (J.1) can now be approximated as

$$\begin{aligned}\frac{\sigma_\mathrm{p}(\mathbf{x},\lambda)}{4\pi}\int_{4\pi}\Phi(\mathbf{s},\mathbf{s}')\, I_\lambda(\mathbf{x},\mathbf{s}')\;\mathrm{d}\mathbf{s}' &\approx \sigma_\mathrm{p}(\mathbf{x},\lambda)\left(\chi_\mathrm{f} I_\lambda(\mathbf{x},\mathbf{s}) + \frac{1}{\delta\Omega^*}(1-\chi_\mathrm{f})\int_{\delta\Omega^*} I_\lambda(\mathbf{x},\mathbf{s}')\;\mathrm{d}\mathbf{s}'\right)\\ &= \sigma_\mathrm{p}(\mathbf{x},\lambda)\Big(\chi_\mathrm{f}\, I_\lambda(\mathbf{x},\mathbf{s}) + (1-\chi_\mathrm{f})\, U^*(\mathbf{x},\lambda)\Big) \quad \text{(J.3)}\end{aligned}$$

where $\chi_\mathrm{f} = \chi_\mathrm{f}(r,\lambda) = \chi_\mathrm{f}(\mathbf{x},\lambda)$ is a fraction of the total intensity originally within the solid angle $\delta\Omega^l$ that is scattered into the same angle, $\delta\Omega^l$. The calculation of χ_f is discussed in section 6.3.3. Using the definition of U^* in Eq. (J.2), the RTE is now:

$$\mathbf{s}\cdot\nabla I_\lambda(\mathbf{x},\mathbf{s}) = -\kappa_\mathrm{p}(\mathbf{x},\lambda)\, I_\lambda(\mathbf{x},\mathbf{s}) + \kappa_\mathrm{p}(\mathbf{x},\lambda)\, I_{\mathrm{b,p}}(\mathbf{x},\lambda) + \sigma_\mathrm{p}(\mathbf{x},\lambda)\,(1-\chi_\mathrm{f})\left(\frac{U(\mathbf{x},\lambda) - \delta\Omega^l\, I_\lambda(\mathbf{x},\mathbf{s})}{\delta\Omega^*} - I_\lambda(\mathbf{x},\mathbf{s})\right) \quad \text{(J.4)}$$

An effective scattering coefficient is next defined

$$\overline{\sigma}_\mathrm{p}(\mathbf{x},\lambda) = \frac{4\pi}{4\pi-\delta\Omega^l}\Big(1-\chi_\mathrm{f}(\mathbf{x},\lambda)\Big)\;\sigma_\mathrm{p}(\mathbf{x},\lambda) \quad \text{(J.5)}$$

Using Eq. (J.5) and $\delta\Omega^* = 4\pi - \delta\Omega^l$, the scattering coefficient can be written as:

$$\sigma_{\mathrm{p}}(\mathbf{x},\lambda) = \frac{\overline{\sigma}_{\mathrm{p}}(\mathbf{x},\lambda)}{4\pi}\frac{\delta\Omega^*}{(1-\chi_{\mathrm{f}})} \tag{J.6}$$

Substituting this in the previous form of the RTE yields:

$$\mathbf{s}\cdot\nabla I_\lambda(\mathbf{x},\mathbf{s}) = -\kappa_{\mathrm{p}}(\mathbf{x},\lambda)\,I_\lambda(\mathbf{x},\mathbf{s}) + \kappa_{\mathrm{p}}(\mathbf{x},\lambda)\,I_{\mathrm{b,p}}(\mathbf{x},\lambda) + \frac{\overline{\sigma}_{\mathrm{p}}(\mathbf{x},\lambda)}{4\pi}\left(U(\mathbf{x},\lambda) - \left(\delta\Omega^l + \delta\Omega^*\right)I_\lambda(\mathbf{x},\mathbf{s})\right) \tag{J.7}$$

Using $\delta\Omega^l + \delta\Omega^* = 4\pi$, the RTE simplifies to:

$$\mathbf{s}\cdot\nabla I_\lambda(\mathbf{x},\mathbf{s}) = -\left[\kappa_{\mathrm{p}}(\mathbf{x},\lambda) + \overline{\sigma}_{\mathrm{p}}(\mathbf{x},\lambda)\right]I_\lambda(\mathbf{x},\mathbf{s}) + \kappa_{\mathrm{p}}(\mathbf{x},\lambda)\,I_{\mathrm{b,p}}(\mathbf{x},\lambda) + \frac{\overline{\sigma}_{\mathrm{p}}(\mathbf{x},\lambda)}{4\pi}U(\mathbf{x},\lambda) \tag{J.8}$$

Appendix K

Absorption Coefficients of Liquid Fuels

The burning rate of liquid pool fires depends in part on the convective and radiative heat feedback from the flames to the fuel surface. For large pool fires, radiation heat transfer dominates. Studies have been conducted to determine the spectra of emitted radiation [121] as well as to characterize radiation absorption by gases within the flame [122]. Depending on the fuel, thermal radiation can be absorbed at the surface or in depth. For fuels such as wood, most of the incident radiation is absorbed within a thin layer near the surface. For semi-transparent materials such as plastics or liquid fuels, thermal radiation may penetrate deeper. The in-depth radiation absorption by semi-transparent fuels has been studied for PMMA [123], polymer films [124] and liquid pool fires [121]. Most of the research related to the in-depth radiation absorption in liquids considers the boil-over of liquid pool fires on water [125]. The effect of in-depth radiation absorption on evaporation of fuel droplets has also received some attention [126]. Most liquids are highly selective absorbers, absorbing intensively in some wavelength regions while being transparent in others. This results in radiation transport models that are both computationally expensive and for which experimental data is scarce. In this appendix, we attempt to characterize the absorption of radiation by liquid fuels using effective absorption coefficients similar to those used in Refs. [127] and [128].

Where data on absorption coefficients of liquids exists in the open literature, such as the Coblentz Society data found on the NIST Chemistry WebBook [129], it usually only contains data for wavelengths from approximately 2.5 μm upwards. A large part of the total energy in the emission spectrum of flames may easily be contained in wavelengths shorter than 2.5 μm. However absorption spectra that begin from 1 μm exists for a few liquids, including toluene ([130], [131]), methanol [132], benzene [133] and water [134]. Furthermore, Ref. [121] includes spectrally resolved transmission spectra of ethanol, heptane, JP-8, and an ethanol-toluene blend. Complex refractive index spectra for a few diesel fuels were reported in Ref. [126]. Different diesel fuels have slightly different absorption spectra, due to differing additives. However the data reported in Ref. [126] can perhaps be used to obtain an order of magnitude estimate for the absorption coefficient of diesel fuel.

Often we are not interested in resolving the spectra of the transmitted radiation; rather, we are interested in modeling the total transmitted radiation. In these cases, it is convenient to write the radiation transport equations in terms of mean absorption coefficients. This is done to avoid the time-consuming integrations over all wavelengths. For this reason, a number of mean absorption coefficients have been introduced, such as the Rosselland-mean absorption coefficient and the Planck-mean absorption coefficient. These correspond to the optically-thin approximation and the Rosselland diffusion approximation of radiation transport. The absorption coefficients of liquids are highly wavelength dependent and are even transparent in some areas. In this case, the Planck-mean absorption coefficients are too large by several orders of magnitude. It is preferable to determine an effective absorption coefficient that attempts to replicate the absorption of radiation over a certain path length over which the majority of the radiation is absorbed.

Table K.1 lists effective absorption coefficients for a few selected liquids. It contains two types of absorption coefficients. One type is determined by assuming the incoming radiation is blackbody radiation at a temperature of 1450 K. The other type is based on actual flame radiation spectra. If the wavenumber range is listed, then a blackbody temperature 1450 K is assumed in calculating the transmission. If the wavenumber range is not listed, then transmission data from Ref. [121] is used. The path length is 3 mm in all cases.

The assumption of blackbody radiation is adequate for sooty flames in which radiation from soot dominates the flame radiation spectra. However, for fuels with low sooting flames, the incoming radiation spectrum differs considerably from the blackbody spectrum. This explains the large difference in listed absorption coefficients for ethanol and methanol. The ethanol absorption coefficient is based on actual emission spectra of an ethanol flame, whereas the methanol absorption coefficient is calculated based on the blackbody spectrum. The correct value for methanol is likely to be closer to that of ethanol.

Table K.1: Effective absorption coefficients for selected liquids.

Liquid	Wavenumber Range (1/cm)	Effective Absorption Coefficient, κ
JP-8 [121]	-	301.4
Ethanol-Toluene blend [121]	-	680.1
Ethanol [121]	-	1534.3
Heptane [121]	-	187.5
Toluene [131]	436-6500	160.8
Methanol[132]	2-8000	52
Water [134]	1-15000	1578
Benzene [133]	11.5-6200	123

Appendix L

Solving the 1-D Heat Conduction Equation

The 1-D heat conduction equation in Cartesian coordinates is:

$$\rho_s c_s \frac{\partial T_s}{\partial t} = \frac{\partial}{\partial x}\left(k_s \frac{\partial T_s}{\partial x}\right) + \dot{q}_s''' \tag{L.1}$$

In cylindrical and spherical coordinates, the equation becomes:

$$\rho_s c_s \frac{\partial T_s}{\partial t} = \frac{1}{r^I}\frac{\partial}{\partial r}\left(r^I k_s \frac{\partial T_s}{\partial r}\right) + \dot{q}_s''' \tag{L.2}$$

where I is 1 for cylindrical and 2 for spherical coordinates. Since for $I = 0$, the Cartesian formulation is recovered, from this point on we will consider the general form of the equation (L.2). The indexing system used for the discretization of the equations is shown in Fig. L.1.

The temperature at the center of each solid cell, $T_{s,i}$, is updated in time using a Crank-Nicolson scheme:

$$\begin{aligned}(\rho_s c_s)_i \frac{T_{s,i}^{n+1} - T_{s,i}^{n}}{\delta t} = \frac{1}{2 r_{c,i}^I \delta r_i}\left(r_i^I k_{s,i+\frac{1}{2}} \frac{T_{s,i+1}^{n} - T_{s,i}^{n}}{\delta r_{i+\frac{1}{2}}} - r_{i-1}^I k_{s,i-\frac{1}{2}} \frac{T_{s,i}^{n} - T_{s,i-1}^{n}}{\delta r_{i-\frac{1}{2}}}\right) \\ [0.1in] + \frac{1}{2 r_{c,i}^I \delta r_i}\left(r_i^I k_{s,i+\frac{1}{2}} \frac{T_{s,i+1}^{n+1} - T_{s,i}^{n+1}}{\delta r_{i+\frac{1}{2}}} - r_{i-1}^I k_{s,i-\frac{1}{2}} \frac{T_{s,i}^{n+1} - T_{s,i-1}^{n+1}}{\delta r_{i-\frac{1}{2}}}\right) + \dot{q}_s'''\end{aligned} \tag{L.3}$$

$k_{i+\frac{1}{2}}$ is the thermal conductivity at the border of the cells i and $i+1$, δr_i is the width of cell i, and $\delta r_{i+\frac{1}{2}}$ is the distance from the center of cell i to the center of cell $i+1$. The radial coordinate, $r_{c,i}$, denotes the cell center:

$$r_{c,i}^I = \begin{cases} (r_i^2 - r_{i-1}^2)/(2\,\delta r_i) & I = 1 \quad \text{(cylindrical)} \\ \sqrt{(r_i^3 - r_{i-1}^3)/(3\,\delta r_i)} & I = 2 \quad \text{(spherical)} \end{cases} \tag{L.4}$$

The temperatures at the front and back surface of a Cartesian slab (or center of a cylinder or sphere) are determined from the boundary conditions. In any of the coordinate systems, the boundary condition at the front surface is

$$-k_{s,1} \frac{T_{s,1}^{n+1} - T_{s,0}^{n+1}}{\delta r_{\frac{1}{2}}} = \dot{q}_c'' + \dot{q}_r'' \tag{L.5}$$

Note that $T_{s,0}$ does not represent the gas temperature, but rather it is used to establish the temperature gradient at the surface. Note also that the thermal conductivity is that of the first node. The convective heat flux is

$$\dot{q}_c'' = h\left(T_g - \frac{1}{2}\left(T_{s,\frac{1}{2}}^{n} + T_{s,\frac{1}{2}}^{n+1}\right)\right) \tag{L.6}$$

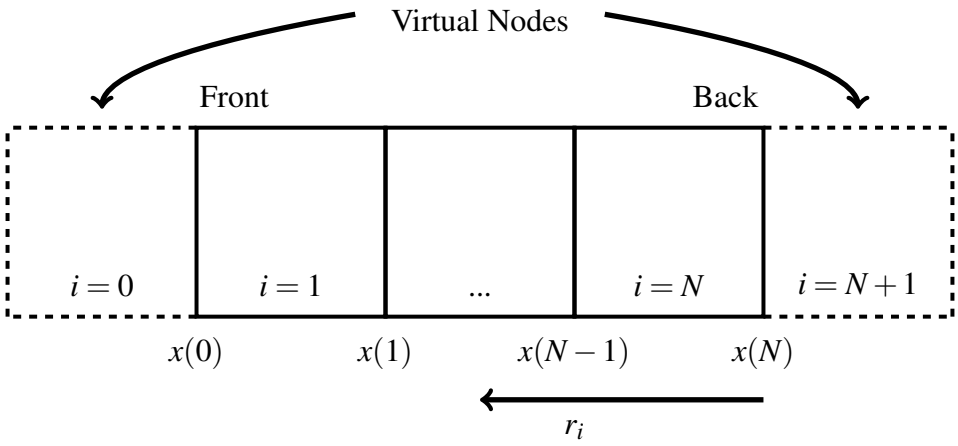

Figure L.1: Solid phase nodes and indexes. r is the radius from the back of the material.

where T_g is the gas temperature in the first grid cell abutting the surface, and $T_{s,\frac{1}{2}}$ is the surface temperature, defined as the average of $T_{s,0}$) and $T_{s,1}$). $(T^{n+1})^4$ can be approximated using a Taylor series expansion:

$$(T^{n+1})^4 \approx (T^n)^4 + 4\,(T^n)^3(T^{n+1}-T^n) \tag{L.7}$$

which leads to approximation for the radiative flux

$$\dot{q}''_r = \dot{q}''_{r,in} - \varepsilon\sigma\left(T^{n+1}_{s,\frac{1}{2}}\right)^4 \approx \dot{q}''_{r,in} - \varepsilon\sigma\left(T^{n}_{s,\frac{1}{2}}\right)^4 - 4\varepsilon\sigma\left(T^{n}_{s,\frac{1}{2}}\right)^3\left(T^{n+1}_{s,\frac{1}{2}} - T^{n}_{s,\frac{1}{2}}\right) \tag{L.8}$$

Now the front boundary condition is

$$-k_{s,1}\frac{T^{n+1}_{s,1}-T^{n+1}_{s,0}}{\delta r_{\frac{1}{2}}} \approx h\left(T_g - \frac{1}{2}\left(T^n_{s,\frac{1}{2}} + T^{n+1}_{s,\frac{1}{2}}\right)\right) + \dot{q}''_{r,in} - 4\varepsilon\sigma\left(T^n_{s,\frac{1}{2}}\right)^3 T^{n+1}_{s,\frac{1}{2}} + 3\varepsilon\sigma\left(T^n_{s,\frac{1}{2}}\right)^4 \tag{L.9}$$

The wall surface temperature is defined:

$$T_{s,\frac{1}{2}} = \frac{T_{s,1}+T_{s,0}}{2} \tag{L.10}$$

and therefore the boundary condition becomes

$$-k_{s,1}\frac{T^{n+1}_{s,1}-T^{n+1}_{s,0}}{\delta r_{\frac{1}{2}}} + \left(\frac{h}{2} + 4\varepsilon\sigma\left(T^n_{s,\frac{1}{2}}\right)^3\right)\frac{T^{n+1}_{s,1}+T^{n+1}_{s,0}}{2} \approx h\left(T_g - \frac{1}{2}T^n_{s,\frac{1}{2}}\right) + \dot{q}''_{r,in} + 3\varepsilon\sigma\left(T^n_{s,\frac{1}{2}}\right)^4 \tag{L.11}$$

Rearranging terms, the temperature at node 0 becomes:

$$T^{n+1}_{s,0} = \underbrace{\frac{\frac{k_{s,1}}{\delta r_{\frac{1}{2}}} - \left(\frac{1}{4}h + 2\varepsilon\sigma\left(T^n_{s,\frac{1}{2}}\right)^3\right)}{\frac{k_{s,1}}{\delta r_{\frac{1}{2}}} + \left(\frac{1}{4}h + 2\varepsilon\sigma\left(T^n_{s,\frac{1}{2}}\right)^3\right)}}_{\texttt{RFACF2}} T^{n+1}_{s,1} + \underbrace{\frac{h\left(T_g - \frac{1}{2}T^n_{s,\frac{1}{2}}\right) + \dot{q}''_{r,in} + 3\varepsilon\sigma\left(T^n_{s,\frac{1}{2}}\right)^4}{\frac{k_{s,1}}{\delta r_{\frac{1}{2}}} + \left(\frac{1}{4}h + 2\varepsilon\sigma\left(T^n_{s,\frac{1}{2}}\right)^3\right)}}_{\texttt{QDXKF}} \tag{L.12}$$

Note that `RFACF2` and similar names are used in the actual source code to represent these quantities. In case of non-insulated backing in Cartesian geometry, the temperature of virtual node $N+1$ is calculated the same way. For a Cartesian geometry with an insulated backing or for cylindrical and spherical geometries, ε, $\dot{q}''_{r,in}$, and h are set to 0.

After re-arranging the terms, Eq. (L.3) becomes (using the nomenclature of the source code) for each wall cell i:

$$B_i\, T_{i-1}^{n+1} + D_i\, T_i^{n+1} + A_i\, T_{i+1}^{n+1} = C_i \quad i = 1, ..., N \tag{L.13}$$

where

$$\begin{aligned}
A_i &= -\frac{k_{i+\frac{1}{2}}\,\delta t}{2(\rho_s c_s)_i}\,\frac{1}{r_{c,i}^I \delta r_i}\,\frac{r_i^I}{\delta r_{i+\frac{1}{2}}} \\
B_i &= -\frac{k_{i-\frac{1}{2}}\,\delta t}{2(\rho_s c_s)_i}\,\frac{1}{r_{c,i}^I \delta r_i}\,\frac{r_{i-1}^I}{\delta r_{i-\frac{1}{2}}} \\
C_i &= T_{s,i}^n - A_i\,(T_{i+1}^n - T_i^n) + B_i\,(T_i^n - T_{i-1}^n) \\
D_i &= 1 - A_i - B_i
\end{aligned} \tag{L.14}$$

To solve Eq. (L.13), a tri-diagonal linear solver is used:

$$\begin{aligned}
C_1 &= C_1 - B_1 \cdot \texttt{QDXKF} \\
C_N &= C_N - A_N \cdot \texttt{QDXKB} \\
\\
D_1 &= D_1 + B_1 \cdot \texttt{RFACF2} \\
D_N &= D_N + A_N \cdot \texttt{RFACB2} \\
\\
D_i &= D_i - \frac{B_i\, A_{i-1}}{D_{i-1}} \quad i = 2, ..., N-1 \\
C_i &= C_i - \frac{B_i\, C_{i-1}}{D_{i-1}} \quad i = 2, ..., N-1 \\
\\
C_N &= \frac{C_N}{D_N} \\
\\
T_{s,N}^{n+1} &= C_N \\
T_{s,i}^{n+1} &= \frac{C_i - A_i\, C_{i+1}}{D_i} \quad i = N-1, ..., 1
\end{aligned} \tag{L.15}$$